To the Graduate Council:

I am submitting herewith a dissertation written by Willie Tan King entitled "Feasibility of ^{252}Cf Source Driven Neutron Noise Measurements in Water Moderated Reactors." I recommend that it be accepted in partial fulfillment of the requirements for the degree of Doctor of Philosophy, with a major in Nuclear Engineering.

James C. Robinson

James C. Robinson, Major Professor

We have read this dissertation
and recommend its acceptance:

John T. Mihalczo

Lawrence F. Miller

B.F. Rogue

Harold C. Schweinler

Paul H. Stelson

Accepted for the Council:

L. Evans Reid

Vice Chancellor
Graduate Studies and Research

X

FEASIBILITY OF ^{252}Cf SOURCE DRIVEN NEUTRON NOISE MEASUREMENTS IN WATER MODERATED REACTORS

A Dissertation

Presented for the

Doctor of Philosophy

Degree

The University of Tennessee, Knoxville

Willie Tan King

August 1980

3045034

To Billie-Jo,

without whom this effort would have been meaningless.

ACKNOWLEDGEMENTS

Support for this work was provided in the form of a research assistantship through The University of Tennessee (Knoxville) from the Instrumentation and Controls Division of the Oak Ridge National Laboratory. The laboratory is operated by the Union Carbide Corporation for the United States Department of Energy.

In the process of planning, performing, and analyzing this experiment, I tapped the many resources of the laboratory and the university. I wish to express my appreciation to all who contributed their time and talents towards the completion of this work, in particular, to:

J. T. Mihalczo, from UT and ORNL, who provided guidance in the planning, execution, and analysis of this experiment,

R. S. Booth, from ORNL, for extending the support of the laboratory,

C. D. Cagle, J. H. Swanks, S. S. Hurt III, T. P. Hamrick, and E. B. Johnson, all from ORNL, for help in planning and obtaining permission for the experiment,

J. T. DeLorenzo, M. M. Chiles, K. Rush, N. W. Hill, C. O. McNew, and O. C. Cole, all from ORNL, in assisting in the assembly of the detection instrumentation system,

H. J. Stripling and G. W. Allin, both from ORNL, for guidance in the mechanical design of the detection instrumentation,

R. H. Miles, and others in the machine shop (ORNL), for fabricating aluminum and plexiglass pieces with very short notice,

J. L. Finchum, R. M. Childs, and others in the computer/terminal maintenance section (ORNL), for repairing and maintaining the signal analysis system,

D. N. Fry, R. C. Kryter, and V. K. Paré, all from ORNL, for sharing their experience in putting together the signal analysis hardware and in writing the signal analysis software,

K. E. Howard, E. D. Lance, J. R. Thomas, W. A. Duggins, T. M. Simms, and all the reactor operators (ORNL), for assisting in the performance of the experiment,

L. F. Miller, J. O. Johnson, C. A. Baldwin, from UT, J. A. Bucholz, D. R. Vondy, L. M. Petrie, J. R. Knight, and T. B. Fowler, from ORNL, for guidance in performing the core calculations,

J. C. Robinson, from UT, whose suggestions were invaluable in interpreting the measured results, and

M. W. Davis, from ORNL, for obtaining research materials and expediting the production of the graphics for this dissertation.

ABSTRACT

Previous experiments in fast critical assemblies demonstrated a method of determining reactivity from power spectral density measurements with ^{252}Cf. This method determines reactivity from properties of the reactor only at the subcritical state of interest, thus it does not require a calibration near delayed criticality. The interpretation of the measured data to obtain reactivity does not require knowledge of the relative or absolute values of the source intensity, knowledge of the detection efficiencies, or knowledge of the detection instrumentation frequency responses.

An experiment was performed at the Pool Critical Assembly to evaluate the possibility of ^{252}Cf source driven neutron noise spectral density measurements in light water moderated reactors. This experiment showed that using commercially available detectors, such measurements can be performed in a reasonable time, that is, the measurement of the quantity of interest (the ratio of spectral densities directly related to reactivity) at $\sim$12 dollars subscritical can be made to within 10% uncertainty in $\sim$15 min using detectors with efficiencies of 10^{-3} counts per reactor fission and $\sim$3-4 h using detectors with efficiencies of 10^{-4} counts per reactor fission.

Because of constraints on the location of the source and the detectors, slowly decaying higher modes affected the measured results and these effects increased with increasing subcriticality. Reactivities obtained from higher mode contaminated measurements do not compare favorably with reactivities obtained by other techniques.

It was found that a first order propagation of the standard errors of the measured coherence functions adequately described the standard error of the measured quantity of interest. An empirical equation was developed which describes the relationship of the standard errors of the measured coherence functions to the values of the true coherence functions and the measurement time. Therefore, the measurement time in a given system at a certain level of subcriticality using detectors with certain efficiencies can be estimated since the values of the true coherence functions can be estimated.

These first ^{252}Cf source driven neutron noise spectral density measurements in a water moderated system showed that such measurements are possible and may be applicable to such water moderated systems as: light water reactors, fuel reprocessing, fuel fabrication, and fuel storage facilities. However, care is required in locating the source and the detectors to assure proper interpretability of the measured quantities.

TABLE OF CONTENTS

CHAPTER		PAGE
1.	INTRODUCTION	1
2.	THEORY OF FREQUENCY DOMAIN REACTIVITY MEASUREMENTS WITH ^{252}Cf	7
	A. Detector Response Spectral Densities and Coherence Amplitudes	7
	B. Reactivity Determination	11
3.	DETECTION INSTRUMENTATION AND SIGNAL ANALYSIS SYSTEMS	15
	A. Detection Instrumentation System	15
	B. Signal Analysis System	17
4.	REACTOR EXPERIMENT	22
	A. Brief Description of the Reactor	22
	B. Detector Placement in the Reactor	22
	C. Experiment Procedures	24
5.	PRESENTATION AND DISCUSSION OF RESULTS	29
	A. Power Spectral Densities	29
	B. Prompt Neutron Decay Constants	31
	C. Coherence Amplitudes	36
	D. Ratio of Spectral Densities	40
	E. Measured Reactivities	42
	F. Effects of Higher Spatial Modes	50
	G. Measurement Time	65
6.	STATISTICAL ERRORS IN THE ESTIMATE OF THE RATIO OF SPECTRAL DENSITIES	69
	A. Convergence Characteristics of the Measured Coherence Function	69
	B. Convergence Characteristics of the Ratio of Measured Coherence Functions	72
7.	SUMMARY AND RECOMMENDATIONS	78
	A. Findings of the Experiment	78
	1. Measurement Time	78
	2. Interpretation of Measured Results	78

CHAPTER PAGE

3. Convergence Characteristics of the Ratio of Measured Spectral Densitites 79
4. Conclusions from the Experiment 79
B. Recommendations for Further Investigation 80
1. Systematic Study into the Effects of the Higher Spatial Harmonics 80
2. Measurement Time 81
3. More Measurements in a Variety of Systems 82

REFERENCES 83

APPENDICES 90

A. THEORY OF TIME AND FREQUENCY DOMAIN MEASUREMENTS WITH ^{252}Cf 91

B. DESCRIPTION OF THE DETECTION INSTRUMENTATION SYSTEM 115

C. DESCRIPTION OF THE POOL CRITICAL ASSEMBLY 135

D. NONLINEAR LEAST SQUARES FITTING ALGORITHM 141

E. PARAMETERS REQUIRED TO OBTAIN REACTIVITIES FROM MEASURED QUANTITIES 150

F. TABULATION OF MEASURED QUANTITIES AND INFERRED REACTIVITIES 193

G. INVERSE KINETICS ROD DROP ALGORITHMS 212

VITA 222

LIST OF TABLES

TABLE		PAGE
4.1.	Core Configurations for Reactivity Measurements	26
5.1.	Comparison of Reactivities (-$) Obtained from the Ratio of Spectral Densities, $G_{12}^{*}G_{13}/G_{11}G_{23}$, Using Different Detection Systems	46
5.2.	Inferred Decay Constants of the First Two Modes	60
B.1.	Specifications for the ^{3}He Proportional Counter	128
B.2.	Specifications for the Fission Chamber	133
E.1.	Nuclides Selected from the ENDF/B-IV 218 Group Library	152
E.2.	Energy Group Structure and Group Fluxes	154
E.3.	Material Compositions for the ORR Fuel and BSR Shim Element Models	159
E.4.	Material Composition for the BSR Shim Element Model with and without Control Rods	162
E.5.	Smeared Number Densities of the Different Homogenized Regions (Atoms/Barn-cm)	163
E.6.	Fractions of Smeared Number Densities Contained in Each Zone for the Zone Weighting Calculations	165
E.7.	Averaged 1/v Cross Sections $(cm/sec)^{-1}$	167
E.8.	Reflector Weights for KENO-IV	168
E.9.	Axial Leakage Cross Sections (DB^2) from KENO-IV $(cm)^{-1}$	171
E.10.	Calculated K-effectives	173
E.11.	Delayed Fractions for ^{235}U and ^{238}U Fissions	177
E.12.	Integrated Delayed Neutron Energy Spectrums	183
E.13.	Calculated Effective Delayed Neutron Fractions	184

TABLE		PAGE
E.14.	Some Calculated Reactor Kinetics Parameters	185
E.15.	Integrated Energy Spectrums of Fission Neutrons	188
E.16.	Ratios of Detection Efficiencies	190
E.17.	Delayed Neutron Precursor Decay Constants	192
F.1.	Run Identification for Spectral Density Measurements	194
F.2.	Ratios of Spectral Densities, $G^{*}_{12}G_{13}/G_{11}G_{23}$	195
F.3.	Reactivities (-$) from Ratios of Spectral Densities	196
F.4.	Prompt Neutron Decay Constants (sec^{-1}) Measured Using Li Detectors in the Current Mode	197
F.5.	Prompt Neutron Decay Constants (sec^{-1}) Measured Using Li Detectors in the Pulse Mode	198
F.6.	Prompt Neutron Decay Constants (sec^{-1}) Measured Using ^{3}He Detectors	199
F.7.	Prompt Neutron Decay Constants (sec^{-1}) Measured Using Fission Chambers	200
F.8.	Reactivities (-$) from α Measured Using Li Detectors in the Current Mode	201
F.9.	Reactivities (-$) from α Measured Using Li Detectors in the Pulse Mode	202
F.10.	Reactivities (-$) from α Using ^{3}He Detectors	203
F.11.	Reactivities (-$) from α Measured Using Fission Chambers	204
F.12.	Primary Fission Chamber Count Rates	205
F.13.	Auxiliary Fission Chamber Count Rates	206
F.14.	Reactivities (-$) from Primary Fission Chamber Count Rates by the Source Multiplication Technique	207

TABLE PAGE

F.15. Reactivities (-$) from Auxiliary Chamber Count Rates by the Modified Source Multiplication Technique 208

F.16. Low Frequency Coherence (γ^2_{23}) Amplitudes 209

F.17. Reactivities (-$) from Low Frequency Coherence (γ^2_{23}) Amplitudes 210

F.18. Reactivities (-$) by Other Methods 211

LIST OF FIGURES

FIGURE		PAGE
2.1.	Low Frequency Coherence Values for the FFTF and a Typical PWR at Various Reactivities for Detection Efficiencies of 10^{-4} Counts Per Reactor Fission	12
3.1.	Signal Analysis System Configuration	18
3.2.	Flowchart of the Signal Analysis Procedure	20
4.1.	Structural Arrangement of the Pool Critical Assembly . . .	23
4.2.	Core Configuration Used in the Spectral Density Measurements	25
5.1.	PSD of the ^{252}Cf System Signal Sampled at 2 kHz	30
5.2.	Corrected PSDs Measured at Core Configurations 1, 3, 4, and 7 Using a Li Detector (Detector 2) Operated in the Current Mode	32
5.3.	Corrected CPSDs Measured at Core Configurations 3 and 9 Using the ^{3}He Detection System	33
5.4.	Real and Imaginary Parts of the Corrected CPSD Between the ^{252}Cf Detector Signal and the Signal from a Li Detector (Detector 2) Operated in the Current Mode	34
5.5.	Prompt Neutron Decay Constant Obtained from the Product of the Angular Frequency and the Ratio of the Real to the Imaginary Parts of the Corrected CPSD Between the Outputs of Detectors 1 and 2	35
5.6.	Coherence Amplitudes Measured at Core Configurations 2 and 7 Using the Li Detection System Operated in the Pulse Mode	37
5.7.	Low Frequency Coherence Amplitudes at Various Reactivities Using the Li Detection System	38
5.8.	Low Frequency Coherence Amplitudes at Various Reactivities Using the ^{3}He and Fission Counting System . .	39
5.9.	Ratio of Spectral Densities, $G^{*}_{12}G_{13}/G_{11}G_{23}$, Measured at Core Configurations 3 and 9 Using the ^{3}He Detection System	41

FIGURE		PAGE
5.10.	Ratios of Spectral Densities Measured at ∿1.71 Dollars Subcritical Using the Li Detection System Operated in the Pulse Mode with the ^{252}Cf Detection System Discrimination Level Set at Various Points	43
5.11.	Reactivities Obtained from the Ratio of Spectral Densities Measured with the ^{252}Cf Source at Core Locations E-5 and C-6 and Using the Li Scintillators Operated in the Pulse Mode	45
5.12.	Reactivities from Ratios of Spectral Densities Compared with Reactivities from Prompt Neutron Decay Constants Obtained from CPSD23 Using the Li Detection System	47
5.13.	Reactivities from Ratios of Spectral Densities Compared with Reactivities from Prompt Neutron Decay Constants Obtained from CPSD23 Using the ^{3}He and Fission Counting Systems	48
5.14.	Percent Difference of the Reactivities from the CPSD23 Breakfrequencies and from the Ratios of Spectral Densities	49
5.15.	Spatial Shapes of the First Even and Odd Modes	54
5.16.	Spatial Distributions of the Neutron Density at Different Times after the Introduction of a Source Pulse at Location 0.5 (Half the Distance from the Center to the Edge)	56
5.17.	Prompt Neutron Decay Constant from the Product of the Angular Frequency and the Ratio of the Real to the Imaginary Parts of the Corrected CPSD12 Measured at Core Configuration 7 Using a Fission Chamber	59
5.18.	Prompt Neutron Decay Constant Obtained from the Product of the Angular Frequency and the Ratio of the Real to the Imaginary Parts of the CPSD12 Measured at Core Configurations 3 and 9 Using the ^{3}He Detection System and Plotted as a Function of Normalized Frequency	61
5.19.	Corrected Squared Magnitude of the CPSD12 Measured at Core Configuration 9 Using the Fission Counting System . .	63
5.20.	Ratio of Spectral Densities Measured at Core Configurations 3 and 9 Using the ^{3}He Detectors and Plotted on a Normalized Frequency Scale	66

FIGURE		PAGE
6.1.	Schematic of the Operational Amplifier Manifold Setup Used in Producing Signal Pairs with Known Coherences . . .	70
6.2.	Curves of Measured Coherence as a Function of the Number of Data Blocks Averaged for Various Values of "True" Coherence	73
6.3.	Curves of Standard Deviation of Measured Coherence as a Function of the Number of Data Blocks Averaged for Various Values of "True" Coherence	74
6.4.	Comparison Between the Predicted and the Measured Relative Standard Deviations of the Ratios of Spectral Densities	76
6.5.	Comparison Between the Predicted and the Measured Standard Deviations of the Ratio of Spectral Densities Obtained from Previous Measurements in a Uranium Metal Sphere and Uranium Metal Cylinders	77
A.1.	Block Diagram for Detector Response Spectral Densities . .	106
B.1.	Block Diagram of the ^{252}Cf Fission Counting System	116
B.2.	Sketch of the Double Contained Fission Chamber Containing ^{252}Cf	117
B.3.	^{252}Cf Fission Chamber Output after Preamplifier and Integrator	119
B.4.	^{252}Cf Count Rates at Various Discriminator Settings . . .	120
B.5.	Li Glass Scintillator and Voltage Divider Network	122
B.6.	Block Diagram of the Pulse Mode Li Glass Scintillation System	124
B.7.	Block Diagram of the Current Mode Li Glass Scintillation System	126
B.8.	Block Diagram of the ^{3}He Proportional Counting System . .	127
B.9.	Sketch of a ^{3}He Proportional Counter	129
B.10.	Block Diagram of the Fission Counting System	131
B.11.	Sketch of a Fission Counter	134

FIGURE		PAGE
C.1.	Standard BSR Fuel Element	136
C.2.	Standard BSR Shim Element	137
C.3.	Standard ORR Fuel Element	139
C.4.	Cross Section View of the Control Rods	140
E.1.	Flow Diagram of the Core Calculation Procedure	151
E.2.	ORR Fuel and BSR Shim Element Models for the CSAS2 Calculation Sequence	158
E.3.	Model of the BSR Shim Element for the Cell Weighting Calculations	161
E.4.	Reactor Model for the Zone Weighting Calculations	164
E.5.	Reactor Model for the KENO-IV Calculations	169
E.6.	Reactor Model for the 2-D, X-Y, Diffusion, k-Calculations	172
E.7.	Comparison Between the Calculated and Measured Ratios of Auxiliary Fission Chamber Count Rates with the ^{252}Cf Source at Core Location E-5 to the Count Rates with the Source at Various Locations Around the Core	175
E.8.	Energy Spectrum of the Group 1 Delayed Neutrons	178
E.9.	Energy Spectrum of the Group 2 Delayed Neutrons	179
E.10.	Energy Spectrum of the Group 3 Delayed Neutrons	180
E.11.	Energy Spectrum of the Group 4 Delayed Neutrons	181
E.12.	Energy Spectrum of the Groups 5 and 6 Delayed Neutrons	182
E.13.	Energy Spectrum of the ^{252}Cf Fission Neutrons	187

CHAPTER 1

INTRODUCTION

Detected counts in a reactor depend on other neutrons in the fission chains because of the chain-reacting nature of nuclear processes. Therefore, the dynamic properties of the nuclear system determine the statistical properties of the count sequence.[1] The relationship of the count sequence to the dynamics of the reactor is the basis of a variety of reactivity measurement techniques in both the time[1-8] and frequency[9-14] domains. The domain in which measurements are performed is selected for convenience and efficiency of data collection. This work is concerned with the frequency domain reactivity measurement method proposed by Mihalczo and Paré[14] and tested in measurements in fast critical assemblies.[15] The advantages of this technique over other methods are explained in the following brief historical account of frequency domain reactivity measurement methods.

Reactivity measurements in subcritical systems using detector response spectral densities were first reported by Ricker and others.[9] They measured the power spectral density (PSD) of the response of a detector observing neutrons from fission chains in the reactor. After corrections for the frequency response of the electronic components of the detection instrumentation, the measured PSD can be broken down into the sum of two parts: a white noise component arising from the statistical nature of the detection process (detection noise) and a component proportional to the response of a single-order lag system (frequency

response of the reactor production rate to the source) whose breakfrequency is the prompt neutron decay constant, α. The prompt neutron decay constant is evaluated by least squares analysis on the measured PSD.

The neutron multiplication, k, can be obtained from α if both the prompt neutron lifetime, ℓ, and the effective total delayed fraction, β, are known. If ℓ and β are unknown, but are assumed not to change with reactivity, then the reactivity, in dollar units, can be inferred from the ratio of α to α_c, the prompt neutron decay constant measured at delayed criticality. This measured reactivity can be corrected using the ratios of the values of ℓ and β at delayed criticality to their values at the state of interest. (A calculation of these ratios is usually more accurate than a calculation of ℓ and β directly.)

As the reactor gets more subcritical, the white noise component begins to dominate the PSD such that the determination of α becomes more difficult. Almost simultaneously, Nomura[10] from Japan and Borgwaldt and Stegemann[11] from Germany suggested measuring the cross power spectral density (CPSD) between the responses of two detectors observing neutrons from fission chains in the reactor. The CPSD is a measure of the amplitude of the correlated components of the two signals. After correcting for the frequency response of the detection instrumentation, the measured CPSD, unlike the PSD, does not contain a white noise component since detection noise in one detector is independent of that in the other. Therefore, the use of the CPSD makes possible, reactivity measurements in systems far more subcritical than was possible with PSD

measurements. The prompt neutron decay constant is estimated by a least squares fit of the measured CPSD to the same single-order lag model.

Mihalczo and Paré[14] reported that α could be evaluated from the same single-order lag model by using two detectors: one detecting fissions of a ^{252}Cf source inserted into the core, and the other observing neutrons from reactor fission chains initiated by the source. The square of the magnitude of the corrected CPSD between the responses of these detectors is proportional to the frequency response of the reactor production rate to the source. They also presented a different method of obtaining α from this corrected CPSD. The product of the angular frequency, ω, and the ratio of the real part to the imaginary part is equal to α. An estimate of α is obtained by averaging this product over frequency. This product is equal to α and is constant in frequency only if the single-order lag model adequately describes the frequency response of the reactor production rate to the source. The presence of higher spatial decay modes will make the value of the product a function of frequency.

Seifritz[12] proposed using the coherence between the responses of two detectors observing neutrons from fission chains in the reactor. This method requires a calibration measurement at or near delayed criticality, and in addition, requires the knowledge of the changes in detection efficiencies from the calibration state to the state of interest. Ackermann and Buhl[13] have shown that this change can be substantial.

Time domain measurements of the ratio of correlated counts per ^{252}Cf fission in a randomly pulsed neutron measurement to correlated

counts per count in a Rossi-α measurement suggested a frequency domain equivalent for obtaining the reactivity. Mihalczo and Paré[14] proposed a method of determining reactivity by using three detectors: one measuring fissions of a ^{252}Cf source in the reactor (detector 1) and a pair detecting neutrons from fission chains in the reactor (detectors 2 and 3). The ratio of spectral densities, $G_{12}^{*}G_{13}/G_{11}G_{23}$,[a] is proportional to the reactivity in k units (* denotes complex conjugate). The proportionality constant depends on properties of the reactor at the state of interest which are easily measured or calculated and are weak functions of reactivity. It also depends on properties of the ^{252}Cf detector which can be determined outside the reactor. It does not require knowledge of the inherent source strength, detection efficiencies, and frequency response of the detection instrumentation. This method does not require a calibration at or near delayed criticality nor does it require correction for the change in the prompt neutron lifetime.

This method of determining reactivity could be used where sufficient material to achieve criticality is not available or where loading to criticality is undesirable, for example, fuel reprocessing tanks, new and spent fuel storage pools. This method can be used in the initial loading of reactors where subcriticality determination cannot depend on some calibration near delayed criticality.

If spectral density measurements with ^{252}Cf can provide the subcritical reactivity during the initial loading of light water moderated reactors, safety could be enhanced and loading time may be decreased.[16]

---

[a] These quantities are defined in Eqs. (2.1) thru (2.4) in Chap. 2.

Also, with the development of more sensitive (gamma insensitive) fission counters,[17-19] this method may be made useful during refueling and perhaps, during postaccident recovery operations.

Mihalczo and Paré[16] suggested that this measurement might be feasible in light water moderated systems. Compared to measurements in the critical mock-up of the Fast Flux Test Facility (FFTF) they estimated that measurements in light water moderated systems would take 300 times longer to obtain results of comparable precision. However, this measurement time is not excessive, that is, reactivities can be measured to within 10% uncertainty in 2 hours at 30 dollars subcritical with detection efficiencies of 10^{-4} counts per reactor fission.

These estimates are extrapolations from measurements in fast critical assemblies. No measurements in light water moderated systems have been reported. The purpose of this work is to determine if these measurements are possible in light water moderated reactors by performing an experiment in a small plate-type light water moderated research reactor with a prompt neutron lifetime ($\sim$57 μs) which is $\sim$3 times longer than that of a pressurized water reactor (PWR) and $\sim$1.5 times longer than that of a boiling water reactor (BWR). Since the measurement time for a given precision in the spectral densities is proportional to the prompt neutron lifetime (that is, inversely proportional to the bandwidth over which the spectral densities can be measured), these experiments are severe tests of the possibility of performing such measurements in light water reactors (LWRs). In particular, this experiment is being performed to determine if measurements in a light water moderated system can be

performed in a reasonable time, and to determine what problems may arise in the interpretation of the measured results. Also, the convergence characteristics of the ratio of measured spectral densities will be studied to determine if measurement times to achieve a certain precision can be predicted.

A review of the theory of reactivity measurements with ^{252}Cf is presented in Chap. 2. Chapter 3 describes the detection instrumentation, signal analysis instrumentation, and signal analysis procedures. Chapter 4 describes the reactor and the experiment procedures. Chapter 5 presents and discusses the results of the experiment. An analysis of the statistical error is shown in Chap. 6. Chapter 7 summarizes the findings of this experiment and lists some recommendations for further investigation. Finally, the appendices at the end of the text provide details of the theory and the experiment as well as tabulations of the measured results.

CHAPTER 2

THEORY OF FREQUENCY DOMAIN REACTIVITY MEASUREMENTS WITH ^{252}Cf

Consider a subcritical reactor with three detectors: a fission chamber (detector 1) which contains the spontaneous fission isotope, ^{252}Cf, and a pair (detectors 2 and 3) that detects neutrons from fission chains in the reactor. The ^{252}Cf chamber serves as a source of neutron noise for the reactor and, as a detector, provides a highly correlated electrical representation of that noise for use in the analysis. Detectors 2 and 3 detect neutrons emitted from fission chains initiated by neutrons from the spontaneous fission of ^{252}Cf, by neutrons from the spontaneous fission of inherent sources, and by delayed neutrons.

A. Detector Response Spectral Densities and Coherence Amplitudes

The one-sided PSDs[a] of the detector responses and the CPSDs between them (derived in detail in Appendix A) are as follows:

$$G_{11}(\omega) = 2\,|h_1(\omega)|^2\,\{31\,F_c\overline{q_\alpha^2} + F_c\overline{q_c^2}\}\,, \tag{2.1}$$

$$G_{22}(\omega) = |h_2(\omega)|^2\left\{2W_2F\overline{q_2^2} + \frac{W_2^2\overline{q_2^2}}{\overline{\nu_p^2}}\,|H_s(\omega)|^2\,G_s\right\}\,, \tag{2.2}$$

---

[a] Spectral density function defined for frequencies from 0 to ∞. See ref. 20.

$$G_{12}(\omega) = 2h_1^*(\omega)h_2(\omega)\bar{q}_c \frac{W_2\bar{q}_2}{\bar{\nu}_p} H_s(\omega) \frac{\bar{\nu}_c F_c I_c}{I} , \text{ and} \tag{2.3}$$

$$G_{23}(\omega) = h_2^*(\omega)h_3(\omega) \frac{W_2\bar{q}_2}{\bar{\nu}_p} \frac{W_3\bar{q}_3}{\bar{\nu}_p} |H_s(\omega)|^2 G_s , \tag{2.4}$$

where

$h_1(\omega)$, $h_2(\omega)$, $h_3(\omega)$ = response of the electronic components of detection systems 1, 2, and 3 at angular frequency ω,

$\bar{q}_c$, $\bar{q}_\alpha$ = average charge released in detector 1 per ^{252}Cf spontaneous fission, average charge per α-decay,

$\bar{q}_2$, $\bar{q}_3$ = average charge released per interaction in detectors 2 and 3,

W_2, W_3 = detection efficiency of detection systems 2 and 3 in counts per reactor fission (W_1 = 1 count per ^{252}Cf fission),

G_s = PSD of the reactor noise-equivalent source,

$$= 2\bar{\nu}_p^2 XFR \left\{1 + \frac{V}{XR} + \frac{F_i I_i}{FI} \frac{\overline{\nu_i^2}}{XR\bar{\nu}_p^2} + \frac{F_c I_c}{FI} \frac{\overline{\nu_c^2}}{XR\bar{\nu}_p^2}\right\},$$

$$= 2\bar{\nu}_p^2 X'FR , \tag{2.5}$$

X = neutron dispersion number or Diven factor,

$$= \frac{\overline{\nu_p(\nu_p - 1)}}{\bar{\nu}_p^2} , \tag{2.6}$$

X' = modified neutron dispersion number defined in Eq. (2.5),

R = factor which corrects point kinetics for spatial effects,[21-23]

I, I_c, I_i = average importance of a neutron from reactor fission, ^{252}Cf fission, and inherent source fission,

F, F_c, F_i = reactor fission rate, ^{252}Cf fission rate, and inherent source fission rate,

$\bar{\nu}_p$, $\bar{\nu}_c$, $\bar{\nu}_i$ = average number of prompt neutrons per reactor fission, per ^{252}Cf fission, and per inherent source fission,

$$\bar{V} = \frac{(2\beta - \rho)}{(1 - \beta)\bar{\nu}_p} , \tag{2.7}$$

β = effective total delayed fraction,

ρ = reactivity,

$$= \frac{(k - 1)}{k} , \tag{2.8}$$

k = neutron multiplication factor,

$H_s(\omega)$ = response of the reactor production rate to the source at angular frequency ω,

$$= \frac{1}{j\omega\Lambda + (\beta - \rho)} , \quad (\omega \gg \text{any } \lambda_i) \tag{2.9}$$

$j = \sqrt{-1}$,

Λ = neutron generation time, and

λ_i = delayed group i precursor decay constant.

The expressions for $G_{33}(\omega)$ and $G_{13}(\omega)$ are similar to Eqs. (2.2) and (2.3) respectively.

The coherence between detector outputs can be written as

$$\gamma_{12}^2(\omega) = \frac{|G_{12}(\omega)|^2}{G_{11}(\omega)G_{22}(\omega)} = \frac{1}{B_c(1 + C_\alpha)} \left(\frac{\bar{\nu}_c I_c}{\bar{\nu}_p I} \right)^2 \frac{F_c}{F} \frac{1}{RX'} \frac{1}{1 + 1/Q_2(\omega)} , \tag{2.10}$$

and

$$\gamma_{23}^2(\omega) = \frac{|G_{23}(\omega)|^2}{G_{22}(\omega)G_{33}(\omega)} = \frac{1}{1 + 1/Q_2(\omega)} \frac{1}{1 + 1/Q_3(\omega)} , \tag{2.11}$$

where

$$B_c = \overline{q_c^2}/\overline{q_c^2} , \quad B_2 = \overline{q_2^2}/\overline{q_2^2} , \quad B_3 = \overline{q_3^2}/\overline{q_3^2} , \tag{2.12}$$

$$C_\alpha = 31 \, \overline{q_\alpha^2}/\overline{q_c^2} , \tag{2.13}$$

$$Q_2(\omega) = \frac{W_2 X' R}{B_2 \Lambda^2} \frac{1}{\alpha^2 + \omega^2} , \quad Q_3(\omega) = \frac{W_3 X' R}{B_3 \Lambda^2} \frac{1}{\alpha^2 + \omega^2} , \tag{2.14}$$

and

α = prompt neutron decay constant,

$$= \frac{(\beta - \rho)}{\Lambda} . \tag{2.15}$$

The expression for $\gamma_{13}^2(\omega)$ is similar to Eq. (2.10). Low frequency ($\omega \ll \alpha$) coherence values were calculated using parameters for the Fast Flux Test Facility (FFTF)[15] and a typical pressurized water reactor (PWR)[16] at various reactivities (Fig. 2.1). A detection efficiency of 10^{-4} counts per reactor fission was used in the calculations. It was projected that measurement times in light water moderated systems would be much longer than in fast systems like the FFTF because of the lower coherence values. Also, α, which determines the frequency range over which the spectral density could be measured, for a light water moderated system is much smaller than α for fast systems.

B. Reactivity Determination

Consider the following ratio of spectral densities:

$$\frac{G_{12}^*(\omega)G_{13}(\omega)}{G_{11}(\omega)G_{23}(\omega)} = \frac{\gamma_{12}(\omega)\gamma_{13}(\omega)}{\gamma_{23}(\omega)} = \frac{1}{B_c(1 + C_\alpha)} \left(\frac{\bar{\nu}_c I_c}{\bar{\nu}_p I} \right)^2 \frac{1}{RX'} \frac{F_c}{F} . \quad (2.16)$$

Equation (2.16) is independent of frequency. The constancy of the measured ratio of spectral densities as a function of frequency could be used to validate the point kinetics model of the system being measured. Reactivity can be expressed as the source emission rate divided by the production rate in the reactor (Sections C and D, Appendix A), that is

$$-\rho = \left(\frac{F_c I_c \bar{\nu}_c}{I} + \frac{F_i I_i \bar{\nu}_i}{I} \right) \Bigg/ F\bar{\nu} \approx \frac{F_c I_c \bar{\nu}_c + F_i I_i \bar{\nu}_i}{FI\bar{\nu}_p} , \quad (2.17)$$

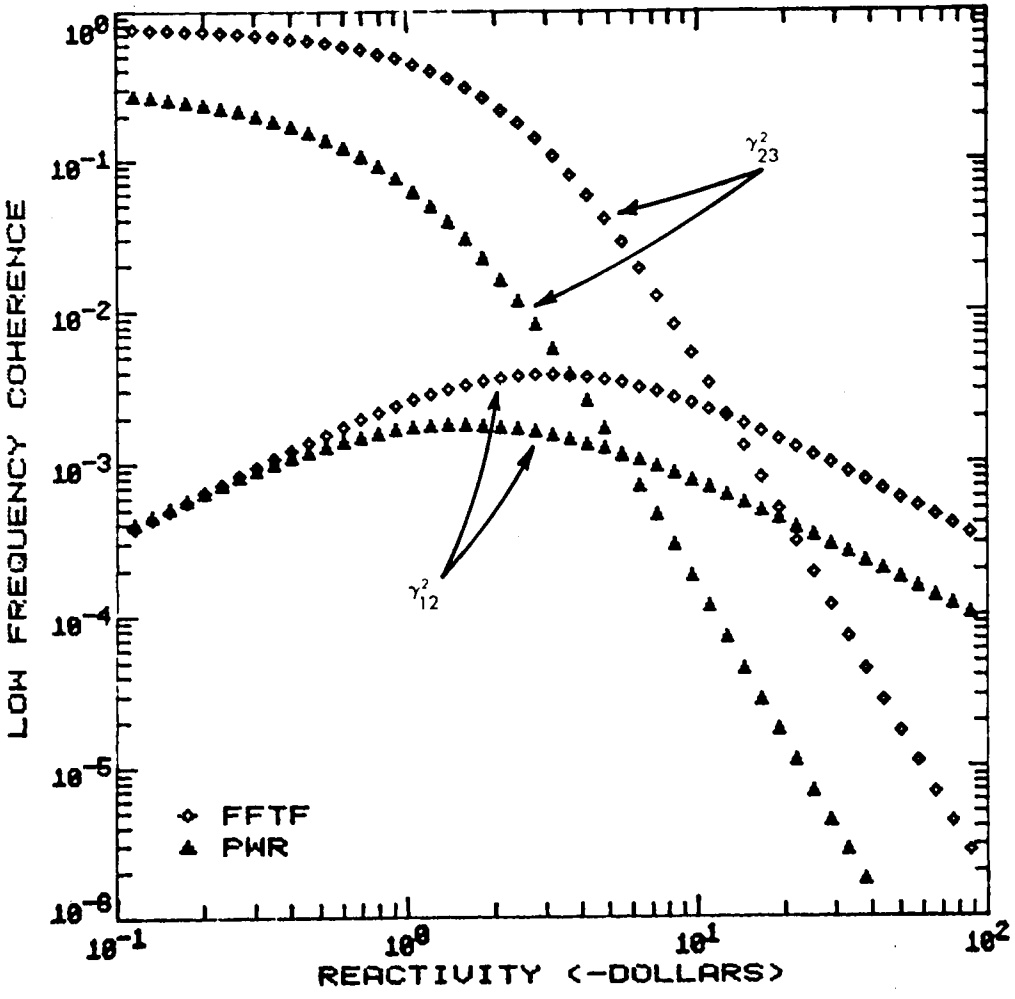


Fig. 2.1. Low frequency coherence values for the FFTF and a typical PWR at various reactivities for detection efficiencies of 10^{-4} counts per reactor fission (refs. 15 and 16).

where $\bar{\nu}$ is the average number of neutrons per reactor fission. The reactivity can be obtained by combining Eqs. (2.16) and (2.17) and using the expression for X' in Eq. (2.5), that is,

$$-\rho = Y_6 Y \frac{Y_1 Y_4}{1 - Y_6 Y \frac{Y_1 Y_5}{\beta}} , \tag{2.18}$$

where

$$Y_6 = \frac{G_{12}^*(\omega) G_{13}(\omega)}{G_{11}(\omega) G_{23}(\omega)} = \frac{\gamma_{12}(\omega)\gamma_{13}(\omega)}{\gamma_{23}(\omega)} , \tag{2.19}$$

$$Y = \frac{F_c I_c \bar{\nu}_c + F_i I_i \bar{\nu}_i}{F_c I_c \bar{\nu}_c} , \tag{2.20}$$

$$Y_1 = \frac{B_c (1 + C_\alpha) RXI \bar{\nu}_p}{I_c \bar{\nu}_c} , \tag{2.21}$$

$$Y_2 = \left(\frac{\overline{\nu_i^2}}{\bar{\nu}_i} (Y - 1) + \frac{\overline{\nu_c^2}}{\bar{\nu}_c} \right) \Bigg/ XRY , \tag{2.22}$$

$$Y_3 = \frac{2\beta}{XR(1 - \beta)\bar{\nu}_p} , \tag{2.23}$$

$$Y_4 = 1 + Y_3 , \tag{2.24}$$

and

$$Y_5 = \frac{Y_3}{2} + \frac{\beta Y_2}{\bar{\nu}_p} . \tag{2.25}$$

Equation (2.18) does not depend on detection efficiency nor on frequency response of the detection instrumentation, but it does depend on the properties of the fission counter (for current mode operation) containing the ^{252}Cf source, $B_c(1 + C_\alpha)$, which can be determined outside the reactor. The ratio of effective neutron production rates, Y, can be determined from the change in count rates when the ^{252}Cf source is inserted into the subcritical reactor. The value of R can be determined from calculations and other measurements and is insensitive to large changes in reactivity. The values of X and the number of neutrons per fission are known, and the relative importance I/I_c, can be calculated or obtained from other measurements. The use of Eq. (2.18) results in reactivity in k units. This method requires neither a calibration near delayed criticality nor corrections for neutron lifetime and detection efficiency changes.

For the pulse mode operation of the ^{252}Cf detection system in which all the alpha pulses are discriminated, $C_\alpha = 0$ and $B_c = 1$. Thus for pulse mode operation, the reactivity determination does not depend on the properties of the ^{252}Cf detection system.

CHAPTER 3

DETECTION INSTRUMENTATION AND SIGNAL ANALYSIS SYSTEMS

The detection instrumentation and signal analysis systems used in this experiment were essentially the same as those used in previous reactor noise measurements.[15,24] The detection instrumentation system was slightly modified because some instruments were no longer available or were not suitable for the environment of the present experiment. The signal analysis hardware had been upgraded; therefore, new software was written to take advantage of the added capabilities of the new system.

A. Detection Instrumentation System

The nuclear instrumentation consisted of:

1. a ^{252}Cf fission counting system,
2. a two-channel Li glass scintillation system,
3. a two-channel ^{3}He proportional counting system, and
4. a two-channel fission counting system.

The ^{252}Cf system (0.13 μg ^{252}Cf in the ionization chamber) provided the signal designated as coming from detector 1. This system is similar to that used and described by Mihalczo, and others.[15] Signals from detectors 2 and 3 were supplied primarily by the Li system with the ^{3}He and fission counting systems serving as alternatives. The Li, ^{3}He, and fission counting systems were similar to those described by Mathis, and others.[24] Detailed descriptions of all instrumentation systems are given in Appendix B.

The experiment was planned to be performed in an assembly of newly fabricated fuel elements; therefore, problems with background gamma radiation were not anticipated. Neutron- and gamma-sensitive Li glass scintillators (38.1 mm diameter and 25.4 mm thick with 6.6 wt% Li enriched to 95% ^{6}Li) were chosen to provide a highly efficient detection system. Prior to the start of the experiment, it was learned that four irradiated ($\sim$5 R/h at the surface) fuel elements modified to receive control rods had to be used. Assembly of the ^{3}He proportional counting system was started in case the Li glass scintillators were overwhelmed by the background gamma radiation.

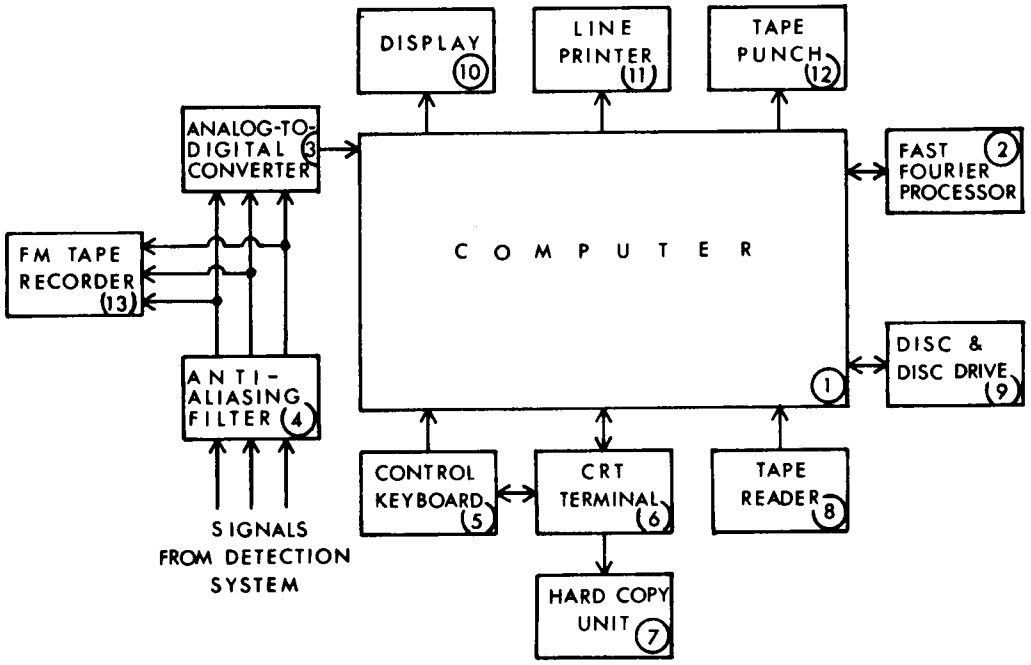
Attempts were made to alleviate the effects of the gamma radiation by shielding the scintillators from the control rod fuel elements with as many new fuel elements as possible and still retain a more or less square core. Close to criticality, counts due to reactor fissions greatly outnumbered counts due to background radiation; therefore, the detection efficiency was as expected. However, as the reactor was made more subcritical, the proportion of counts due to background gamma radiation to counts due to reactor fissions increased. Since counts due to background gamma radiation in detector 2 were uncorrelated to those in detector 3 and both uncorrelated to the ^{252}Cf fissions in detector 1, the coherences between detector responses were lower than those expected in a clean core with the same detection efficiencies. Viewed another way, the detection efficiencies inferred from the coherences [using Eq. (2.10)] decreased as the subcriticality increased.

The ^{3}He proportional counting system (∿29 counts/sec/nv-thermal) was assembled to perform measurements at other locations in and around the core to determine if measurements were position dependent. It was presumed that the ^{3}He detectors would work in a low gamma radiation environment. However, when the detectors were placed in positions in the core close to the irradiated control rod fuel elements, the gamma radiation ionized the gas in the counters to such an extent that high voltage periodically arced from one electrode to the other. This limited measurements with the ^{3}He system to the same detector location as with the Li measurements.

Measurements with the ^{3}He detectors indicated that the efficiency of the ^{3}He detection system was a decade higher (10^{-3} instead of 10^{-4} counts per reactor fission) than was estimated from preliminary scoping calculations (3 group, 2-D, diffusion). This led to the assembly of the fission counting system (∿1.2 counts/sec/nv-thermal) in the last few days of the experiment to determine if measurements were possible with lower sensitivity detectors. Measurements were performed at the same detector location as with the Li and ^{3}He measurements to determine if the results were reproducible.

B. Signal Analysis System

The signal analysis system (Fig. 3.1) consisted of a commercial digital Fourier analyzer (Hewlett-Packard, 5451B), additional software to adapt the analyzer for reactivity noise measurements, and a frequency modulated (FM) tape recorder (Bell & Howell, Datatape CPR 4010) to store analog data in case of analyzer failure.



1. Hewlett-Packard 2100A Computer
2. Hewlett-Packard 5470A Fourier Processor
3. Hewlett-Packard 5466B Analog-to-Digital Converter
4. Rockland 1520 and 1022F HI/LO Filters
5. Hewlett-Packard 5475A Control Unit
6. Tektronix 4012 Computer Display Terminal
7. Tektronix 4631 Hard Copy Unit
8. Hewlett-Packard 2748A Tape Reader
9. Hewlett-Packard 7900A Disc Drive with 12869A Disc Pack
10. Hewlett-Packard 5460A Display Unit with 181A Oscilloscope
11. Centronics 101A Line Printer
12. Hewlett-Packard 2895B Tape Punch
13. Bell & Howell Datatape CPR 4010

Fig. 3.1. Signal analysis system configuration.

The Fourier analyzer used in this experiment is an upgraded version of the one used and described in detail by Mathis, and others.[24] The present system is equipped with a disc and disc drive unit for extended program and data storage capability. A cathode ray tube (CRT) terminal has been added for faster input/output (IO) operations and enhanced graphics capability. The new analog-to-digital converters (ADCs) are slower with maximum sampling rates of 100 kHz instead of 200 kHz.

As shown in Fig. 3.1, the signals from the detection instrumentation system (see Appendix B for the origins of these signals) were low pass filtered before digitization to prevent aliasing.[20] The filtered signals were recorded on analog tape as a back-up in case of problems with the Fourier analyzer. Because of tape recorder noise, the recorded data are not of the same quality as the data analyzed directly.

Figure 3.2 shows schematically the procedure followed in analyzing the signals at each core configuration. After the transition to a certain core configuration, the analysis began by loading and starting the Fourier System (FS). The FS is a memory-resident computer program supplied by the manufacturer to coordinate the functions of all the peripherals to reduce the many tasks of signal analysis (sampling, windowing, Fourier transform, block arithmetic, and others) into simple keyboard commands. Keyboard-callable user subprograms (FORTRAN-II or ASSEMBLY) could be incorporated into the system to perform special tasks. Keyboard commands could be stacked into keyboard programs with branching, looping, and multiple entry capabilities to perform tasks sequentially under computer control.

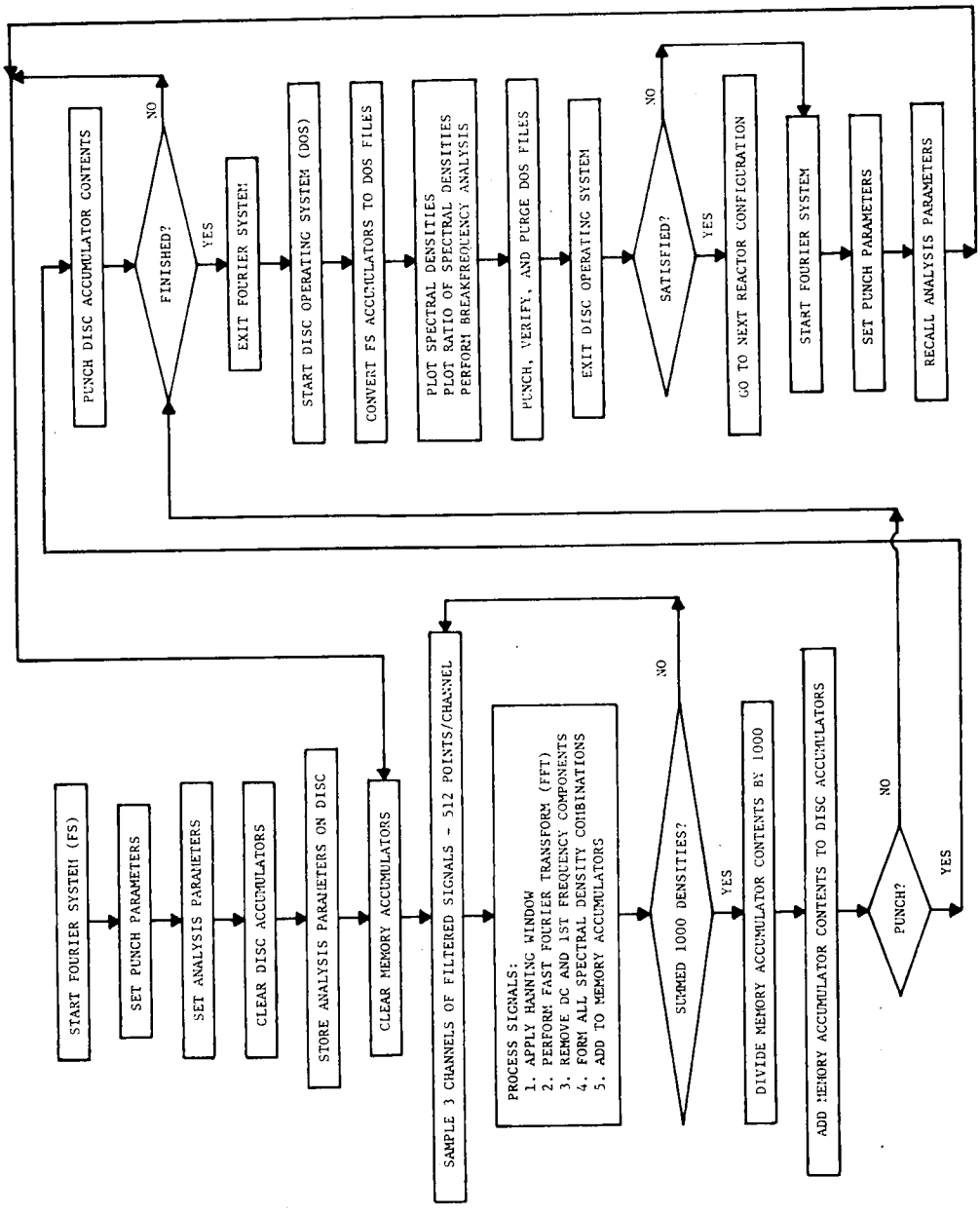


Fig. 3.2. Flowchart of the signal analysis procedure.

A guess of the breakfrequency was made in order to determine the sampling rate required. A thousand blocks of each spectral density were summed and stored on disc. At this point, the Disc Operating System (DOS) was loaded into the computer and started. DOS is a system monitor that allows the use of the computer as a stand-alone processor. Programs to examine the accumulated spectra were written under DOS control because more memory was available and programming procedures were simpler compared to the FS.

Under DOS control, the average spectral densities were plotted, the ratios of spectral densities averaged over frequency, and breakfrequency analyses performed. A decision was then made as to whether the sampling rate was optimal. (A sampling rate of $\sim$20 $\times$ breakfrequency was considered optimal. This sampling rate was chosen so that the sampled bandwidth would contain frequency information $\sim$1 decade before and $\sim$1 decade after the breakfrequency.) If it was far from optimal, the analysis was restarted using a better sampling rate. If the sampling rate was judged adequate, the precision of the measured results was examined. If the precision was not acceptable, the analysis returned to the FS and more spectra were accumulated. If the precision was sufficient, the data were punched on paper tape for storage. The experiment then proceeded to the next core configuration.

CHAPTER 4

REACTOR EXPERIMENT

Power spectral density measurements with ^{252}Cf were performed in the Pool Critical Assembly (PCA)[25] at the Oak Ridge National Laboratory (ORNL) in the Spring of 1979. The reactor, fuel elements, and control rods are described in detail in Appendix C.

A. Brief Description of the Reactor

The PCA (Fig. 4.1) is a light water moderated and reflected pool-type facility. The core is heterogeneous and uses Materials Testing Reactor (MTR)-type enriched uranium (93% enriched in ^{235}U) fuel elements. It accepts either 18-plate Bulk Shielding Reactor (BSR) or 19-plate Oak Ridge Research Reactor (ORR) fuel elements ($\sim$80 × 80 × 600 mm). The PCA is operated with 3 safety rods and a regulating rod which move within control rod receiving fuel elements (shim elements).

B. Detector Placement in the Reactor

The ^{252}Cf chamber was positioned at the core midplane inside a watertight aluminum pipe (1" schedule 40, 1.315" OD, 1.049" ID, 6061 Al). Plexiglass spacers were used above and below the detector. The last 30 inches of the pipe was machined to the width of a control rod for insertion into a shim element.

The two Li glass scintillators were positioned in an aluminum pipe (2" schedule 40, 2.375" OD, 2.067" ID, 6061 Al) such that the active

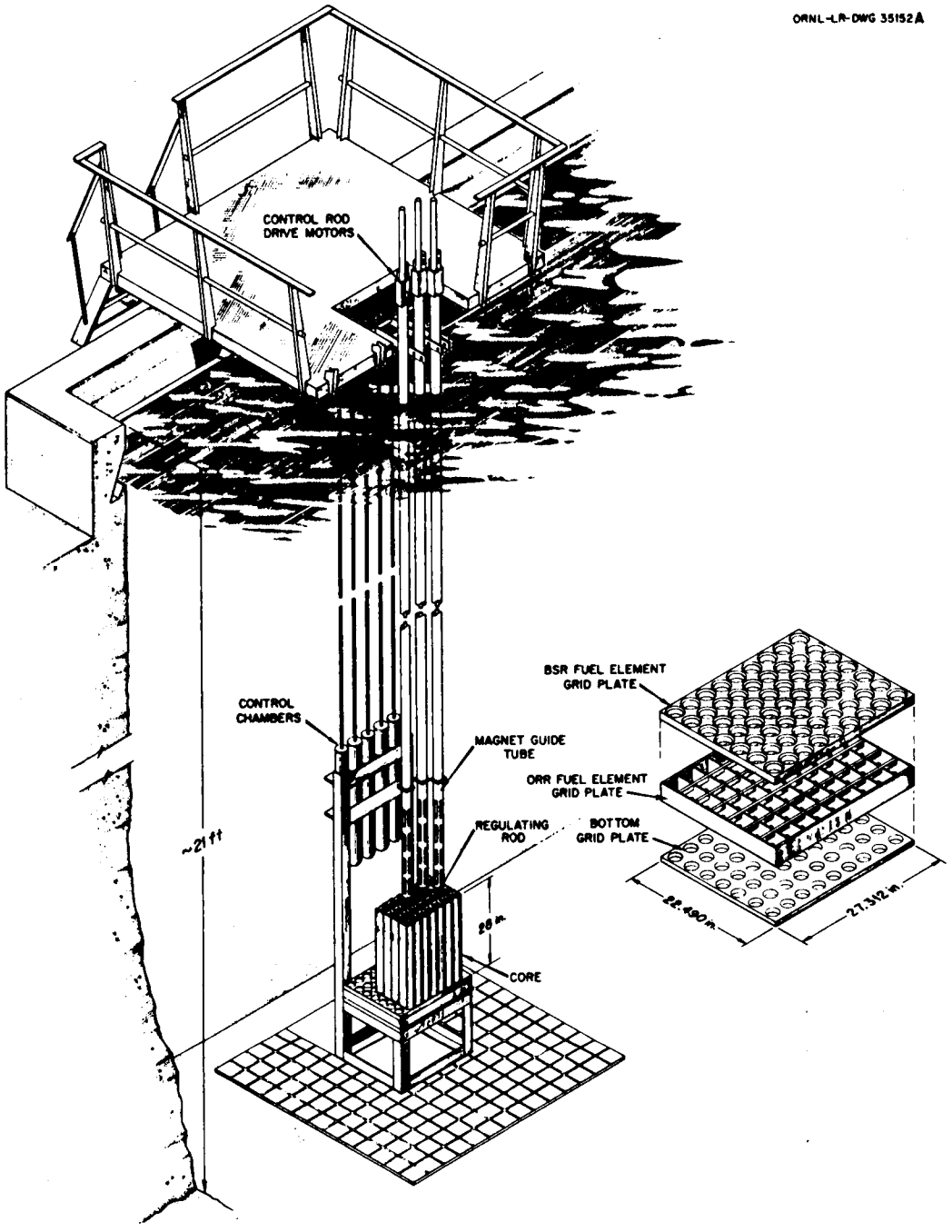


Fig. 4.1. Structural arrangement of the Pool Critical Assembly.

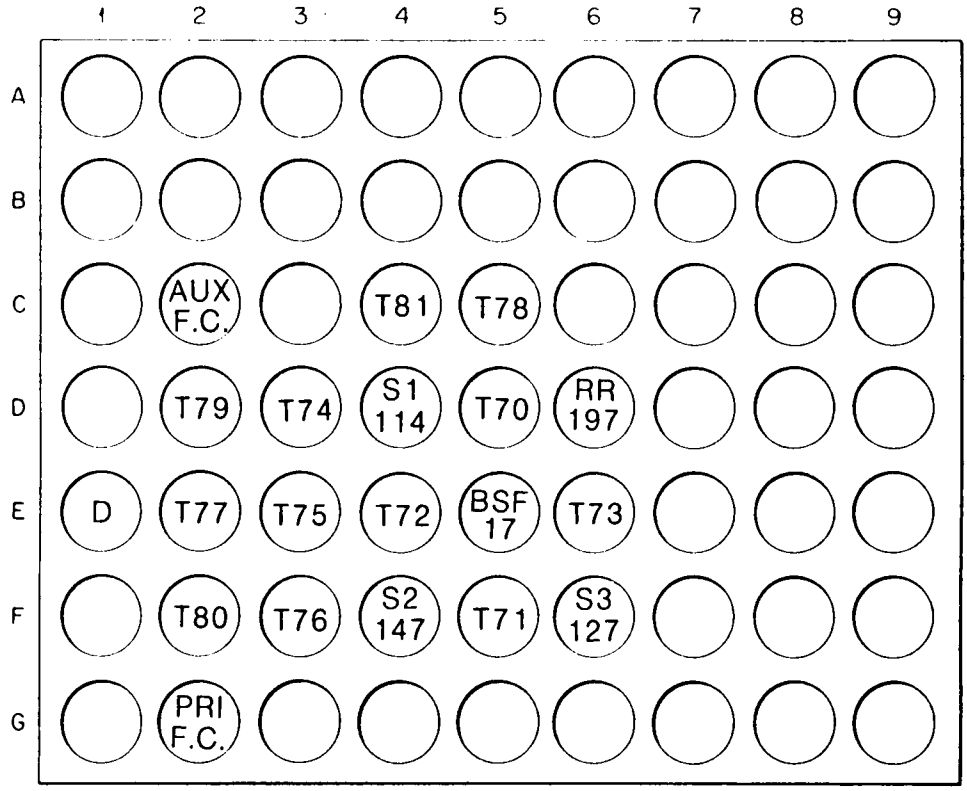
elements were ∿152 mm above and below the core midplane. The detectors were held in place with set screws. This pipe was then inserted into a watertight aluminum pipe (2-1/2" schedule 40, 2.875" OD, 2.469" ID, 6061 Al) with an end piece shaped like a BSR fuel element end box. The ^{3}He detectors were placed sidebyside in a similar set of aluminum pipes such that the midpoints of the active regions corresponded to the core midplane. The fission chambers were stacked like the scintillators; however, because the fission chambers were longer than the scintillators, the midpoint of the active area of one chamber was placed ∿276 mm above the core midplane, and the other was placed ∿124 mm below.

The pipe bearing the ^{252}Cf chamber was located inside the control rod fuel element, BSF-17, in core location E-5 (Fig. 4.2). The reactor was loaded such that fuel elements would be distributed symmetrically on both sides of the source. However, the Li detectors in such a core were so close to the irradiated control rod fuel elements that the background current accounted for >99% of the total detector output. Therefore, the Li detectors were moved one row further out and fuel elements were added to shield the detectors from the background radiation source resulting in an asymmetric core configuration.

C. Experiment Procedures

The reactor was loaded to criticality with the final configuration shown in Fig. 4.2. The control rod positions for the critical configuration are listed in Table 4.1 as configuration 0.

LOADING #252



D	Pipe with Detectors 2 & 3
AUX F.C.	Auxiliary Fission Chamber
PRI F.C.	Primary Fission Chamber
T#	ORR Fuel Element
S#	Control Rod Fuel Element
RR	Regulating Rod Fuel Element
BSF	BSR Control Rod Fuel Element

Fig. 4.2. Core configuration used in the spectral density measurements. (Gamma-sensitive detectors in E-1 were shielded from the control rod fuel elements by two rows of fuel elements.)

Table 4.1. Core configurations for reactivity measurements

Configuration number	Safety rod position (cm)[a]			Regulating rod position (cm)[b]	Core fission chamber position (cm)[c]		Fuel elements removed
	S1	S2	S3		PRI	AUX	
0[d]	56.4	56.4	56.4	0	63.5	63.5	none
1	51.6	51.6	51.6	33.3	63.5	63.5	none
2	51.6	51.6	51.6	0	63.5	63.5	none
3	56.4	56.4	0	56.4	63.5	0	none
4	56.4	28.2	56.4	56.4	63.5	0	none
5	56.4	0	56.4	56.4	63.5	0	none
6	0	56.4	56.4	56.4	63.5	0	none
7	0	0	0	0	63.5	0	none
8	0	0	0	0	63.5	0	C-4
9	0	0	0	0	63.5	0	C-4, C-5

[a] 0 cm = fully inserted and 61.0 cm = fully withdrawn.

[b] 0 cm = fully inserted and 56.4 cm = fully withdrawn.

[c] 0 cm = core midplane and 63.5 cm = fully withdrawn.

[d] Reactor critical at this configuration.

The regulating rod was calibrated by withdrawal of small increments and measuring the positive period (criticality was reestablished by insertion of the three safety rods). The reactivity was obtained by using the inhour equation.[26] This calibration provided a reference subcritical configuration (configuration 2) for breakfrequency noise analysis.

The different subcritical states were achieved by control rod insertion and/or fuel removal. Table 4.1 lists the configurations wherein spectral density measurements were performed in accordance to the procedure described in Chap. 3. During the spectral density measurements, count rates from the primary and auxiliary fission chambers (reactor operating instrumentation) were recorded for reactivity determination using the modified source multiplication technique. Measurements were performed with the Li glass scintillators operating in the current mode. Measurements with the scintillators operating in the pulse mode, with the ^{3}He proportional counters, and with the fission chambers were made at some of the configurations in Table 4.1. The reactivity change due to replacing the scintillators with the ^{3}He detectors ($\sim$ -\$0.30) and fission chambers ($\sim$ +\$0.30) were not compensated for.

After all the reactor noise measurements were performed, rod drop measurements were done to estimate the worth of the safety rods. Count rates from the auxiliary fission chamber were taken at configuration 7 with the ^{252}Cf source located at various locations in and around the core. The calculated variations in the auxiliary fission chamber count rates

with the source at various locations compare favorably with those measured, thus increasing the confidence in the accuracy of the cross section set and reactor model used in performing the core calculations. (See subsection 10, section A, Appendix E.)

CHAPTER 5

PRESENTATION AND DISCUSSION OF RESULTS

Reactivities were obtained from ratios of spectral densities, $G_{12}^{*}G_{13}/G_{11}G_{23}$. Other reactor noise techniques were also used: reactivities from α using the corrected PSDs[9] of detectors 2 and 3, the corrected CPSDs[10,11,14] between detectors 1 and 2, 1 and 3, and 2 and 3; and reactivities using the low frequency coherence amplitude[12,13] between detectors 2 and 3. Reactivities were also obtained by the modified source multiplication technique,[27,28] inverse kinetics rod drop measurements,[29] and calculations (2-D diffusion).

A. Power Spectral Densities

Spectral density measurements were made at 3 different sampling rates (500, 1000, and 2000 Hz) to account for changes in breakfrequency as reactivity changed. The antialiasing filters for all detection systems were set at 40% of the sampling rate. Figure 5.1 shows the PSD of the signal from the ^{252}Cf detection system sampled at 2 kHz. The low frequency roll-off is due to the high pass circuit of the RC Time-Constant unit. The high frequency roll-off at 800 Hz is due to the antialiasing filter. Except for the antialiasing filter, no other instrument settings in the ^{252}Cf detection system were changed for measurements at other sampling rates.

The corrected PSDs of the signal measured at core configurations 1, 3, 4, and 7 using one of the Li detectors (detector 2) operated in the

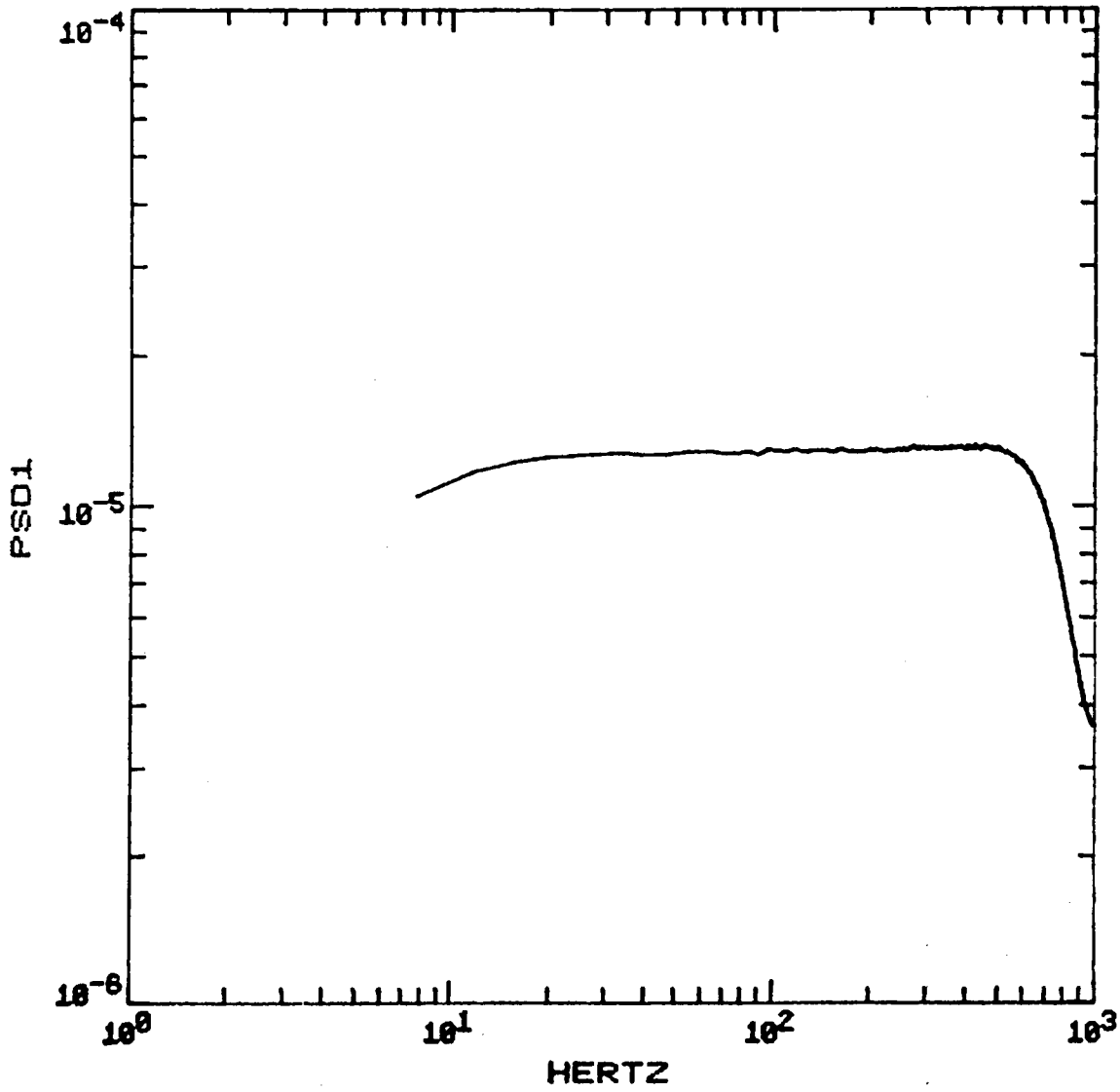


Fig. 5.1. PSD of the ^{252}Cf system signal sampled at 2 kHz. (The y-axis units are arbitrary.)

current mode are shown in Fig. 5.2. It can be seen in the figure that as the reactor gets more subcritical (increasing configuration number), the white noise component dominates the PSD such that the determination of the breakfrequency gets more difficult. The corrected PSDs of the signal from the other Li detector (detector 3) are similar to those on Fig. 5.2.

Corrected CPSDs measured at core configurations 3 and 9 using the ^{3}He detection system are shown in Fig. 5.3. Compared to the corrected PSDs (included for comparison), the corrected CPSDs do not contain a white noise component that dominates at high subcriticalities.[10,11] The fitted curves were obtained using a nonlinear least squares algorithm detailed in Appendix D.

B. Prompt Neutron Decay Constants

Figure 5.4 shows the real and imaginary parts of the corrected CPSD between the ^{252}Cf detector signal and the signal from a Li detector (detector 2) operated in the current mode. The CPSD was measured at core configuration 4. The product of the angular frequency, ω, and the ratio of the real to the imaginary parts of the corrected CPSD (Fig. 5.4) between the responses of detectors 1 and 2 (or 1 and 3) equals the prompt neutron decay constant, α. This product measured at core configurations 3 and 9 using a ^{3}He detector (detector 2) is shown in Fig. 5.5 as a function of frequency. According to the equation for the corrected CPSD, which was derived assuming point kinetics behavior of the reactor, this product should be independent of frequency. The

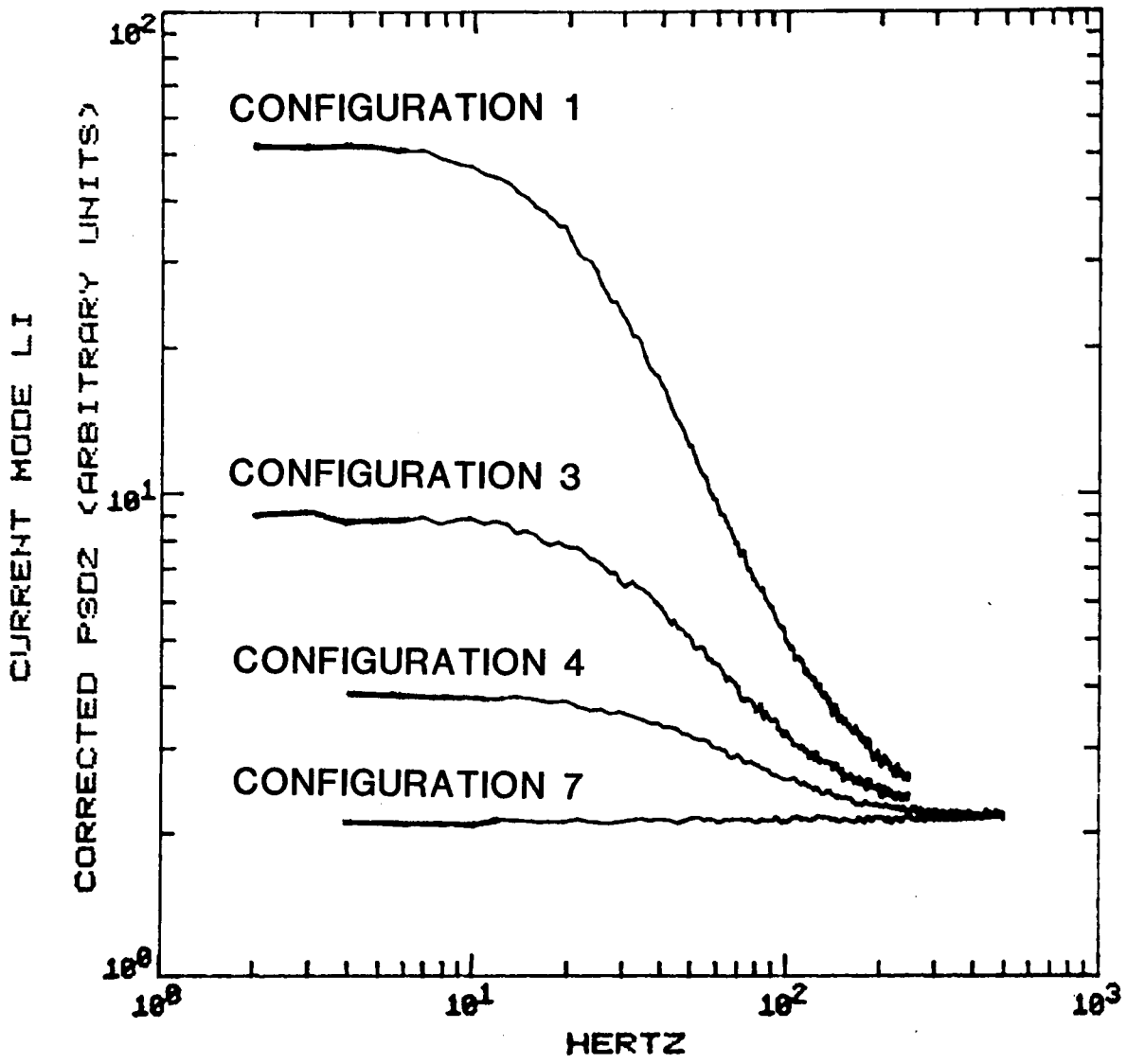


Fig. 5.2. Corrected PSDs measured at core configurations 1, 3, 4, and 7 using a Li detector (detector 2) operated in the current mode.

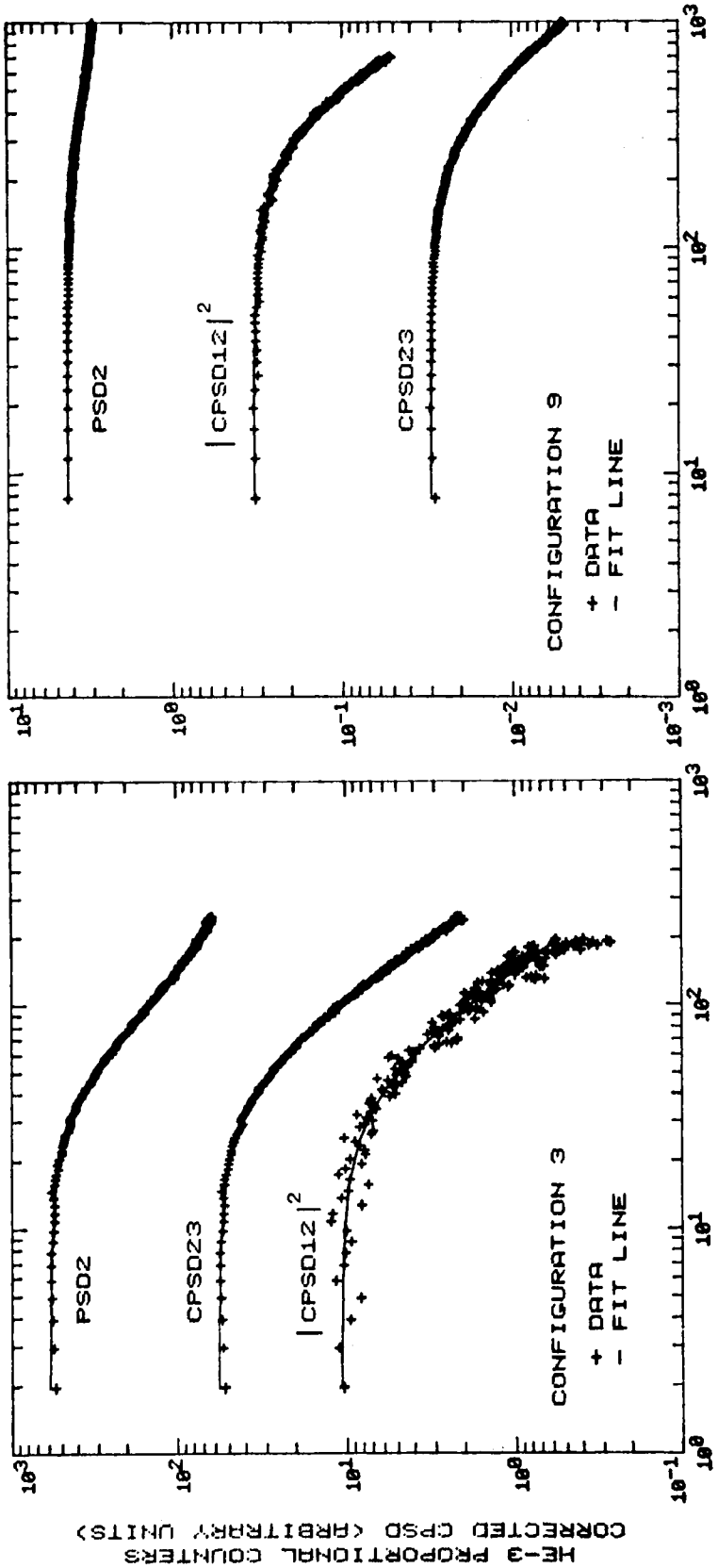


Fig. 5.3. Corrected CPSDs measured at core configurations 3 and 9 using the ^{3}He detection system. (Corrected PSDs included for comparison.)

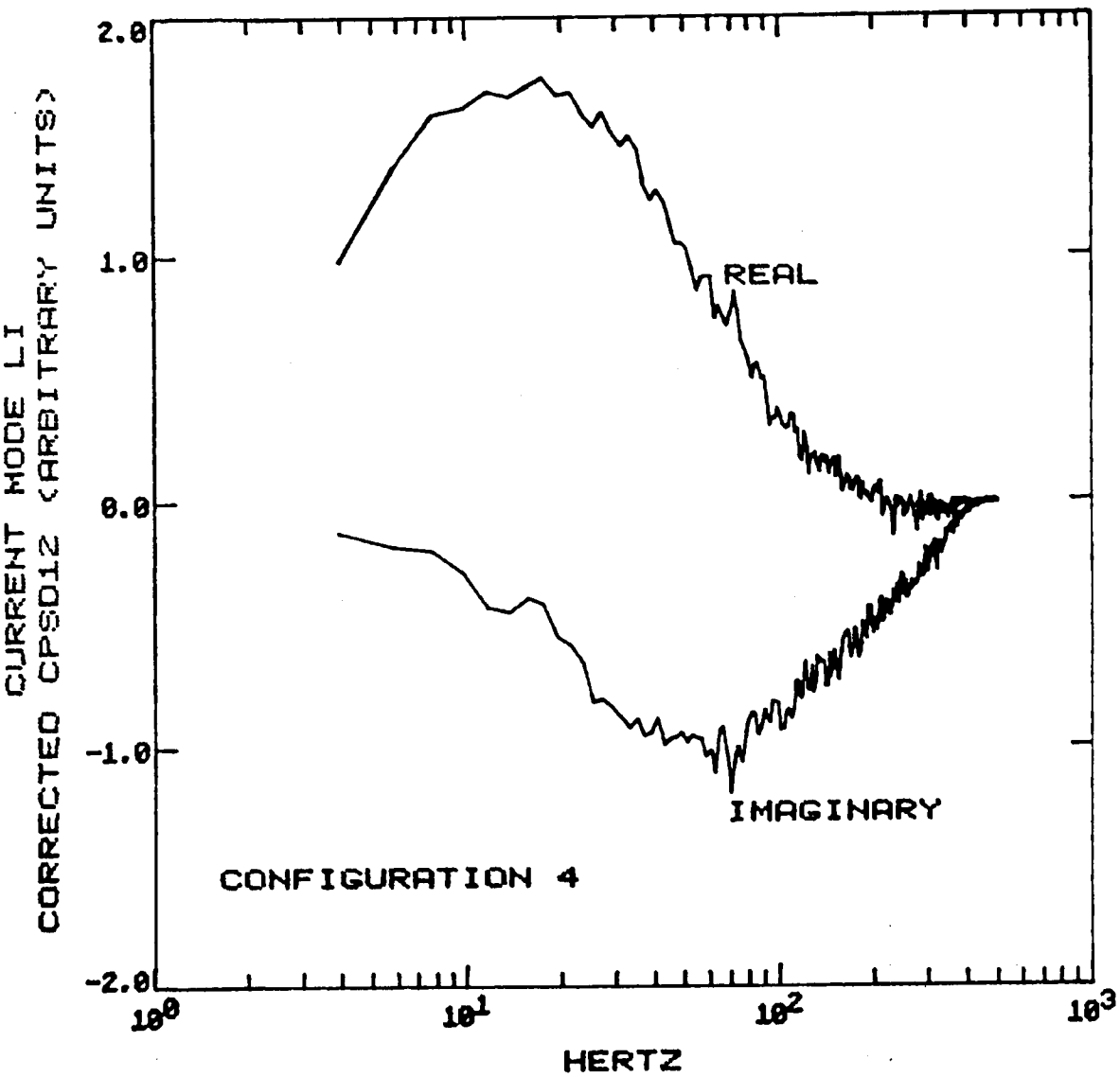


Fig. 5.4. Real and imaginary parts of the corrected CPSD between the ^{252}Cf detector signal and the signal from a Li detector (detector 2) operated in the current mode. CPSD was measured at core configuration 4.

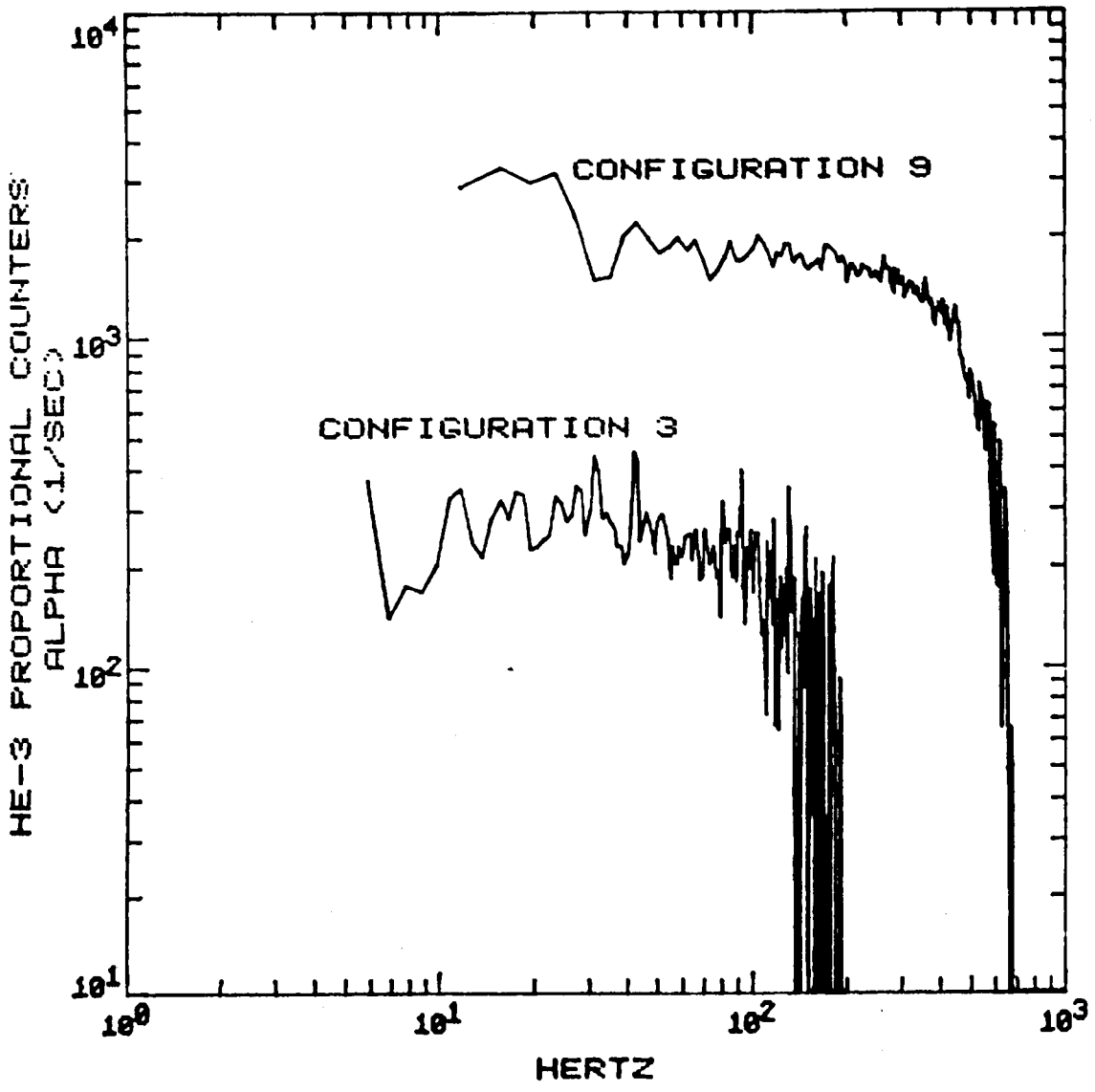


Fig. 5.5. Prompt neutron decay constant obtained from the product of the angular frequency and the ratio of the real to the imaginary parts of the corrected CPSD between the outputs of detectors 1 and 2. (Detector 2 was a ^{3}He detector.) CPSDs were measured at core configurations 3 and 9.

frequency dependence of the results shown in Fig. 5.5 indicates that the single-order lag model (single decay mode) is inadequate for this particular measurement. The frequency dependence of this product was predicted by Mihalczo and Paré[14] for systems with higher decay modes. This subject will be discussed later in this chapter.

C. Coherence Amplitudes

The coherence amplitudes from measurements at core configurations 2 and 7 using the Li detection system operated in the pulse mode are shown in Fig. 5.6. At configuration 2 (closer to criticality than at configuration 7), the fission rate in the reactor (a noise source for the CPSD between the two Li detector outputs) is much higher than the ^{252}Cf fission rate (the noise source for the CPSD between the ^{252}Cf signal and each of the Li detector signals). Therefore, the coherence between the two Li detector signals at configuration 2 is higher than the coherence between the ^{252}Cf signal and each of the Li detector signals. The opposite is true at configuration 7.

The low frequency coherence amplitudes measured at various reactivities using the Li detection system are shown in Fig. 5.7. Coherence amplitudes using the ^{3}He and fission counting systems are shown in Fig. 5.8. Average detection efficiencies in counts per reactor fission inferred from coherence values at ∿-1 dollar subcritical are: $\sim 2 \times 10^{-4}$ for current mode Li, $\sim 4 \times 10^{-4}$ for pulse mode Li, $\sim 1 \times 10^{-3}$ for ^{3}He, and $\sim 1 \times 10^{-4}$ for fission chambers.

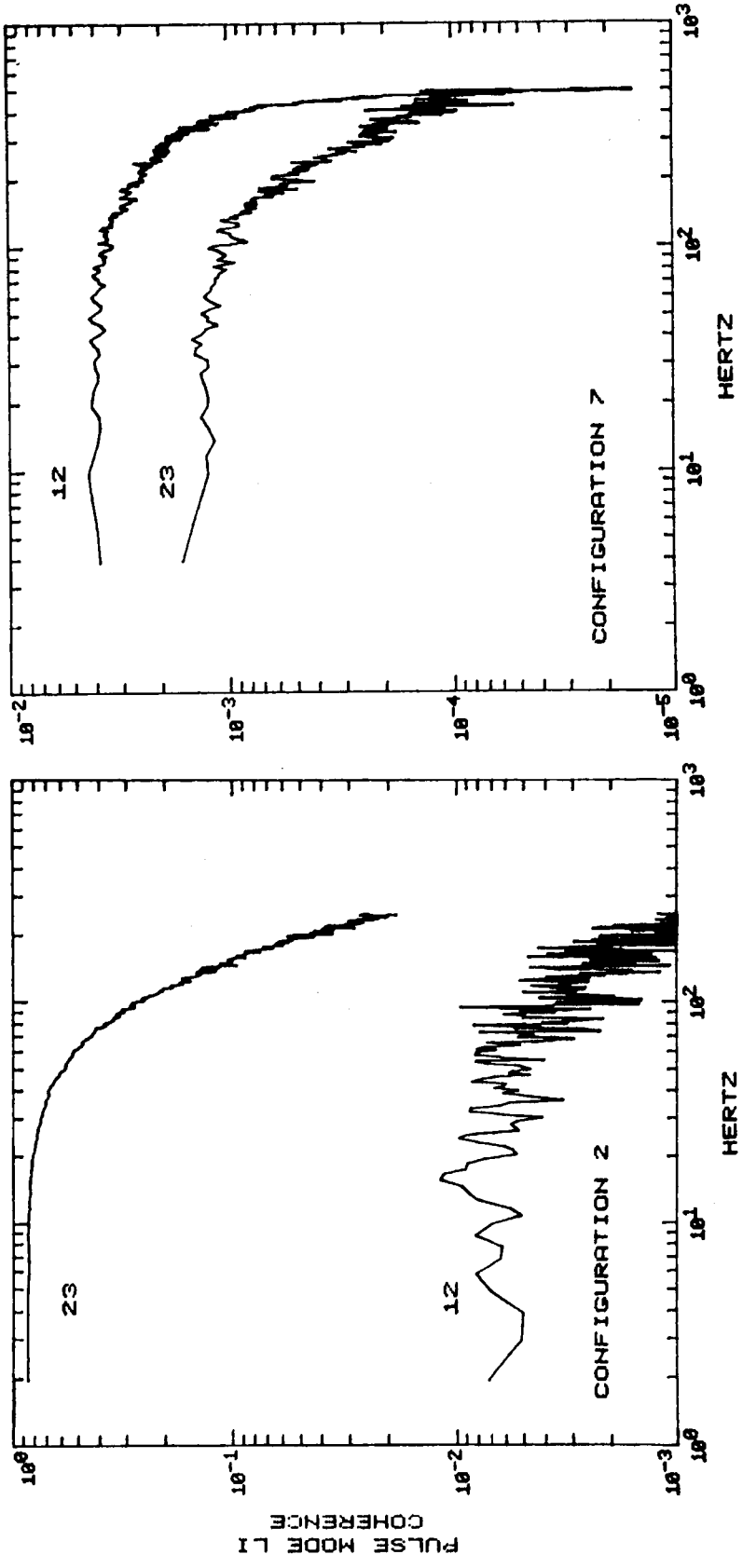


Fig. 5.6. Coherence amplitudes measured at core configuations 2 and 7 using the Li detection system operated in the pulse mode.

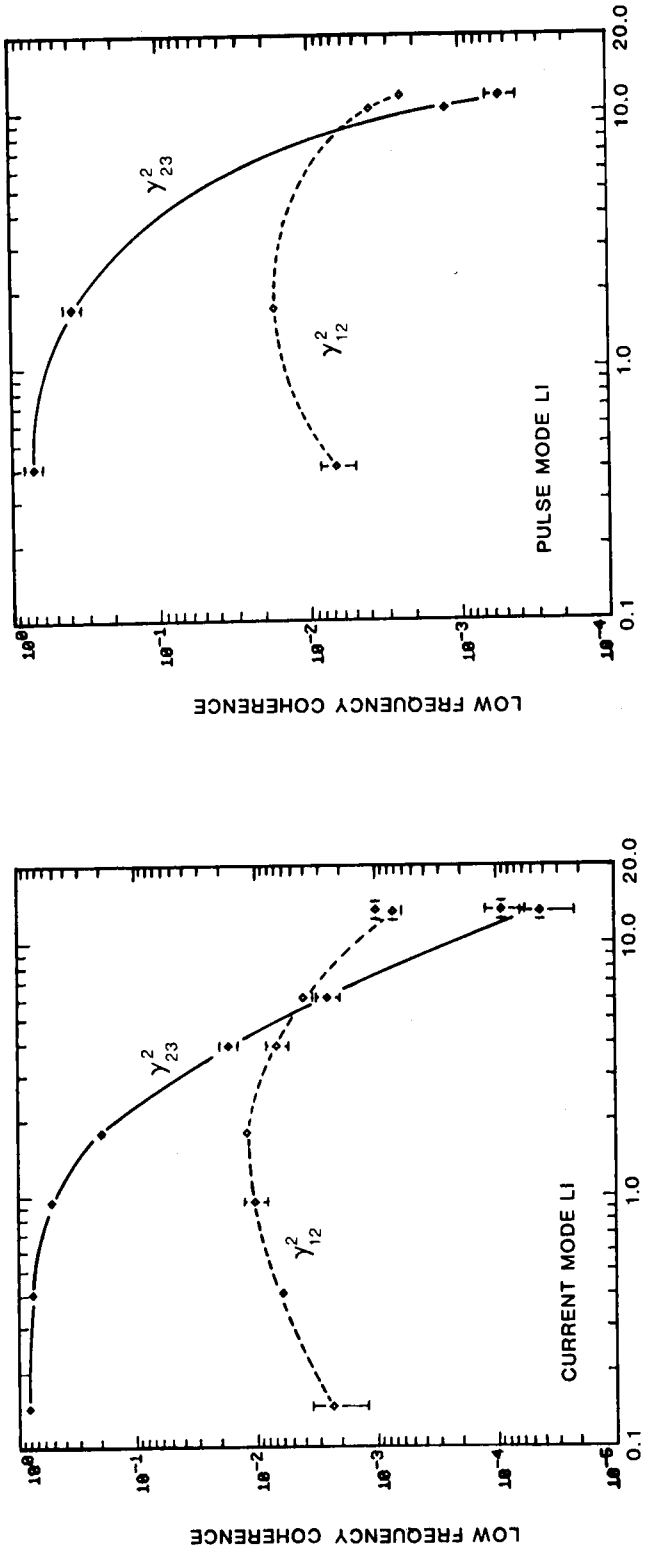


Fig. 5.7. Low frequency coherence amplitudes at various reactivities using the Li detection system.

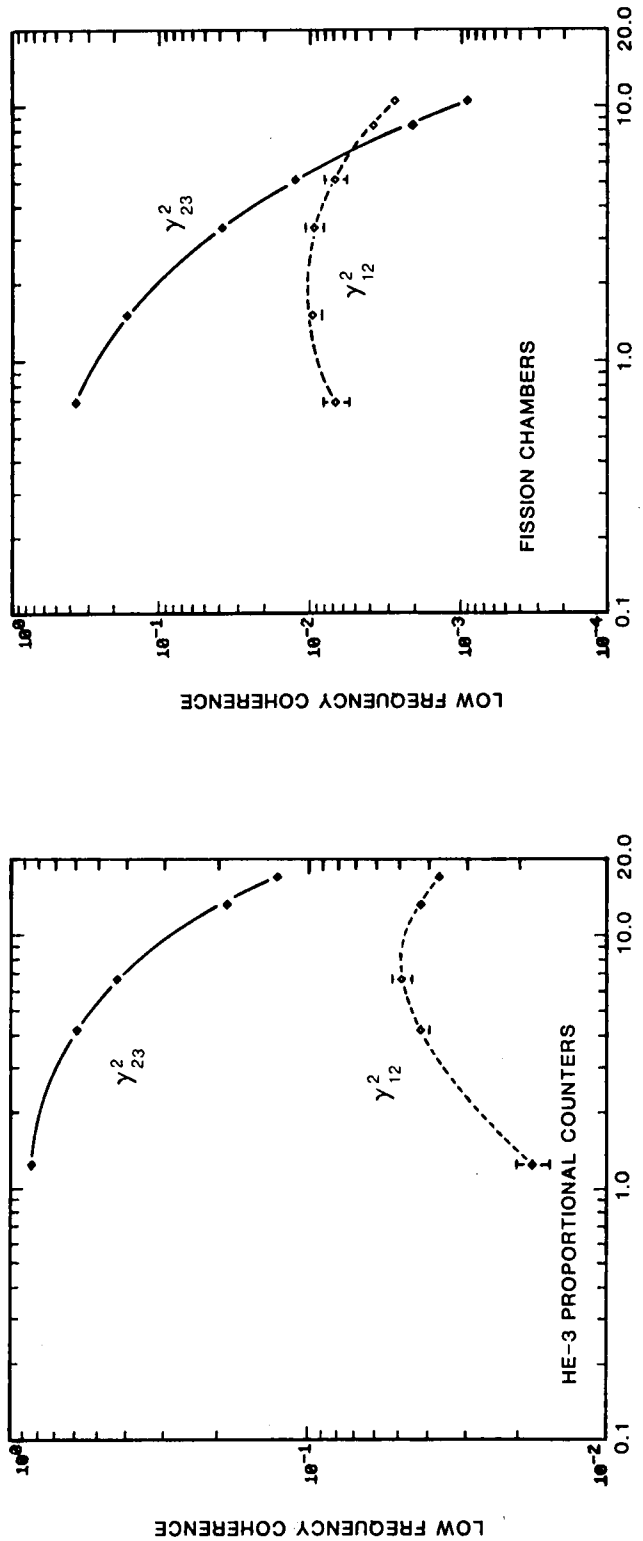


Fig. 5.8. Low frequency coherence amplitudes at various reactivities using the ^{3}He and fission counting system.

D. Ratio of Spectral Densities

The ratios of spectral densities, $G_{12}^{*}G_{13}/G_{11}G_{23}$, measured at core configurations 3 and 9 using the ^{3}He detection system are plotted in Fig. 5.9 as a function of frequency. At configuration 3, this ratio is, as predicted by theory, constant with frequency. The sharp drop of this ratio beyond 200 Hz is due to the poor signal-to-noise ratio caused by the antialiasing filter. The sharp drop of the ratio of spectral densities beyond 800 Hz at configuration 9 is also due to the antialiasing filter. However, this ratio at configuration 9 is constant only up to 200 Hz. The slow roll-off starting at 200 Hz is contrary to the predictions of Eq. (2.16) which was developed assuming point kinetics behavior of the reactor. This phenomenon will be discussed later.

The equation [Eq. (2.16)] for the ratio of spectral densities from Chap. 2 can be written, by using Eq. (2.17), as

$$\frac{G_{12}^{*}G_{13}}{G_{11}G_{23}} = \frac{\gamma_{12}\gamma_{13}}{\gamma_{23}} = -\rho \frac{F_c I_c \bar{\nu}_c}{F_c I_c \bar{\nu}_c + F_i I_i \bar{\nu}_i} \frac{I_c \bar{\nu}_c}{I\bar{\nu}_p} \frac{1}{B_c(1 + C_\alpha)} \frac{1}{X'R} \quad . \qquad (5.1)$$

The dependence of this ratio of spectral densities on the ratio of importance weighted neutron production rates, $F_c I_c \bar{\nu}_c/(F_i I_i \bar{\nu}_i + F_c I_c \bar{\nu}_c)$, was determined by measurements in which the discrimination level of the ^{252}Cf detection system was raised such that some ^{252}Cf fissions were not detected. The rejected ^{252}Cf fissions effectively acted as inherent fission sources, F_i, with the same neutron importance and the

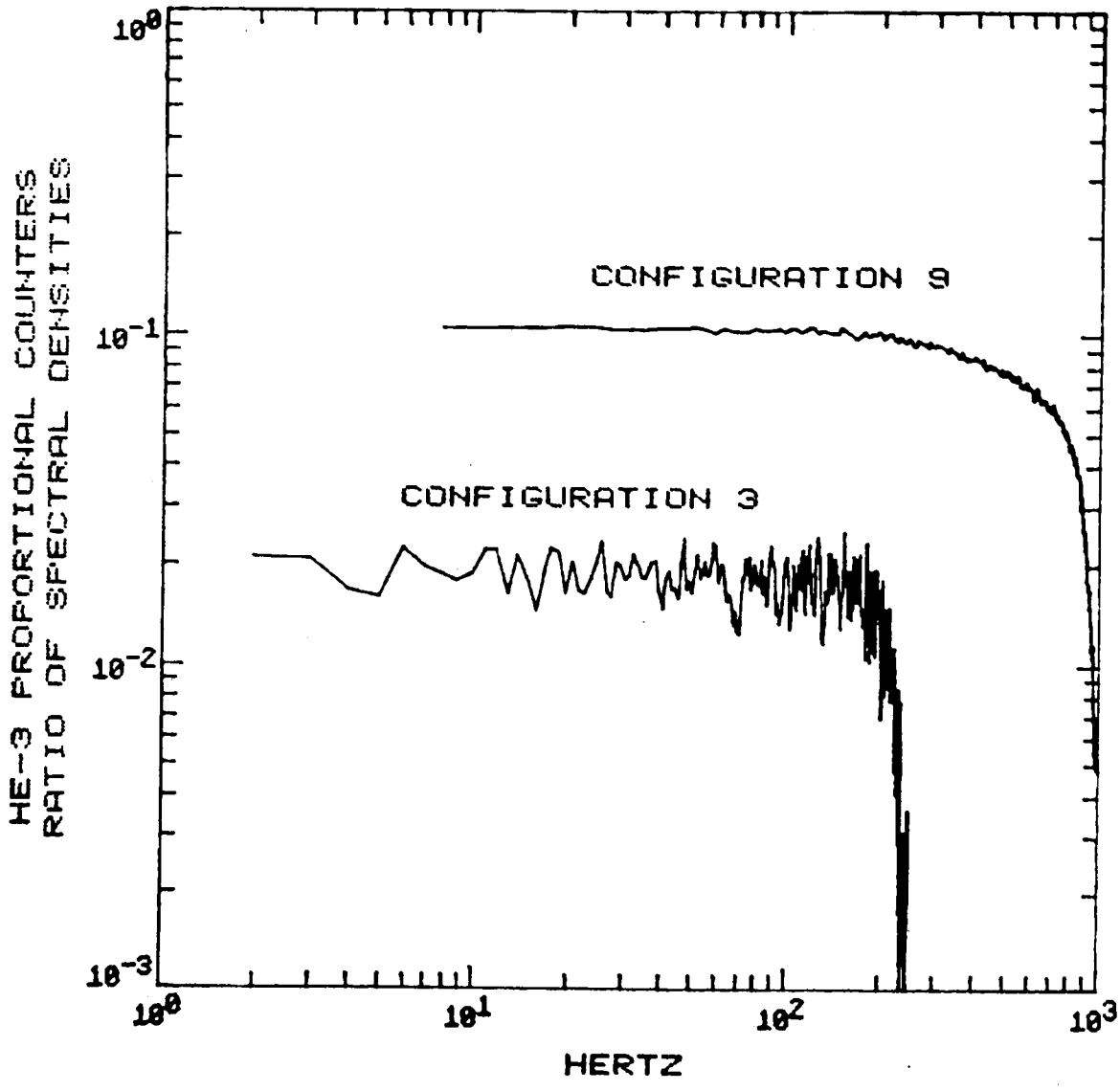


Fig. 5.9. Ratio of spectral densities, $G^{*}_{12}G_{13}/G_{11}G_{23}$, measured at core configurations 3 and 9 using the ^{3}He detection system.

same number of neutrons per fission. If R is the ratio of spectral densities measured with >99.9% of the ^{252}Cf fissions counted and R_c is this ratio measured with the fraction, C, of the ^{252}Cf spontaneous fissions counted, then from Eq. (5.1)

$$R_c = CR \ . \tag{5.2}$$

Figure 5.10 shows the results of measurements at ∿1.71 dollars subcritical using the Li detection system operated in the pulse mode and with ∿100%, ∿75%, and ∿50% of the ^{252}Cf fissions detected (plotted as a function of the fraction of ^{252}Cf fissions rejected). The straight line is a plot of Eq. (5.2). The agreement of the measured results to the predictions of Eq. (5.2) is very good.

E. Measured Reactivities

A discussion of how some of the parameters required to obtain reactivity from the measured ratios of spectral densities were calculated appears in Appendix E. This appendix also lists the sources of the parameters not calculated. The quantities measured to determine reactivity are tabulated in Appendix F together with the reactivities inferred from them. The measured ratios of spectral densities, $G^*_{12}G_{13}/G_{11}G_{23}$, are listed in Table F.2 and the reactivities inferred from them are in Table F.3. The measured prompt neutron decay constants are listed in Tables F.4 thru F.7 and the reactivities obtained from them are in Tables F.8 thru F.11. Tables F.12 and F.13 list primary

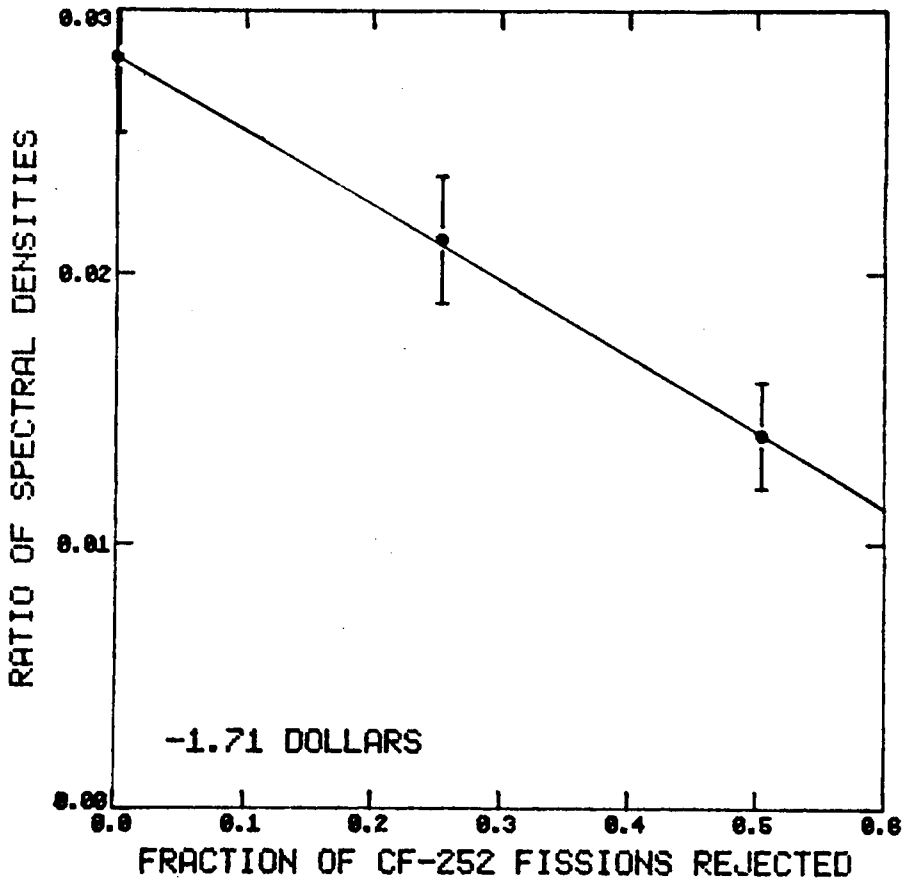


Fig. 5.10. Ratios of spectral densities measured at ∿1.71 dollars subcritical using the Li detection system operated in the pulse mode with the ^{252}Cf detection system discrimination level set at various points.

and auxiliary fission chamber count rates and Tables F.14 and F.15 list the reactivities obtained by the modified source multiplication technique. Low frequency coherence (γ^2_{23}) amplitudes are listed in Table F.16 and the reactivities inferred from them are in Table F.17. Finally, reactivities obtained by inverse kinetics methods and from calculations are listed in Table F.18.

Figure 5.11 compares reactivities from the ratios of spectral densities measured with the ^{252}Cf source at core location E-5 and C-6 using the Li scintillators in the pulse mode. The change in reactivity due to moving the pipe from position E-5 to C-6 was compensated for by partial insertion of safety rod 3. The disagreement between the two measurements are within the uncertainties of the experiment.

Table 5.1 lists some of the average reactivities obtained from the ratios of spectral densities. The measured ratios of spectral densities were the same for all detection systems. This confirms the prediction of the theory, that is, the ratio of spectral density is independent of detection instrumentation frequency response and detection efficiencies.

Reactivities obtained from the ratios of spectral densities are compared in Figs. 5.12 (using the Li detection system) and 5.13 (using the ^3He and fission counting systems) to reactivities determined from the prompt neutron decay constants obtained from the CPSDs between the outputs of detectors 2 and 3. The agreement between the two measurements is good at low subcriticalities. As the reactor was made more subcritical, the two results diverge. The percentage difference between the two methods are shown in Fig. 5.14 as a function of the reactivities obtained

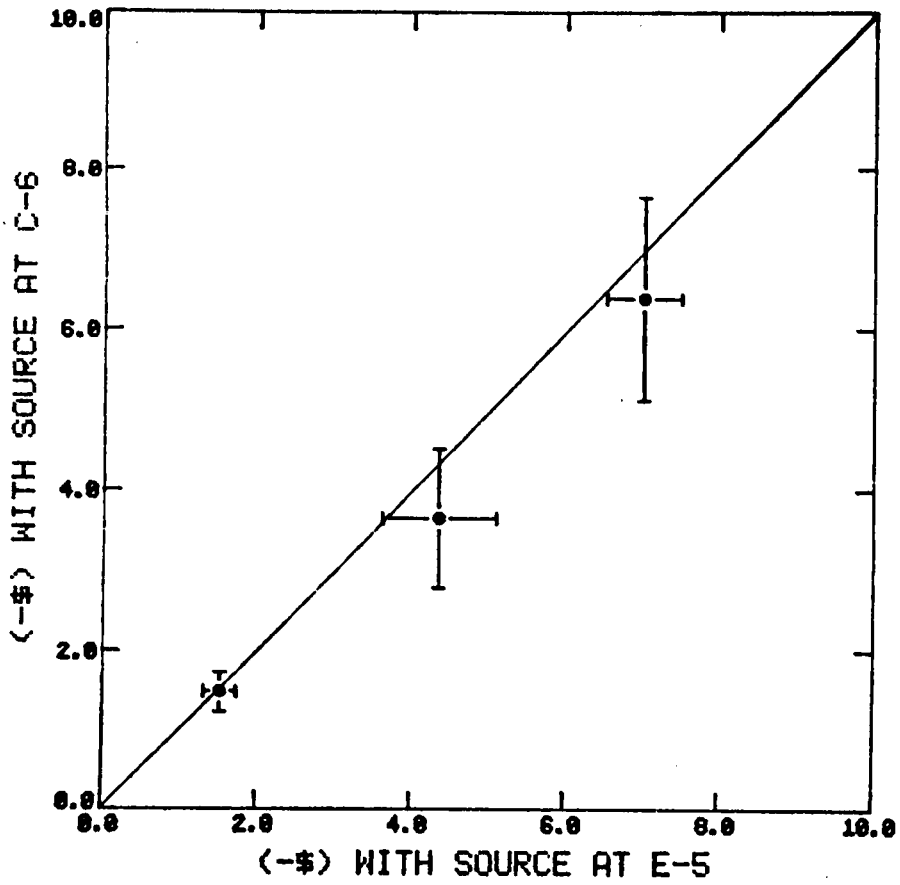


Fig. 5.11. Reactivities obtained from the ratio of spectral densities measured with the ^{252}Cf source at core locations E-5 and C-6 and using the Li scintillators operated in the pulse mode.

Table 5.1. Comparison of reactivities (-$) obtained from the ratio of spectral densities, $G^*_{12}G_{13}/G_{11}G_{23}$, using different detection systems

Configuration Number	Current Mode Li	Pulse Mode Li	^{3}He[a]	Fission Chambers[a]
3	8.60E-1[b] ±1.94E-1		7.57E-1 ±1.56E-1	9.58E-1 ±1.37E-1
4	1.53E+0 ±1.68E-1	1.53E+0 ±2.13E-1		1.69E+0 ±1.93E-1
5	3.12E+0 ±5.56E-1		2.86E+0 ±2.00E-1	3.23E+0 ±6.25E-1
6	4.76E+0 ±1.51E+0		3.91E+0 ±3.16E-1	4.32E+0 ±7.27E-1
7	6.97E+0 ±2.70E+0	6.99E+0 ±7.94E-1	6.29E+0 ±3.51E-1	6.86E+0 ±6.50E-1

[a] Reactivities adjusted for effects of replacing detectors.

[b] Error estimates are ±1 standard deviation.

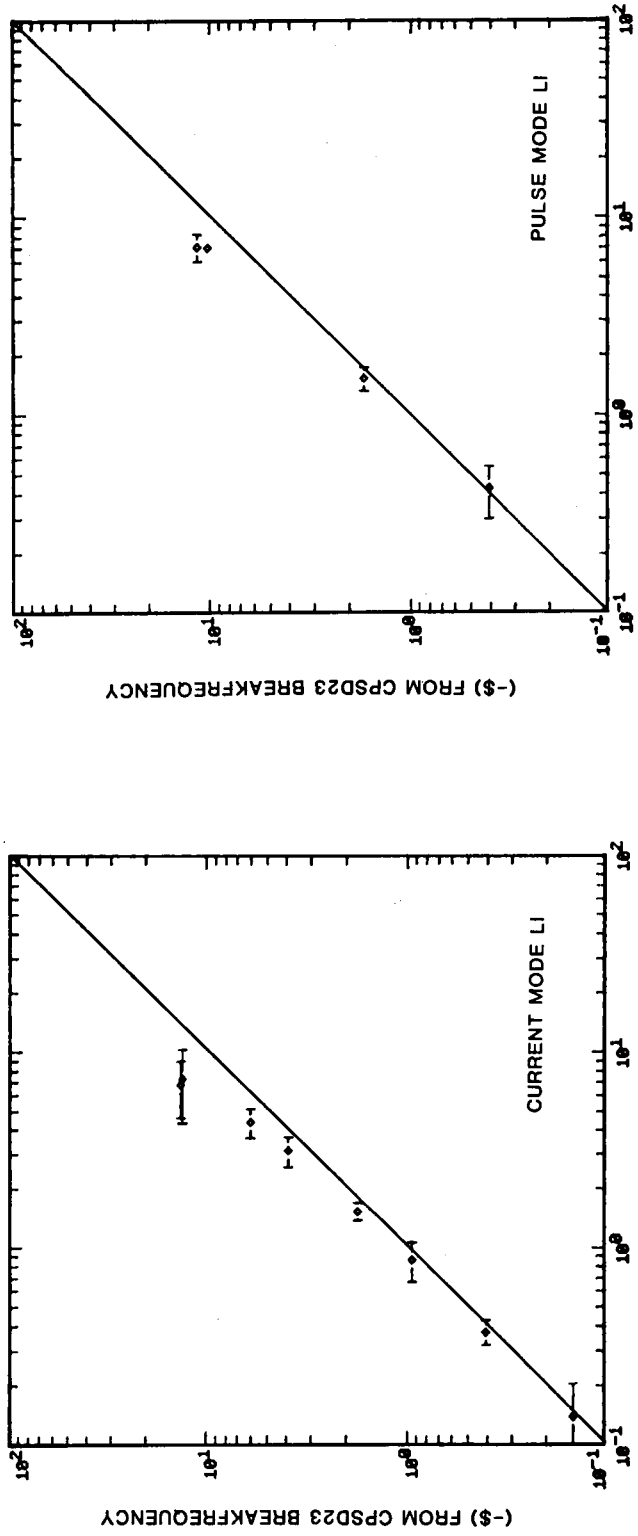


Fig. 5.12. Reactivities from ratios of spectral densities compared with reactivities from prompt neutron decay constants obtained from CPSD23 using the Li detection system.

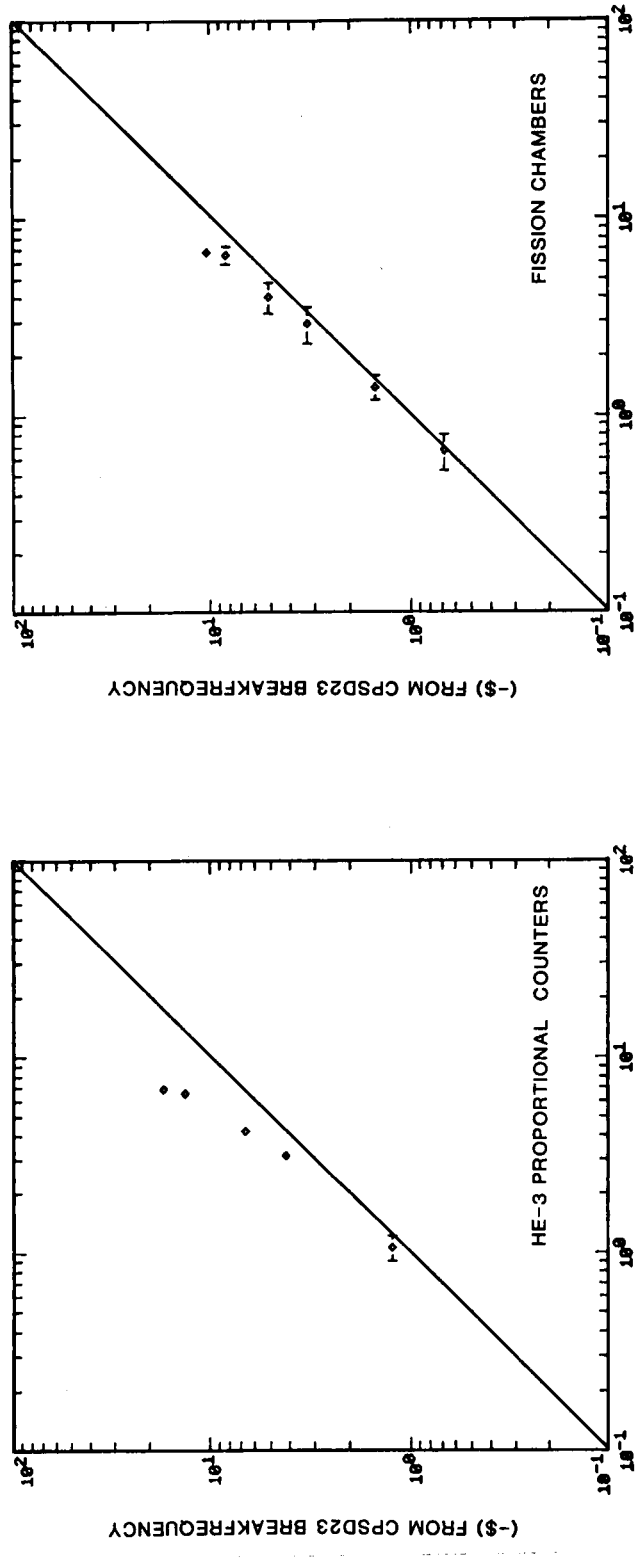


Fig. 5.13. Reactivities from ratios of spectral densities compared with reactivities from prompt neutron decay constants obtained from CPSD23 using the ^{3}He and fission counting systems.

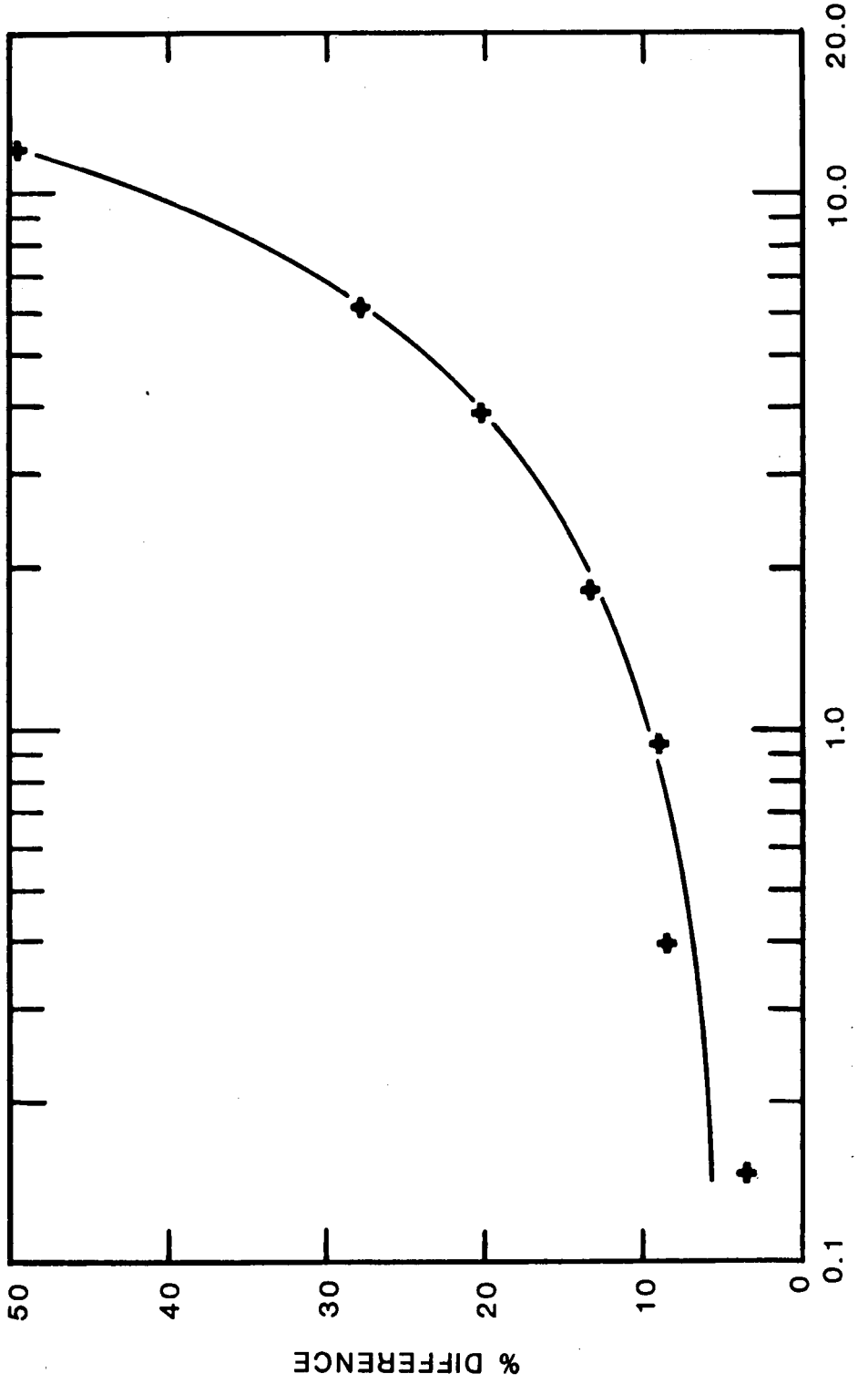


Fig. 5.14. Percent difference of the reactivities from the CPSD23 breakfrequencies and from the ratios of spectral densities. Li scintillators operated in the current mode were used for these measurements.

from CPSD23 breakfrequencies. The increase in the difference between the two methods as subcriticality is increased is clearly illustrated in the figure.

Other methods of reactivity determination produced results comparable to the CPSD23 breakfrequency results except for the following:

1. Reactivities from the prompt neutron decay constants obtained from CPSD12 or (CPSD13) are lower than those obtained from CPSD23. This will be explained in the next section.

2. Reactivities determined by the modified source multiplication technique using count rates from the primary fission chambers were not corrected for efficiency changes. The primary fission chamber was located deep in the reflector above the reactor. This is the third (uncalculated) dimension of the 2-D calculations. Efficiency change correction factors were calculated for the auxiliary fission chamber in most core configurations.

3. The background gamma radiation affected the measured coherence between detectors 2 and 3 for the Li and ^{3}He detection systems. Reactivities obtained from the low frequency coherence amplitudes for measurements using these detection systems were not adjusted for this effect, thus making these reactivities in error.

F. Effects of Higher Spatial Modes

The effects of higher spatial harmonics on the measurement of the ratio of spectral densities can best be illustrated in the time domain. The relationship between time and frequency domain measurements will be explained.

Some work had been done in the past that dealt with the effects of higher spatial harmonics on pulsed neutron measurements. Unfortunately, most of the work was performed using methods now referred to as modified pulsed neutron techniques first introduced by Sjöstrand.[30] In a modified pulsed neutron measurement, the prompt and delayed detector responses to a pulsed neutron source are combined to determine reactivity. The prompt detector response is due to detections of fissions caused by source neutrons and their prompt progeny. The delayed detector response is due to detections of fissions caused by delayed neutrons and their progeny, whether prompt or delayed.

Modified pulsed neutron measurements involve integrals of the detector response after a pulsed neutron source, hence, are extremely sensitive to the presence of higher spatial harmonics (harmonics increase or decrease detector count rates depending on source detector configuration). Sjöstrand[30] corrected his measurements by using calculated contributions of higher harmonics, making the accuracy of the measurement dependent on difficult calculations. Gozani[31] attempted to eliminate the higher harmonics by waiting until they have decayed before counting prompt neutrons and then extrapolating the counting history back to time zero. Garelis and Russell[32] introduced a weighting function that essentially ignores the early counting times when higher harmonic effects are at their peaks. Burgart[33] found that such corrections were inadequate for far subcritical cases and/or poor source detector placements because the effects of the higher harmonics so dominate the neutron population decay that by the time their effects diminish, the fundamental mode decay is undetectable.

The method to measure reactivity now referred to as pulsed neutron measurement was presented by Simmons and King.[34] They measured reactivity by obtaining the prompt neutron decay constant by fitting the detector response to a single exponential model. They avoided the effects of higher harmonics by choosing that portion of the detector response after the higher harmonics have decayed to insignificance. Again, this can not be done in some cases because of relatively slow decaying higher harmonics.

A neutron source in a subcritical reactor excites higher spatial modes which have positive contributions to the total flux near the source and negative contributions away from the source. The higher harmonics decay more rapidly than the fundamental mode; therefore, some time after the source pulse, the neutron population at all locations in the core must experience an exponential decay with the decay constant of the fundamental mode.[34]

The measurement of the CPSD between the response of detector 1 and the output of either detectors 2 or 3 is related to a pulsed neutron measurement (see section E, Appendix A). The effects of higher decay modes on pulsed neutron measurements will first be examined.

A pulsed neutron experiment is a measurement of the decay constant of the fundamental mode (see sections B and E, Appendix A). Even though the higher harmonics decay more rapidly than the fundamental mode, for some combinations of source location, detector location, and reactor properties, the harmonics so dominate the fundamental that by the time the harmonics die out, the fundamental mode itself will have decayed to very low levels.[33,34]

Consider the position of the source in the reactor in this experiment (Fig. 4.2, page 25). The source was placed in the middle of the fourth element in an array of five (see Fig. 4.2). If the three fuel elements in column 2 (Fig. 4.2) were placed in column 7 as originally planned, the source would have been closer to the center of the reactor. However, these fuel elements were required to shield the Li detectors from the irradiated control rod fuel elements. The source location in this experiment is nearly half the distance from the center to the edge of the core. The source in this location excites the odd spatial modes, in particular, the first odd mode. Figure 5.15 shows the spatial shapes of the first even and odd modes for a symmetric and homogeneous core. Note that the positive peak of the odd mode is close to the same relative location (location divided by a/2, where a is the distance from one extrapolated edge to the other) of the source in the reactor with the control rods withdrawn. With the control rods inserted, the source is effectively closer to the edge of the reactor which would also excite the higher spatial modes.

At time 0, when the source pulse is introduced into the reactor, the spatial distribution of the neutron population can be described by a delta function at the source location. It takes an infinite number of modes to represent a delta function. Assume that at time t_1 following a source pulse at relative position 0.5 (half the distance from the center to the edge), all modes have decayed to insignificance except for the first even and odd modes. Assume also that at time t_1, the relative amplitudes of the two remaining modes are as shown in Fig. 5.15.

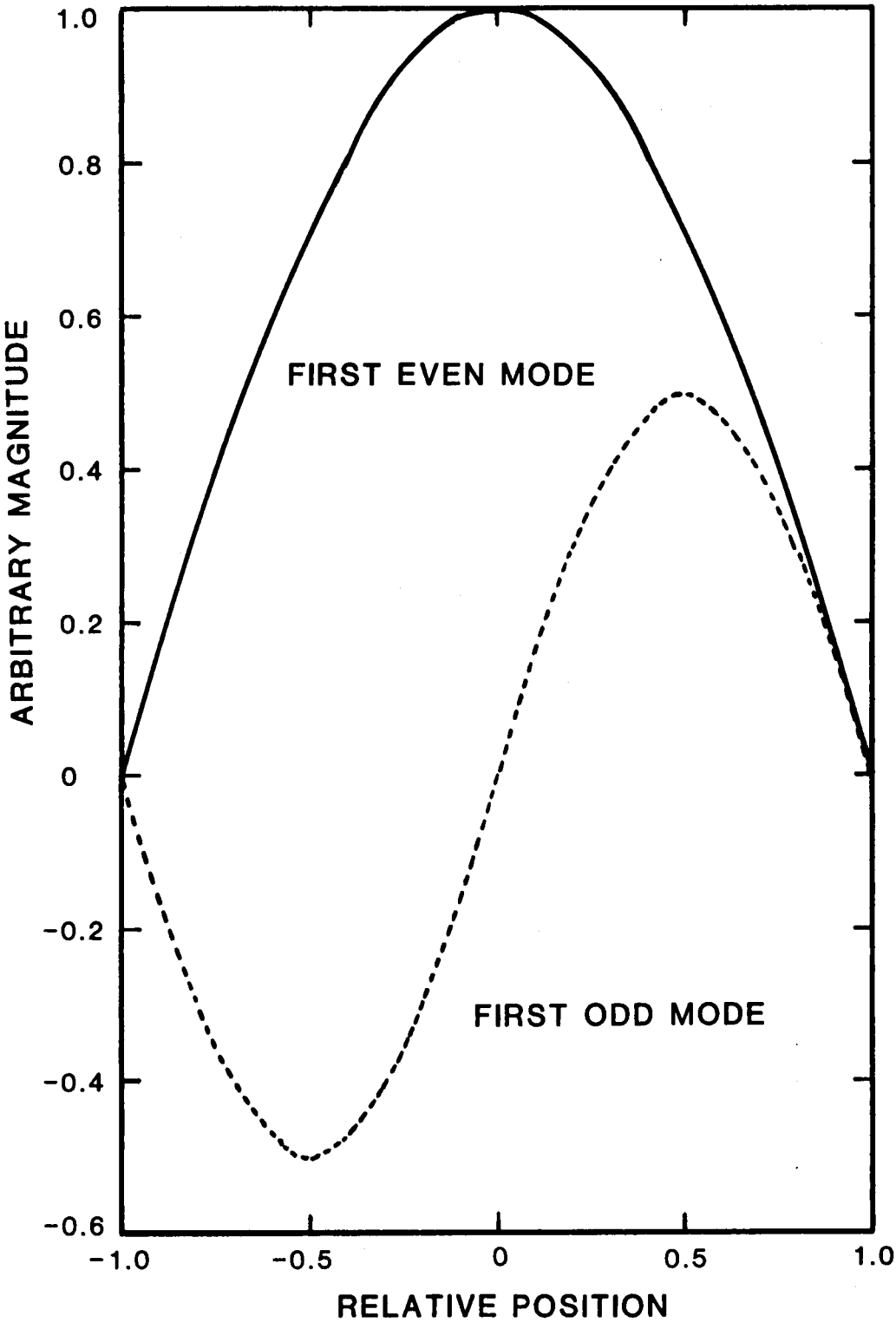


Fig. 5.15. Spatial shapes of the first even and odd modes. (The odd mode is half the amplitude of the even mode. Relative positions -1.0 and 1.0 are the left and right extrapolated edges of the core.)

Figure 5.16 shows the spatial distributions of the neutron population (taken as the sum of the modes) at time t_1 and after. Assuming the decay constants of the even and odd modes are 1000 sec^{-1} and 4000 sec^{-1} respectively: $t_2 = t_1 + 1 \times 10^{-4}$ sec, $t_3 = t_1 + 2 \times 10^{-4}$ sec, $t_4 = t_1 + 5 \times 10^{-4}$ sec, and $t_5 = t_1 + 1 \times 10^{-3}$ sec. Except for relative location 0, where the contribution of the odd mode is zero, the neutron population at any position in the core changes with two time constants. At time t_5, the neutron population distribution is close to the fundamental (first even) mode. Thereafter, the neutron population decays with the decay constant of the fundamental mode. Depending on the initial amplitudes of the modes present and their decay constants, t_5 might not occur until the total neutron population decays to undetectable levels.

In section E of Appendix A, it is shown that a measurement of the CPSD between the output of a detector observing the source and the response of a detector detecting neutrons from fission chains in the reactor is essentially a pulsed neutron measurement in the frequency domain. For a reactor with higher spatial modes, the time and frequency responses will be of the form

$$h(t) = \sum_{i=0}^{\infty} a_i e^{-\alpha_i t} , \tag{5.3}$$

and

$$H(\omega) = \sum_{i=0}^{\infty} \frac{a_i}{\alpha_i + j\omega} . \tag{5.4}$$

If a_i is small, then mode i's contribution to the total response will be

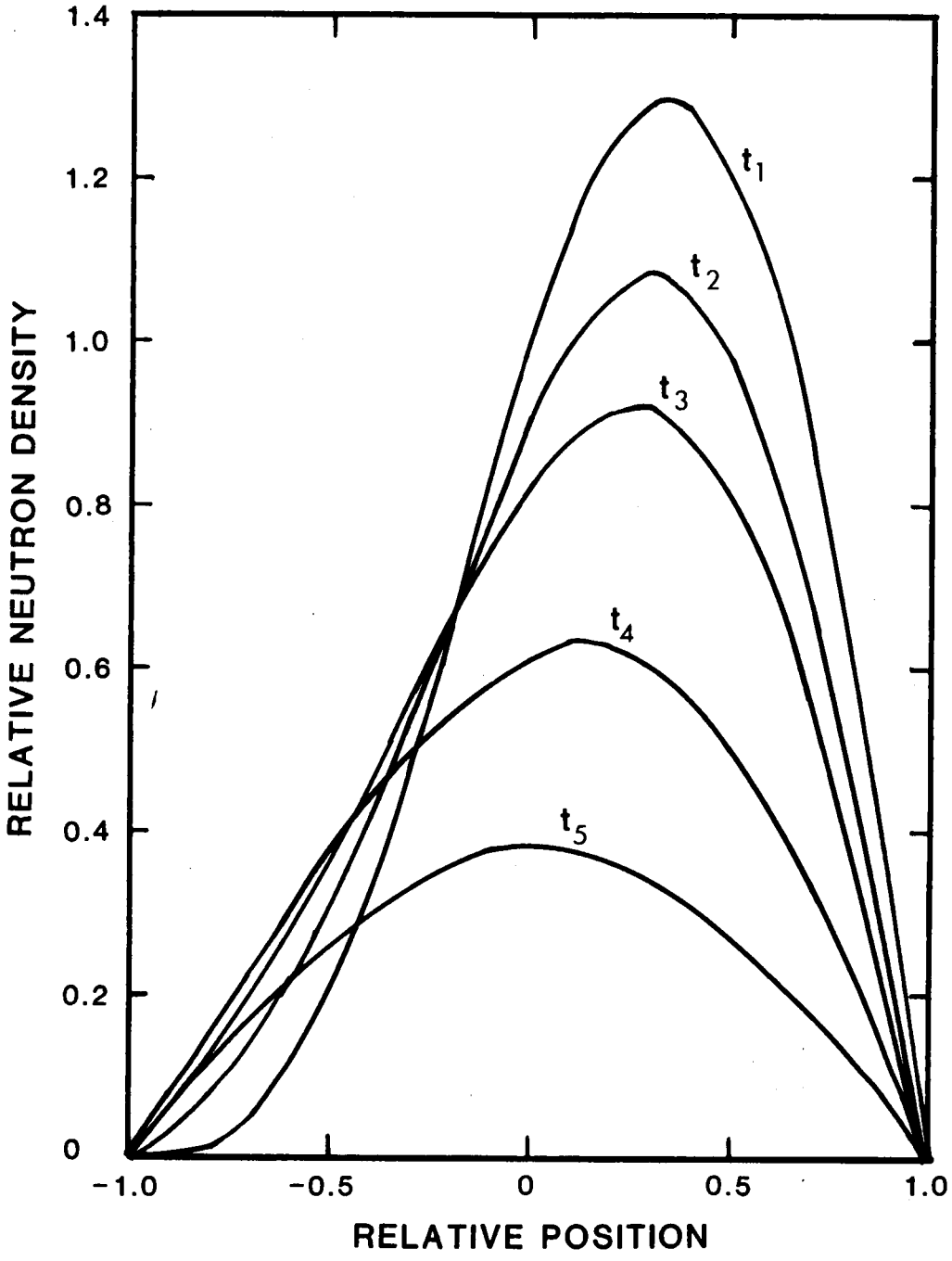


Fig. 5.16. Spatial distributions of the neutron density at different times after the introduction of a source pulse at location 0.5 (half the distance from the center to the edge).

small. If $\alpha_i \gg \alpha_0$ for $i > 0$, then mode i's contribution, no matter how large, will not last long and its effect on the CPSD (or pulsed neutron) measurement will be small.

If only the fundamental mode exists, then the measured frequency response will be of the form

$$H(\omega) = \frac{a_0}{\alpha_0 + j\omega} , \tag{5.5}$$

and the following product will produce α_0:

$$\alpha_0 = -\omega \frac{\text{real}}{\text{imaginary}} . \tag{5.6}$$

Assume that in this experiment, all modes were excited and that $\alpha_i \gg \alpha_0$ for all $i > 1$. Therefore, the frequency response measured will be of the form

$$H(\omega) = \frac{a_0}{\alpha_0 + j\omega} + \frac{a_1}{\alpha_1 + j\omega} \tag{5.7}$$

which can be written as

$$H(\omega) = \frac{A}{(\alpha_0 + j\omega)(\alpha_1 + j\omega)} , \tag{5.8}$$

where A is a complex quantity. However, note that the location of detectors 2 and 3 is close to relative -1.0 in Fig. 5.15. Therefore, a_0 is a positive quantity and a_1, negative. If it is assumed that $|a_0| = |a_1|$, then A in Eq. (5.8) reduces to a real constant. The basis

for making this assumption is that its consequences are manifested by the experimental results.

If the product similar to Eq. (5.6) is formed from Eq. (5.8), the following result is obtained:

$$-\omega \frac{\text{real}}{\text{imaginary}} = \frac{\alpha_0\alpha_1 - \omega^2}{\alpha_0 + \alpha_1} \quad . \tag{5.9}$$

This product measured at core configuration 7 using detector 2 of the fission counting system is shown in Fig. 5.17.

Using Eq. (5.9) as a model, the measured results were used to obtain α_0 and α_1. These decay constants are listed in Table 5.2 for measurements using the Li detectors operated in the current mode. Except for configuration 1, which has large uncertainties associated with it, α_1 approaches α_0 as the reactor gets more subcritical. Simmons and King[34] calculated the values of α_0 and α_1 for a highly enriched, hydrogen moderated cylindrical assembly. They calculated α_1/α_0 to be $\sim$20 at delayed criticality and $\sim$2 at \$15 subcritical. The values of α_1/α_0 inferred from this experiment are: $\sim$20 at configuration 2 ($\sim$-\$0.40) and $\sim$3 at configuration 6 ($\sim$-\$6.00).

Using Eq. (5.9) and the values in Table 5.2, the frequencies at which ω^2 equal 10% of $\alpha_0\alpha_1$ were calculated. The ratios of these frequencies to their respective values of α_0 are, in ascending configuration number: 0.55, 1.4, 1.18, 1.19, 0.83, and 0.56. Except for the first result, this ratio tends to decrease with increasing subcriticality. This is illustrated in Fig. 5.18 using the ^{3}He detector measurements at core configurations 3 and 9. Using normalized frequencies

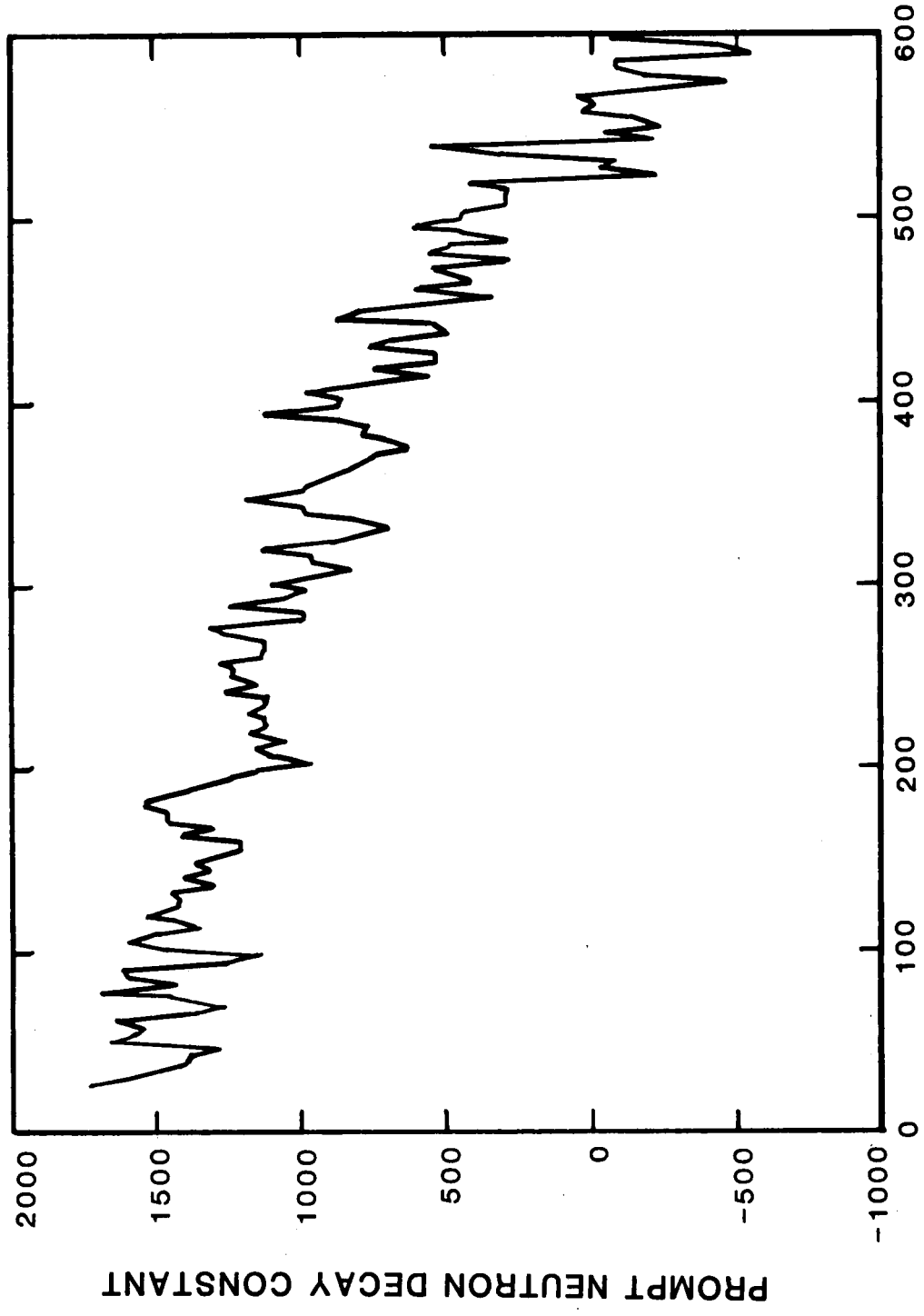


Fig. 5.17. Prompt neutron decay constant from the product of the angular frequency and the ratio of the real to the imaginary parts of the corrected CPSD12 measured at core configuration 7 using a fission chamber.

Table 5.2. Inferred decay constants of the first two modes

Configuration number	α_0 $(sec^{-1})^a$	α_1 $(sec^{-1})^a$	α_1/α_0	α_0 from CPSD23 (sec^{-1})
1	233 ± 160	1690 ± 1200	7.25	156 ± 0.3
2	188 ± 24	3710 ± 480	19.7	192 ± 0.4
3	287 ± 97	3970 ± 1300	13.8	256 ± 0.7
4	380 ± 52	5400 ± 750	14.2	381 ± 0.9
5	604 ± 210	4150 ± 1400	6.87	677 ± 13
6	1120 ± 230	3490 ± 720	3.12	977 ± 18

[a]Parameters obtained by fitting measurements using the Li scintillation system (detector 2) operated in the current mode.

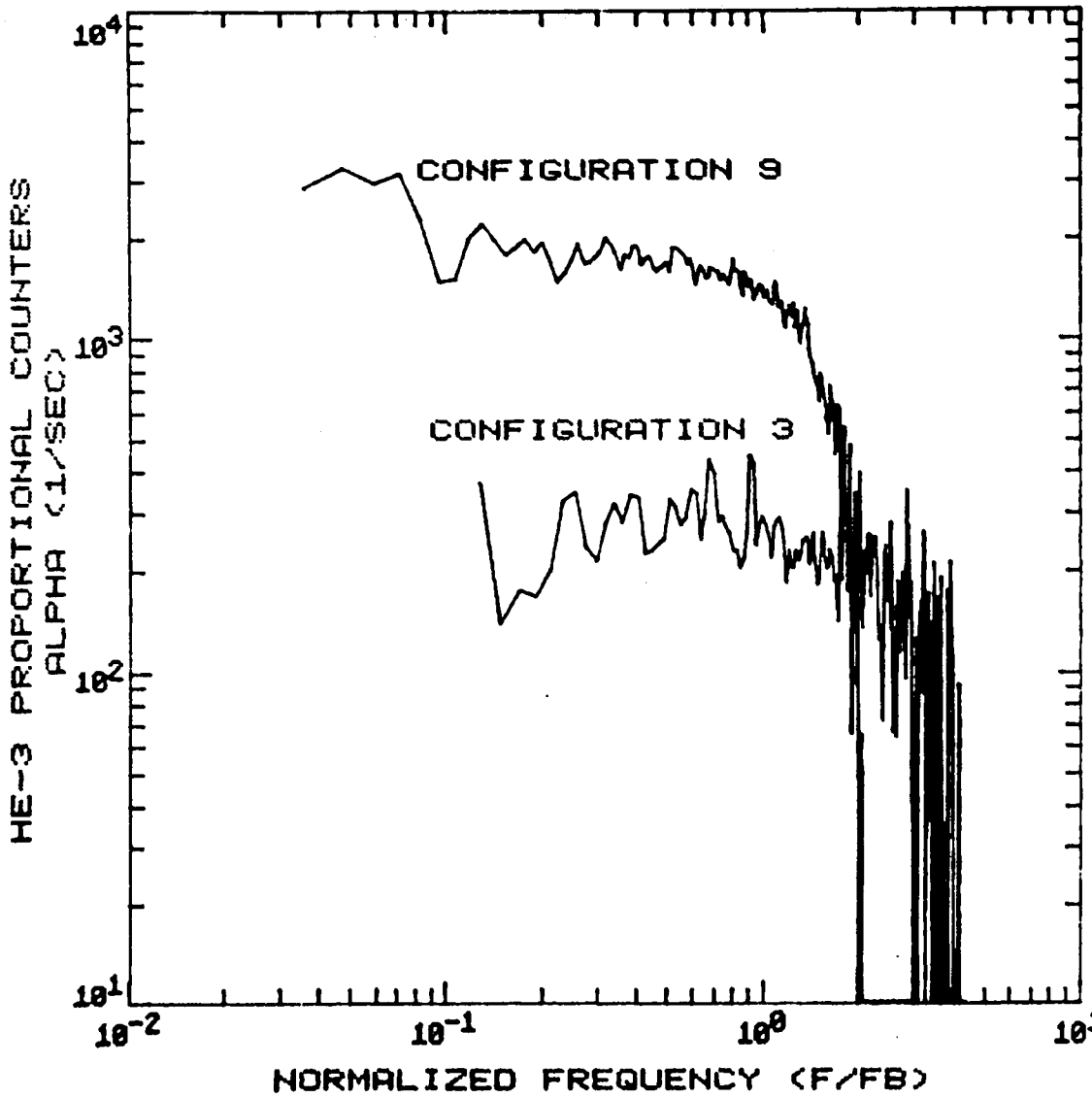


Fig. 5.18. Prompt neutron decay constant obtained from the product of the angular frequency and the ratio of the real to the imaginary parts of the CPSD12 measured at core configurations 3 and 9 using the ^{3}He detection system and plotted as a function of normalized frequency. ($\omega = 2\pi f$; therefore, $f/f_b = \omega/\alpha_0$.)

(ω/α_0), ω^2 in Eq. (5.9) becomes significant at lower frequencies in configuration 9 (more subcritical configuration) than in configuration 3.

Also, if the neutron population is indeed decaying with two decay constants and the frequency response is described by Eq. (5.8) (again assuming A being real), then the measured CPSD12 should exhibit two breakfrequencies. This effect can be seen in Fig. 5.19 which shows the corrected $|CPSD12|^2$ measured at configuration 9 using the fission counting system. The estimated breakfrequencies using Eq. (5.9) are 337 Hz and 536 Hz compared to 270 Hz and 650 Hz from Fig. 5.19. The differences are within the uncertainties of the measurement. This effect is not seen in most of the data either because the sampled bandwidths were too low to observe the second breakfrequency, or because the coherences were too low at high frequencies such that the measured CPSDs were not converged.

In a pulsed neutron experiment, the prompt neutron decay constant is inferred from the decay of the number of related counts from a detector after the reactor is pulsed by the source. In a Rossi-α measurement, the decay constant is inferred from the decay of the number of related counts from a detector after a detection in the same of in another detector. The measurement of the CPSD between the responses of two detectors observing neutrons from fission chains in the reactor is essentially a Rossi-α measurement in the frequency domain.[1] The pulsed neutron measurement starts counting immediately after a source pulse, while the Rossi-α measurement waits for a detection in one detector before counting. There is a built in delay in a Rossi-α measurement

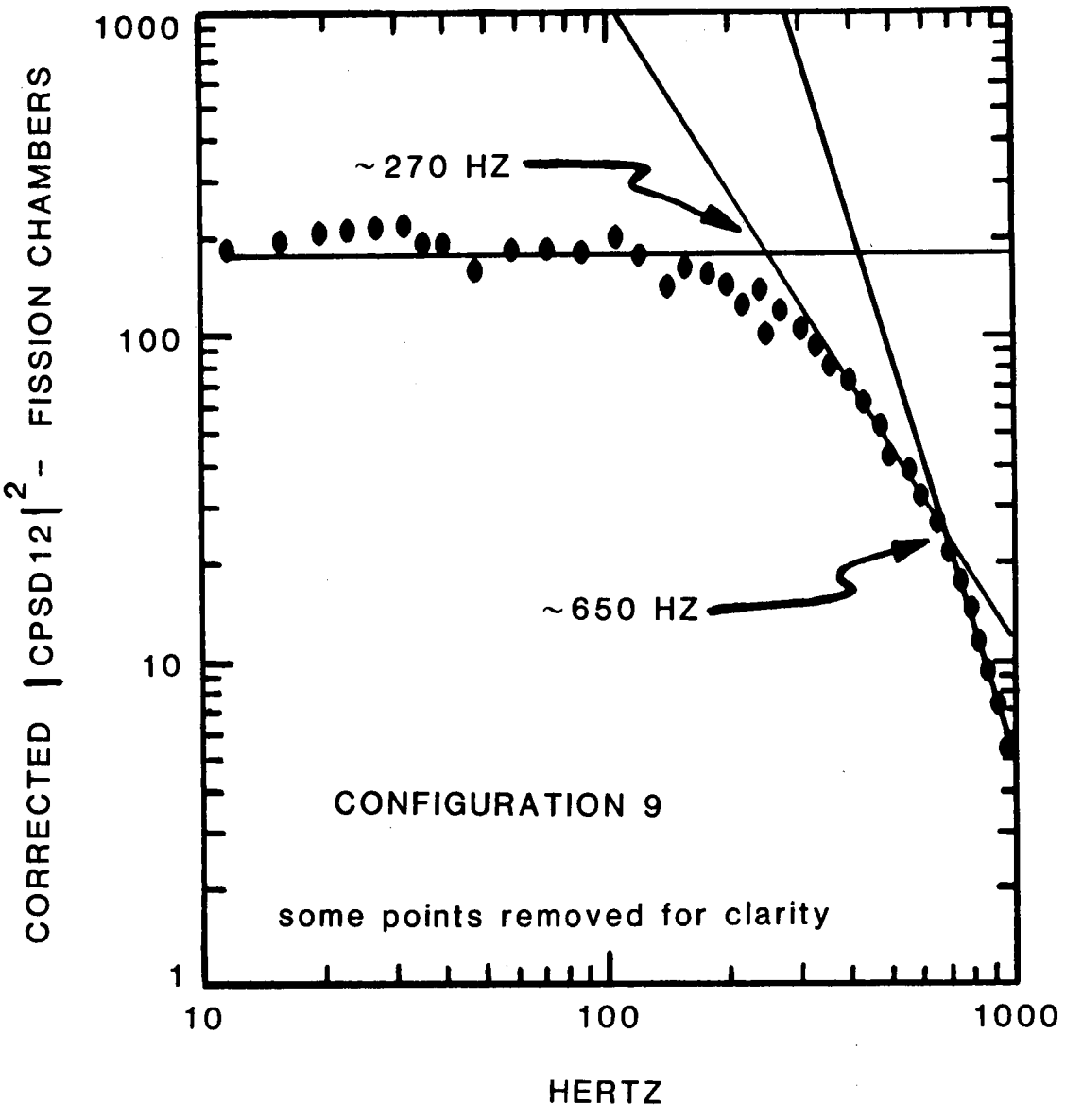


Fig. 5.19. Corrected squared magnitude of the CPSD12 measured at core configuration 9 using the fission counting system. Slopes of straight lines drawn are 0, 2, and 4 decades per decade. (Y-axis units are arbitrary.)

that weights it towards measuring the fundamental mode decay. However, as seen in the discussion above, some higher spatial modes with relatively small decay constants may be excited. In principle then, the Rossi-α measurement should also be affected by slowly decaying higher spatial modes.

This experiment was not performed like classical pulsed neutron or Rossi-α measurements where the reactor is pulsed and neutron population decays are measured. In this experiment, the reactor was randomly pulsed, on the average, once every 10 μsec. After some time, the delayed neutron precursor concentrations reached steady-state levels and their spatial distributions are closer to that of the fundamental mode. For the pulse neutron measurement, the delayed neutrons appear after the fundamental mode has decayed to insignificance. However, in a Rossi-α measurement, the delayed neutrons are driving sources for the reactor and complement the ^{252}Cf source. Since the delayed neutron population is distributed more like the fundamental mode, the Rossi-α measurement has a better chance of observing the fundamental mode decay. (This effect is more pronounced near delayed criticality.)

Therefore, in this experiment, the excited higher spatial harmonics will more likely affect the measurement of CPSD12 (and CPSD13) than the measurement of CPSD23. The detectors were placed in the reactor where the contribution of the first odd spatial harmonic is negative; therefore, a_1 in Eq. (5.7) will be negative. Relative to a measurement of CPSD12 and CPSD13 in a single-order system (assumed in the theory developed in Chap. 2), the effect of the first odd spatial mode on the measured

CPSD12 and CPSD13 is to decrease their magnitudes. The effect, then, of this odd harmonic on the ratio of spectral densities, $G_{12}^{*}G_{13}/G_{11}G_{23}$, is to decrease the numerator more than it would decrease the denominator. The presence of this odd harmonic could, therefore, be the cause of underestimating the subcriticality using the ratios of spectral densities. Furthermore, as the reactor gets more subcritical, α_1 approaches α_0. The contribution of this odd spatial mode (second term in Eq. (5.7)] to the measured CPSD becomes more significant, causing an increasing underestimation of the subcriticality.

In a single mode system, the numerator of the ratio of spectral densities would break at the same frequency as the denominator, hence the ratio would be constant in frequency. However, in a measurement where CPSD12 and CPSD13 contains a second breakfrequency (not accounted for in the theory) while CPSD23 does not, then the ratio of spectral densities would be frequency dependent. As the reactor gets more subcritical, the second breakfrequency gets closer to the first (that is, $\alpha_1/\alpha_0 \rightarrow 1$); hence, the frequency dependence of the ratio of spectral densities would occur sooner in frequency relative to the first. This is illustrated in Fig. 5.20. On a normalized frequency scale (ω/α_0), the ratio of spectral densities becomes frequency dependent sooner in frequencies at configuration 9 than at configuration 3.

G. Measurement Time

At $\sim$12 dollars subcritical, the measurement times using the different detection systems were as follows:

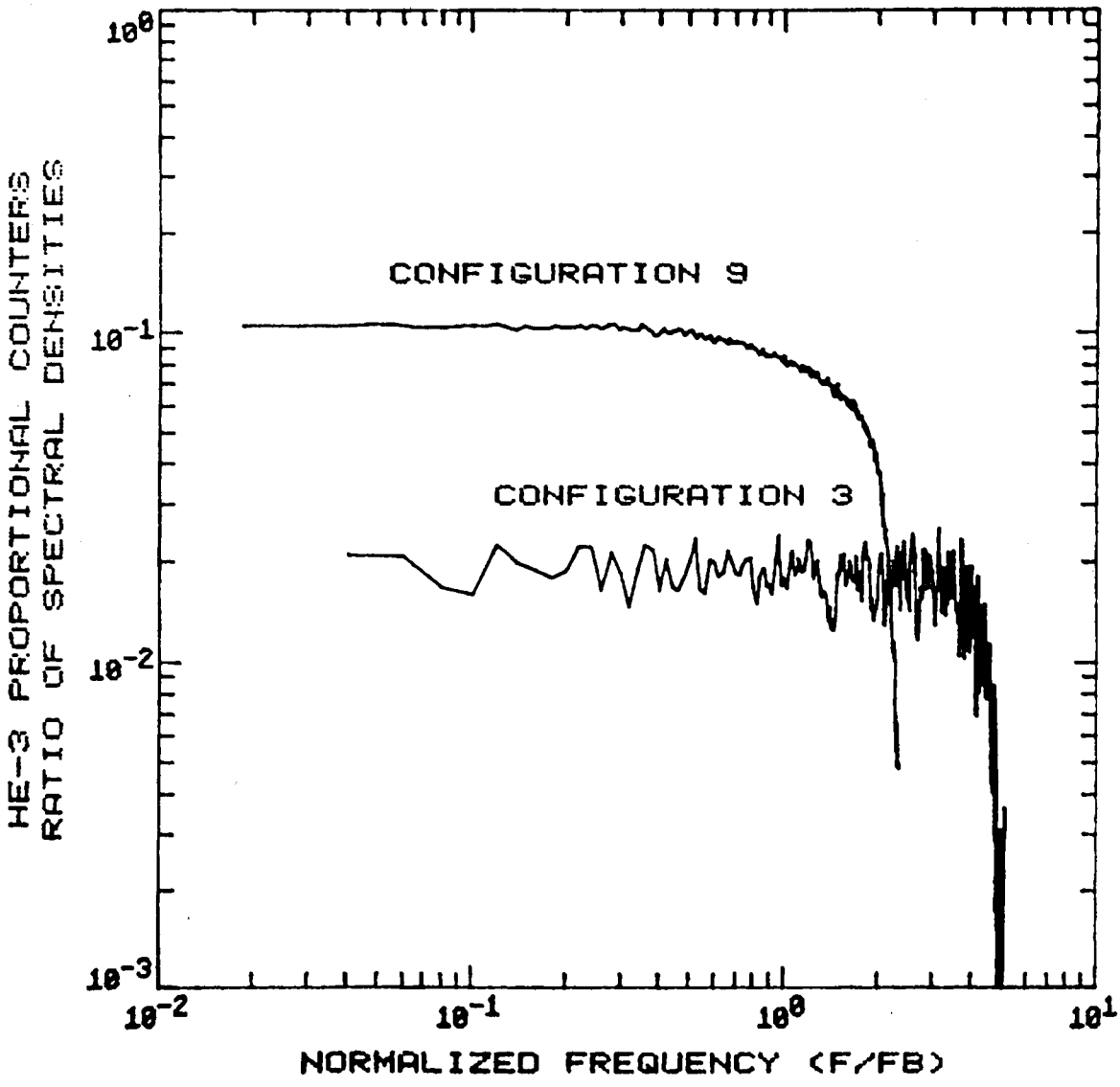


Fig. 5.20. Ratio of spectral densities measured at core configurations 3 and 9 using the ^{3}He detectors and plotted on a normalized frequency scale.

1. 14.2 h to obtain 36% precision using the Li detectors in the current mode,

2. 40.1 h to obtain 6.2% precision using the Li detectors in the pulse mode,

3. 0.7 h to obtain 4.8% precision using the ^{3}He detectors, and

4. 12.9 h to obtain 8.9% precision using the fission chambers.

These numbers are not comparable. There are factors which affect different detectors differently and factors which affect all detectors equally.

The high background gamma radiation severely affected the Li detectors. The difference in the detector output currents with and without the ^{252}Cf source in the reactor was imperceptible (<1%) at this level of subcriticality. Although the pulse mode operation of the detection system allowed some discrimination against the gamma pulses, the difference in count rates with and without the source was unnoticable (<1%). This caused the coherence between detector responses to be lower than that expected in a clean core for a given detection efficiency. Viewed another way, the apparent detection efficiency (as inferred from the coherence function) of the detection system was significantly decreased by the background gamma radiation.

The effect of the gamma radiation on the ^{3}He detection system was small and assumed insignificant. The gamma radiation did not affect the fission chambers.

The presence of the higher harmonics caused an underestimation of the breakfrequencies. The fitting algorithm was designed to fit the

measured data to a single-order lag model [Eq. (5.5)]. The presence of the second breakfrequency (not accounted for in the model) caused an underestimation of α_0. This in turn caused sampling rates to be chosen which were lower than optimal (20 × breakfrequency). Sampling rates in measurements using the Li detectors were four times lower than optimal. Sampling rates in measurements using the ^{3}He detectors and the fission chambers were two times lower than optimal. These caused measurement times to be 2 to 4 times longer than necessary.

The higher harmonics also increased the measurement time in another way. The coherences between the responses of detectors 1 and 2 and between the outputs of detectors 1 and 3 were decreased by the higher harmonics (negative contribution to the CPSDs). This decreased coherence increased the required measurement time for statistical uncertainties to diminish.

Taking all these effects into consideration, it is estimated that the measurement of the ratio of spectral densities to within 10% at ∿12 dollars subcritical would take:

1. ∿15 min if the detection efficiency is 10^{-3} counts per reactor fission, and

2. ∿3-4 h if the detection efficiency is 10^{-4} counts per reactor fission.

CHAPTER 6

STATISTICAL ERRORS IN THE ESTIMATE OF THE RATIO OF SPECTRAL DENSITIES

The quantity of interest in this experiment is the ratio of spectral densities, that is,

$$R = \frac{G_{12}^{*} G_{13}}{G_{11} G_{23}} = \frac{\gamma_{12}\gamma_{13}}{\gamma_{23}} \quad . \tag{6.1}$$

It was found in all cases that both ratios in Eq. (6.1) produced the same estimates of R and its standard deviation. (The statistical errors introduced by PSD2 and PSD3 in forming the coherences cancel each other in forming the ratio of coherences.) This being the case, it was decided that the coherences would be used in studying statistical errors since the coherences involves only real numbers while the spectral densities involves complex numbers.

An empirical study was first performed to determine the convergence characteristics of the measured coherence function.[35] The errors were then propagated to determine the statistical errors of $\hat{R}$, the ratio of measured coherence functions.

A. Convergence Characteristics of the Measured Coherence Function

Experimentally, two independent broadband white noise signals were combined using an operational amplifier manifold as shown in Fig. 6.1.

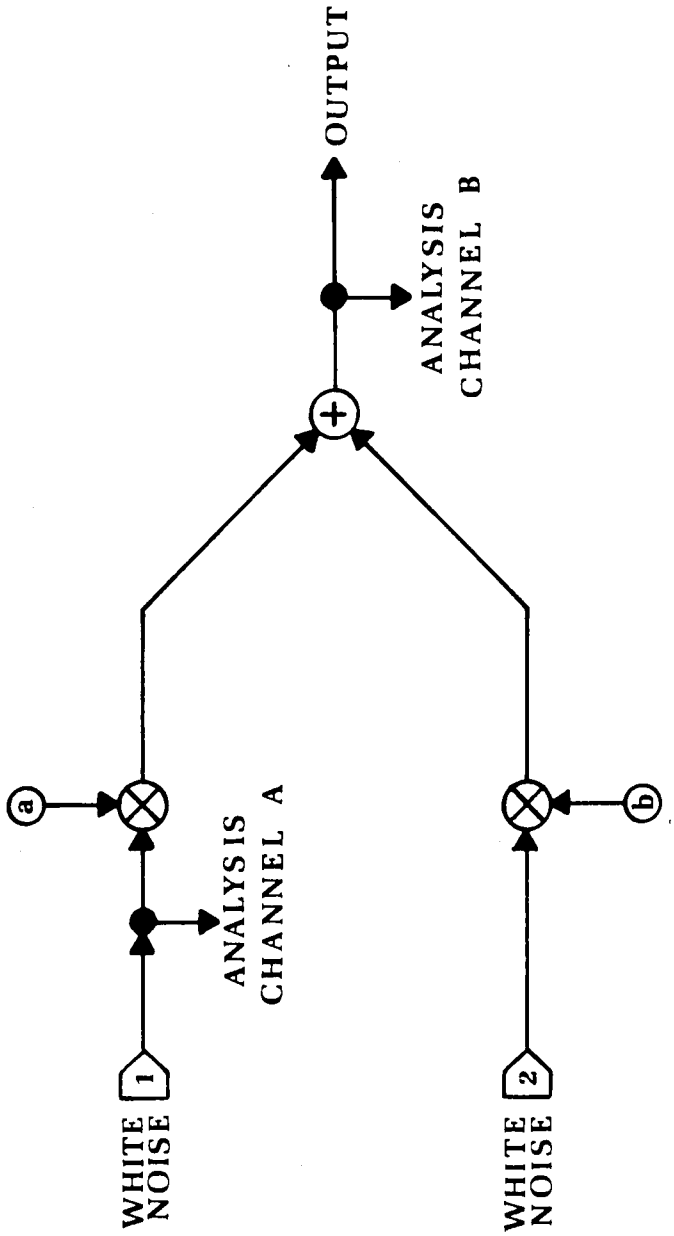


Fig. 6.1. Schematic of the operational amplifier manifold setup used in producing signal pairs with known coherences.

The attenuation values a and b were adjusted to obtain different signal-to-noise ratios (S/N), and hence different coherence values. The true coherence was determined from

$$\gamma^2 = \frac{S/N}{1 + S/N} . \tag{6.2}$$

Analysis channels A and B were low pass filtered before sampling to prevent aliasing. Data blocks of length 512 were sampled, Hanned, and Fourier transformed. Coherence functions were calculated from averages of 2 to 2000 data blocks. (Tests of up to half a million data blocks were made to verify results.) The values of S/N were chosen to obtain coherence values that ranged from $\sim$0.001 to $\sim$0.8.

Using every fifth frequency point, 25 coherence values were averaged across frequency to obtain a value for the measured coherence, $\hat{\gamma}^2$. The standard deviation, $\sigma_{\hat{\gamma}^2}$, of these 25 points about $\hat{\gamma}^2$ was also calculated. Two empirical fits were performed at each S/N level to obtain the functional dependencies of $\hat{\gamma}^2$ and $\sigma_{\hat{\gamma}^2}$ on the number of data blocks, n, and the true coherence, γ^2.

The measured coherence was found to satisfy the relation

$$\hat{\gamma}^2 = \gamma^2 + \frac{(1 - \gamma^2)^2}{n} , \tag{6.3}$$

for all cases except when n = 1 and γ^2 is neither 0 or 1. The measured standard deviation was found to satisfy the relation

$$\sigma_{\hat{\gamma}^2} = \frac{\hat{\gamma}^2(1 - \gamma^2)}{\sqrt{1 + n\gamma^2/2}}, \tag{6.4}$$

for all cases where $n \geqslant 5$.

Equation (6.3) is plotted in Fig. 6.2 together with the measured coherence values. The deviations of the measured values from the plotted lines can be accounted for by the uncertainties in the values of the operational amplifier manifold components. Figure 6.3 shows Eq. (6.4) plotted with the measured standard deviations.

The bias error, $\hat{\gamma}^2 - \gamma^2$, diminishes as $1/n$, while the standard error (standard deviation) decreases as $1/\sqrt{n}$. Therefore, in reducing the standard error to acceptable levels, the bias error will have been reduced to insignificant levels and will not be considered in the error analysis of R.

B. Convergence Characteristics of the Ratio of Measured Coherence Functions

The standard errors of the measured coherence functions are propagated to $\hat{R}$ by

$$\sigma^2_{\hat{R}} = \left(\frac{\partial \hat{R}}{\partial \hat{\gamma}^2_{12}}\right)^2 \sigma^2_{\hat{\gamma}^2_{12}} + \left(\frac{\partial \hat{R}}{\partial \hat{\gamma}^2_{13}}\right)^2 \sigma^2_{\hat{\gamma}^2_{13}} + \left(\frac{\partial \hat{R}}{\partial \hat{\gamma}^2_{23}}\right)^2 \sigma^2_{\hat{\gamma}^2_{23}} + \text{CROSS TERMS} . \tag{6.5}$$

In a first order approximation, the cross terms are ignored. Inserting the partial derivatives into Eq. (6.5), the relative standard deviation of $\hat{R}$ can be expressed as

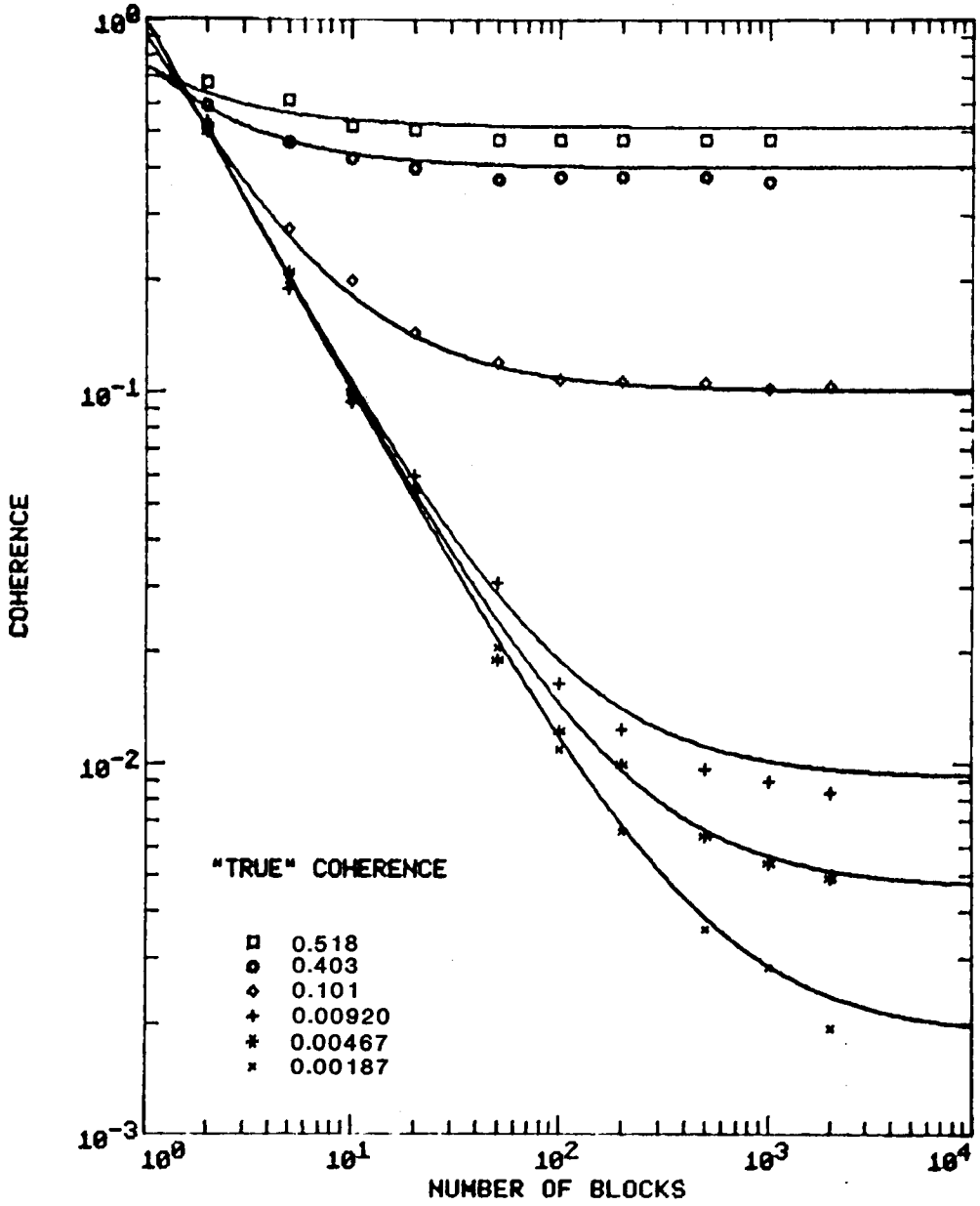


Fig. 6.2. Curves of measured coherence as a function of the number of data blocks averaged for various values of "true" coherence.

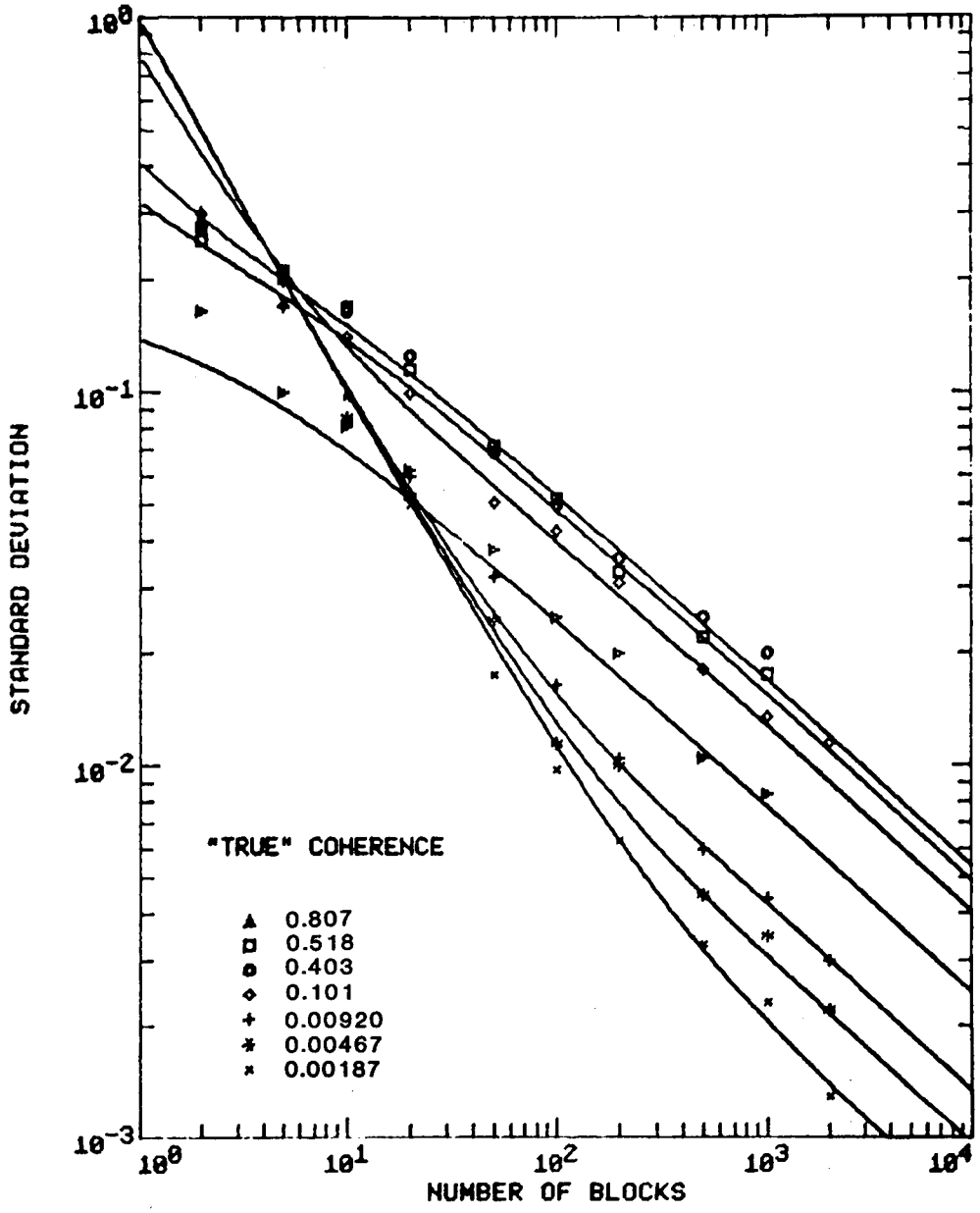


Fig. 6.3. Curves of standard deviation of measured coherence as a function of the number of data blocks averaged for various values of "true" coherence.

$$\varepsilon_{\hat{R}} = \frac{\sigma_{\hat{R}}}{\hat{R}} = \frac{\left[\varepsilon^2_{\hat{\gamma}^2_{12}} + \varepsilon^2_{\hat{\gamma}^2_{13}} + \varepsilon^2_{\hat{\gamma}^2_{23}}\right]^{1/2}}{2} , \tag{6.6}$$

The relative standard error of the coherence function can be obtained from Eq. (6.4), that is,

$$\varepsilon_{\hat{\gamma}^2} = \frac{\sigma_{\hat{\gamma}^2}}{\hat{\gamma}^2} = \frac{(1 - \gamma^2)}{\sqrt{1 + n\gamma^2/2}} . \tag{6.7}$$

The predictions of Eq. (6.6) compare favorably with the actual measured relative standard errors obtained from the experiment. This comparison is shown in Fig. 6.4. Predicted standard deviations obtained from Eq. (6.6) are compared with measured standard deviation from previous measurements in a uranium metal sphere and uranium metal cylinders[15] in Fig. 6.5. Agreement between predictions and measurements is good.

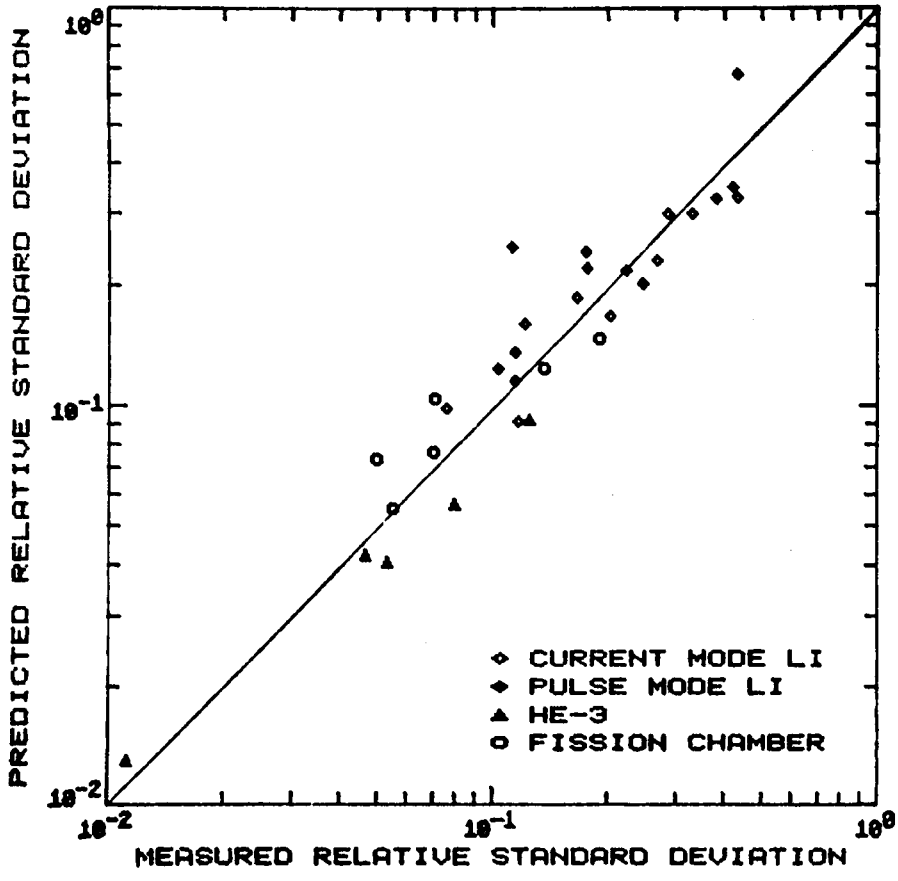


Fig. 6.4. Comparison between the predicted and the measured relative standard deviations of the ratios of spectral densities.

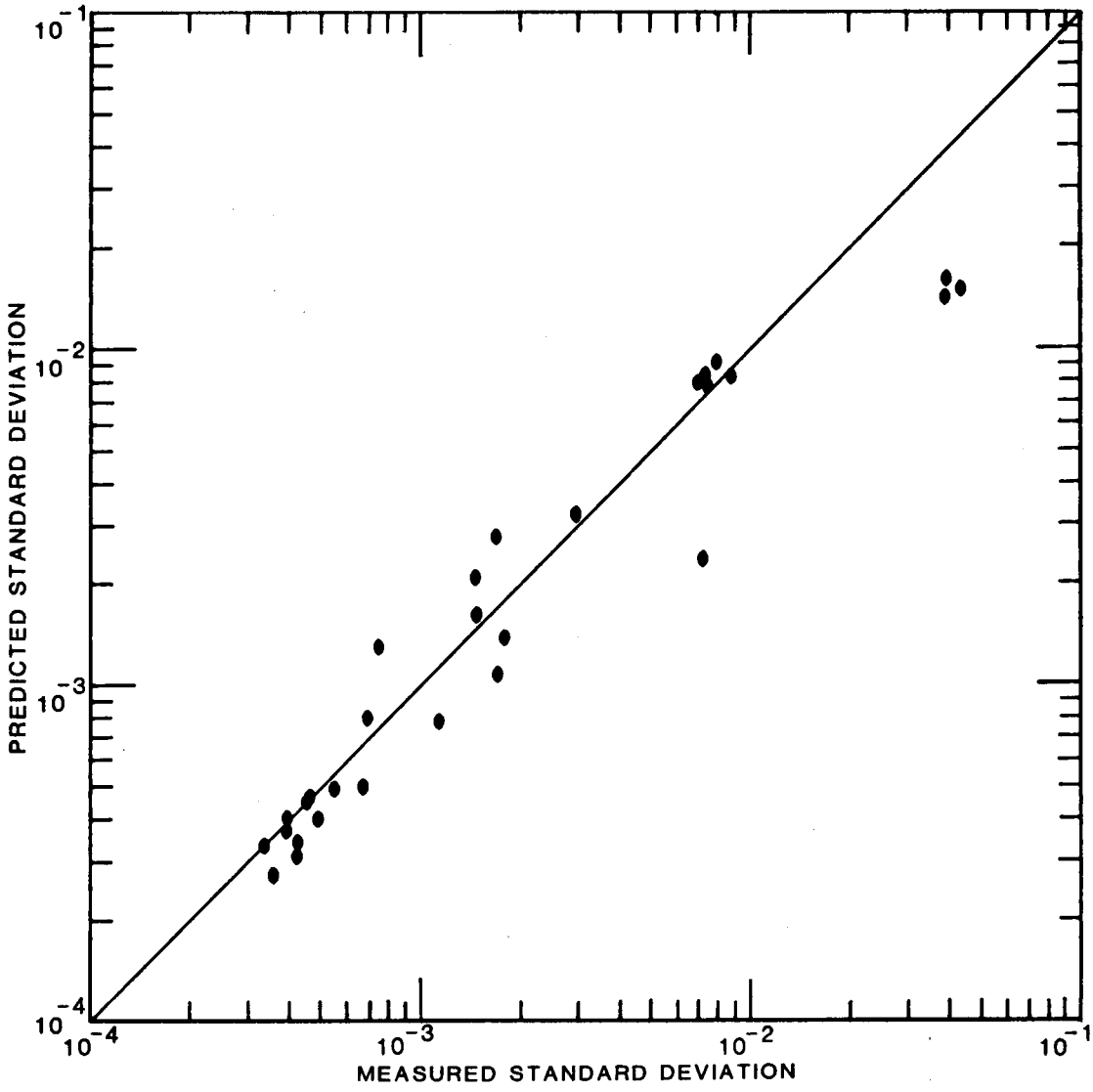


Fig. 6.5. Comparison between the predicted and the measured standard deviations of the ratio of spectral densities obtained from previous measurements in a uranium metal sphere and uranium metal cylinders (ref. 15).

CHAPTER 7

SUMMARY AND RECOMMENDATIONS

^{252}Cf source driven neutron noise spectral density measurements were performed in the Pool Critical Assembly, a light water moderated research reactor.

A. Findings of the Experiment

1. Measurement Time

The main objective of this experiment was to determine if neutron noise spectral density measurements with ^{252}Cf in light water moderated systems could be performed in a reasonable time. This experiment showed that using commercially available detectors, the measurement can be performed in a reasonable amount of time, that is, measurement of the ratio of spectral densities at ∿12 dollars subcritical can be made to within 10% uncertainty in: (a) ∿15 min using ^{3}He proportional counters (efficiency $\sim 10^{-3}$ counts/reactor fission, sensitivity ∿29 counts/sec/nv-thermal), and (b) ∿3-4 h using 2 gram (^{235}U) fission chambers (efficiency $\sim 10^{-4}$ counts/reactor fission, sensitivity ∿1.2 counts/sec/nv-thermal).

2. Interpretation of Measured Results

There is evidence to suggest that higher spatial harmonic modes present in the system caused difficulties in interpreting the measured results. Far subcritical reactivities obtained from the ratio of spectral densities do not compare favorably with reactivities determined by other

techniques. The presence of the irradiated fuel elements precluded the movement of the Li detectors to other locations in and around the core to systematically study the effects of the higher harmonic modes on the measured spectral densities. Scheduling constraints prevented the use of the fission chamber for this study. The ^{252}Cf source was not moved closer to the detectors because of the possible direct contributions from the source to the detectors.

3. Convergence Characteristics of the Ratio of Measured Spectral Densities

Empirical equations were developed which describe the relationships of the bias and standard errors of the measured coherence functions to the value of the true coherence and the number of data blocks averaged. It was found that a first order propagation of the standard error adequately described the standard error of the measured ratio of spectral densities.

4. Conclusions from the Experiment

These first ^{252}Cf source driven neutron noise spectral density measurements in water moderated systems showed that such measurements are possible in water moderated systems, that is, the measurement time is not excessive. There is, therefore, the possibility of measuring reactivity using the ^{252}Cf method in systems like light water reactors and fuel storage facilities if the effects of higher spatial harmonics can be accounted for or minimized by careful choice of source and detector locations. Also, the possibility exists in using the ^{252}Cf

technique to monitor reactivity changes in the fuel reprocessing and fuel fabrication facilities.

It was mentioned in Chap. 2 that the constancy of the measured ratio of spectral densities as a function of frequency could be used to validate the application of point kinetics model to the system being measured. This is also true for the constancy of the product of the angular frequency and the ratio of the real to the imaginary parts of CPSD12 (or CPSD13) as a function of frequency. The presence of higher spatial harmonics in this experiment demonstrated for the first time, this self-checking feature of the ^{252}Cf method of reactivity measurement.

B. Recommendations for Further Investigation

1. Systematic Study into the Effects of the Higher Spatial Harmonics

It has been shown that the measurement of the ratio of spectral densities in a light water moderated system can be performed in a reasonable amount of time. Its interpretation depends upon understanding the effects of higher harmonics. This technique of reactivity determination could be made useful if: (a) the effects of the higher harmonics could be incorporated into the theory of this measurement, (b) the effects of the higher harmonics can be measured and removed from the desired measured quantities, and/or (c) the system is well understood and flexible enough to avoid the excitement or the measurement of higher harmonics by judicious choice of source and detector locations.

This study should be carried out: (a) theoretically, that is, developing equations from space dependent transport or diffusion

equations, (b) experimentally, that is, performing parametric measurements in known systems by systematically changing the source and detector locations, and/or (c) empirically, that is, simulating experiments using deterministic and/or stochastic computer codes.

Past methods[30-34] of dealing with the higher harmonic effects cannot be used for the present measurement. However, understanding these methods might provide the clue on how to correct the ^{252}Cf reactivity measurement methods for spatial harmonic effects.

2. Measurement Time

In this experiment, the sampling rates used were low enough such that the calculation time was less than the sampling time, hence all available data were sampled and analyzed on line. However, in systems with slightly shorter prompt neutron lifetimes, higher sampling rates would be required. In such systems, the calculation time (using the same or similar signal analysis system) will exceed the sampling time resulting in lost data between sampled data sets.

The coherences between signals 1 and 2 and between 1 and 3 are, in most cases, vastly different from the coherence between signals 2 and 3. The calculation time could be decreased if the number of spectral densities averaged for each signal pair was chosen so that the standard errors of all coherences were equal.

This manner of accumulating spectral densities would produce a higher standard error in the measured ratio of spectral densities compared to the normal method if the number of data blocks sampled is

used as the criterion. However, if the total analysis time is used as the basis of comparison, the opposite might be true. A study is required to determine if indeed such averaging procedure can be used.

In Chap. 6, an empirical formula was developed that relates the true coherence and number of data blocks averaged to the measured coherence. Conceivably, the true coherence could be extracted from the measured coherence long before the bias error is reduced to insignificance.

If this is so, then the ratio of coherences could be projected from unconverged measurements of the coherence functions. Again, more studies are required to determine if such projections can be made. Time savings of factors of five are not inconceivable if this method could be used.

3. More Measurements in a Variety of Systems

To date, three measurements have been performed: in the critical mockup of the Fast Flux Test Facility, in uranium metal spheres and cylinders, and in the PCA. These systems are widely scattered in the spectrum of configurations and compositions of neutron multiplying systems. More measurements are needed in a variety of systems to assess the full potential of this reactivity measurement technique and to gain experience so necessary in exploiting it.

REFERENCES

REFERENCES

1. Uhrig, R. E., *Random Noise Techniques in Nuclear Reactor Systems*, The Ronald Press Company, New York, 1970.

2. Orndoff, J. D., "Prompt Neutron Periods of Metal Critical Assemblies," *Nuclear Science and Engineering*, Vol. 2, p. 450, 1957.

3. Feynman, R. P., DeHoffman, F., and Serber, R., "Dispersion of the Neutron Emission in U-235 Fission," *Journal of Nuclear Energy*, Vol. 3, p. 64, 1956.

4. Mogilner, A. I. and Zolotukhin, V. G., "The Statistical r-Method of Measuring the Kinetic Parameters of a Reactor," *Atomic Energy (USSR)*, Vol. 10, p. 377, 1961.

5. Babala, D., *Neutron Counting Statistics in Nuclear Reactors*, Norwegian Report KR-114, November, 1966.

6. Bennett, E. F., "The Rice Formulation of Reactor Noise," *Nuclear Science and Engineering*, Vol. 8, p. 53, 1960.

7. Srinivasan, M. and Sahni, D. C., "A Modified Statistical Technique for the Measurement of α in Fast and Intermediate Reactor Assemblies," *Nukleonik*, Vol. 9, p. 155, 1967.

8. Seifritz, W. and Stegemann, D., "Reactor-Noise Analysis," *Nukleonik*, Vol. 9, p. 129, 1971.

9. Ricker, C. W., Colomb, A. L., and Mann, E. R., *Feasibility Study of Measurements of Negative Reactivity by Analysis of Neutron Fluctuation Spectral Density*, ORNL-TM-690, Oak Ridge National Laboratory, September, 1963.

10. Nomura, T., "Improvement in S/N Ratio of Reactor Noise Spectral Density," *Journal of Nuclear Science and Technology (Tokyo)*, Vol. 2, p. 76, 1965.

11. Borgwaldt, H. and Stegemann, D., "A Common Theory for Neutronic Noise Analysis Experiments in Nuclear Reactors," *Nukleonik*, Vol. 7, p. 313, 1965.

12. Seifritz, W., "The Polarity Correlation of Reactor Noise in the Frequency Domain," *Nuclear Applications and Technology*, Vol. 7, p. 513, 1969.

13. Ackermann, N. J., Jr. and Buhl, A. R., "The Detection Efficiency Dependence of Subcritical Measurements by the Polarity Spectral Coherence Method," *Nuclear Technology*, Vol. 12, p. 320, 1971.

14. Mihalczo, J. T. and Paré, V. K., "Theory of Correlation Measurements in Time and Frequency Domains with ^{252}Cf," *Annals of Nuclear Energy*, Vol. 2, p. 97, 1975.

15. Mihalczo, J. T., Paré, V. K., Ragan, G. L., Mathis, M. V., and Tillet, G. C., "Determination of Reactivity from Power Spectral Density Measurements with Californium-252," *Nuclear Science and Engineering*, Vol. 66, p. 29, 1978.

16. Mihalczo, J. T. and Paré, V. K., "Feasibility of Reactivity Determination from Neutron Noise Spectral Density with ^{252}Cf in the Initial Loading of Light-Water-Moderated Reactors," *Transactions of the American Nuclear Society*, Vol. 28, p. 799, 1978.

17. DeLorenzo, J. T., *Optimization of RC-CR Filters for Processing Current Pulses from a Fission Counter Operating in a High Gamma Background*, ORNL-TM-4982, Oak Ridge National Laboratory, August, 1975.

18. Clay, W. T., DeLorenzo, J. T., Paré, V. K., and Guerrant, G. C., *ORNL Fission Counter FC-3, Quality Assurance Report, Vol. 1: Fission Counter Development*, ORNL/TM-5725, (Vol. 1), Oak Ridge National Laboratory, March, 1977.

19. Paré, V. K., *Model of a Fission Counter System for Optimizing Performance at High Gamma Dose Rates*, ORNL/TM-6408, Oak Ridge National Laboratory, November, 1978.

20. Bendat, J. S. and Piersol, A. G., *Random Data: Analysis and Measurement Procedure*, Wiley-Interscience, New York, 1971.

21. Otsuka, M. and Iijima, T., "Space-Dependent Formula for Rossi-α Measurements," *Nukleonik*, Vol. 7, p. 488, 1965.

22. Harris, D. R., "Neutron Fluctuations in a Reactor of Finite Size," *Nuclear Science and Engineering*, Vol. 21, p. 369, 1965.

23. Bell, G. I., "On the Stochastic Theory of Neutron Transport," *Nuclear Science and Engineering*, Vol. 21, p. 390, 1965.

24. Mathis, M. V., Mihalczo, J. T., and Paré, V. K., *Reactivity Surveillance Instrumentation for Measurements with the FFTF Engineering Mockup Core*, ORNL/TM-4511, Oak Ridge National Laboratory, August, 1976.

25. Stanford, L. E., *Description and Safety Analysis of the Pool Critical Assembly*, ORNL-TM-3035, Oak Ridge National Laboratory, May, 1970.

26. Lamarsh, J. R., *Introduction to Nuclear Reactor Theory*, Addison-Wesley Publishing Co., Inc., New York, 1966.

27. Serber, R., *The Definition of "Neutron Multiplication,"* USAEC Report LA-335 (Rev.), Los Alamos Scientific Laboratory, July, 1945.

28. Walter, J. F., "Detector Response to the Subcritical Reactor," *Nuclear Applications*, Vol. 3, p. 271, 1967.

29. Sastre, C. A., "The Measurement of Reactivity," *Nuclear Science and Engineering*, Vol. 8, p. 443, 1960.

30. Sjöstrand, N. G., "Measurements on a Subcritical Reactor Using a Pulsed Neutron Source," *Arkiv för Fysik*, Vol. 11, p. 233, 1956.

31. Gozani, T., "A Modified Procedure for the Evaluation of Pulsed Source Experiments in Subcritical Reactors," *Nukleonik*, Vol. 4, p. 348, 1962.

32. Garelis, E. and Russell, J. L., "Theory of Pulsed Neutron Source Measurements," *Nuclear Science and Engineering*, Vol. 16, p. 263, 1963.

33. Burgart, C. E., *Determination of Subcritical Reactivity Using Modified Pulsed Neutron Source Techniques*, Unpublished Thesis, Nuclear Engineering Department, The University of Tennessee, Knoxville, March, 1968.

34. Simmons, B. E. and King, J. S., "A Pulsed Neutron Technique for Reactivity Determination," *Nuclear Science and Engineering*, Vol. 3, p. 595, 1958.

35. King, W. T., *The Convergence of the Coherence Function*, WTK-IC-80-001, Unpublished internal report, Instrumentation and Controls Division, Oak Ridge National Laboratory, February, 1980.

36. Mihalczo, J. T., "The Use of Californium-252 as a Randomly Pulsed Neutron Source for Prompt Neutron Decay Measurements," *Nuclear Science and Engineering*, Vol. 53, p. 393, 1974.

37. Cohn, C. E., "A Simplified Theory of Pile Noise," *Nuclear Science and Engineering*, Vol. 7, p. 472, 1960.

38. Prince, A., "Nuclear and Physical Properties of Cf-252," *Proceedings of the Symposium on Californium-252*, CONF-681032, p. 23, October, 1968.

39. Mihalczo, J. T., "New Method for Measurement of the Effective Fractions of Delayed Neutrons from Fission," *Nuclear Science and Engineering*, Vol. 46, p. 147, 1971.

40. Hill, N. W. and Albritton, W. P., "An Input-Capacity-Insensitive, Charge-Sensitive Preamplifier for Simultaneous Use in Vacuum with Fast Amplifiers for Charged-Particle Studies with Semi-conductor Detectors," *Nuclear Instruments and Methods*, Vol. 75, p. 18, 1969.

41. Hill, N. W., Mihalczo, J. T., and Gillespie, F. F., "^{252}Cf as a Nanosecond Pulsed Fission Neutron Source," *Instrumentation and Controls Division Annual Progress Report, September 1, 1970*, Oak Ridge National Laboratory, 1971.

42. LaFara, R. L., *Computer Methods for Science and Engineering*, Hayden Book Co., Inc., New Jersey, 1973.

43. Ford, W. E., III, Webster, C. C., and Westfall, R. M., *A 218-Group Neutron Cross Section Library in the AMPX Master Library Format for Criticality Safety Studies*, ORNL/CSD/TM-4, Oak Ridge National Laboratory, July, 1976.

44. Greene, N. M., Lucius, J. L., Petrie, L. M., Ford, W. E., III, White, J. E., and Wright, R. Q., *AMPX: A Modular Code System for Generating Coupled Multigroup Neutron-Gamma Library from ENDF/B*, ORNL/TM-3706, Oak Ridge National Laboratory, March, 1976.

45. Vondy, D. R., Fowler, T. B., and Cunningham, G. W., *Venture: A Code Block for Solving Multigroup Neutronics Problems Applying the Finite-Difference Diffusion-Theory Approximation to Neutron Transport, Version II*, ORNL-5062, Oak Ridge National Laboratory, October, 1975.

46. Vondy, D. R., Fowler, T. B., Cunningham, G. W., and Petrie, L. M., *A Computation System for Nuclear Core Analysis*, ORNL-5158, Oak Ridge National Laboratory, April, 1977.

47. Vondy, D. R., Fowler, T. B., and Cunningham, G. W., *Input Data Requirements for Special Processors in the Computational System Containing the Venture Neutronics Code*, ORNL-5229/R1, Oak Ridge National Laboratory, July, 1979.

48. Bosler, G. E., O'Dell, R. D., and Resnik, W. M., *LASP-III, A Generalized Processor for Standard Interface Files*, LA-6280-MS, Los Alamos Scientific Laboratory, April, 1976.

49. Vondy, D. R., and Fowler, T. B., *Reference Test Problems for the Venture Neutronics and Related Computer Codes*, ORNL/TM-5887, Oak Ridge National Laboratory, August, 1977.

50. Westfall, R. M., Petrie, L. M., Bucholz, J. A., Elrod, D. C., Hermann, O. W., Knight, J. R., Landers, N. F., Turner, W. D., and West, J. T., *SCALE: A Modular Code System for Performing Standardized Computer Analysis for Licensing Evaluation*, ORNL/NUREG/CSD-2, Oak Ridge National Laboratory, October, 1979.

51. Petrie, L. M. and Cross, N. F., *KENO-IV: An Improved Monte Carlo Criticality Program*, ORNL-4938, Oak Ridge National Laboratory, November, 1975.

52. Petrie, L. M., and Cross, N. F., "Energy and Region Dependent Bucklings for the FFTF Engineering Mock-Up Core from Monte Carlo," *Transactions of the American Nuclear Society*, Vol. 18, p. 348, June, 1974.

53. Knight, J. R. and Petrie, L. M., *16 and 123 Group Weighting Function for KENO*, ORNL-TM-4660, Oak Ridge National Laboratory, November, 1975.

54. Fowler, T. B., Vondy, D. R., and Cunningham, G. W., *Nuclear Reactor Core Analysis Code: CITATION*, ORNL-TM-2496, Rev. 2, Oak Ridge National Laboratory, July, 1969.

55. Keepin, G. R., *Physics of Nuclear Kinetics*, Addison-Wesley Publishing Co., Reading, Massachusetts, 1965.

56. Batchelor, R. and Hyder, H. R. McK, "The Energy of Delayed Neutrons from Fission," *Journal of Nuclear Energy*, Vol. 3, p. 7, 1956.

57. Selby, D. L. and Flanagan, G. F., *Subcriticality Calculations in Support of the Reactivity Surveillance Procedures Experiments for the FFTF Engineering Mock-Up Facility*, ORNL-5061, Oak Ridge National Laboratory, October, 1976.

58. Mihalczo, J. T., *Neutron Importance and Fission Density in Enriched Uranium and Plutonium Metal Spheres*, Y-1959, Oak Ridge Y-12 Plant, January, 1975.

59. Green, L., Mitchell, J. A., and Steen, N. M., "The Californium-252 Fission Neutron Spectrum from 0.5 to 13 MeV," *Nuclear Science and Engineering*, Vol. 50, p. 257, 1973.

60. DeVolpi, A., *Discrepancies and Possible Adjustments in the 2200-m/s Fission Parameters*, ANL-7830, Argonne National Laboratory, June, 1971.

61. Cox, S., Fields, P., Friedman, A., Sjoblom, R., and Smith, A., "Delayed Neutrons from the Spontaneous Fission of ^{252}Cf," *Physical Review*, Vol. 112, p. 960, 1958.

62. Boldeman, J. W., "Prompt-Neutron Yield from the Spontaneous Fission of Californium-252," *Nuclear Science and Engineering*, Vol. 55, p. 188, 1974.

63. Diven, B. C., Martin, H. C., Taschek, R. F., and Terrel, J., "Multiplicities of Fission Neutrons," *Physical Review*, Vol. 101, p. 1012, 1956.

64. Miller, L. F., Professor, Nuclear Engineering Department, The University of Tennessee, Knoxville, Private Communication, 1979.

65. Allen, J. W., *Development and Application of a Three-Point Inverse Kinetics Rod-Drop Technique for Subcriticality Determination*, ORNL-TM-4758, Oak Ridge National Laboratory, November, 1975.

APPENDICES

APPENDIX A

THEORY OF TIME AND FREQUENCY DOMAIN MEASUREMENTS WITH ^{252}Cf

This experiment is primarily concerned with frequency domain measurements. However, in order to provide a consistent set of notations and some background for understanding the frequency domain results, this development starts with a review of the theory of Rossi-α and pulsed neutron measurements. Then, in the frequency domain, the reactor source transfer function is derived. The power spectral density (PSD) of the fluctuations in the neutron production rate in a reactor is calculated. Contributions from a ^{252}Cf source and inherent spontaneous fission sources to these fluctuations are explicitly included.

Consideration is then given to a system consisting of a reactor, a fission chamber containing a ^{252}Cf source, and two detectors observing neutrons from fission chains in the reactor. The PSDs of the individual detector outputs as well as the cross power spectral densities (CPSDs) between them are obtained.

A. Rossi-α Measurement

This section summarizes the development by Orndoff.[2,3] In a neutron multiplying system, the rate of change of the prompt neutron population can be expressed as the difference between the prompt neutron gain and loss rates, the prompt neutron gain per generation divided by the prompt

neutron lifetime, or as a decay rate, that is

$$\frac{dN_p(t)}{dt} = \frac{\bar{\nu}_p N_p(t)}{\tau_f} - \frac{N_p(t)}{\ell} = \frac{k_p - 1}{\ell} N_p(t) = -\alpha N_p(t) \ , \qquad (A.1)$$

where

$N_p(t)$ = prompt neutron population at time t,

$\bar{\nu}_p$ = average number of prompt neutrons produced per reactor fission,

τ_f = mean time of a prompt neutron to fission,

ℓ = prompt neutron lifetime, mean life of a prompt neutron for absorption and leakage,

k_p = prompt neutron multiplication factor, and

α = prompt neutron decay constant.

The following relations can be obtained from Eq. (A.1):

$$k_p = \frac{\bar{\nu}_p \ell}{\tau_f} \ , \qquad (A.2)$$

and

$$\alpha = \frac{1 - k_p}{\ell} \ . \qquad (A.3)$$

If β is the effective total delayed fraction, then

$$\bar{\nu}_p = \bar{\nu}(1 - \beta) \ , \qquad (A.4)$$

and

$$k_p = k(1 - \beta) \ , \qquad (A.5)$$

where

$\bar{\nu}$ = average number of neutrons produced per reactor fission, and

k = neutron multiplication factor.

Equations (A.2), (A.4), and (A.5) can be combined to obtain a definition for τ_f in more familiar terms, that is

$$\tau_f = \frac{\bar{\nu}_p \ell}{k_p} = \frac{\bar{\nu}\ell}{k} = \bar{\nu}\Lambda \ , \tag{A.6}$$

where Λ is the neutron generation time and is equal to ℓ/k.

Integrating Eq. (A.1) from t_1 to t gives

$$N_p(t) = N_p(t_1)e^{-\alpha(t - t_1)} \ . \tag{A.7}$$

Equation (A.7) describes the average behavior of individual neutron chains.

Consider two detectors (detectors 2 and 3) in a neutron multiplying system. The probability, $P_3(t)dt$, of a count in detector 3 at time t in dt after a count in detector 2 at time 0 will be equal to the probability of a chance count, $P_{3c}(t)dt$, plus the probability of a related count, $P_{3r}(t)dt$, that is

$$P_3(t)dt = P_{3c}(t)dt + P_{3r}(t)dt \ . \tag{A.8}$$

If W_3 is the efficiency of detector 3 in counts per reactor fission and F is the average reactor fission rate, then

$$P_{3c}(t)dt = W_3 F dt \ . \tag{A.9}$$

The probability, $g_1(t_0)dt_0$, of a fission at time t_0 in dt_0 is

$$g_1(t_0)dt_0 = F dt_0 \ . \tag{A.10}$$

Of the ν_p neutrons produced in this fission, $[\nu_p e^{-\alpha(t_1 - t_0)}]$ will survive to time t_1 and will cause $[\nu_p e^{-\alpha(t_1 - t_0)} / \tau_f]$ fissions. The probability, $g_2(t_1)dt_1$, of a count in detector 2 at time t_1 in dt_1 as a result of the fission at t_0 is

$$g_2(t_1)dt_1 = \frac{W_2 \nu_p e^{-\alpha(t_1 - t_0)}}{\tau_f} dt_1 \ . \tag{A.11}$$

The probability, $g_3(t_2)dt_2$, of a related count in detector 3 at time t_2 in dt_2 after the count in detector 2 at t_1 is

$$g_3(t_2)dt_2 = \frac{W_3(\nu_p - 1)e^{-\alpha(t_2 - t_0)}}{\tau_f} dt_2 \ . \tag{A.12}$$

The probability of a count in detector 2 at time t_1 in dt_1 followed by a count in detector 3 at time t_2 in dt_2 from a common ancestor is obtained by integrating the product, $g_1(t_0)dt_0 \cdot g_2(t_1)dt_1 \cdot g_3(t_2)dt_2$, over all possible time t_0 (that is, from $-\infty$ to t_1) and averaging over the distribution of neutrons emitted per fission. This is just the probability of a count in detector 2 at time t_1 in dt_1 times the probability of a related count in detector 3 at time t_2 in dt_2, that is

$$[W_2 F dt_1][P_{3r}(t_2)dt_2] = \frac{F W_2 W_3}{2\ell} \frac{\overline{\nu_p(\nu_p - 1)}}{\bar{\nu}_p^2} \frac{k_p^2}{(1 - k_p)} e^{-\alpha(t_2 - t_1)} dt_2 dt_1 \ . \tag{A.13}$$

If time is counted from $t_1 = 0$, and if t_2 is any arbitrary time t, then

$$P_{3r}(t)dt = \frac{W_3}{2\ell} \frac{k_p^2}{(1 - k_p)} \frac{\overline{\nu_p(\nu_p - 1)}}{\bar{\nu}_p^2} e^{-\alpha t} dt \ . \tag{A.14}$$

The Diven factor, X, is defined as

$$X = \frac{\overline{\nu_p(\nu_p - 1)}}{\bar{\nu}_p^2} \ . \tag{A.15}$$

In performing a Rossi-α measurement, the time dependent term is multiplied by R, a spatial effects correction factor.[21-23] Therefore, Eq. (A.8) can be written an

$$P_3(t)dt = W_3 F dt + \frac{W_3 X R k_p^2}{2\ell^2 \alpha} e^{-\alpha t} dt \ . \tag{A.16}$$

B. Pulsed Neutron Measurement with ^{252}Cf

This section summarizes the development by Mihalczo.[36] A fission chamber (detector 1) containing ^{252}Cf is placed in the reactor sufficiently far from detectors 2 and 3 such that the number of direct contributions is not significant. The fission chamber is operated in the pulse mode and is so designed as to count >99.9% of the ^{252}Cf fissions.

After a ^{252}Cf fission, the effective average number of source neutrons introduced into the reactor is

$$N_0 = \frac{\bar{\nu}_c I_c}{I} \quad , \tag{A.17}$$

where

$\bar{\nu}_c$ = average number of neutrons produced per ^{252}Cf fission,

I_c = average importance of a ^{252}Cf fission neutron, and

I = average importance of a reactor fission neutron.

The probability of a related count in detector 2 (derived quantities will be similar for detector 3) at time t in dt after a ^{252}Cf fission is

$$P_{2r}(t)dt = \frac{W_2 \bar{\nu}_c I_c e^{-\alpha t}}{I \tau_f} dt \quad . \tag{A.18}$$

The probability of a chance count is

$$P_{2c}(t)dt = W_2' F_c dt \quad , \tag{A.19}$$

where

W_2' = detection efficiency of detector 2 in counts per ^{252}Cf fission, and

F_c = ^{252}Cf fission rate.

Therefore, the probability of a count in detector 2 at time t in dt after a ^{252}Cf fission at time 0 is

$$P_2(t)dt = W_2 F_c dt + \frac{W_2 \bar{\nu}_c I_c e^{-\alpha t}}{I \tau_f} dt \ . \qquad (A.20)$$

C. Reactor Source Transfer Function

The dynamic behavior of a subcritical reactor can be described by the following point kinetics equations:

$$\frac{dN(t)}{dt} = - \frac{\beta - \rho}{\Lambda} N(t) + \sum_{i=1}^{6} \lambda_i C_i(t) + S(t) \ , \qquad (A.21)$$

and

$$\frac{dC_i(t)}{dt} = \frac{\beta_i}{\Lambda} N(t) - \lambda_i C_i(t) \ , \qquad (A.22)$$

where

$N(t)$ = neutron population at time t,

β_i = effective delayed neutron fraction of the ith delayed group,

$C_i(t)$ = ith delayed group precursor population at time t,

λ_i = decay constant of the ith delayed group precursor,

ρ = reactivity of the system which equals (k - 1)/k, and

$S(t)$ = rate at which external source neutrons are introduced into the system at time t.

Because of the stochastic nature of the neutron interactions in the reactor, the neutron and precursor populations fluctuate about their steady-state values. If the source emission rate also fluctuate about

a mean rate, then N, C_i, and S can be expressed as follows:

$$N(t) = N_0 + \delta N(t) \ , \tag{A.23}$$

$$C_i(t) = C_{i0} + \delta C_i(t) \ , \tag{A.24}$$

and

$$S(t) = S_0 + \delta S(t) \ . \tag{A.25}$$

Note that at steady-state

$$\frac{dN_0}{dt} = 0 = - \frac{\beta - \rho}{\Lambda} N_0 + \sum_{i=1}^{6} \lambda_i C_{i0} + S_0 \ , \tag{A.26}$$

and

$$\frac{dC_{i0}}{dt} = 0 = \frac{\beta_i}{\Lambda} N_0 - \lambda_i C_{i0} \ ; \tag{A.27}$$

therefore

$$C_{i0} = \frac{\beta_i N_0}{\lambda_i \Lambda} \ , \tag{A.28}$$

and

$$N_0 = - \frac{S_0 \Lambda}{\rho} \ . \tag{A.29}$$

Combining Eqs. (A.21) thru (A.25), and ignoring second order terms, we get

$$\frac{d\delta N(t)}{dt} = - \frac{\beta - \rho}{\Lambda} \delta N(t) + \sum_{i=1}^{6} \lambda_i \delta C_i(t) + \delta S(t) \ , \tag{A.30}$$

and

$$\frac{d\delta C_i(t)}{dt} = \frac{\beta_i}{\Lambda}\,\delta N(t) - \lambda_i \delta C_i(t) \quad . \tag{A.31}$$

Laplace transform Eqs. (A.30) and (A.31) and combine into one equation to produce

$$\left[s + \frac{\beta - \rho}{\Lambda} - \sum_{i=1}^{6} \frac{\lambda_i \beta_i}{\Lambda(s + \lambda_i)} \right] \delta N(s) = \delta S(s) \quad , \tag{A.32}$$

where s is the Laplace transform variable. The source-to-neutron transfer function is

$$H_S(s) = \frac{\delta N(s)}{\delta S(s)} = \frac{\Lambda}{s\Lambda + (\beta - \rho) - \sum_{i=1}^{6} \frac{\lambda_i \beta_i}{s + \lambda_i}} \quad . \tag{A.33}$$

The frequency response is obtained by setting $s = j\omega$, where j is $\sqrt{-1}$ and ω is the angular frequency. If $\omega \gg$ any λ_i, then

$$H_S(\omega) = \frac{\Lambda}{j\omega\Lambda + (\beta - \rho)} \quad . \tag{A.34}$$

D. Noise-Equivalent Source

The random fluctuations in the neutron population may be considered to arise from a random noise-equivalent neutron source driving the reactor. This noise-equivalent source takes into account the statistical fluctuations in the neutron absorption and fission rates and precursor decay rates. For the present measurement, the statistical fluctuations

in the fission rates of inherent sources and a ^{252}Cf source is also considered.

By analogy to the theory of electrical shot-noise, the one-sided PSD of the fluctuations in the neutron emission rates from neutron sources can be expressed as[37]

$$G_s(\omega) = 2 \sum_{i=1}^{M} \gamma_i m_i^2 , \tag{A.35}$$

where

γ_i = rate of type i interactions,

m_i = net number of neutrons emitted per type i interaction, and

M = total number of interactions considered.

At steady-state, the neutron absorption rate can be expressed as

$$F_{ab} = N_0/\ell . \tag{A.36}$$

If Σ_a is the macroscopic absorption cross section including leakage and Σ_f is the macroscopic fission cross section, then the nonfission absorption rate can be expressed as

$$F_{nfab} = \frac{N_0}{\ell} \frac{\Sigma_a - \Sigma_f}{\Sigma_a} . \tag{A.37}$$

There is a net loss of one neutron per nonfission absorption.

The fission rate can be expressed as

$$F = \frac{N_0}{\ell} \frac{\Sigma_f}{\Sigma_a} . \tag{A.38}$$

Define P(n) as the probability that n prompt neutrons are emitted per fission, and

$$\sum_{n=0}^{\infty} P(n) = 1 \ , \tag{A.39}$$

$$\sum_{n=0}^{\infty} nP(n) = \bar{\nu}_p \ , \tag{A.40}$$

and

$$\sum_{n=0}^{\infty} n^2 P(n) = \overline{\nu_p^2} \ . \tag{A.41}$$

The net number of neutrons produced per n prompt neutron producing fission is n - 1.

The decay rate of the group i delayed neutron precursors is $\lambda_i C_{i0}$. Using Eq. (A.28) and summing up all the delayed groups, the total decay rate is

$$F_d = \sum_{i=1}^{6} \lambda_i C_{i0} = \sum_{i=1}^{6} \frac{\beta_i N_0}{\Lambda} = \frac{\beta N_0}{\Lambda} \ . \tag{A.42}$$

Each precursor decay produces one neutron.

For spontaneous fission sources in the reactor with total fission rate, F_i, each fission produces n neutrons with probability $P_i(n)$. These probabilities obey relationships similar to those given in Eqs. (A.39) thru (A.41). The neutrons produced by inherent source fissions may or may not have the same importance as reactor fission neutrons; therefore,

the fission rate will be adjusted by the ratio of average importance of an inherent fission neutron, I_i, to the average importance of a reactor fission neutron, I. The effective fission rate is then

$$F_{ei} = \frac{F_i I_i}{I} . \tag{A.43}$$

Similarly, for a ^{252}Cf source with a fission rate F_c, the effective fission rate is

$$F_{ec} = \frac{F_c I_c}{I} , \tag{A.44}$$

where I_c is the average importance of a ^{252}Cf fission neutron.

Combining all the above information, the PSD of the noise-equivalent source is

$$\frac{G_s(\omega)}{2} = \frac{N_0}{\ell} \frac{\Sigma_a - \Sigma_f}{\Sigma_a} + \frac{N_0}{\ell} \frac{\Sigma_f}{\Sigma_a} \sum_{n=0}^{\infty} (n - 1)^2 P(n) + \frac{\beta N_0}{\Lambda}$$

$$+ \frac{F_i I_i}{I} \sum_{n=0}^{\infty} n^2 P_i(n) + \frac{F_c I_c}{I} \sum_{n=0}^{\infty} n^2 P_c(n) , \tag{A.45}$$

where $P_c(n)$ is the probability that each ^{252}Cf fission produces n neutrons. Absorption and fission cross sections are related by the neutron multiplication factor, that is

$$k = \frac{\overline{\nu}\Sigma_f}{\Sigma_a} . \tag{A.46}$$

Using Eqs. (A.4), (A.5), (A.39) thru (A.41), and (A.46), the PSD of the noise-equivalent source reduces to

$$\frac{G_s(\omega)}{2} = \frac{N_0}{\ell}\left\{1 - k(1-\beta) + k(1-\beta)\frac{\overline{\nu_p^2} - \overline{\nu}_p}{\overline{\nu}_p}\right\} + \frac{\beta N_0}{\Lambda} + \overline{\nu_i^2}\frac{F_i I_i}{I} + \overline{\nu_c^2}\frac{F_c I_c}{I}, \tag{A.47}$$

or

$$\frac{G_s(\omega)}{2} = \frac{N_0}{\Lambda}\{2\beta - \rho + (1-\beta)\overline{\nu}_p XR\} + \frac{\overline{\nu_i^2 F_i I_i}}{I} + \frac{\overline{\nu_c^2 F_c I_c}}{I}, \tag{A.48}$$

where the spatial effects correction factor, R, has been applied.

Since the reactor fission rate is

$$F = \frac{N_0}{\ell}\frac{\Sigma_f}{\Sigma_a} = \frac{N_0}{\ell}\frac{k(1-\beta)}{\overline{\nu}_p} = \frac{N_0}{\Lambda}\frac{(1-\beta)}{\overline{\nu}_p}, \tag{A.49}$$

Eq. (A.48) can be written as

$$\frac{G_s(\omega)}{2} = F\left\{\frac{\overline{\nu}_p(2\beta - \rho)}{(1-\beta)} + \overline{\nu_p^2}XR\right\} + \frac{\overline{\nu_i^2 F_i I_i}}{I} + \frac{\overline{\nu_c^2 F_c I_c}}{I}. \tag{A.50}$$

E. Spectral densities of Detector Responses

Consider the fission chamber containing the ^{252}Cf source. Its function is to produce a current proportional to the ^{252}Cf fission rate. Therefore, the detector transfer function can be defined as

$$U_1(s) = \frac{F_c \overline{q}_c}{F_c} = \overline{q}_c, \tag{A.51}$$

where $\bar{q}_c$ is the average charge produced per ^{252}Cf fission.

The output current of a detector in a reactor would contain a white noise component due to the stochastic nature of the detection process. This is because the events in the detector would be Poisson distributed even if the neutron production rate in the reactor was uniform. Since ^{252}Cf fissions spontaneously and the ^{252}Cf is placed inside the fission chamber, the detection process in detector 1 is deterministic. However, ^{252}Cf also decays by α-particle emission which adds to the detector output current. The PSD of the detector output current due to the fluctuations in α-particle emissions will be treated as detector noise. Using the shot-noise formula, this PSD component is

$$\frac{G_1(\omega)}{2} = F_\alpha \overline{q_\alpha^2} \quad , \tag{A.52}$$

where

F_α = the α-particle emission rate, and

$\bar{q}_\alpha$ = the average charge produced per α-particle emission.

The α-particle emission rate is 31 times the spontaneous fission rate;[38] therefore

$$\frac{G_1(\omega)}{2} = 31\ F_c \overline{q_\alpha^2} \ . \tag{A.53}$$

The PSD of the detector output current due to the fluctuations in spontaneous fission is

$$\frac{G_1'(\omega)}{2} = F_c \overline{q_c^2} \ . \tag{A.54}$$

The PSD of the total detector response is

$$G_{11}(\omega) = 2|h_1(\omega)|^2\{31\ F_c\overline{q_\alpha^2} + F_c\overline{q_c^2}\} \ , \tag{A.55}$$

where $h_1(\omega)$ is the frequency response of the electronic components associated with detector 1. Let

$$B_c = \overline{q_c^2}/\bar{q}_c^2 \ , \tag{A.56}$$

then Eq. (A.55) can be written as

$$G_{11}(\omega) = |h_1(\omega)|^2\{G_1(\omega) + |U_1(\omega)|^2 G_c(\omega)\} \ , \tag{A.57}$$

where

$$G_c(\omega) = G_1'(\omega)/\bar{q}_c^2 = 2F_c B_c \ . \tag{A.58}$$

Equation (A.57) is shown schematically in part A of the block diagram in Fig. A.1.

The function of detector 2 (or 3) is to produce a current proportional to the neutron production rate in the reactor. Its transfer function can be defined as

$$U_2(s) = \frac{W_2 F \bar{q}_2}{F\bar{\nu}} = \frac{W_2\bar{q}_2}{\bar{\nu}} \ . \tag{A.59}$$

The input to this transfer function is the fluctuations in neutron production rate. The output of $H_S(s)$ [Eq. (A.34)] is the fluctuations in neutron population. Therefore, a transfer function is required to convert fluctuations in neutron population to fluctuations in neutron

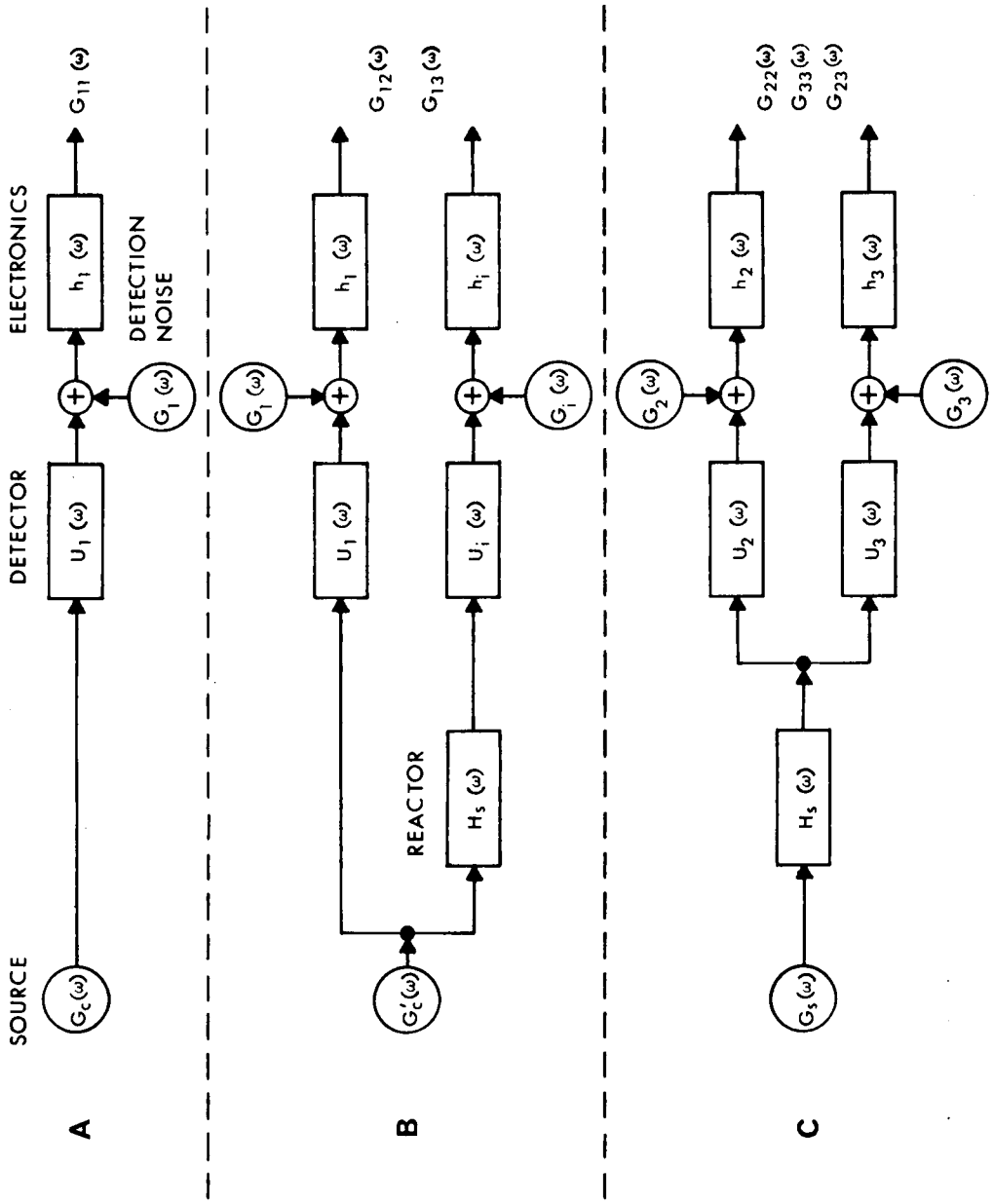


Fig. A.1. Block diagram for detector response spectral densities.

production rate. Analogous to Eq. (A.38), the fission rate at time t is related to the neutron population at time t by

$$F(t) = \frac{N(t)}{\ell} \frac{\Sigma_f}{\Sigma_a} \quad . \tag{A.60}$$

Using Eq. (A.46) to relate the ratio of cross sections to k, the neutron production rate can be expressed as

$$\bar{\nu}F(t) = N(t) \frac{k}{\ell} = \frac{N(t)}{\Lambda} \quad . \tag{A.61}$$

The transfer function being sought is

$$\frac{\delta[\bar{\nu}F(s)]}{\delta[N(s)]} = \frac{1}{\Lambda} \, . \tag{A.62}$$

Define a new reactor transfer function as

$$H_s(s) = H_S(s) \frac{1}{\Lambda} \quad . \tag{A.63}$$

Using part C of the block diagram on Fig. A.1, the PSD of the output current of detector 2 can be expressed as

$$G_{22}(\omega) = |h_2(\omega)|^2 \{G_2(\omega) + |U_2(\omega)|^2 |H_s(\omega)|^2 G_s(\omega)\} \quad , \tag{A.64}$$

where $G_2(\omega)$ is the detection noise PSD which can be expressed as

$$G_2(\omega) = 2W_2 F \overline{q_2^2} \quad . \tag{A.65}$$

Similarly, the CPSD between the output current of detectors 2 and 3 can be written as

$$G_{23}(\omega) = h_2^*(\omega)h_3(\omega)U_2^*(\omega)U_3(\omega)\left|H_s(\omega)\right|^2 G_s(\omega) \quad , \tag{A.66}$$

where * denotes complex conjugate. The detection noise in each detector is assumed to be uncorrelated; therefore, they do not contribute to the CPSD.

The CPSD between the output currents of detectors 1 and 2 can be obtained by using part B of the block diagram in Fig. A.1, that is

$$G_{12}(\omega) = h_1^*(\omega)h_2(\omega)U_1^*(\omega)U_2(\omega)H_s(\omega)G_c'(\omega) \quad . \tag{A.67}$$

From the ^{252}Cf source, the noise source for detector 2 (through the reactor) is the fluctuations in the neutron production rate. However, for the fission chamber containing the ^{252}Cf, the noise source is the fluctuations in the spontaneous fission rate. The value of $G_c'(\omega)$ can be obtained from the theory of pulsed neutron measurements.

From Eq. (A.20), the probability of a related count in detector 2 in time interval dt about t after a ^{252}Cf fission is

$$P_{2r}(t)dt = \frac{W_2\bar{\nu}_c I_c e^{-\alpha t}}{I\tau_f}\,dt \quad . \tag{A.68}$$

The probability of a ^{252}Cf fission in time interval dt_1 about t_1 and a related count in detector 2 in time interval dt_2 about t_2 is

$$P(t_1,t_2)dt_1dt_2 = \frac{F_c W_2 \bar{\nu}_c I_c e^{-\alpha (t_2-t_1)}}{I\tau_f} dt_1dt_2 \quad . \tag{A.69}$$

Therefore, the probability of correlated counts at times t_1 and t_2 is simply

$$P(t_1,t_2) = \frac{W_2 \bar{\nu}_c F_c I_c e^{-\alpha (t_2-t_1)}}{I\tau_f} \quad . \tag{A.70}$$

From Uhrig,[1] Eq. (A.70) is the nonconstant part of the cross-correlation function between the outputs of both detectors. (The constant term adds to the DC component of the frequency domain results. The DC component is not considered in the measurement.) Let

$$\xi = t_2 - t_1 \ , \tag{A.71}$$

then the cross-correlation function is

$$\phi_{12}(\xi) = \frac{W_2 \bar{\nu}_c F_c I_c e^{-\alpha\xi}}{I\tau_f} \quad . \tag{A.72}$$

The CPSD is the Fourier transform of the cross-correlation function, that is

$$G_{12}(\omega) = 2 \int_0^\infty \frac{W_2 \bar{\nu}_c F_c I_c e^{-(\alpha+j\omega)\xi}}{I\tau_f} d\xi \ , \tag{A.73}$$

or

$$G_{12}(\omega) = \frac{2W_2 \bar{\nu}_c F_c I_c}{I(\alpha + j\omega)\tau_f} \quad . \tag{A.74}$$

From Eq. (A.3), α can be expressed as

$$\alpha = \frac{1 - k_p}{\ell} = \frac{1 - k(1 - \beta)}{\ell} = \frac{\beta - \rho}{\Lambda} \quad . \tag{A.75}$$

Using the definition in Eq. (A.6) for τ_f, the CPSD between the two detector responses can be written as

$$G_{12}(\omega) = \frac{W_2}{\bar{\nu}} \frac{1}{(\beta - \rho) + j\omega\Lambda} \frac{2\bar{\nu}_c F_c I_c}{I} \quad . \tag{A.76}$$

A pulsed neutron measurement is done with the detectors operated in the pulse mode; therefore

$$h_1(\omega) = 1 \quad , \tag{A.77}$$

$$h_2(\omega) = 1 \quad , \tag{A.78}$$

$$U_1(\omega) = 1 \quad , \tag{A.79}$$

and

$$U_2(\omega) = \frac{W_2}{\bar{\nu}} \quad . \tag{A.80}$$

$G_c'(\omega)$ can be obtained by comparing Eqs. (A.67) and (A.76), that is

$$G_c'(\omega) = \frac{2\bar{\nu}_c F_c I_c}{I} \quad . \tag{A.81}$$

A similar derivation starting from the Rossi-α results can be used to obtain the relation for G_s.

F. Coherence Between Detector Responses

To simplify notation, the PSD of the noise-equivalent source [Eq. (A.50)] can be expressed as

$$G_s(\omega) = 2F\bar{\nu}_p^2 X' R \quad , \tag{A.82}$$

where

$$X' = X \left(1 + \frac{V}{XR} + \frac{\overline{\nu_i^2 F_i I_i}}{\bar{\nu}_p^2 FIXR} + \frac{\overline{\nu_c^2 F_c I_c}}{\bar{\nu}_p^2 FIXR} \right) , \tag{A.83}$$

and

$$V = \frac{2\beta - \rho}{(1 - \beta)\bar{\nu}_p} \quad . \tag{A.84}$$

Equation (A.83) defines a modified Diven factor which includes the contributions from delayed neutrons and inherent and ^{252}Cf source neutrons.

In the expression for the detector transfer function of detectors 2 and 3, an assumption will be made that $\bar{\nu}_p \approx \bar{\nu}$, such that

$$U_2(s) = \frac{W_2 \bar{q}_2}{\bar{\nu}} \approx \frac{W_2 \bar{q}_2}{\bar{\nu}_p} \quad . \tag{A.85}$$

The coherence between the responses of detectors 1 and 2 can be expressed as

$$\gamma_{12}^2(\omega) = \frac{|G_{12}(\omega)|^2}{G_{11}(\omega) G_{22}(\omega)} = \frac{1}{B_c(1 + C_\alpha)} \left(\frac{\bar{\nu}_c I_c}{\bar{\nu}_p I} \right)^2 \frac{F_c}{FX'R} \frac{1}{1 + 1/Q_2(\omega)} \quad , \tag{A.86}$$

where

$$C_\alpha = 31\ \overline{q_\alpha^2}/\overline{q_c^2} \quad , \tag{A.87}$$

$$Q_2(\omega) = \frac{W_2 X' R}{B_2 \Lambda^2} \frac{1}{\alpha^2 + \omega^2} \quad , \tag{A.88}$$

and

$$B_2 = \overline{q_2^2}/\bar{q}_2^2 \quad . \tag{A.89}$$

The coherence between the outputs of detectors 2 and 3 can be written as

$$\gamma_{23}^2(\omega) = \frac{|G_{23}(\omega)|^2}{G_{22}(\omega)G_{33}(\omega)} = \frac{1}{1 + 1/Q_2(\omega)} \frac{1}{1 + 1/Q_3(\omega)} \quad . \tag{A.90}$$

G. Reactivity Determination in the Time Domain

This section summarizes the development by Mihalczo.[39] In a Rossi-α measurement, the probability of a correlated count in detector 3 in dt about t after a count in detector 2 at time 0 is (from Eq. (A.16)]

$$P_{3r}(t)dt = \frac{W_3 X R k^2 p}{2\ell^2 \alpha} e^{-\alpha t}\, dt \quad . \tag{A.91}$$

The correlated count rate in detector 3 is

$$C_{R-\alpha} = W_2 F \int_0^\infty P_{3r}(t)\, dt = \frac{W_2 F W_3 X R k^2 p}{2\ell^2 \alpha^2} \quad . \tag{A.92}$$

If only one detector is used (that is, the trigger detector is the same as the counting detector), then $W_2 = W_3 = W$; therefore,

$$C_{R-\alpha} = \frac{W^2 F X R k_p^2}{2\ell^2\alpha^2} \quad . \tag{A.93}$$

Similarly, in a pulsed neutron experiment (with ^{252}Cf), the correlated count rate is [using Eq. (A.18)]

$$C_{RPN} = \frac{F_c W \bar{\nu}_c I_c k_p}{\alpha \bar{\nu}_p I \ell} \quad . \tag{A.94}$$

The ratio, A, of the correlated count rate in a pulsed neutron measurement (with ^{252}Cf) to that in a Rossi-α measurement is

$$A = 2 \frac{I_c}{I} \frac{\bar{\nu}_c}{\bar{\nu}_p} \frac{1}{XR} \frac{1 - k_p}{k_p} \frac{F_c}{WF} \quad . \tag{A.95}$$

Consider the following:

$$A \frac{\frac{1}{F_c}}{\frac{1}{WF}} = 2 \frac{I_c}{I} \frac{\bar{\nu}_c}{\bar{\nu}_p} \frac{1}{XR} \frac{1 - k_p}{k_p} \quad . \tag{A.96}$$

If the Rossi-α measurement is performed simultaneously with the pulsed neutron measurement (with ^{252}Cf), the left side of Eq. (A.96) is a measurable quantity, that is, it is the ratio of the number of correlated counts per ^{252}Cf fission in a pulsed neutron measurement (with ^{252}Cf) to the number of correlated counts per detector count in a Rossi-α

measurement. The values of $\overline{\nu}_c$, $\overline{\nu}_p$, X, R, I, and I_c can be calculated or measured and are weak functions of reactivity. Therefore, the use of Eq. (A.96) to obtain reactivity depends on properties of the reactor only at the subcritical state of interest. It does not require calibration near delayed criticality. This technique was demonstrated by Mihalczo[39] in 1971.

This reactivity measurement technique in the time domain is the basis of the three detector frequency domain method also developed by Mihalczo and Paré[14] and reviewed in Chap. 2 of this dissertation.

APPENDIX B

DESCRIPTION OF THE DETECTION INSTRUMENTATION SYSTEM

Discussion of off-the-shelf electronic components, either commercial or of standard ORNL design will include functional descriptions only. More details on these instrumentation systems can be found in the report by Mathis, and others.[24]

A. ^{252}Cf Fission Counting System

The ^{252}Cf fission counting system (Fig. B.1) consisted of a fission chamber containing the ^{252}Cf, high voltage battery supply, current pulse preamplifier, signal processing electronics, and cables.

^{252}Cf (0.13 μg) was electroplated on one side of a platinum foil (0.254 mm thick, 21.59 mm diameter) with a spot diameter of 8 mm. The platinum foil was placed in a double contained 304 stainless steel fission chamber (ORNL, Q-5106-1) as shown in Fig. B.2. The chamber was evacuated and filled with methane to a pressure of 760 mm Hg (absolute). Five 45 V batteries (Burgess Z30NX) maintained a potential of 202.5 V (one cell of the fifth battery was not used) between the nickel collection plate and the platinum foil, spaced 1 mm apart.

Signal pulses from the ionization chamber were input to a low-input-impedance, low-noise, current pulse preamplifier,[40,41] which had a gain of ∿3500 and a rise time of ∿3.5 nsec, via a 12.2 m long RG-58 (50 Ω impedance) coaxial cable. The preamplifier was designed to be close-coupled to the fission chamber. To properly terminate the

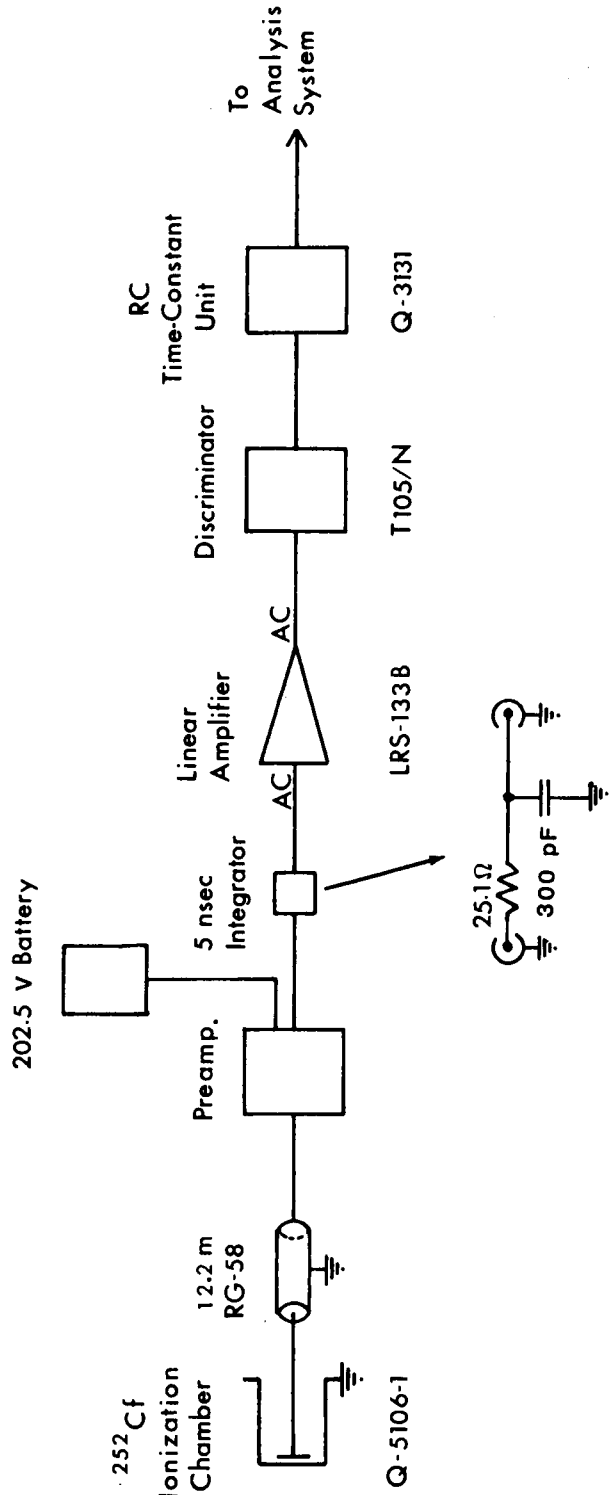


Fig. B.1. Block diagram of the ^{252}Cf fission counting system. (Preamplifier was designed by N. W. Hill, refs. 40 and 41.)

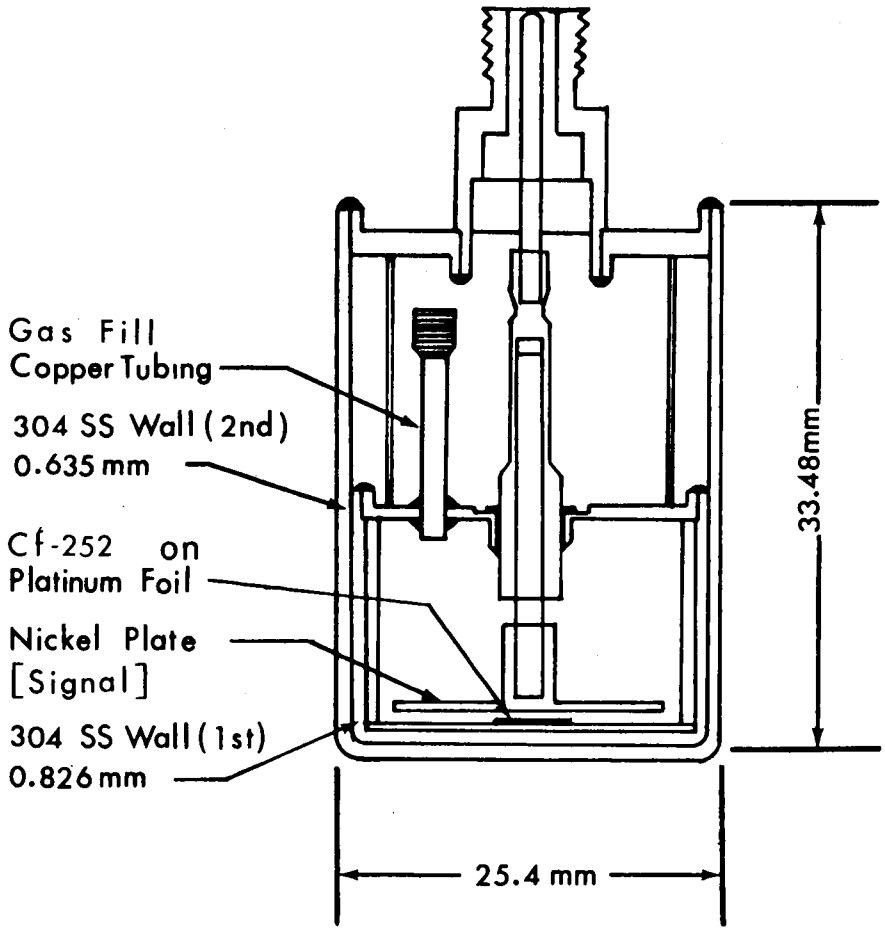


Fig. B.2. Sketch of the double contained fission chamber containing ^{252}Cf.

cable, a 19.6 Ω resistor was put in series to the input of the preamplifier. This resistance was chosen because the reflections in such a system, compared to the signal pulses, were small in magnitude and opposite in polarity. The output of the preamplifier was smoothed by a 5 nsec RC integrator. Typical output signal pulses from the integrator are shown in Fig. B.3.

It can be seen from Fig. B.3 that the ionization pulses produced by the alpha particle decay and electronic noise (about the same size as the alpha pulses) can easily be discriminated out. To get the output pulses from the integrator in the operating range of the discriminator (Egerton, Germeshausen, and Grier, Inc., EG&G T105/N), a linear amplifier (LeCroy Research Systems Corp., LRS 133B) was used to amplify the signal.

Count rates vs. discriminator settings (Fig. B.4) determined the discrimination level at which >99.9% of the spontaneous fission pulses were counted. This level was set at 150 mV.

The 12 nsec, 32 mA, square output pulses from the discriminator were filtered and amplified with an RC Time-Constant unit (ORNL, Q-3131) to produce a voltage signal with lower bandwith (∿40 kHz), and greater amplitude (∿8 V). This voltage signal was suitable for the high input impedance of the analysis system. This instrument was designed for measurements in fast critical assemblies where a bandwith of 40 kHz was required. Time and budgetary constraints precluded the redesign of this instrument to obtain a lower bandwith signal for measurements in water moderated systems.

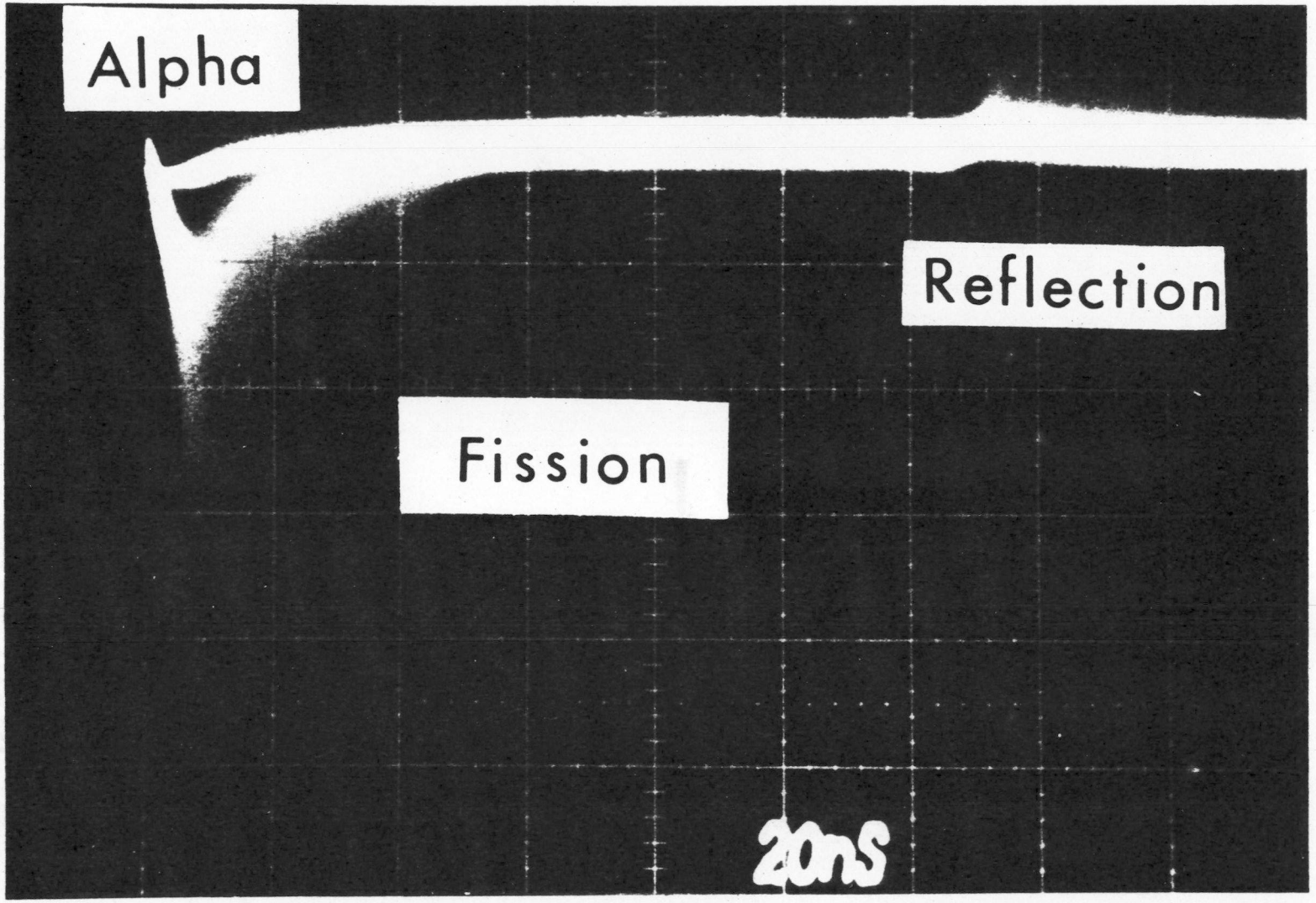


Fig. B.3. ^{252}Cf fission chamber output after preamplifier and integrator. (Voltage scale is 100 mV/division.)

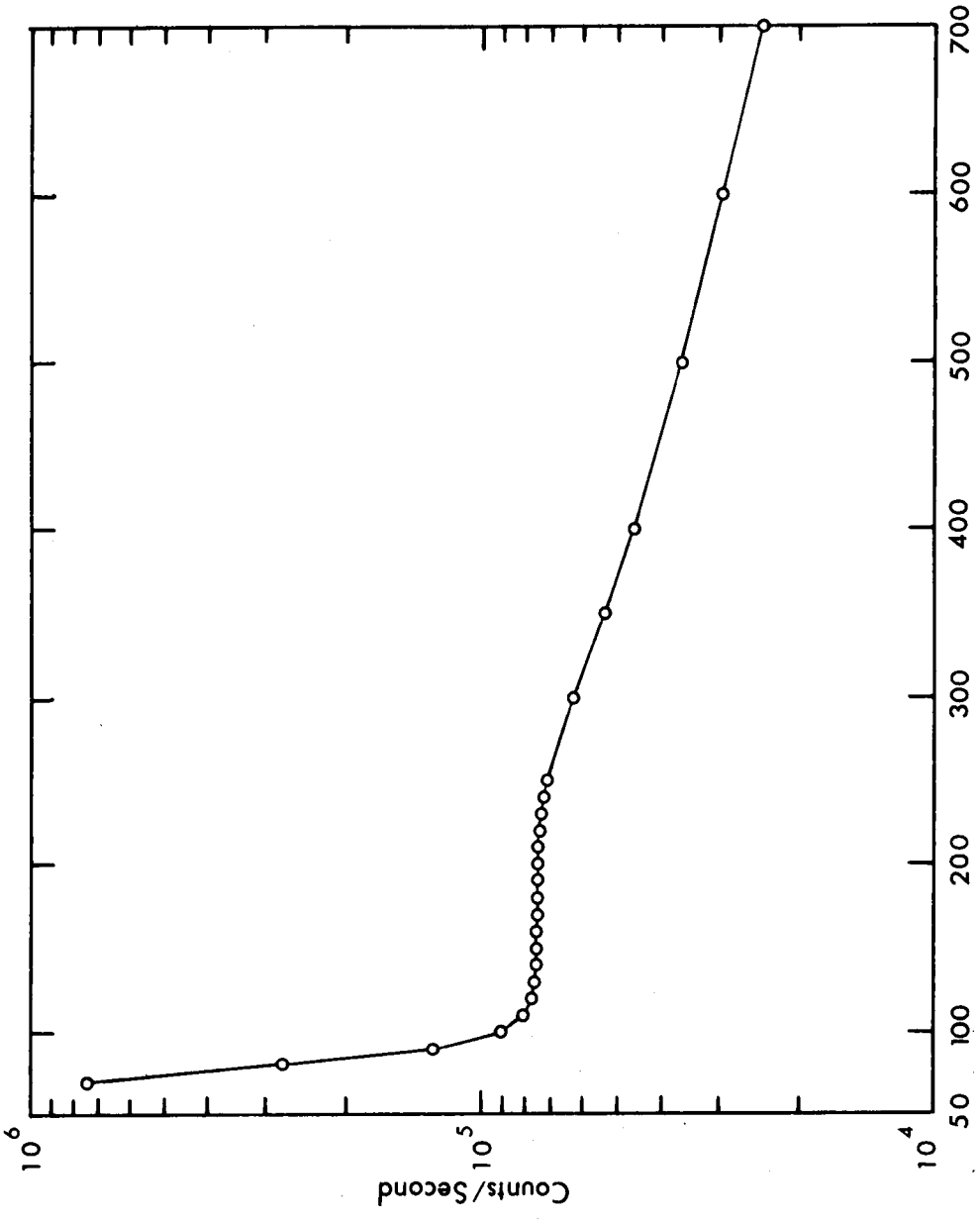


Fig. B.4. ^{252}Cf count rates at various discriminator settings.

B. Li Glass Scintillation System

Two sets of instrumentation, one for pulse mode operation and one for current mode operation, comprise the Li glass scintillation system. These two sets shared the same pair of detectors, high voltage power supplies, and cables; but used different signal processing electronics.

The neutron- and gamma-sensitive detector (ORNL, Q-5167-1, Fig. B.5 consisted of a 38.1 mm diameter, 25.4 mm thick Li (6.6 wt% Li, 95% enriched in ^{6}Li) glass scintillator (Nuclear Enterprises, NE 905) optically coupled to a photomultiplier tube (RCA, C7151Q). A voltage divider network, mounted on an etched wiring board and attached to the base of the photomultiplier tube, was designed to maintain a near maximum allowable voltage (∿400 V) from the photocathode to the first dynode to ensure good linearity of the photomultiplier tube. This voltage was regulated by a Zener diode so that the voltage would be constant at all levels of photomultiplier tube current. The scintillator, photomultiplier tube assembly (both shielded within a 101.6 mm long magnetic shield), and voltage divider network were housed in an aluminum can (50 mm OD, 157.2 mm long). The common mode component of the output shown in Fig. B.5 was not used in this experiment.

High voltage (∿1200 V) was supplied by a high voltage power supply (ORTEC, Inc., ORTEC 456) through a 12.2 m long RG-59 (75 Ω impedance) coaxial cables. Output current was carried to the signal processing electronics through a 12.2 m long Essex 21-541 (75 Ω impedance) coaxial cable.

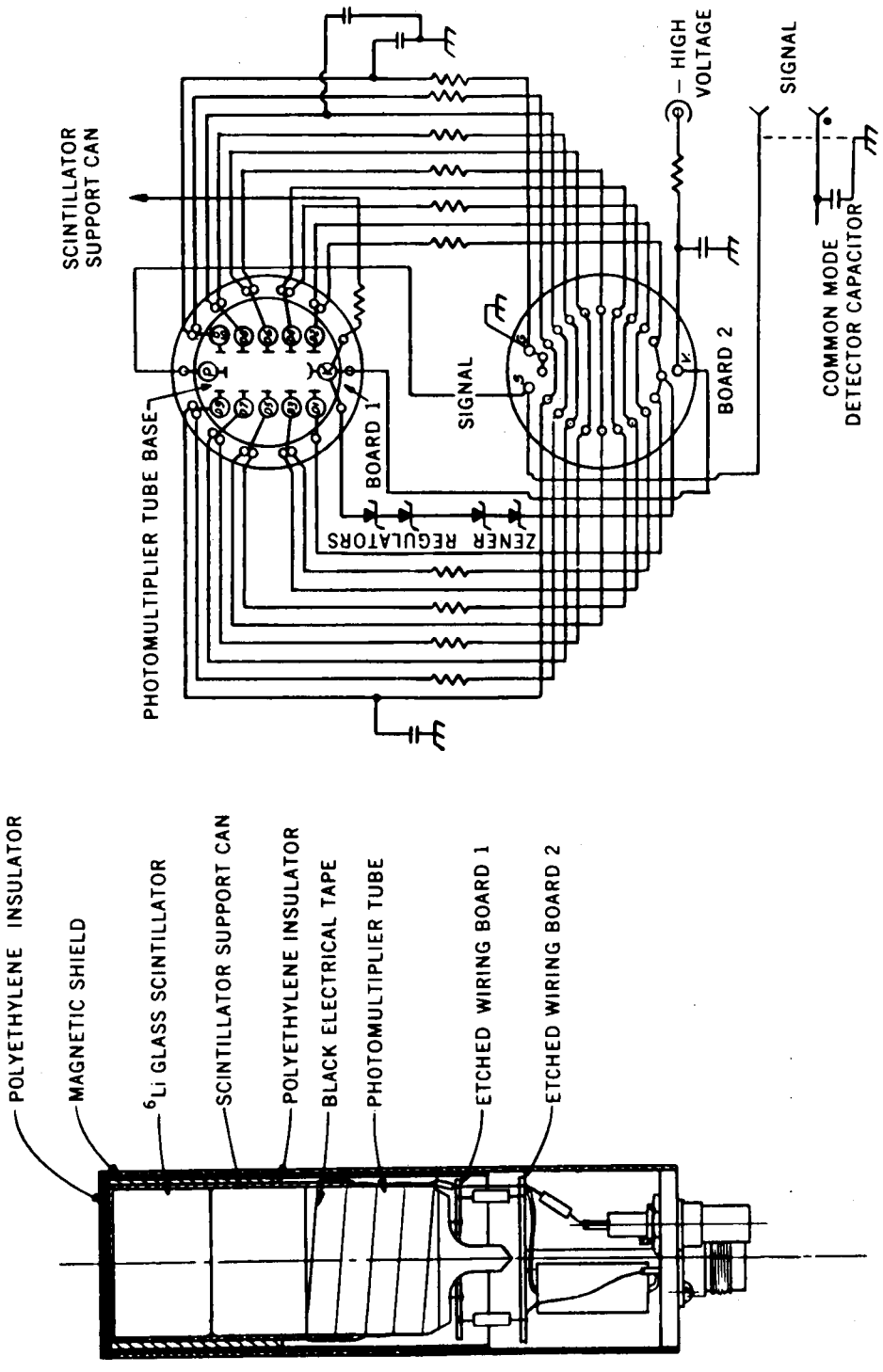


Fig. B.5. Li glass scintillator and voltage divider network.

1. Pulse Mode Signal Processing Electronics

Signal processing for the pulse mode Li glass scintillation system (Fig. B.6) was done with instruments as outlined by Mathis, and others[24] for the fission counter instrumentation system.

The current from the scintillation detector was input to a low-noise current pulse preamplifier (ORNL, Q-3125 prototype) with a gain of ∿100 and a rise time of ∿3 nsec. Gain on the preamplifier output signal was supplied by two linear amplifiers (LeCroy, LRS 107) interconnected with 27 nsec RC-CR filters (C2 and RC2 in Fig. B.6) to control the system bandwidth for improved signal-to-noise ratio. In the system used in previous measurements,[24] a third linear amplifier and a 2 nsec RC integrator was used to reduce the peaking of electronic noise by high frequency resonance in the differentiating and integrating networks. This was not employed in the pulse mode Li system because high frequency electronic noise was not found to be a problem and the added gain from the third amplifier was undesirable.

A discriminator (EG&G, T105/N) was used to discriminate out electronic noise and, in some cases, change the detection efficiency of the detection channel to match the count rate of the other channel in the system. As in the ^{252}Cf system, the output of the discriminator was filtered and amplified with an RC Time-Constant unit (ORNL, Q-3136). A Q-3136 is essentially a Q-3131 with added features not used in this experiment.

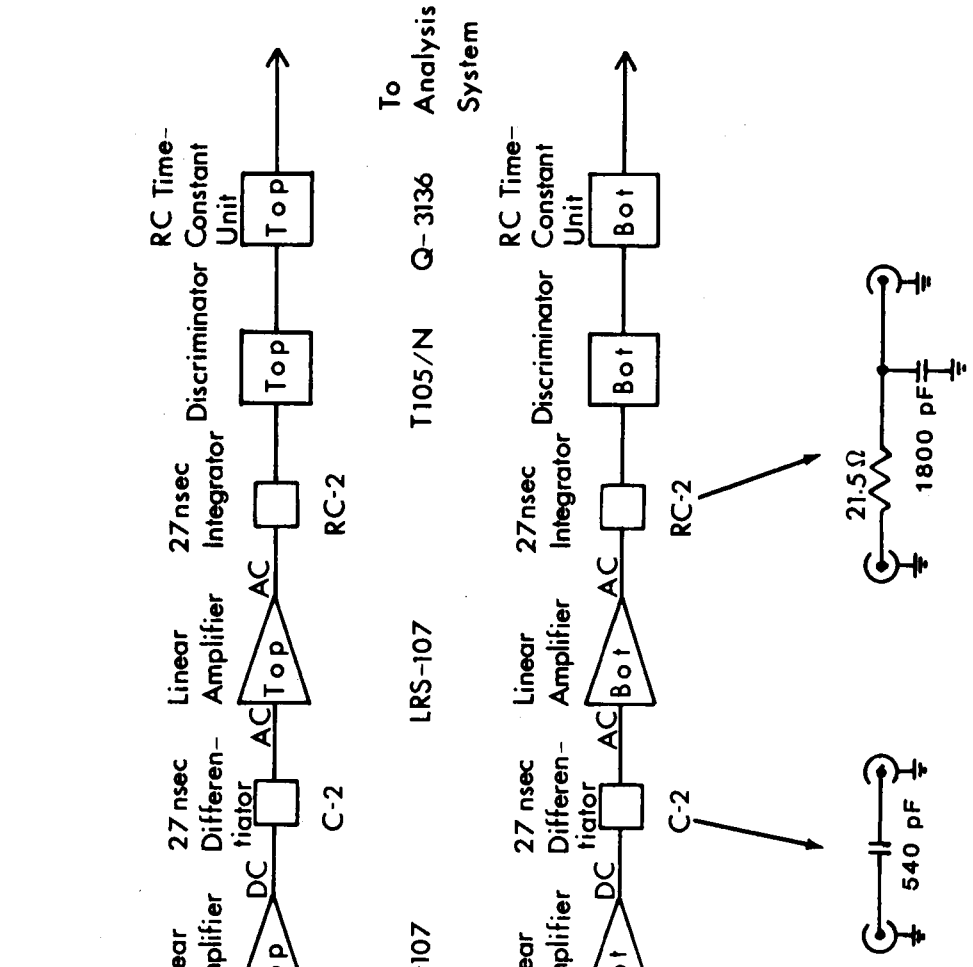


Fig. B.6. Block diagram of the pulse mode Li glass scintillation system.

2. Current Mode Signal Processing Electronics

In the current mode operation, the fluctuating current from the scintillation detector was passed through a resistor. The fluctuating voltage drop across the resistor was amplified and analyzed. The system (Fig. B.7) used in this experiment consisted of a set of 12 switch-selectable resistors (ranging from 10 MΩ to 1 kΩ) and a low-noise preamplifier (Princeton Applied Research Corp., PAR 113), used as a voltage amplifier.

C. ^{3}He Proportional Counting System

The ^{3}He proportional counting system (Fig. B.8) consisted of neutron-sensitive, ^{3}He-filled proportional counters, two high voltage bias supplies, two charge-sensitive preamplifiers, two channels of signal processing electronics, and cables.

The detectors were 343 mm long, 25.4 mm OD, ^{3}He filled proportional counters (Reuter Stokes, RS-P4-0810-207). Specifications for the counter are listed in Table B.1. A sketch is shown in Fig. B.9.

The charge-sensitive preamplifier (ORNL, Q-5703), with a sensitivity of 1 V/pC and a decay time of 50 μsec, was mounted in a small aluminum can (152 mm long, 48 mm OD) so that it can be close-coupled to the detectors to eliminate noise pick-up from cables. High voltage (3500 V) from the bias supply (ORTEC 459) was fed to the detector through the preamplifier. At the start of the experiment, the preamplifier output signal was observed to saturate periodically. It was thought that this was caused by the high voltage arcing in the preamplifier due to the

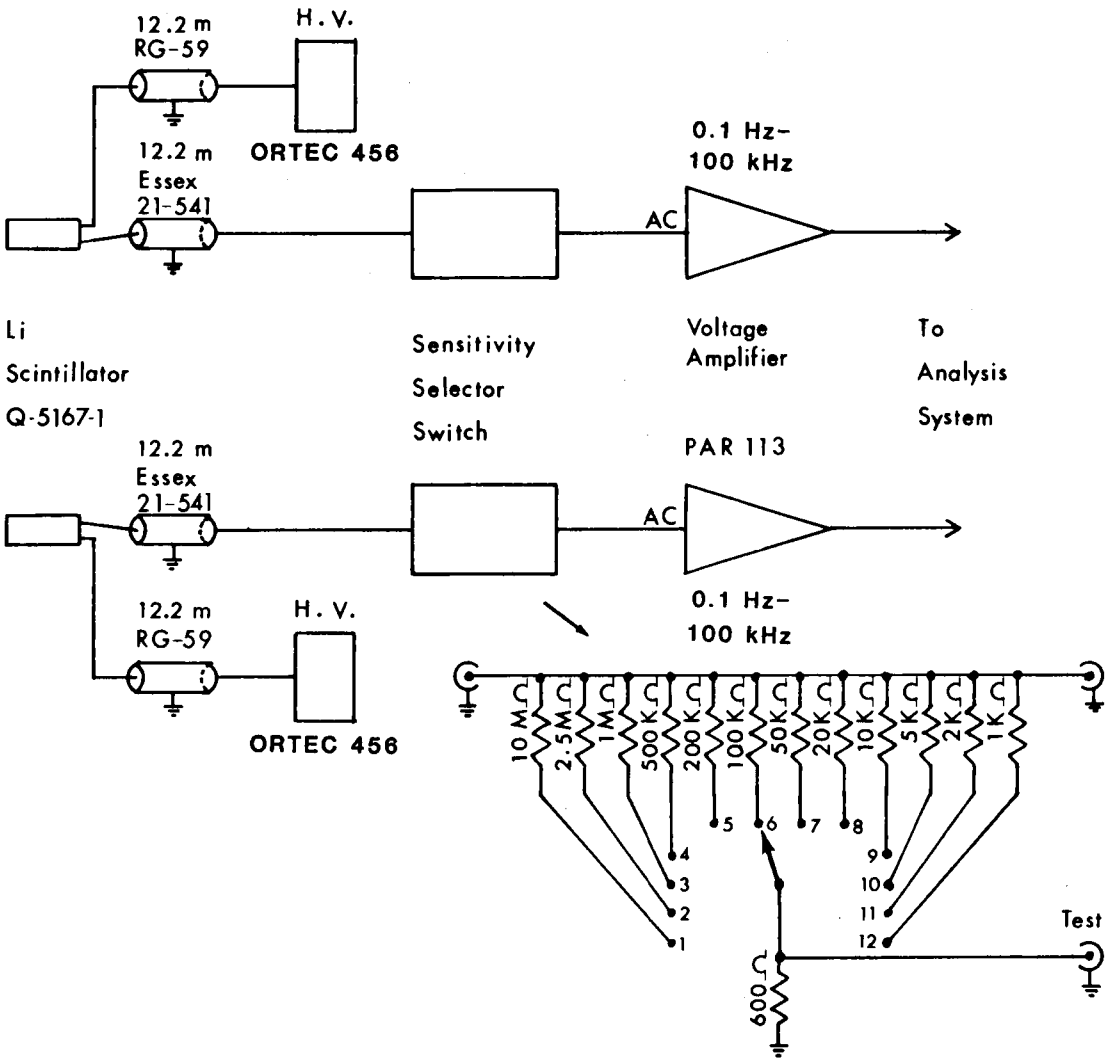


Fig. B.7. Block diagram of the current mode Li glass scintillation system.

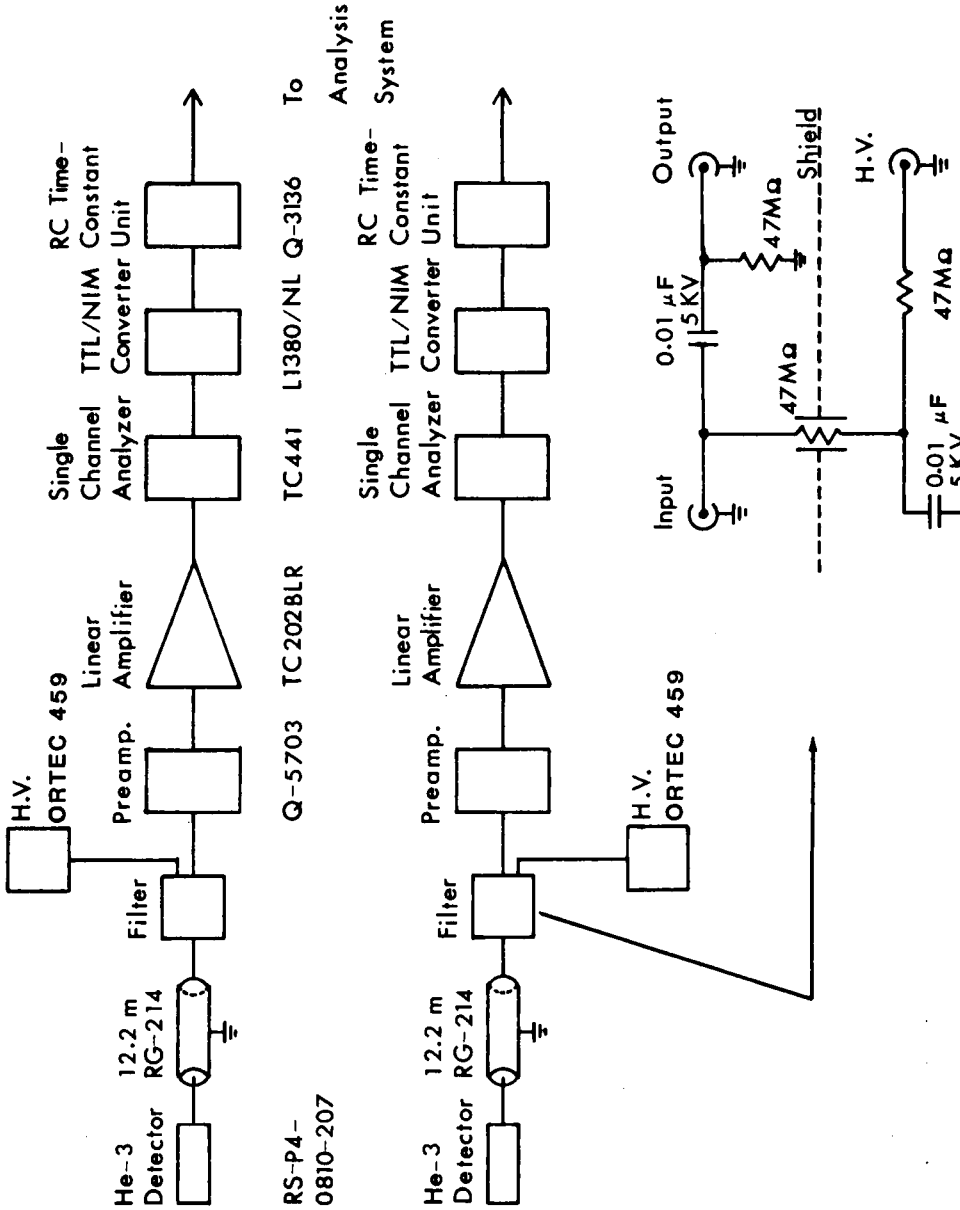


Fig. B.8. Block diagram of the ^{3}He proportional counting system.

Table B.1. Specifications for the ^{3}He proportional counter

Description	Specification
Manufacturer	Reuter Stokes
Manufacturer's model number	RS-P4-0810-207
Shell diameter, mm OD	25.4
Total length, mm	343
Sensitive length, mm	254
Anode material and size, mm diameter	W, 0.102
Cathode material and size, mm thickness	304 SS, 0.813
Filling gas	75% ^{3}He-0.5% CO_2-24.5% Ar
Pressure, mm Hg (absolute)	7600
Operating voltage	3500
Thermal neutron sensitivity counts/sec/nv-thermal	∿29

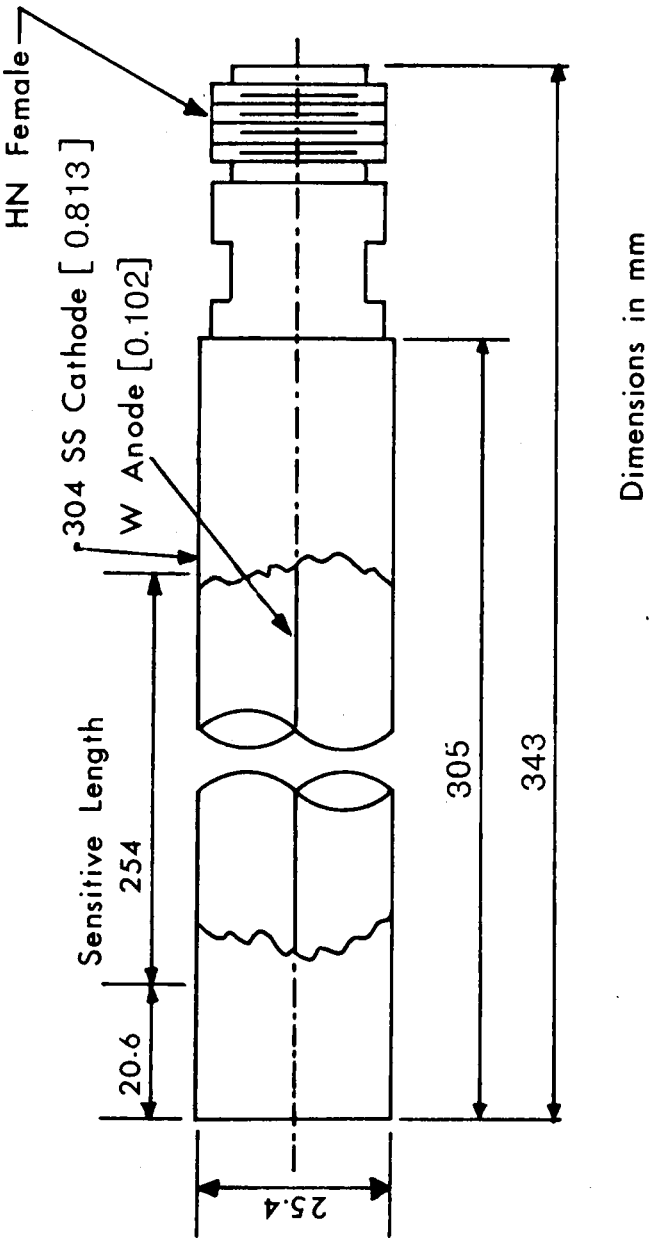


Fig. B.9. Sketch of a ^{3}He proportional counter.

humid environment. The system was reconfigured to that shown in Fig. B.8. A filter was used to bypass the preamplifier in supplying the high voltage to the detector. A 12.2 m long RG-214 (50 Ω impedance) coaxial cable was used to keep the filter and preamplifier away from the humidity of the original location. It was then determined that the saturation was due to ionization caused by the background gamma radiation from irradiated control rod fuel elements. This background ionization caused the high voltage to periodically arc across the electrodes of the chamber. The system was left in the final configuration because the noise pick-up from the cables was not found to be a problem.

A linear amplifier (TENNELEC, TC 202 BLR) was used to amplify and shape the preamplifier output signal such that pulses due to neutron detections were ∿2 V. A single-channel analyzer (TENNELEC, TC 441) was used to discriminate out signals <1.8 V and >6.8 V. Single channel analyzer output pulses were of Transistor-to-Transistor Logic (TTL) type pulses. The RC Time-Constant unit (ORNL, Q-3136, same unit used in the pulse mode Li system) required Nuclear Instrument Module (NIM) type pulses. A TTL-to-NIM converter (ORTEC L 1380/NL) was used to provide these pulses. As in the previous case, the RC Time-Constant unit was used to condition the signal for the analysis system.

D. Fission Counting System

The fission counting system (Fig. B.10) consisted of two enriched uranium coated fission counters, two high voltage power supplies, two low-noise current pulse preamplifiers, two channels of signal processing electronics, and cables.

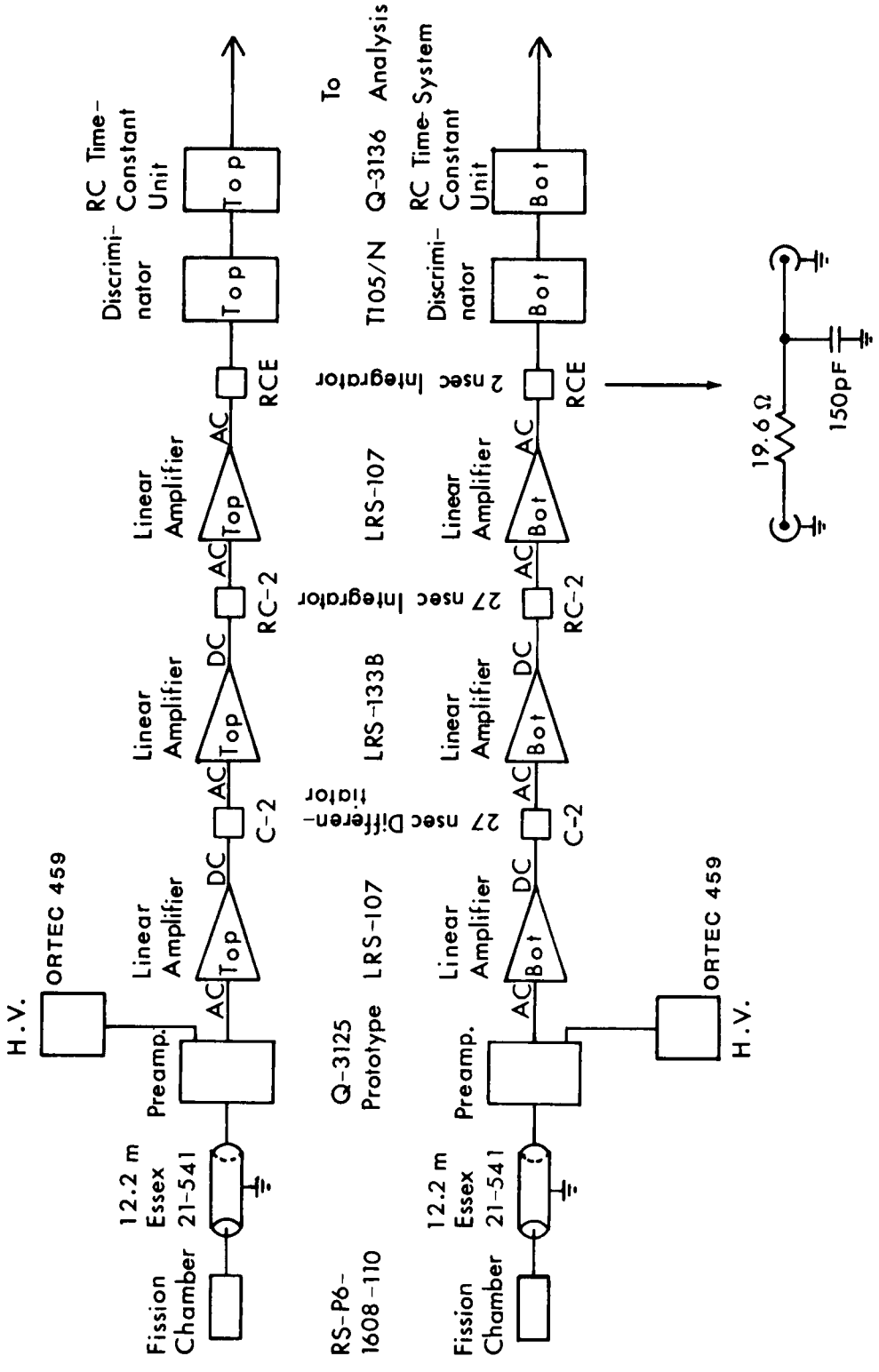


Fig. B.10. Block diagram of the fission counting system.

The detectors (Reuter Stokes, RS-P6-1608-110) were modified versions of the RSN-10A fission counters. They were modified by the manufacturer to increase their sensitivity and to reduce both the number of alpha pulses and the counting loss at high count rates. These improvements were achieved by coating the electrodes with U_3O_8 enriched to 99.7 wt% ^{235}U (containing <0.05% ^{234}U) and by filling the counters with 95% Ar-5% CO_2 to a pressure of 760 mm Hg (absolute). Specifications for this detector are listed in Table B.2. A sketch is shown in Fig. B.11.

The electronics of the pulse mode Li system was slightly modified for use in the fission counting system. ORTEC 459 bias supplies were used instead of the ORTEC 456 high voltage power supplies. High voltage (200 V) was supplied through the current pulse preamplifiers. A third linear amplifier (LeCroy, LRS 133B) was added to each instrument channel to accommodate the 2 nsec integrator (RCE in Fig. B.10) mentioned in the description of the pulse mode Li system.

Table B.2. Specifications for the fission chamber

Description	Specification
Manufacturer	Reuter Stokes
Manufacturer's model number	RS-P6-1608-110
Outside diameter, mm	51.0
Total length, mm	305.0
Sensitive length, mm	181.0
Outer shell and electrode material	Al
Electrode coating thickness, mg/mm^2	∿0.02
Electrode area, mm^2	∿100,000
Electrode spacing, mm	∿4.6, 3.8
Fissile coating	99.7% ^{235}U-<0.05% ^{234}U
Filling gas	95% Ar-5% CO_2
Pressure, mm Hg (absolute)	760
Thermal neutron sensitivity, counts/sec/nv-thermal	∿1.2
Electron pulse collection time, nsec	∿80

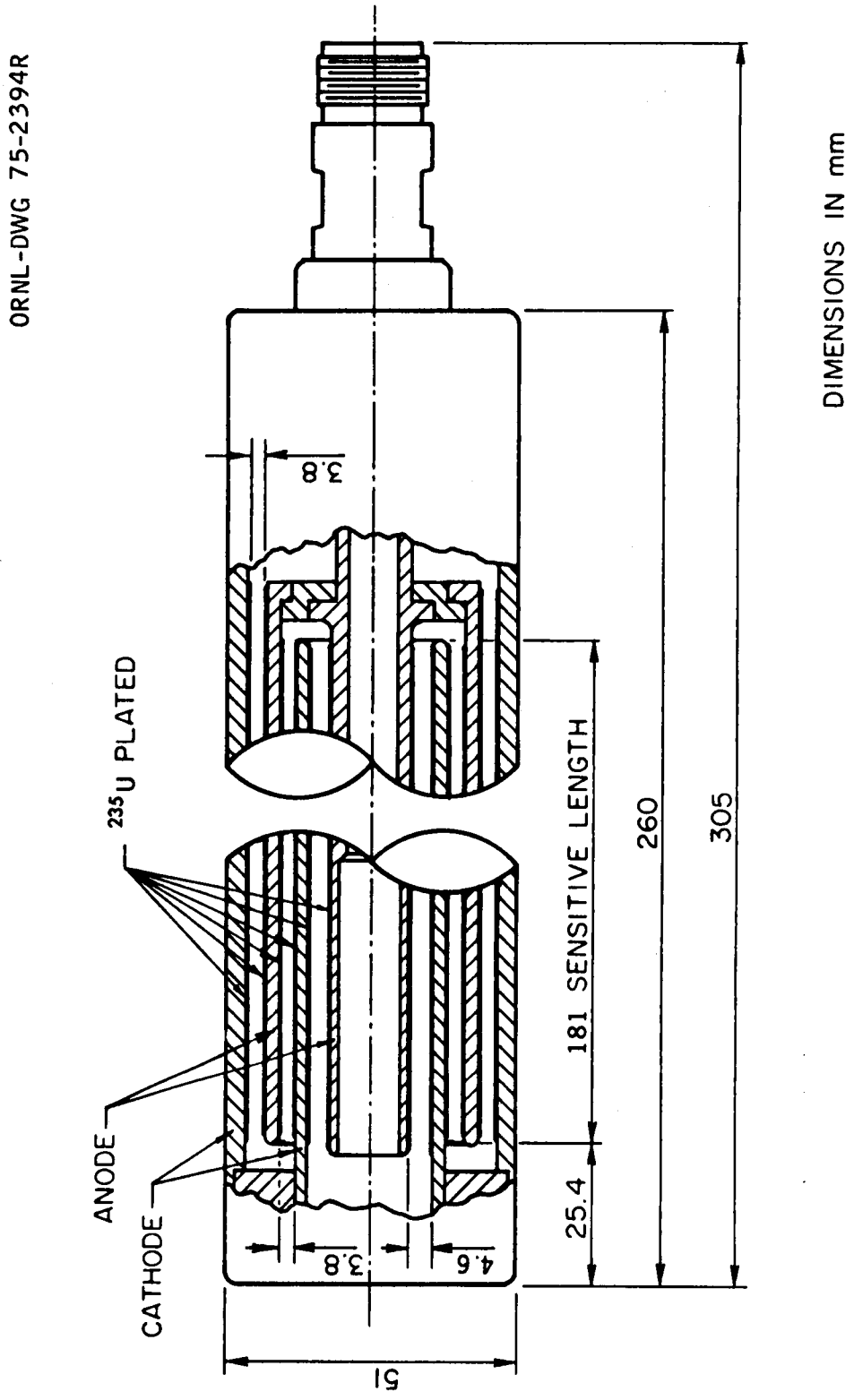


Fig. B.11. Sketch of a fission counter.

APPENDIX C

DESCRIPTION OF THE POOL CRITICAL ASSEMBLY

The Pool Critical Assembly (PCA)[25] is a light water moderated and cooled, usually light water reflected pool-type facility as the Oak Ridge National Laboratory (ORNL). The core is heterogenous and uses Materials Testing Reactor (MTR)-type enriched uranium fuel elements. One of the unique features of the PCA is the versatility of the core's design, which permits it to accept either 18-plate Bulk Shielding Reactor (BSR) or 19-plate Oak Ridge Research Reactor (ORR) fuel elements. This is accomplished by means of stacked grid plates; the BSR-type grid plate, which has round holes to accommodate the BSR end-boxes, may be aligned on top of the ORR-type grid plate, which has square holes to accommodate ORR end-boxes.

A standard BSR fuel element (Fig. C.1) consists of 18 curved (1524 mm radius of curvature), composite-type fuel plates, each 76.2 mm wide, 609.6 mm long, and 1.524 mm thick. Each fuel plate consists of a sheet (0.508 mm thick) of aluminum-uranium alloy (uranium is 93% enriched in ^{235}U) sandwiched between two aluminum sheets. This assembly is hot-rolled into a solid plate of proper dimensions. The complete standard element contains $\sim$140 g of ^{235}U. BSR-type fuel elements are equipped with single cylindrical end-boxes that fit into the grid plate and have no upper end-boxes.

The control rod receiving fuel element (shim element, Fig. C.2) is similar to the standard BSR fuel element except for the slot provided

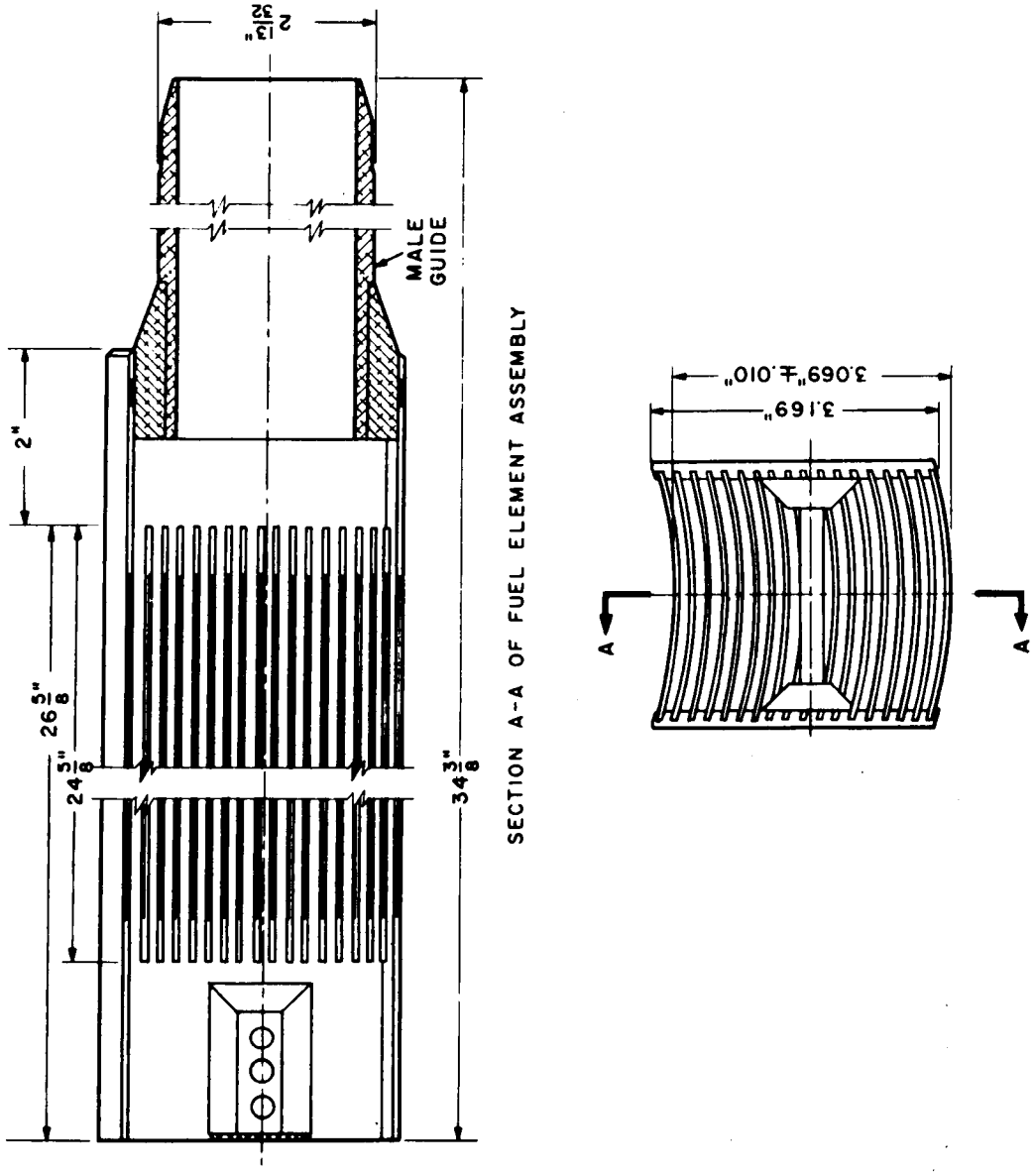
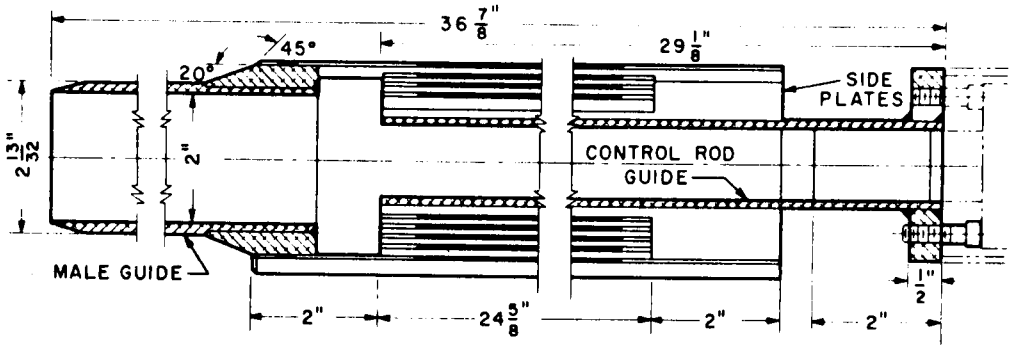
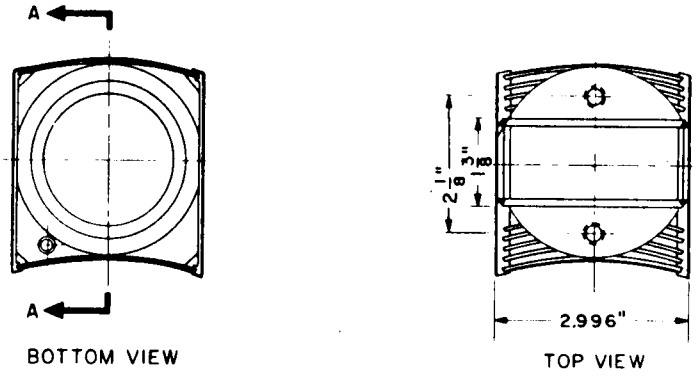


Fig. C.1. Standard BSR fuel element.

ORNL DWG. 65-3146A



SECTION A-A OF SPECIAL FUEL ELEMENT ASSEMBLY



BOTTOM VIEW

TOP VIEW

Fig. C.2. Standard BSR shim element.

for the entry of the control rod. The slot was obtained by omitting the middle half of the fuel plates and inserting a rectangular tube with internal dimensions of 28.575 mm by 66.675 mm.

The ORR fuel elements (Fig. C.3) used in this experiment are similar to the BSR fuel elements with the following differences:

1. the ORR fuel elements consist of 19 curved fuel plates (1.27 mm thick),
2. they contain ∿240 g of ^{235}U,
3. each fuel plate consists of a sheet of aluminum-uranium-oxide (U_3O_8) alloy sandwiched between two aluminum sheets, and
4. the elements are fitted with rectangular end-boxes on both ends.

Fuel and other elements rest in an aluminum grid (711.2 mm by 635 mm and 127 mm deep) with a total of 63 holes to permit loading of any array of up to 9 by 7 elements.

The PCA is normally operated with three safety rods, each of which consists of boron carbide canned in aluminum, and a hollow stainless steel regulating rod which is of the same external size as the safety rods. The control rods are oval-shaped and are 22.2 mm thick, 57.2 mm wide, and 610 mm long. They have a 610 mm vertical travel and move within the shim elements. Cross section views of the control rods are shown in Fig. C.4.

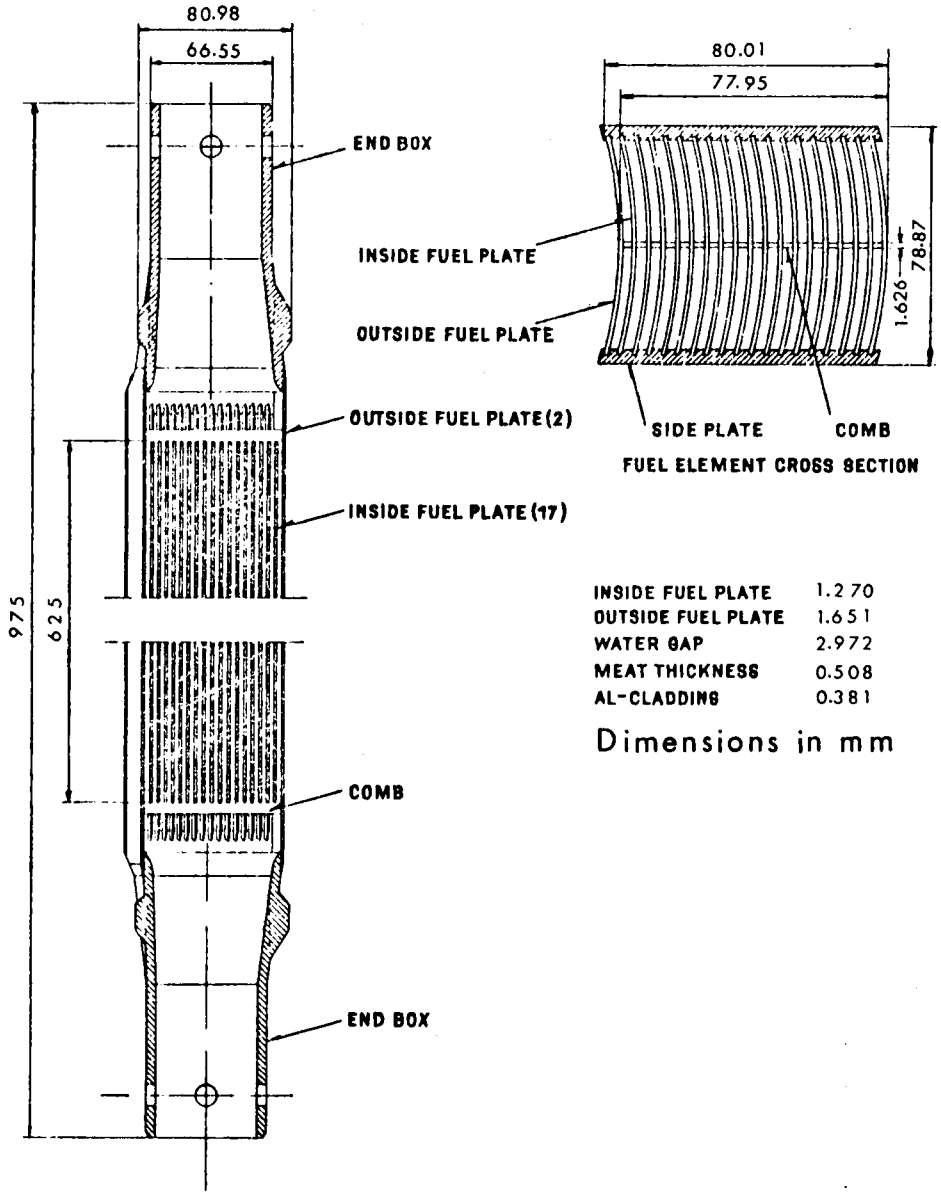


Fig. C.3. Standard ORR fuel element.

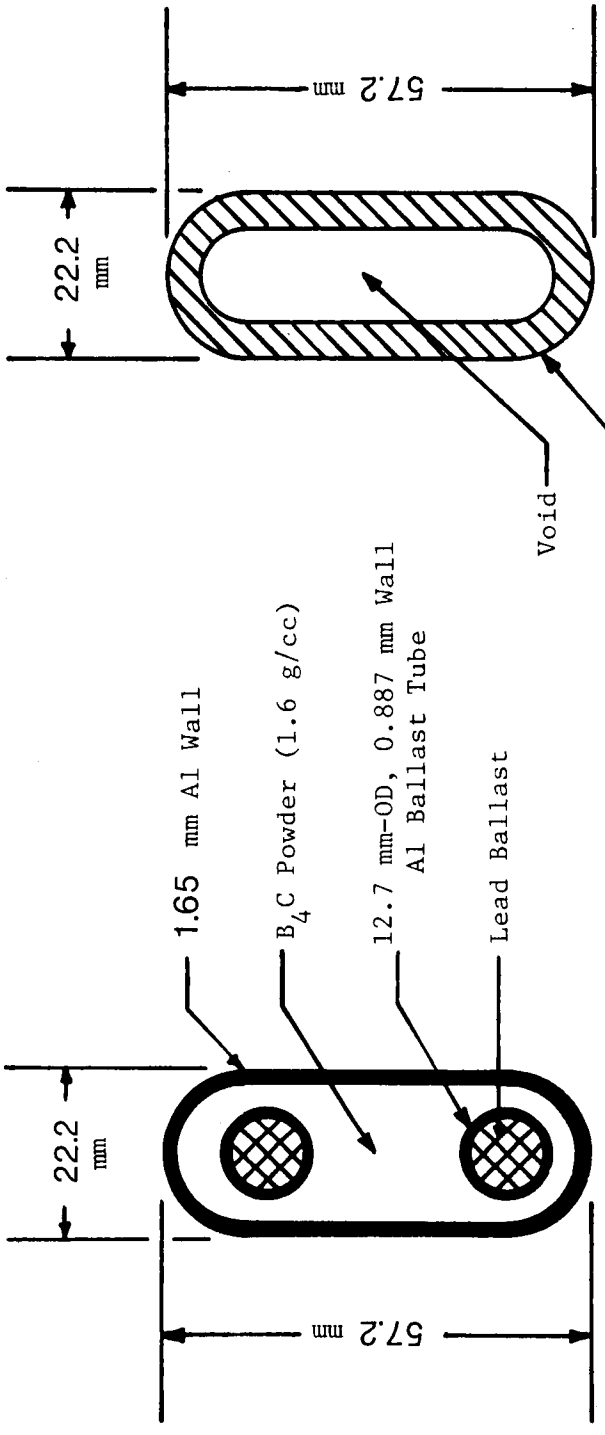


Fig. C.4. Cross section view of the control rods.

APPENDIX D

NONLINEAR LEAST SQUARES FITTING ALGORITHM

The derivation below follows the procedure outlined by LaFarra.[42] The nonlinear equation of interest is

$$y = C_0/[1 + (f/f_b)^2]^p + D_0 \quad , \tag{D.1}$$

where C_0, f_b, p, and D_0 are the parameters needed. In breakfrequency reactivity measurements,

y = corrected CPSD at frequency f,

C_0 = constant magnitude,

f_b = breakfrequency,

p = roll-off slope, and

D_0 = high frequency tail magnitude.

The four parameters in Eq. (D.1) will be estimated as follows. Define the weighted sum of the square of the residuals as:

$$\Theta = \sum_{i=1}^{N} w_i(\ell_i - L_i)^2 \quad , \tag{D.2}$$

where:

Θ = weighted sum of the squares of the residuals,

N = number of data points included in the fit,

w_i = weight associated with the ith data point,

L_i = least squares estimate of the ith ordinate, and

ℓ_i = the measured ith ordinate.

Since the parameters are unknown, an initial guess of their values are required. These will be labeled C_0^0, f_b^0, p^0, and D_0^0.

The ith ordinate is estimated by a first order Taylor expansion, that is

$$L_i = (y_i)|_0 + \Delta C_0(\partial y_i/\partial C_0)|_0 + \Delta f_b(\partial y_i/\partial f_b)|_0 + \Delta p(\partial y_i/\partial p)|_0 + \Delta D_0(\partial y_i/\partial D_0)|_0 \ . \qquad (D.3)$$

where $|_n$ means evaluated using the nth estimate of the parameters. Combining Eqs. (D.2) and (D.3), the weighted sum of the squares of the residuals becomes

$$\theta = \sum_{i=1}^{N} w_i \left[\ell_i - (y_i)|_0 - \Delta C_0(\partial y_i/\partial C_0)|_0 - \Delta f_b(\partial y_i/\partial f_b)|_0 - \Delta p(\partial y_i/\partial p)|_0 - \Delta D_0(\partial y_i/\partial D_0)|_0\right]^2 \ . \qquad (D.4)$$

In Eq. (D.4), the unknown quantities are ΔC_0, Δf_b, Δp, and ΔD_0. These quantities will be obtained by the least squares method. The weighted sum of the squares of the residuals will be minimized if the partial derivatives of Eq. (D.4) with respect to each of the four unknown quantities are set to zero. In particular

$$\partial\Theta/\partial\Delta C_0 = 0 = -\sum_{i=1}^{N} w_i\,[\ell_i - (y_i)|_0]\,(\partial y_i/\partial C_0)|_0$$

$$+\,\Delta C_0 \sum_{i=1}^{N} w_i[(\partial y_i/\partial C_0)|_0]^2$$

$$+\,\Delta f_b \sum_{i=1}^{N} w_i(\partial y_i/\partial C_0)|_0\,(\partial y_i/\partial f_b)|_0$$

$$+\,\Delta p \sum_{i=1}^{N} w_i(\partial y_i/\partial C_0)|_0\,(\partial y_i/\partial p)|_0$$

$$+\,\Delta D_0 \sum_{i=1}^{N} w_i(\partial y_i/\partial C_0)|_0\,(\partial y_i/\partial D_0)|_0 \quad , \qquad \text{(D.5)}$$

$$\partial\Theta/\partial\Delta f_b = 0 = -\sum_{i=1}^{N} w_i\,[\ell_i - (y_i)|_0]\,(\partial y_i/\partial f_b)|_0$$

$$+\,\Delta C_0 \sum_{i=1}^{N} w_i(\partial y_i/\partial f_b)|_0\,(\partial y_i/\partial C_0)|_0$$

$$+\,\Delta f_b \sum_{i=1}^{N} w_i\,[(\partial y_i/\partial f_b)|_0]^2$$

$$+\,\Delta p \sum_{i=1}^{N} w_i(\partial y_i/\partial f_b)|_0\,(\partial y_i/\partial p)|_0$$

$$+\,\Delta D_0 \sum_{i=1}^{N} w_i(\partial y_i/\partial f_b)|_0\,(\partial y_i/\partial D_0)|_0 \quad , \qquad \text{(D.6)}$$

$$\partial\Theta/\partial\Delta p = 0 = -\sum_{i=1}^{N} w_i \left[\ell_i - (y_i)|_0\right] (\partial y_i/\partial p)|_0$$

$$+ \Delta C_0 \sum_{i=1}^{N} w_i (\partial y_i/\partial p)|_0 \, (\partial y_i/\partial C_0)|_0$$

$$+ \Delta f_b \sum_{i=1}^{N} w_i (\partial y_i/\partial p)|_0 \, (\partial y_i/\partial f_b)|_0$$

$$+ \Delta p \sum_{i=1}^{N} w_i \left[\partial y_i/\partial p)|_0\right]^2$$

$$+ \Delta D_0 \sum_{i=1}^{N} w_i (\partial y_i/\partial p)|_0 \, (\partial y_i/\partial D_0)|_0 \quad , \qquad \text{(D.7)}$$

and

$$\partial\Theta/\partial\Delta D_0 = 0 = -\sum_{i=1}^{N} w_i \left[\ell_i - (y_i)|_0\right] (\partial y_i/\partial D_0)|_0$$

$$+ \Delta C_0 \sum_{i=1}^{N} w_i (\partial y_i/\partial D_0)|_0 \, (\partial y_i/\partial C_0)|_0$$

$$+ \Delta f_b \sum_{i=1}^{N} w_i (\partial y_i/\partial D_0)|_0 \, (\partial y_i/\partial f_b)|_0$$

$$+ \Delta p \sum_{i=1}^{N} w_i (\partial y_i/\partial D_0)|_0 \, (\partial y_i/\partial p)|_0$$

$$+ \Delta D_0 \sum_{i=1}^{N} w_i \left[\partial y_i/\partial D_0)|_0\right]^2 \quad . \qquad \text{(D.8)}$$

Let

$$\underline{X} = \begin{bmatrix} \Delta C_0 \\ \Delta f_b \\ \Delta p \\ \Delta D_0 \end{bmatrix} , \tag{D.9}$$

$$\underline{B} = \begin{bmatrix} \sum_{i=1}^{N} w_i \, [\ell_i - (y_i)|_0] \, (\partial y_i/\partial C_0)|_0 \\ \sum_{i=1}^{N} w_i]\ell_i - (y_i)|_0] \, (\partial y_i/\partial f_b)|_0 \\ \sum_{i=1}^{N} w_i [\ell_i - (y_i)|_0] \, (\partial y_i/\partial p \,)|_0 \\ \sum_{i=1}^{N} w_i [\ell_i - (y_i)|_0] \, (\partial y_i/\partial D_0)|_0 \end{bmatrix} , \tag{D.10}$$

and the symmetric matrix $\underline{\underline{A}}$ with elements

$$a_{11} = \sum_{i=1}^{N} w_i \, [(\partial y_i/\partial C_0)|_0]^2 \quad , \tag{D.11}$$

$$a_{22} = \sum_{i=1}^{N} w_i [(\partial y_i/\partial f_b)|_0]^2 \quad , \tag{D.12}$$

$$a_{33} = \sum_{i=1}^{N} w_i [(\partial y_i/\partial p \,)|_0]^2 \quad , \tag{D.13}$$

$$a_{44} = \sum_{i=1}^{N} w_i \left[(\partial y_i/\partial D_0)\big|_0\right]^2 \quad , \tag{D.14}$$

$$a_{12} = a_{21} = \sum_{i=1}^{N} w_i (\partial y_i/\partial C_0)\big|_0 \; (\partial y_i/\partial f_b)\big|_0 \quad , \tag{D.15}$$

$$a_{13} = a_{31} = \sum_{i=1}^{N} w_i (\partial y_i/\partial C_0)\big|_0 \; (\partial y_i/\partial p \;)\big|_0 \quad , \tag{D.16}$$

$$a_{14} = a_{41} = \sum_{i=1}^{N} w_i (\partial y_i/\partial C_0)\big|_0 \; (\partial y_i/\partial D_0)\big|_0 \quad , \tag{D.17}$$

$$a_{23} = a_{32} = \sum_{i=1}^{N} w_i (\partial y_i/\partial f_b)\big|_0 \; (\partial y_i/\partial p \;)\big|_0 \quad , \tag{D.18}$$

$$a_{24} = a_{42} = \sum_{i=1}^{N} w_i (\partial y_i/\partial f_b)\big|_0 \; (\partial y_i/\partial D_0)\big|_0 \quad , \tag{D.19}$$

and

$$a_{34} = a_{43} = \sum_{i=1}^{N} w_i (\partial y_i/\partial p \;)\big|_0 \; (\partial y_i/\partial D_0)\big|_0 \quad . \tag{D.20}$$

With the above definitions, Eqs. (D.5) thru (D.8) reduce to

$$\underline{\underline{A}}\;\underline{X} = \underline{B} \quad . \tag{D.21}$$

$\underline{X}$ is found by

$$\underline{X} = \underline{\underline{A}}^{-1}\;\underline{B} \quad , \tag{D.22}$$

where $\underline{\underline{A}}^{-1}$ is the inverse of $\underline{\underline{A}}$.

The initial set of parameters (C_0^0, f_b^0, p^0, d_0^0) can now be updated by

$$C_0^1 = C_0^0 + \Delta C_0 \quad , \tag{D.23}$$

$$f_b^1 = f_b^0 + \Delta f_b \quad , \tag{D.24}$$

$$p^1 = p^0 + \Delta p \quad , \tag{D.25}$$

and

$$D_0^1 = D_0^0 + \Delta D_0 \quad . \tag{D.26}$$

These updated estimates of the parameters are cycled through the above process to obtain even newer (presumably better) estimates of the parameters. This procedure is continued until the desired degree of convergence is achieved. Convergence is tested by examining

$$\varepsilon_{C_0} = \left|1 - C_0^i/C_0^{i+1}\right| \quad , \tag{D.27}$$

$$\varepsilon_{f_b} = \left|1 - f_b^i/f_b^{i+1}\right| \quad , \tag{D.28}$$

$$\varepsilon_p = \left|1 - p^i/p^{i+1}\right| \quad , \tag{D.29}$$

and

$$\varepsilon_{D_0} = \left|1 - D_0^i/D_0^{i+1}\right| \quad . \tag{D.30}$$

Convergence is reached if ε_{C_0}, ε_{f_b}, ε_p, and ε_{D_0} are all less than a predetermined criterion, for example, 10^{-6}.

The covariance matrix $\underline{\underline{E}}$ is defined as

$$\underline{\underline{E}} = \frac{\theta}{N - 4} \underline{\underline{A}}^{-1} \quad . \tag{D.31}$$

Therefore, the final least squares estimates of the parameters are

$$C_0^{last} \pm \sqrt{e_{11}} \quad , \tag{D.32}$$

$$f_b^{last} \pm \sqrt{e_{22}} \quad , \tag{D.33}$$

$$p^{last} \pm \sqrt{e_{33}} \quad , \tag{D.34}$$

and

$$D_0^{last} \pm \sqrt{e_{44}} \quad . \tag{D.35}$$

The partial derivatives of Eq. (D.1) are

$$\partial y/\partial C_0 = 1/[1 + (f/f_b)^2]^p \quad , \tag{D.36}$$

$$\partial y/\partial f_b = 2pC_0(f/f_b)^2/[f_b\{1 + (f/f_b)^2\}^{p+1}] \quad , \tag{D.37}$$

$$\partial y/\partial p = - C_0 \ln[1 + (f/f_b)^2]/[1 + (f/f_b)^2]^p \quad , \tag{D.38}$$

and

$$\partial y/\partial D_0 = 1 \quad . \tag{D.39}$$

If any of the parameters are to be fixed, for example, set $p = 1$, then all that is required is to set $p^0 = 1$ and $\Delta p = 0$ after each iteration. In implementing this algorithm, it was found that the iterative process

often do not converge. The remedy found effective was to limit the maximum absolute value of Δx (x referring to each of the parameters) to $|0.05\ x^0|$.

APPENDIX E

PARAMETERS REQUIRED TO OBTAIN REACTIVITIES FROM MEASURED QUANTITIES

The interpretation of the measured quantities, that is, determination of reactivity from the ratio of spectral densities, count rates, and others, requires knowledge of some constants characteristic of the reactor. Some parameters were obtained from neutron cross sections in conjunction with calculated forward and adjoint fluxes. Others were obtained from open literature.

A. Core Calculations

Figure E.1 is a flow diagram of the core calculation procedure used to obtain multigroup neutron cross sections which were then used to calculate forward and adjoint fluxes. The ENDF/B-IV 218 group cross section library[43] was processed with modules from the AMPX[44] and VENTURE[45-49] systems of computer codes.

1. Nuclide Selection

Because some modules in the AMPX system process whole cross section libraries, a small subset of the ENDF/B-IV 218 group library containing the cross sections of those nuclides present in ORR fuel elements and BSR shim elements (with and without safety and regulating rods) was formed with AJAX (AMPX). These nuclides are listed in Table E.1.

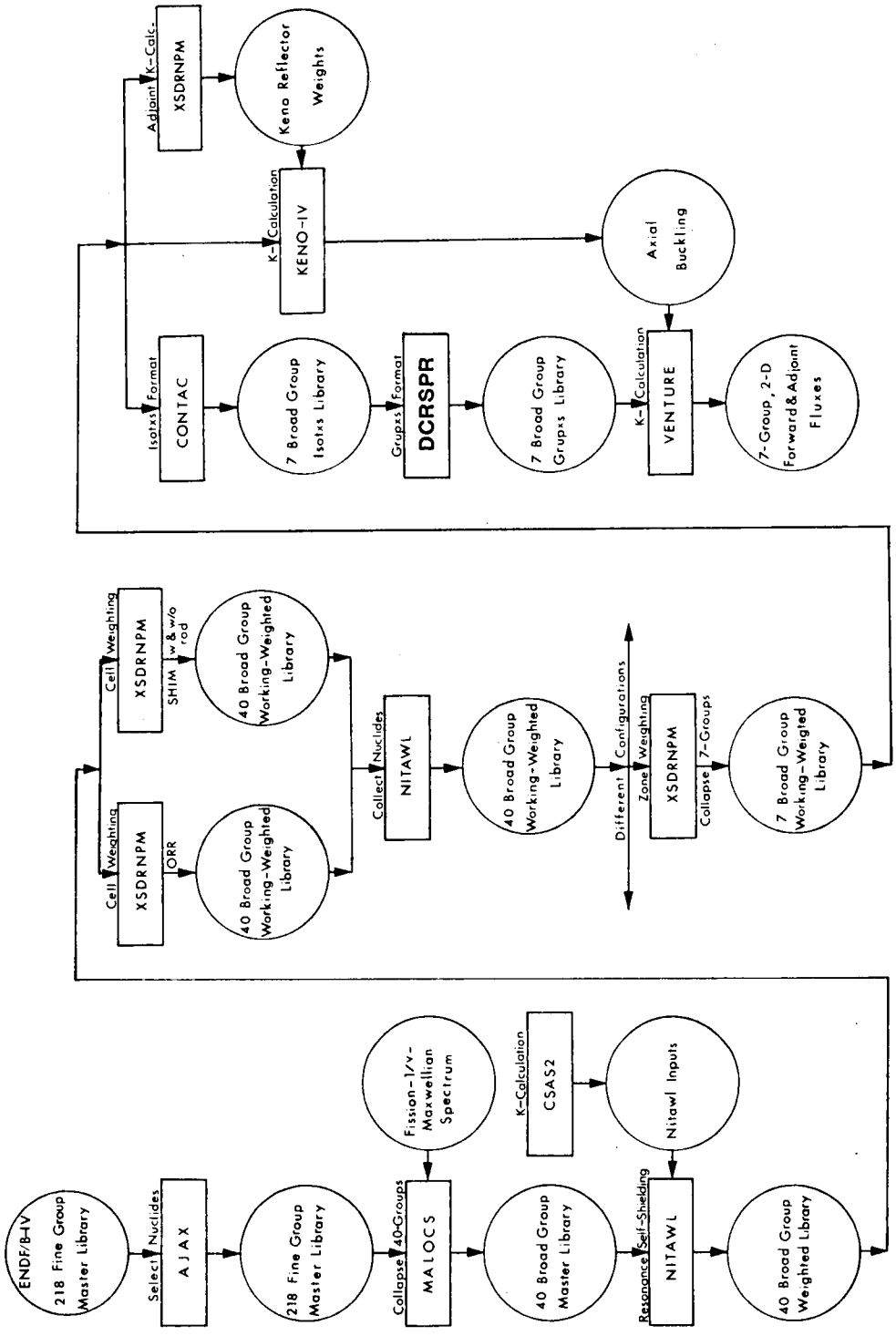


Fig. E.1. Flow diagram of the core calculation procedure.

Table E.1. Nuclides selected from the ENDF/B-IV 218 group library

Nuclide	Reflector	ORR fuel element	BSR shim element w/o rod	BSR shim element w/ safety rod	BSR shim element w/ regulating rod
U-235		X	X	X	X
U-238		X	X	X	X
Al		X	X	X	X
O	X	X	X	X	X
H	X	X	X	X	X
C				X	X
Mn					X
P					X
S					X
Si					X
Cr					X
Ni					X
Fe					X
B-10				X	
B-11				X	
Pb				X	
1/v	X	X	X	X	X

2. Collapse to 40 Energy Groups

MALOCS (AMPX) was used to collapse the cross sections from 218 to 40 energy groups. The weighting function used in this calculation was the fission-1/v-Maxwellian energy spectrum. The 218, 40, and 7 (to be used later) energy boundaries, as well as the weighting function values are listed in Table E.2.

3. Resonance Self-Shielding

NITAWL (AMPX), the neutron resonance self-shielding calculation module, required input parameters (like Dancoff correction factors, mean chord lengths, and others) which were not readily available. SCALE,[50] a system of computer codes written to simplify criticality calculations, contains subroutines which calculate NITAWL input parameters. Short (30 sec) CSAS2 (a calculation sequence in the SCALE system) calculation sequences were performed for the ORR fuel element and the BSR shim element to obtain NITAWL input parameters. The elements were modeled as shown in Fig. E.2. Material compositions are listed in Table E.3. Resonance self-shielding calculations were performed for ^{235}U and ^{238}U in both types of fuel elements using the Nordheim Integral Treatment in NITAWL (AMPX). Other nuclides with resonance data were treated by the Infinite Dilution Method.

4. Cell Weighting

Cell weighting was performed with XSDRNPM (AMPX, 1-D, S_N transport code, P3, S16) in order to generate cross sections consistent with mocking up cell configurations as homogenized regions. The ORR fuel

Table E.2. Energy group structure and group fluxes

Fine (218) Group	Upper energy (eV)	Upper lethargy	Group flux	Broad (40) Group	Broad (7) Group
1	2.00E+7	-6.93E-1	8.33E-1	1	1
2	6.43E+6	4.41E-1	1.79E+0	2	1
3	4.80E+6	7.34E-1	1.07E+0	3	1
4	4.30E+6	8.43E-1	5.15E+0	3	1
5	3.00E+6	1.20E+0	3.54E+0	4	1
6	2.48E+6	1.39E+0	1.02E+0	5	1
7	2.35E+6	1.45E+0	4.90E+0	6	1
8	1.85E+6	1.69E+0	4.23E+0	6	1
9	1.50E+6	1.90E+0	1.34E+0	7	1
10	1.40E+6	1.97E+0	6.06E-1	7	1
11	1.36E+6	2.00E+0	5.47E-1	8	1
12	1.32E+6	2.03E+0	9.59E-1	8	1
13	1.25E+6	2.08E+0	7.31E-1	9	1
14	1.20E+6	2.12E+0	1.50E+0	9	1
15	1.10E+6	2.21E+0	1.39E+0	9	1
16	1.01E+6	2.29E+0	1.43E+0	10	1
17	9.20E+5	2.39E+0	3.22E-1	10	1
18	9.00E+5	2.41E+0	4.04E-1	10	1
19	8.75E+5	2.44E+0	2.26E-1	11	1
20	8.61E+5	2.45E+0	6.71E-1	11	1
21	8.20E+5	2.50E+0	1.15E+0	12	2
22	7.50E+5	2.59E+0	1.18E+0	12	2
23	6.79E+5	2.69E+0	1.50E-1	12	2
24	6.70E+5	2.70E+0	1.16E+0	12	2
25	6.00E+5	2.81E+0	4.48E-1	12	2
26	5.73E+5	2.86E+0	3.81E-1	12	2
27	5.50E+5	2.90E+0	8.31E-1	12	2
28	5.00E+5	3.00E+0	4.82E-1	13	2
29	4.70E+5	3.06E+0	4.86E-1	13	2
30	4.40E+5	3.12E+0	3.21E-1	13	2
31	4.20E+5	3.17E+0	3.18E-1	13	2
32	4.00E+5	3.22E+0	1.09E+0	13	2
33	3.30E+5	3.41E+0	8.89E-1	14	2
34	2.70E+5	3.61E+0	9.65E-1	15	2
35	2.00E+5	3.91E+0	6.23E-1	16	2
36	1.50E+5	4.20E+0	2.48E-1	17	3
37	1.28E+5	4.36E+0	2.99E-1	17	3
38	1.00E+5	4.61E+0	1.63E-1	18	3
39	8.50E+4	4.77E+0	3.59E-2	19	3
40	8.20E+4	4.80E+0	8.92E-2	19	3
41	7.50E+4	4.89E+0	2.70E-2	19	3
42	7.30E+4	4.92E+0	1.96E-1	19	3
43	6.00E+4	5.12E+0	1.43E-1	19	3
44	5.20E+4	5.26E+0	3.92E-2	19	3
45	5.00E+4	5.30E+0	1.05E-1	19	3
46	4.50E+4	5.40E+0	4.05E-1	19	3
47	3.00E+4	5.81E+0	1.82E-1	19	3
48	2.50E+4	5.99E+0	3.86E-1	19	3
49	1.70E+4	6.38E+0	2.68E-1	19	3
50	1.30E+4	6.65E+0	3.14E-1	20	4
51	9.50E+3	6.96E+0	1.68E-1	20	4
52	8.03E+3	7.13E+0	2.91E-1	20	4
53	6.00E+3	7.42E+0	4.31E-1	20	4
54	3.90E+3	7.85E+0	4.19E-2	20	4
55	3.74E+3	7.89E+0	2.20E-1	20	4
56	3.00E+3	8.11E+0	1.51E-1	20	4
57	2.58E+3	8.26E+0	1.19E-1	21	4
58	2.29E+3	8.38E+0	4.01E-2	21	4
59	2.20E+3	8.42E+0	2.01E-1	21	4
60	1.80E+3	8.62E+0	1.50E-1	21	4
61	1.55E+3	8.77E+0	3.28E-2	21	4
62	1.50E+3	8.80E+0	2.66E-1	21	4

Table E.2. (continued)

Fine (218) group	Upper energy (eV)	Upper lethargy	Group flux	Broad (40) group	Broad (7) group
63	1.15E+3	9.07E+0	1.91E-1	21	4
64	9.50E+2	9.26E+0	3.30E-1	21	4
65	6.83E+2	9.59E+0	1.92E-2	21	4
66	6.70E+2	9.61E+0	1.97E-1	21	4
67	5.50E+2	9.81E+0	5.90E-1	21	4
68	3.05E+2	1.04E+1	6.78E-2	22	4
69	2.85E+2	1.05E+1	1.72E-1	22	4
70	2.40E+2	1.06E+1	1.34E-1	22	4
71	2.10E+2	1.08E+1	1.20E-2	22	4
72	2.08E+2	1.08E+1	7.50E-2	22	4
73	1.93E+2	1.09E+1	3.43E-2	22	4
74	1.86E+2	1.09E+1	4.22E-1	22	4
75	1.22E+2	1.13E+1	2.49E-2	23	5
76	1.19E+2	1.13E+1	3.42E-2	23	5
77	1.15E+2	1.14E+1	6.28E-2	23	5
78	1.08E+2	1.14E+1	7.70E-2	23	5
79	1.00E+2	1.15E+1	1.05E-1	23	5
80	9.00E+1	1.16E+1	9.31E-2	24	5
81	8.20E+1	1.17E+1	2.47E-2	24	5
82	8.00E+1	1.17E+1	5.13E-2	24	5
83	7.60E+1	1.18E+1	5.41E-2	24	5
84	7.20E+1	1.18E+1	6.45E-2	24	5
85	6.75E+1	1.19E+1	3.77E-2	24	5
86	6.50E+1	1.19E+1	6.35E-2	24	5
87	6.10E+1	1.20E+1	3.33E-2	24	5
88	5.90E+1	1.20E+1	9.97E-2	24	5
89	5.34E+1	1.21E+1	2.66E-2	24	5
90	5.20E+1	1.22E+1	2.73E-2	24	5
91	5.06E+1	1.22E+1	2.81E-2	24	5
92	4.92E+1	1.22E+1	1.85E-2	24	5
93	4.83E+1	1.22E+1	2.73E-2	24	5
94	4.70E+1	1.23E+1	3.91E-2	24	5
95	4.52E+1	1.23E+1	2.69E-2	24	5
96	4.40E+1	1.23E+1	3.70E-2	24	5
97	4.24E+1	1.24E+1	3.36E-2	24	5
98	4.10E+1	1.24E+1	3.47E-2	24	5
99	3.96E+1	1.24E+1	1.27E-2	24	5
100	3.91E+1	1.25E+1	2.85E-2	24	5
101	3.80E+1	1.25E+1	2.67E-2	24	5
102	3.70E+1	1.25E+1	4.14E-2	24	5
103	3.55E+1	1.25E+1	2.57E-2	24	5
104	3.46E+1	1.26E+1	2.49E-2	24	5
105	3.38E+1	1.26E+1	1.49E-2	24	5
106	3.33E+1	1.26E+1	4.62E-2	24	5
107	3.18E+1	1.27E+1	1.59E-2	24	5
108	3.13E+1	1.27E+1	4.08E-2	24	5
109	3.00E+1	1.27E+1	8.70E-2	24	5
110	2.75E+1	1.28E+1	9.53E-2	25	5
111	2.50E+1	1.29E+1	1.05E-1	25	5
112	2.25E+1	1.30E+1	6.90E-2	25	5
113	2.10E+1	1.31E+1	4.88E-2	25	5
114	2.00E+1	1.31E+1	5.13E-2	25	5
115	1.90E+1	1.32E+1	2.67E-2	25	5
116	1.85E+1	1.32E+1	8.46E-2	25	5
117	1.70E+1	1.33E+1	6.06E-2	25	5
118	1.60E+1	1.33E+1	5.79E-2	25	5
119	1.51E+1	1.34E+1	4.75E-2	25	5
120	1.44E+1	1.35E+1	4.62E-2	25	5
121	1.38E+1	1.35E+1	6.38E-2	25	5
122	1.29E+1	1.36E+1	8.07E-2	25	5
123	1.19E+1	1.36E+1	3.42E-2	25	5
124	1.15E+1	1.37E+1	1.40E-1	25	5

Table E.2. (continued)

Fine (218) group	Upper energy (eV)	Upper lethargy	Group flux	Broad (40) group	Broad (7) group
125	1.00E+1	1.38E+1	9.43E-2	25	5
126	9.10E+0	1.39E+1	1.16E-1	26	5
127	8.10E+0	1.40E+1	1.25E-1	26	5
128	7.15E+0	1.42E+1	2.12E-2	26	5
129	7.00E+0	1.42E+1	3.64E-2	26	5
130	6.75E+0	1.42E+1	3.77E-2	26	5
131	6.50E+0	1.42E+1	3.92E-2	26	5
132	6.25E+0	1.43E+1	4.08E-2	26	5
133	6.00E+0	1.43E+1	1.05E-1	26	5
134	5.40E+0	1.44E+1	7.70E-2	26	5
135	5.00E+0	1.45E+1	5.13E-2	26	5
136	4.75E+0	1 46E+1	1.72E-1	26	5
137	4.00E+0	1.47E+1	6.99E-2	26	5
138	3.73E+0	1.48E+1	6.36E-2	26	5
139	3.50E+0	1.49E+1	1.05E-1	26	5
140	3.15E+0	1.50E+1	3.23E-2	26	5
141	3.05E+0	1.50E+1	1.65E-2	26	5
142	3.00E+0	1.50E+1	1.01E-2	27	5
143	2.97E+0	1.50E+1	3.42E-2	27	5
144	2.87E+0	1.51E+1	3.55E-2	27	5
145	2.77E+0	1.51E+1	3.68E-2	27	5
146	2.67E+0	1.51E+1	3.82E-2	27	5
147	2.57E+0	1.52E+1	3.97E-2	27	5
148	2.47E+0	1.52E+1	3.71E-2	27	5
149	2.38E+0	1.53E+1	3.42E-2	27	5
150	2.30E+0	1.53E+1	3.99E-2	27	5
151	2.21E+0	1.53E+1	4.16E-2	27	5
152	2.12E+0	1.54E+1	5.83E-2	27	5
153	2.00E+0	1.54E+1	3.05E-2	27	5
154	1.94E+0	1.55E+1	4.21E-2	27	5
155	1.86E-0	1.55E+1	4.96E-2	28	6
156	1.77E+0	1.55E+1	5.22E-2	28	6
157	1.68E+0	1.56E+1	5.51E-2	29	6
158	1.59E+0	1.57E+1	5.83E-2	29	6
159	1.50E+0	1.57E+1	3.39E-2	29	6
160	1.45E+0	1.57E+1	3.51E-2	29	6
161	1.40E+0	1.58E+1	3.64E-2	29	6
162	1.35E+0	1.58E+1	3.77E-2	29	6
163	1.30E+0	1.59E+1	3.92E-2	29	6
164	1.25E+0	1.59E+1	2.02E-2	30	6
165	1.22E+0	1.59E+1	2.06E-2	30	6
166	1.20E+0	1.59E+1	2.11E-2	30	6
167	1.17E+0	1.60E+1	2.15E-2	30	6
168	1.15E+0	1.60E+1	8.73E-3	30	6
169	1.14E-0	1.60E+1	8.81E-3	30	6
170	1.13E+0	1.60E+1	8.89E-3	30	6
171	1.12E+0	1.60E+1	8.97E-3	31	6
172	1.11E+0	1.60E+1	9.05E-3	31	6
173	1.10E+0	1.60E+1	9.13E-3	31	6
174	1.09E+0	1.60E+1	9.22E-3	31	6
175	1.08E+0	1.60E+1	9.30E-3	31	6
176	1.07E+0	1.61E+1	9.39E-3	31	6
177	1.06E+0	1.61E+1	9.48E-3	31	6
178	1.05E+0	1.61E+1	9.57E-3	31	6
179	1.04E+0	1.61E+1	9.66E-3	31	6
180	1.03E+0	1.61E+1	9.76E-3	31	6
181	1.02E+0	1.61E+1	9.85E-3	31	6
182	1.01E+0	1.61E+1	9.95E-3	31	6
183	1.00E+0	1.61E+1	2.53E-2	31	6
184	9.75E-1	1.61E+1	2.60E-2	32	6
185	9.50E-1	1.62E+1	2.67E-2	32	6
186	9.25E-1	1.62E+1	2.74E-2	32	6

Table E.2. (continued)

Fine (218) group	Upper energy (eV)	Upper lethargy	Group flux	Broad (40) group	Broad (7) group
187	9.00E-1	1.62E+1	5.72E-2	32	6
188	8.50E-1	1.63E+1	6.06E-2	32	6
189	8.00E-1	1.63E+1	6.45E-2	32	6
190	7.50E-1	1.64E+1	6.90E-2	33	6
191	7.00E-1	1.65E+1	7.41E-2	33	6
192	6.50E-1	1.65E+1	8.00E-2	33	6
193	6.00E-1	1.66E+1	8.70E-2	33	6
194	5.50E-1	1.67E+1	9.53E-2	34	7
195	5.00E-1	1.68E+1	1.05E-1	34	7
196	4.50E-1	1.69E+1	1.18E-1	34	7
197	4.00E-1	1.70E+1	6.45E-2	34	7
198	3.75E-1	1.71E+1	6.90E-2	35	7
199	3.50E-1	1.72E+1	7.41E-2	35	7
200	3.25E-1	1.72E+1	8.00E-2	35	7
201	3.00E-1	1.73E+1	8.70E-2	36	7
202	2.75E-1	1.74E+1	9.53E-2	36	7
203	2.50E-1	1.75E+1	1.05E-1	36	7
204	2.25E-1	1.76E+1	1.18E-1	36	7
205	2.00E-1	1.77E+1	1.34E-1	37	7
206	1.75E-1	1.79E+1	1.54E-1	37	7
207	1.50E-1	1.80E+1	1.82E-1	37	7
208	1.25E-1	1.82E+1	3.11E-1	37	7
209	1.00E-1	1.84E+1	2.06E-1	37	7
210	9.00E-2	1.85E+1	2.74E-1	38	7
211	8.00E-2	1.86E+1	3.59E-1	38	7
212	7.00E-2	1.88E+1	4.62E-1	38	7
213	6.00E-2	1.89E+1	5.80E-1	38	7
214	5.00E-2	1.91E+1	7.04E-1	38	7
215	4.00E-2	1.93E+1	8.12E-1	39	7
216	3.00E-2	1.96E+1	4.04E-1	39	7
217	2.53E-2	1.98E+1	1.21E+0	40	7
218	1.00E-2	2.07E+1	3.59E-1	40	7
219	1.00E-5	2.76E+1		41	8

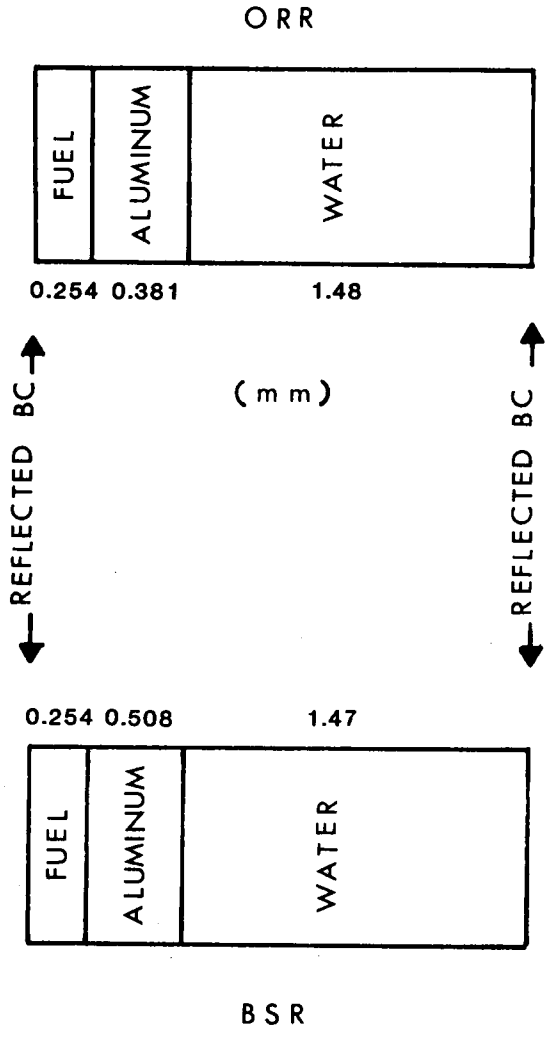


Fig. E.2. ORR fuel and BSR shim element models for the CSAS2 calculation sequence.

Table E.3. Material compositions for the ORR fuel and BSR shim element models

Component	Nuclide	ORR fuel element atoms/barn-cm	BSR shim element atoms/barn-cm
Fuel	^{235}U	1.70E-3	1.03E-3
	^{238}U	1.23E-4	7.65E-5
	Al	5.35E-2	4.71E-2
	O	4.85E-3	N/A[a]
Clad	Al	6.02E-2	6.02E-2
Moderator	H	6.68E-2	6.68E-2
	O	3.34E-2	3.34E-2

[a]Not applicable, that is, nuclide not present in material.

element was modeled as in the resonance self-shielding calculation. Whole BSR shim elements (with and without safety and regulating rods) were modeled as single cells because of asymmetry. Figure E.3 shows how the BSR shim elements were modeled and Table E.4 lists the material compositions.

5. Nuclide Collection

The cell weighting operation produced cell weighted cross section sets for the ORR fuel element, the BSR shim element without control rod, the shim element with a safety rod, and the shim element with a regulating rod. All these cross section sets were collected into a single cross section library with NITAWL (AMPX). In addition, the unweighted aluminum (for structural components) and the 1/v cross section sets were also merged into this composite cross section library. Number densities of the different homogenized regions are listed in Table E.5.

6. Zone Weighting

Zone weighting calculations were performed with XSDRNPM (AMPX, P3, S16) to produce zone dependent weighting functions for collapsing cross sections from 40 to 7 energy groups (group boundaries are listed in Table E.2). The reactor was modeled as shown in Fig. E.4. Table E.6 lists the fractions of each type of homogenized material included in each zone for 4 different core configurations. In addition, the 1/v cross section was included in each zone with a number density of 1.0×10^{-20} atoms/barn-cm. This was done so that the 1/v cross section will be collapsed to 7 energy groups and not affect the flux calculations.

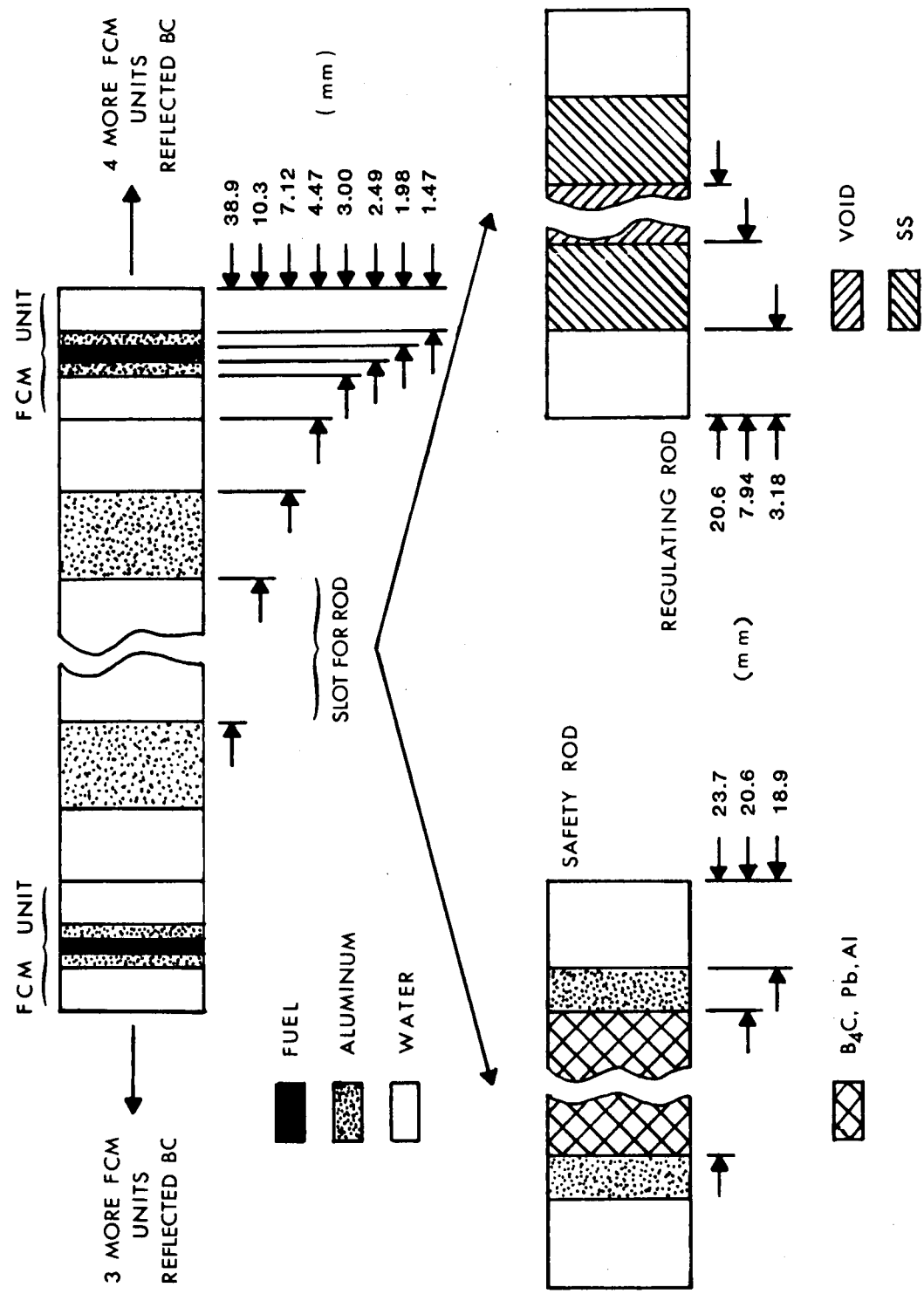


Fig. E.3. Model of the BSR shim element for the cell weighting calculations.

Table E.4. Material composition for the BSR shim element model with and without control rods

Component	Nuclide	atoms/barn-cm
Fuel	^{235}U	1.03E-3
	^{238}U	7.65E-5
	Al	4.71E-2
Clad	Al	6.02E-2
Moderator	H	6.68E-2
	O	3.34E-2
Safety Rod	^{10}B	1.31E-2
	^{11}B	5.66E-2
	C	1.74E-2
	Pb	6.56E-3
	Al	4.22E-3
Regulating Rod	C	3.20E-4
	Mn	1.75E-3
	P	6.98E-5
	S	4.50E-5
	Si	1.71E-3
	Cr	1.66E-2
	Ni	8.60E-3
	Fe	5.88E-2

Table E.5. Smeared number densities of the different homogenized regions (atoms/barn-cm)

Nuclide	ORR fuel element	BSR shim element w/o rod	BSR shim element with reg. rod	BSR shim element with saf. rod	BSR shim element with ^{252}Cf	Reflector	Reflector with detector	Reflector with auxiliary F. C.
^{235}U	1.68E-4	4.90E-5	4.90E-5	4.90E-5	6.70E-5	N/A[a]	N/A	N/A
^{238}U	1.22E-5	3.64E-6	3.64E-6	3.64E-6	4.98E-6	N/A	N/A	N/A
O	2.16E-2	1.92E-2	1.28E-2	1.28E-2	1.59E-2	3.34E-2	1.05E-2	1.88E-2
Al	1.62E-2	1.34E-2	1.34E-2	1.63E-2	1.63E-2	N/A	N/A	N/A
H	4.23E-2	3.84E-2	2.57E-2	2.57E-2	3.17E-2	6.68E-2	2.10E-2	3.75E-2
^{10}B	N/A	N/A	N/A	1.48E-3	N/A	N/A	N/A	N/A
^{11}B	N/A	N/A	N/A	6.38E-3	N/A	N/A	N/A	N/A
C	N/A	N/A	3.11E-5	1.96E-3	N/A	N/A	N/A	N/A
Pb	N/A	N/A	N/A	1.01E-3	N/A	N/A	N/A	N/A
Mn	N/A	N/A	1.70E-4	N/A	N/A	N/A	N/A	N/A
P	N/A	N/A	6.78E-6	N/A	N/A	N/A	N/A	N/A
S	N/A	N/A	4.37E-6	N/A	N/A	N/A	N/A	N/A
Si	N/A	N/A	1.66E-4	N/A	N/A	N/A	N/A	N/A
Cr	N/A	N/A	1.62E-3	N/A	N/A	N/A	N/A	N/A
Ni	N/A	N/A	8.35E-4	N/a	N/A	N/A	N/A	N/A
Fe	N/A	N/A	5.71E-3	N/A	N/A	N/A	N/A	N/A
Al[b]	5.16E-3	1.16E-2	1.16E-2	1.16E-2	1.16E-2	N/A	2.07E-2	7.18E-3

[a] Not applicable, that is, nuclide not present in material.

[b] Unweighted cross section for structural components.

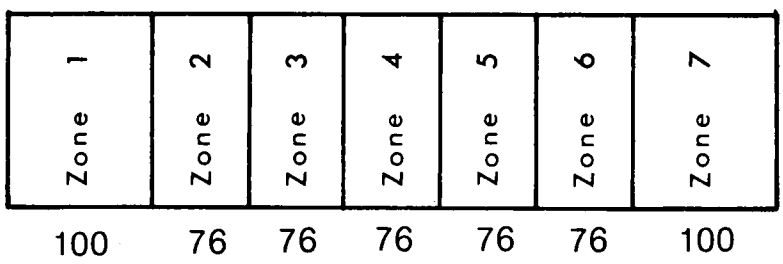


Fig. E.4. Reactor model for the zone weighting calculations.

Table E.6. Fractions of smeared number densities contained in each zone for the zone weighting calculations

Configuration	Zone	Reflector	ORR fuel element	BSR shim element w/o rod	BSR shim element with reg. rod	BSR shim element with saf. rod
Regulating	1	1				
Rod	2		1			
Inserted	3		1			
	4		1/3	2/3		
	5		2/3	1/3		
	6		1/3	1/3	1/3	
	7	1				
Outside	1	1				
Safety	2		1			
Rod	3		1			
Inserted	4		1/3	2/3		
	5		2/3	1/3		
	6		1/3	1/3		1/3
	7	1				
Inside	1	1				
Safety	2		1			
Rod	3		1			
Inserted	4		1/3	1/3		1/3
	5		2/3	1/3		
	6		1/3	2/3		
	7	1				
All	1	1				
Rods	2		1			
Inserted	3		1			
	4		1/3			2/3
	5		2/3	1/3		
	6		1/3		1/3	1/3
	7	1				

The 1/v cross sections were grouped into reflector and fuel regions and separately averaged. The averaged 1/v cross section sets are listed in Table E.7.

7. Format Conversions

CONTAC (AMPX) was used to convert the zone weighted cross sections from AMPX working library format to isotope-ordered CCCC ISOTXS format. This in turn was converted into a group-ordered GRUPXS format with the cross section processor module DCRSPR (VENTURE).

8. Buckling Calculations

Group and region dependent axial neutron leakage was calculated with KENO-IV[51] to determine buckling correction factors for the 2-dimensional, X-Y flux calculations. This type of calculation had been used successfully in the past.[52] The energy group structure of the reflector weights[53] available internally in KENO-IV to speed up calculations did not coincide with the energy group structure of the cross section set processed to this point. These weights were obtained using XSDRNPM (AMPX, P3, S16) following the prescription given by Knight and Petrie.[53] The reactor was modeled as a 190 mm slab of homogenized ORR fuel elements adjacent to a 330 mm slab of water. A reflected boundary condition was used at the fuel edge and vacuum at the water edge. These calculated weights are listed in Table E.8.

KENO-IV runs were performed for the all rods withdrawn, all rods inserted, and number 1 safety rod inserted cases. The reactor was modeled as shown in Fig. E.5. Calculated leakage cross sections (DB^2)

Table E.7. Averaged 1/v cross sections $(cm/sec)^{-1}$

Group	Reflector	Fuel
1	5.12E-10	5.24E-10
2	1.18E-09	1.17E-09
3	3.52E-09	3.51E-09
4	2.54E-08	2.48E-08
5	2.22E-07	2.18E-07
6	7.35E-07	7.33E-07
7	3.83E-06	3.40E-06

Table E.8. Reflector weights for KENO-IV

Distance from core face (mm)	Group 1	Group 2	Group 3	Group 4	Group 5	Group 6	Group 7
0 - 30	5.89E-1	6.30E-1	6.61E-1	6.85E-1	7.23E-1	7.76E-1	8.08E-1
30 - 60	9.01E-1	1.19E+0	1.44E+0	1.63E+0	1.94E+0	2.34E+0	2.52E+0
60 - 90	1.49E+0	2.64E+0	3.70E+0	4.48E+0	5.76E+0	7.27E+0	7.84E+0
90 - 120	2.60E+0	6.44E+0	1.05E+1	1.32E+1	1.77E+1	2.26E+1	2.44E+1
120 - 150	4.65E+0	1.68E+1	3.11E+1	4.02E+1	5.47E+1	7.05E+1	7.61E+1
150 - 180	8.44E+0	4.61E+1	9.46E+1	1.24E+2	1.70E+2	2.20E+2	2.37E+2
180 - 210	1.54E+1	1.30E+2	2.91E+2	3.85E+2	5.30E+2	6.84E+2	7.38E+2
210 - 240	2.80E+1	3.75E+2	9.04E+2	1.20E+3	1.65E+3	2.13E+3	2.30E+3
240 - 270	5.11E+1	1.10E+3	2.81E+3	3.73E+3	5.15E+3	6.65E+3	7.18E+3
270 - 300	9.37E+1	3.30E+3	8.90E+3	1.18E+4	1.64E+4	2.12E+4	2.29E+4
300 - 330	1.77E+2	1.06E+4	3.16E+4	4.31E+4	6.19E+4	8.48E+4	9.40E+4

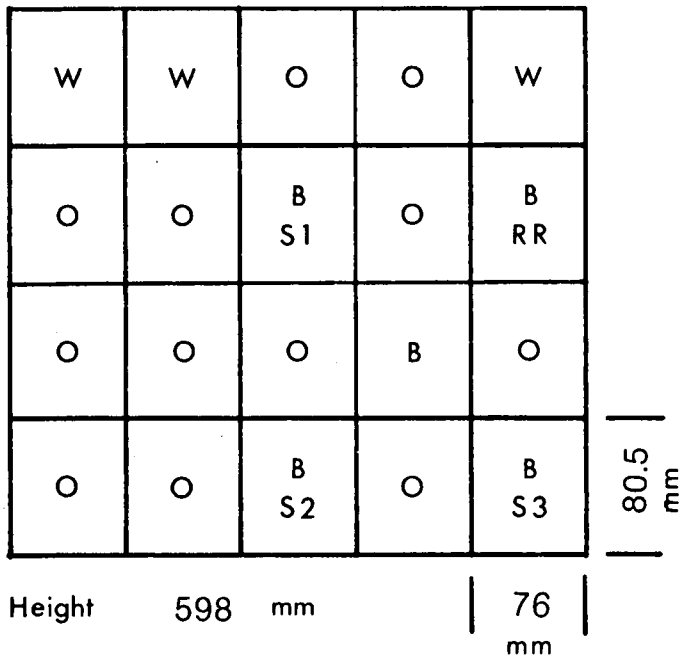


Fig. E.5. Reactor model for the KENO-IV calculations.

were averaged for ORR fuel elements, for BSR shim elements, and water. There were insufficient histories to give good leakage estimates for water; therefore, the geometric buckling was used for the reflector. These leakage cross sections are listed in Table E.9.

9. Forward and Adjoint Flux Calculations

Two-dimensional, X-Y, k-calculations were performed using VENTURE (diffusion) to obtain region and energy dependent forward and adjoint fluxes for the following cases:

1. regulating rod inserted,
2. number 3 safety rod and auxiliary fission chamber inserted,
3. number 2 safety rod and auxiliary fission chamber inserted,
4. number 1 safety rod and auxiliary fission chamber inserted, and
5. all rods and auxiliary fission chamber inserted.

In all cases, the reactor was modeled as shown in Fig. E.6. The calculated k-effectives are listed in Table E.10.

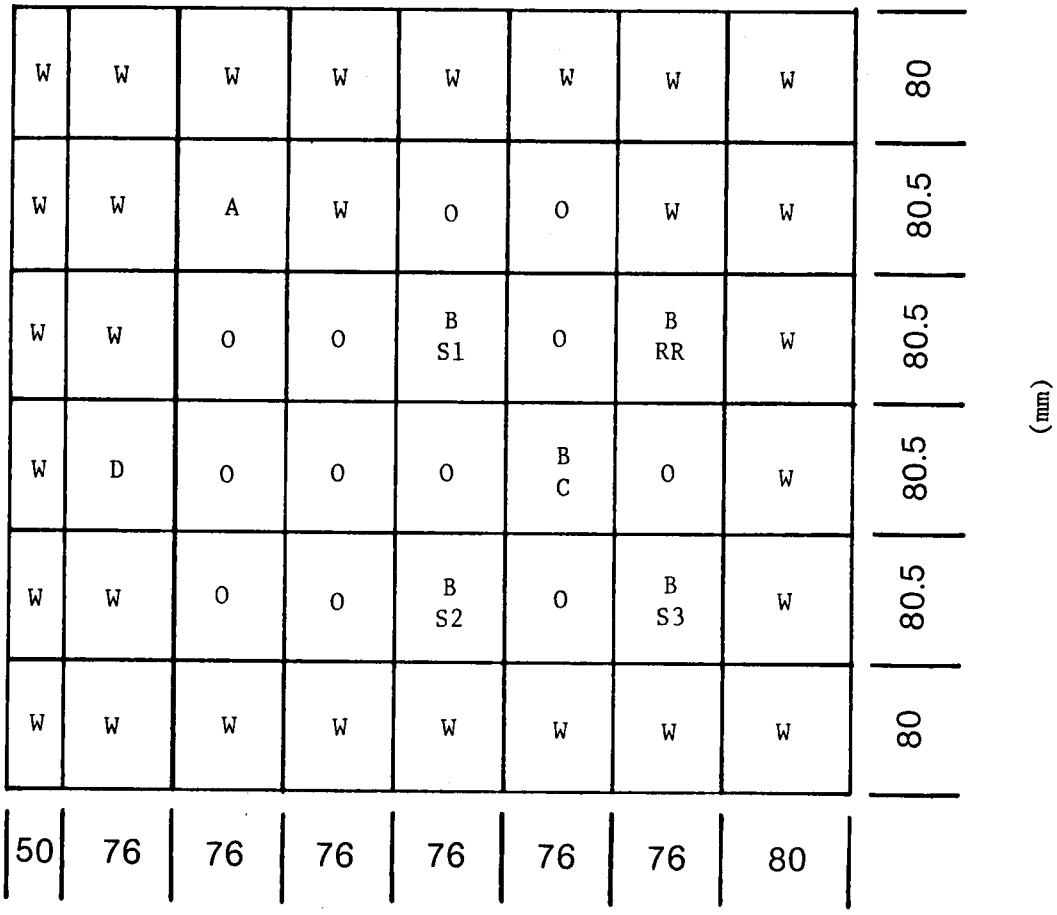
10. Verification Calculation

An adjoint calculation using the reactor model as shown in Fig. E.6 was performed for the case with all control rods and the auxiliary fission chamber inserted. ^{235}U fission cross sections were used as the adjoint source at the auxiliary fission chamber location. The ^{252}Cf fission neutron spectrum (origin of spectrum will be discussed later) was folded into the adjoint flux at various locations in and around the core. This produced auxiliary fission chamber count rates for various source locations. The ratios of the auxiliary fission chamber count

Table E.9. Axial leakage cross sections (DB^2) from KENO-IV $(cm)^{-1}$

Group	ORR fuel element	BSR shim element	Reflector
1	5.31E-3	4.98E-3	5.38E-3
2	3.68E-3	3.25E-3	3.28E-3
3	2.39E-3	2.11E-3	2.32E-3
4	1.75E-3	1.83E-3	1.74E-3
5	1.21E-3	1.53E-3	1.63E-3
6	1.20E-3	6.23E-4	1.54E-3
7	-1.41E-3	-8.23E-4	4.14E-4[a]

[a]Geometric buckling used because the KENO-IV calculation produced a statistically unreliable quantity.



W Water
O ORR Fuel Element
B BSR Shim Element
RR Regulating Rod
Sx Safety Rod
C Cf-252 Channel
D Detector Channel
A Auxiliary Fission Chamber

Fig. E.6. Reactor model for the 2-D, X-Y, diffusion, k-calculations.

Table E.10. Calculated K-effectives

Case number[a]	K-effective
1	1.012
2	1.007
3	0.990
4	0.974
5	0.930

[a]The following are inserted for each case:
1. regulating rod,
2. safety rod #3 and auxiliary fission chamber,
3. safety rod #2 and auxiliary fission chamber,
4. safety rod #1 and auxiliary fission chamber, and
5. all rods and auxiliary fission chamber.

rate with the source at core location E-5 to the count rates with the source at other locations around the reactor were calculated and compared to the measured ratios. This comparison is shown in Fig. E.7. The good agreement between the calculated and the measured ratios increases the confidence level of the accuracy of the cross section set and the reactor model used.

B. Calculation of Reactor Kinetics Parameters

The procedure for calculating some of the reactor kinetics parameters using the processed cross sections and calculated forward and adjoint fluxes will be discussed in the following sections.

1. Effective Delayed Neutron Fractions

In ref. 54, the effective neutron fraction is defined as

$$\beta_j = \frac{\sum_i V_i \sum_g \phi^*_{i,g} \chi'_{j,g} \sum_b N_{b,i} \sum_n \beta_{b,j,n} \sigma_{f,b,i,n} \phi_{i,n}}{\sum_i V_i \sum_g \phi^*_{i,g} \sum_b \chi_{b,g} N_{b,i} \sum_n \nu_{b,n} \sigma_{f,b,i,n} \phi_{i,n}} , \qquad \text{(E.1)}$$

where

β_j = effective group j delayed neutron fraction,

V_i = volume of mesh interval i,

$\phi_{i,g}$ = gth energy group forward flux in mesh interval i,

$\phi^*_{i,g}$ = gth energy group adjoint flux in mesh interval i,

$\chi'_{j,g}$ = fraction of delayed group j emitted in energy group g,

$N_{b,i}$ = number density of nuclide b in mesh interval i,

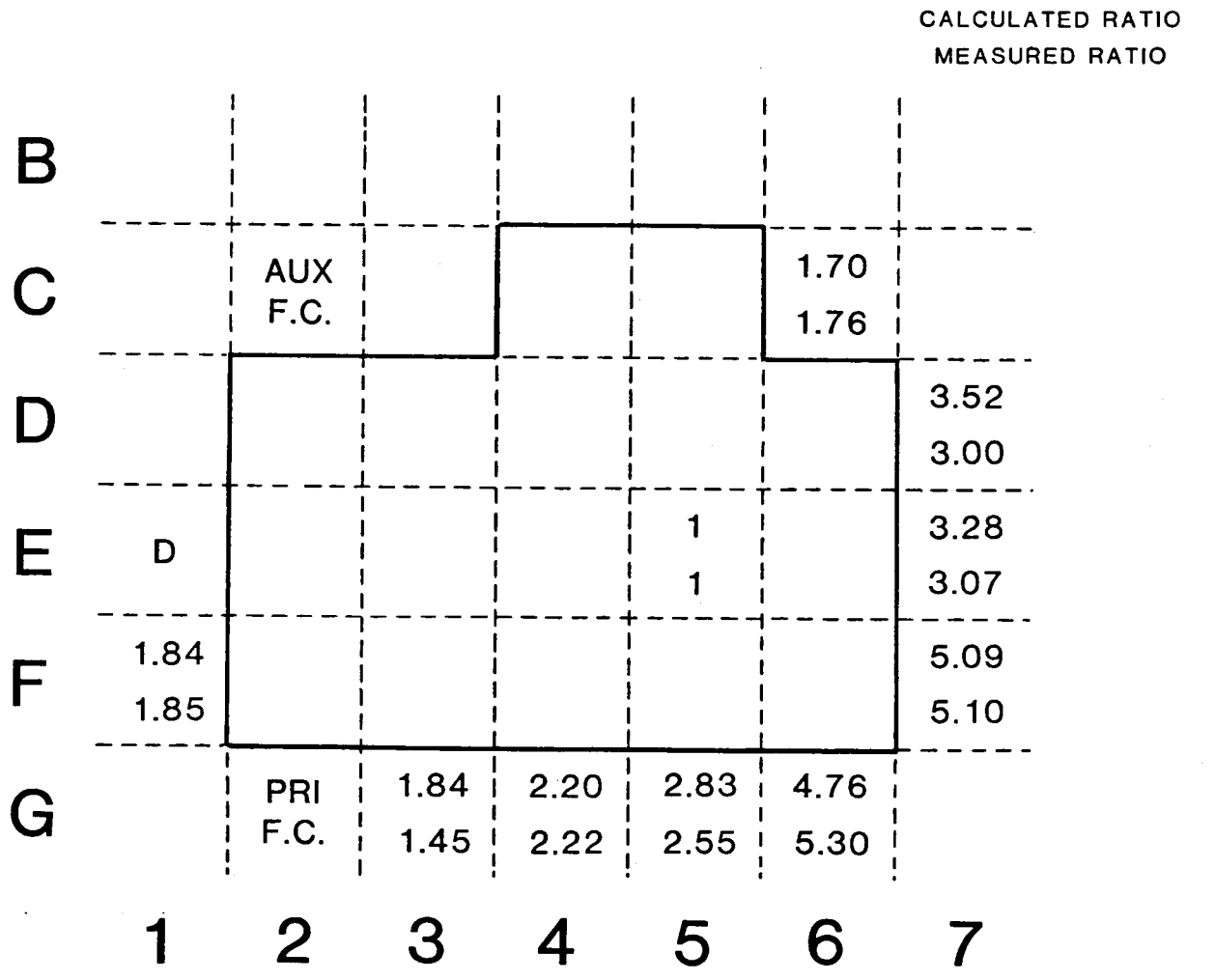


Fig. E.7. Comparison between the calculated and measured ratios of auxiliary fission chamber count rates with the ^{252}Cf source at core location E-5 to the count rates with the source at various locations around the core.

$\beta_{b,j,n}$ = group j delayed neutron fraction from fission of nuclide b, with neutrons from energy group n,

$\sigma_{f,b,i,n}$ = microscopic fission cross section of nuclide b, in mesh interval i, with neutrons from energy group n,

$\chi_{b,g}$ = fraction of fission neutrons from fission of nuclide b emitted in energy group g, and

$\nu_{b,n}$ = number of neutrons emitted from fission of nuclide b with neutrons from energy group n.

The delayed neutron fractions for thermal and fast fission of ^{235}U and fast fission of ^{238}U were taken from Keepin[55] and are listed in Table E.11. The energy spectrum of delayed neutrons were obtained from plots by Batchelor and Hyder[56] and are reproduced in Figs. E.8 thru E.12. These spectrums were numerically integrated into the 7 energy group structure of the neutron cross sections and are listed in Table E.12. The calculated effective delayed neutron fractions are listed in Table E.13.

2. Neutron Generation Time

In ref. 57, the neutron generation time is defined as

$$\Lambda = \frac{\sum_i V_i \sum_g \phi^*_{i,g} \frac{1}{v_{i,g}} \phi_{i,g}}{\sum_i V_i \sum_g \phi^*_{i,g} \sum_b \chi_{b,g} N_{b,i} \sum_n \nu_{b,n} \sigma_{f,b,i,n} \phi_{i,n}}, \qquad \text{(E.2)}$$

where $v_{i,g}$ is the average neutron velocity of energy group g at mesh interval i. The 1/v cross sections are listed in Table E.7. Calculated neutron generation times are listed in Table E.14.

Table E.11. Delayed fractions for ^{235}U and ^{238}U fissions[a]

Delayed Group	From ^{235}U thermal fission	From ^{235}U fast fission	From ^{238}U fast fission
1	2.15E-4	2.43E-4	1.92E-4
2	1.42E-3	1.36E-3	2.03E-3
3	1.27E-3	1.20E-3	2.40E-3
4	2.57E-3	2.61E-3	5.74E-3
5	7.48E-4	8.19E-4	3.33E-3
6	2.73E-4	1.66E-4	1.11E-3

[a]Taken from Keepin.[55]

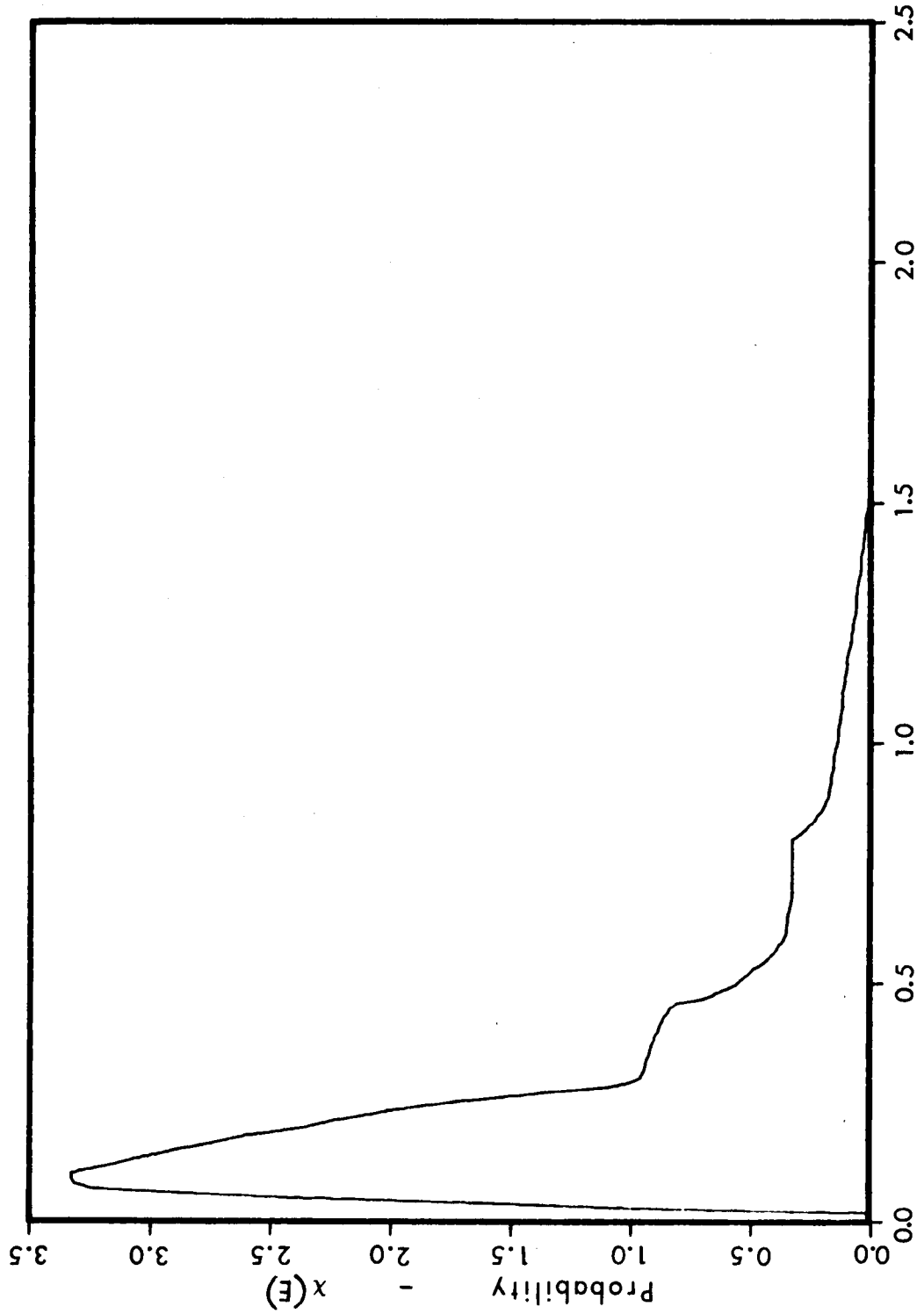


Fig. E.8. Energy spectrum of the group 1 delayed neutrons (ref. 56).

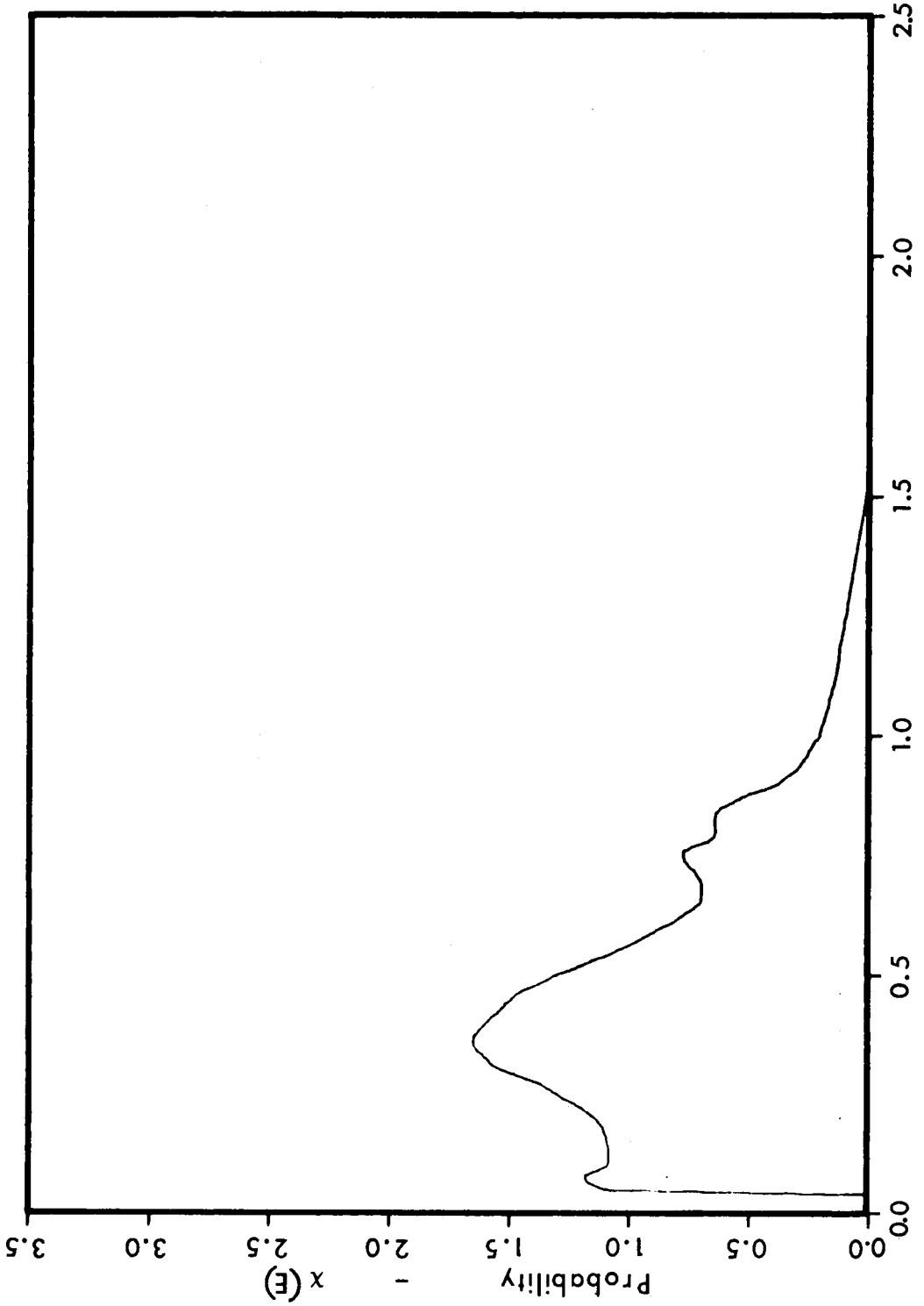


Fig. E.9. Energy spectrum of the group 2 delayed neutrons (ref. 56).

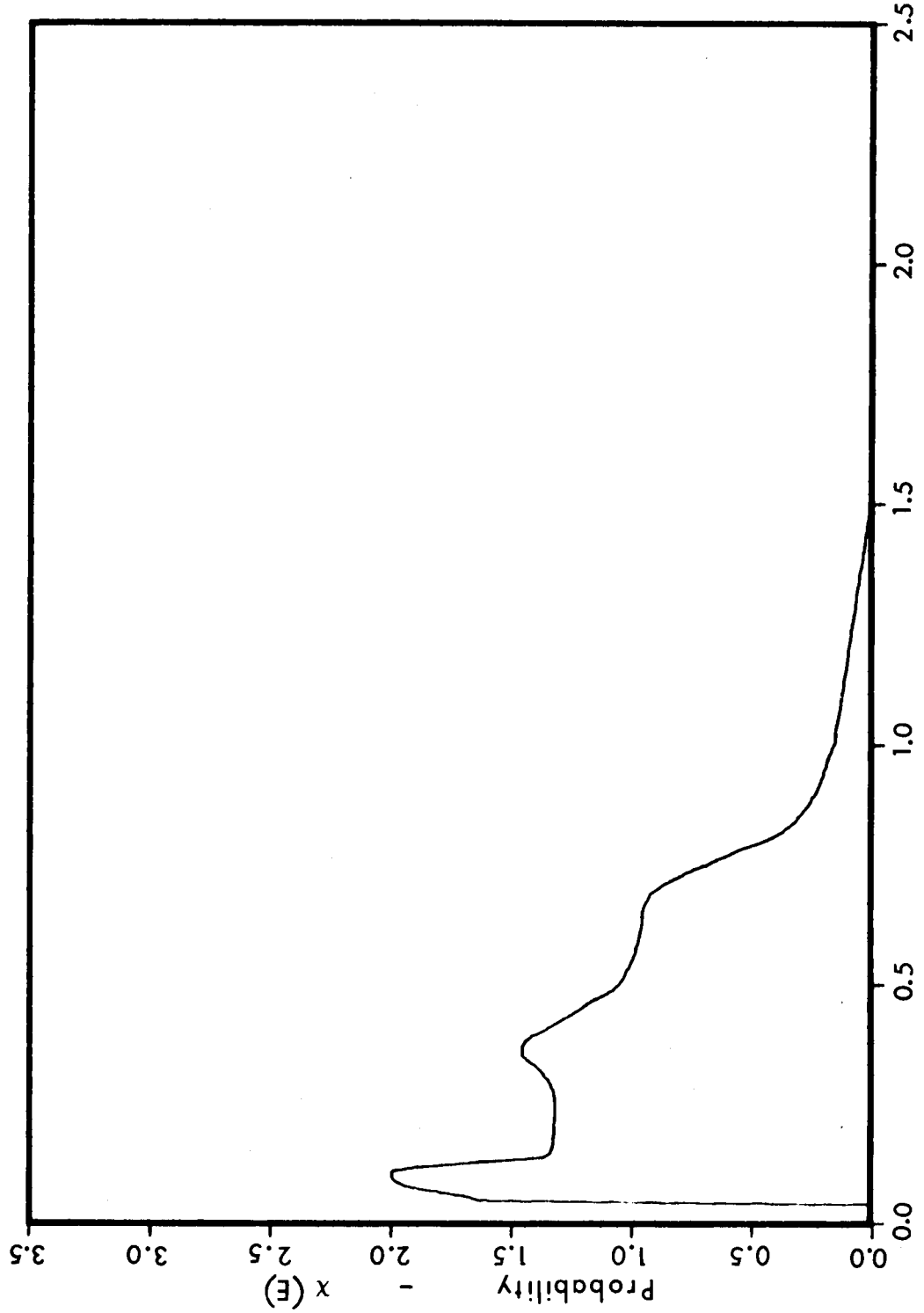


Fig. E.10. Energy spectrum of the group 3 delayed neutrons (ref. 56).

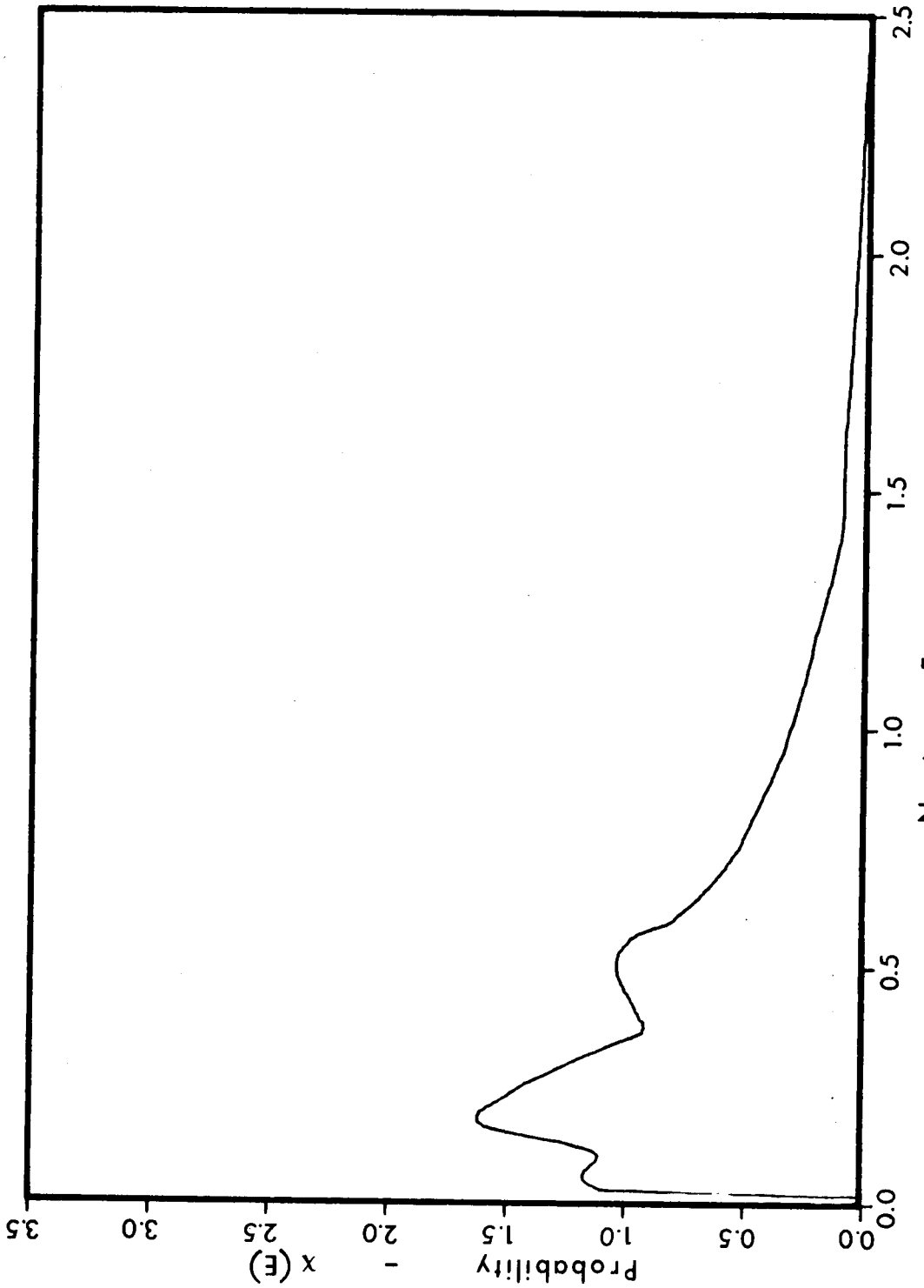


Fig. E.11. Energy spectrum of the group 4 delayed neutrons (ref. 56).

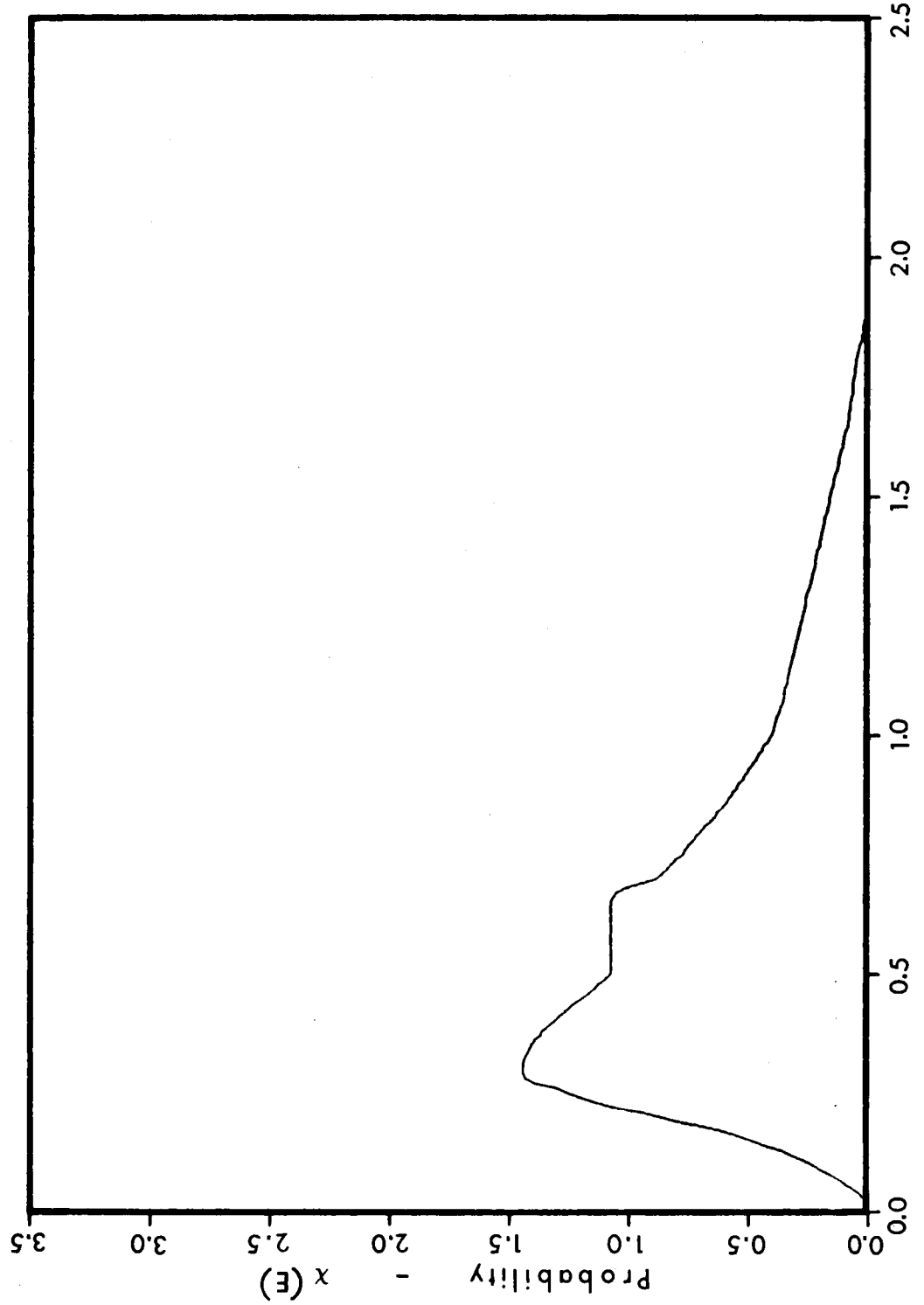


Fig. E.12. Energy spectrum of the groups 5 and 6 delayed neutrons (ref. 56).

Table E.12. Integrated delayed neutron energy spectrums

Delayed group	Energy group 1	Energy group 2	Energy group 3	Energy groups 4 to 7
1	6.86E-2	5.83E-1	3.48E-1	0.0
2	1.21E-1	7.64E-1	1.15E-1	0.0
3	8.09E-2	7.36E-1	1.83E-1	0.0
4	2.06E-1	6.48E-1	1.46E-1	0.0
5-6	2.56E-1	7.18E-1	2.60E-2	0.0

Table E.13. Calculated effective delayed neutron fractions

Delayed group	Case 1[a]	Case 2	Case 3	Case 4	Case 5
1	2.63E-4	2.63E-4	2.63E-4	2.63E-4	2.65E-4
2	1.66E-3	1.66E-3	1.66E-3	1.66E-3	1.67E-3
3	1.51E-3	1.51E-3	1.51E-3	1.51E-3	1.52E-3
4	2.96E-3	2.96E-3	2.96E-3	2.96E-3	2.98E-3
5	8.46E-4	8.46E-4	8.46E-4	8.46E-4	8.50E-4
6	2.99E-4	2.99E-4	2.99E-4	2.99E-4	3.00E-4
Total	7.53E-3	7.54E-3	7.54E-3	7.54E-3	7.58E-3

[a]The following are inserted for each case:
1. regulating rod,
2. safety rod #3 and auxiliary fission chamber,
3. safety rod #2 and auxiliary fission chamber,
4. safety rod #1 and auxiliary fission chamber, and
5. all rods and auxiliary fission chamber.

Table E.14. Some calculated reactor kinetics parameters

Case[a] number	Λ seconds	I	I_c center	I_c corner	$\bar{\nu}$	R
1	5.50E-5	6.60E-5[b]	9.47E-5[b]	5.11E-5[b]	2.42	1.15
2	5.53E-5	6.61E-5	9.32E-5	5.32E-5	2.42	1.15
3	5.59E-5	6.46E-5	9.29E-5	5.63E-5	2.42	1.15
4	5.67E-5	6.34E-5	9.31E-5	5.04E-5	2.42	1.14
5	5.58E-5	6.37E-5	8.49E-5	5.00E-5	2.42	1.15

[a]The following are inserted for each case:
1. regulating rod,
2. safety rod #3 and auxiliary fission chamber,
3. safety rod #2 and auxiliary fission chamber,
4. safety rod #1 and auxiliary fission chamber, and
5. all rods and auxiliary fission chamber.

[b]These are relative numbers. Absolute values depend on how the fluxes were normalized.

3. Average Reactor Fission Neutron Importance

Using the production density to weight the local importance of the reactor fission neutrons,[58] the average importance was obtained by

$$I = \frac{\sum_i V_i \sum_g \phi^*_{i,g} \sum_b \chi_{b,g} N_{b,i} \sum_n \nu_{b,n} \sigma_{f,b,i,n} \phi_{i,n}}{\sum_i V_i \sum_b N_{b,i} \sum_n \nu_{b,n} \sigma_{f,b,i,n} \phi_{i,n}} \quad . \tag{E.3}$$

Calculated average reactor fission neutron importance values are listed in Table E.14.

4. ^{252}Cf Fission Neutron Importance

The importance of ^{252}Cf fission neutrons was obtained by

$$I_c = \sum_g \chi_{c,g} \phi^*_{k,g} \quad , \tag{E.4}$$

where

$\chi_{c,g}$ = fraction of ^{252}Cf fission neutrons emitted in energy group g, and

$\phi^*_{k,g}$ = gth group adjoint flux at mesh interval k where the ^{252}Cf source was located.

An empirical function,[59] which described the energy spectrum of ^{252}Cf fission neutrons (Fig. E.13), was numerically integrated into the 7 energy group structure of the cross sections. This spectrum, together with the ^{235}U and ^{238}U fission neutron energy spectrums from the processed ENDF/B-IV cross section library are listed in Table E.15. The calculated importance values of ^{252}Cf fission neutrons for source positions E-5 and C-6 are listed in Table E.14.

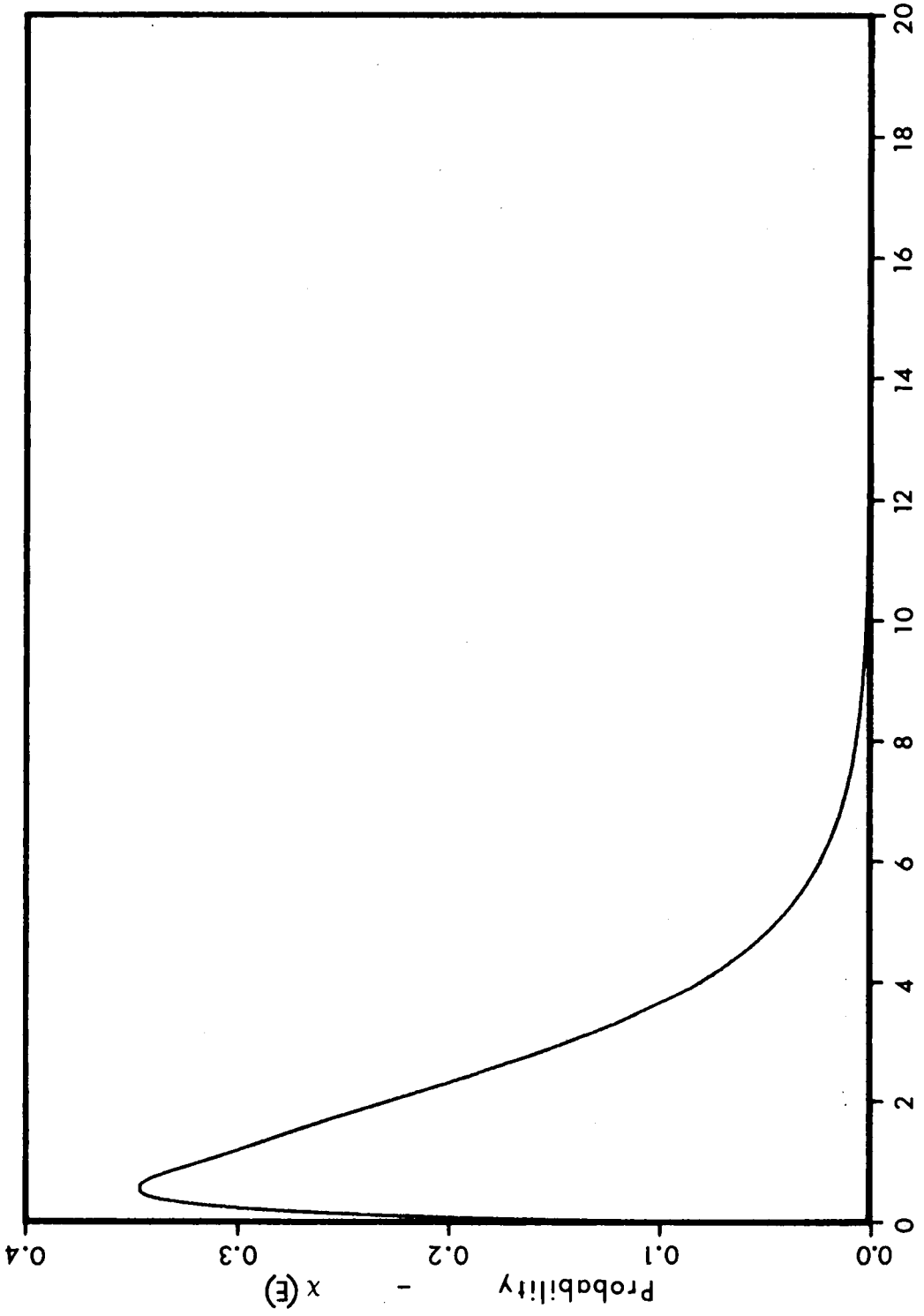


Fig. E.13. Energy spectrum of the ^{252}Cf fission neutrons (ref. 59).

Table E.15. Integrated energy spectrums of fission neutrons

Group	^{235}U	^{238}U	^{235}Cf
1	7.44E-01	7.51E-01	7.51E-01
2	2.30E-01	2.23E-01	2.21E-01
3	2.61E-02	2.52E-02	2.67E-02
4	7.27E-04	7.01E-04	7.49E-04
5	6.64E-07	6.41E-07	6.78E-07
6	1.05E-09	1.01E-09	1.07E-09
7	2.02E-10	1.94E-10	2.05E-10

5. Spatial Effects Correction Factor

In ref. 58, the spatial effects correction factor for point kinetics is defined as

$$R = \frac{\{\sum_i V_i \sum_b N_{b,i} \sum_g \sigma_{f,b,i,g}\phi_{i,g}\}\{\sum_i V_i \sum_b (\sum_g \chi_{b,g}\phi^*_{i,g})^2 N_{b,i} \sum_n \sigma_{f,b,i,n}\phi_{i,n}\}}{\{\sum_i V_i \sum_b N_{b,i} \sum_g \chi_{b,g}\phi^*_{i,g} \sum_n \sigma_{f,b,i,n}\phi_{i,n}\}^2} \quad . \tag{E.5}$$

Calculated spatial effects correction factors are listed in Table E.14.

6. Average Number of Neutrons per Fission

The average number of neutrons per fission is defined as

$$\bar{\nu} = \frac{\sum_i V_i \sum_b N_{b,i} \sum_g \nu_{b,g}\sigma_{f,b,i,g}\phi_{i,g}}{\sum_i V_i \sum_b N_{b,i} \sum_g \sigma_{f,b,i,g}\phi_{i,g}} \quad . \tag{E.6}$$

The average number of neutrons per fission for the different cases are listed in Table E.14.

7. Ratios of Detection Efficiencies

It was assumed that most of the reactions in the detectors were due to the thermal flux. Therefore, the ratio of detection efficiencies were taken to be the ratios of the thermal fluxes at the detector locations. These are listed in Table E.16.

C. Parameters Obtained from Open Literature

The value used for the average number of prompt neutrons per ^{252}Cf fission ($\bar{\nu}_c$) was 3.7224. This was the reevaluated weighted mean from

Table E.16. Ratios of detection efficiencies

Case[a] number	$\frac{W}{W_1}$ aux. F.C.	$\frac{W}{W_1}$ detector
1	-	1.00[b]
2	1.00[b]	1.01
3	1.03	1.02
4	1.01	1.09
5	1.20	1.27

[a]The following are inserted for each case:
1. regulating rod,
2. safety rod #3 and auxiliary fission chamber,
3. safety rod #2 and auxiliary fission chamber,
4. safety rod #1 and auxiliary fission chamber, and
5. all rods and auxiliary fission chamber.

[b]Used as reference.

DeVolpi,[60] 3.731, minus the number of delayed neutrons per fission from ref. 61, 0.0086. The value of $\overline{\nu_c^2}$, 15.541, was taken from Boldeman.[62]

The Diven factor (X), 0.795, was taken from ref. 63. This factor is a property of the fissioning material and is slightly influenced by the energy of the fission causing neutron.

The decay constants of the delayed neutron precursors were taken from Keepin[55] and are listed in Table E.17.

Table E.17. Delayed neutron precursor decay constants[a]

Group	Decay constant (sec^{-1})
1	0.0124
2	0.0305
3	0.111
4	0.301
5	1.14
6	3.01

[a]Taken from Keepin.[55]

APPENDIX F

TABULATION OF MEASURED QUANTITIES AND INFERRED REACTIVITIES

This appendix (Tables F.1 through F.18) is a tabulation of quantities measured to determine reactivity. These quantities include ratios of spectral densities, prompt neutron decay constants, fission chamber count rates, and low frequency coherence amplitudes. The reactivities inferred from these quantities are also listed in this appendix. Reactivities from rod calibrations, inverse kinetics rod drop measurements, and calculations are also included.

Table F.1. Run identification for spectral density measurements

Configuration number	Current mode Li	Pulse mode Li	^{3}He	Fission chamber
1	E 18-Apr-79			
2	D 18-Apr-79 R 24-Apr-79	F 18-Apr-79		
3	I 19-Apr-79		I 22-May-79	M 23-May-79
4	M 19-Apr-79	B 25-Apr-79 F 26-Apr-79[a]		N 23-May-79
5	J 19-Apr-79		H 22-May-79	K 22-May-79
6	K 19-Apr-79 P 23-Apr-79	G 26-Apr-79[a]	E 21-May-79	J 22-May-79
7	L 19-Apr-79 E 25-Apr-79	Q 23-Apr-79 I 28-Apr-79 H 26-Apr-79[a]	F 21-May-79	O 23-May-79
8	N 20-Apr-79 O 20-Apr-79	A 26-Apr-79		
9			G 21-May-79	L 22-May-79

[a] ^{252}Cf source moved from E-7 to C-6. Safety rod #3 moved to 47.8 cm to compensate for reactivity change.

Table F.2. Ratios of spectral densities, $G^*_{12}G_{13}/G_{11}G_{23}$

Configuration number	Current mode Li	Pulse mode Li	^{3}He	Fission chambers
1	2.51E-3 ±1.17E-3[a]			
2	7.08E-3 ±2.00E-3	7.58E-3 ±2.25E-3		
	6.64E-3[b] ±9.54E-4			
3	1.50E-2 ±3.35E-3		1.84E-2 ±2.67E-3	1.16E-2 ±2.39E-3
4	2.72E-2 ±2.90E-3	2.71E-2 ±3.67E-3		2.47E-2 ±3.35E-3
		1.60E-2[c] ±2.61E-3		
5	5.39E-2 ±9.10E-3		5.46E-2 ±3.27E-3	5.09E-2 ±1.03E-2
6	8.81E-2 ±3.17E-2	3.46E-2[c] ±7.64E-3	7.31E-2 ±5.11E-3	7.01E-2 ±1.18E-2
	7.56E-2 ±1.19E-2			
7	1.03E-1 ±2.96E-2	1.05E-1 ±1.36E-2	1.00E-1 ±4.77E-3	9.97E-2 ±8.85E-3
	1.07E-1 ±4.19E-2	1.06E-1 ±6.53E-3		
		5.72E-2[c] ±1.02E-2		
8	1.10E-1 ±3.96E-2	1.07E-1 ±1.52E-2		
	1.11E-1 ±4.36E-2			
9			1.05E-1 ±1.32E-3	1.02E-1 ±7.38E-3

[a] Error estimates are ±1 standard deviation.

[b] Multiple entries are repeat measurements.

[c] ^{252}Cf source located at core location C-6.

Table F.3. Reactivities (-$) from ratios of spectral densities

Configuration number	Current mode Li	Pulse mode Li	^{3}He	Fission chambers
1	1.39E-1 ±6.52E-2[a]			
2	3.94E-1 ±1.12E-1	4.22E-1 ±1.26E-1		
	3.70E-1[b] ±5.34E-2			
3	8.60E-1 ±1.94E-1		1.06E+0 ±1.56E-1	6.58E-1 ±1.37E-1
4	1.53E+0 ±1.68E-1	1.53E+0 ±2.13E-1		1.39E+0 ±1.93E-1
		1.48E+0[c] ±2.49E-1		
5	3.12E+0 ±5.56E-1		3.16E+0 ±2.00E-1	2.93E+0 ±6.25E-1
6	5.15E+0 ±2.02E+0	3.65E+0[c] ±8.57E-1	4.21E+0 ±3.16E-1	4.02E+0 ±7.27E-1
	4.36E+0 ±7.40E-1			
7	6.80E+0 ±2.19E+0	6.97E+0 ±1.01E+0	6.59E+0 ±3.51E-1	6.56E+0 ±6.50E-1
	7.13E+0 ±3.13E+0	7.02E+0 ±4.87E-1		
		6.38E+0[c] ±1.26E+0		
8	7.31E+0 ±2.98E+0	7.14E+0 ±1.14E+0		
	7.42E+0 ±3.29E+0			
9			6.93E+0 ±9.84E-2	6.75E+0 ±5.45E-1

[a] Error estimates are ±1 standard deviation.

[b] Multiple entries are repeat measurements.

[c] ^{252}Cf source located at core location C-6.

Table F.4. Prompt neutron decay constants (sec^{-1}) measured using Li detectors in the current mode

Configuration number	G_{22}	G_{33}	$\|G_{12}\|^2$	$\|G_{13}\|^2$	G_{23}	$-\omega \frac{G_{12R}}{G_{12I}}$	$-\omega \frac{G_{13R}}{G_{13R}}$
1	1.57E+2 ±3.65E-1[a]	1.57E+2 ±3.66E-1	1.46E+2 ±1.23E+1	1.57E+2 ±1.19E+1	1.56E+2 ±2.99E-1	2.05E+2 ±1.42E+2	1.83E+2 ±1.06E+2
2	1.92E+2 ±5.89E-1	1.93E+2 ±5.85E-1	1.74E+2 ±7.12E+0	1.87E+2 ±6.76E+0	1.92E+2 ±4.28E-1	1.79E+2 ±7.19E+1	1.81E+2 ±7.58E+1
	1.92E+2[b] ±3.35E-1	1.92E+2 ±3.25E-1	1.87E+2 ±3.29E+0	1.92E+2 ±3.13E+0	1.92E+2 ±4.28E-1	1.79E+2 ±2.32E+1	1.82E+2 ±3.17E+1
3	2.63E+2 ±1.16E+0	2.60E+2 ±1.63E+0	2.82E+2 ±9.60E+0	2.69E+2 ±8.71E+0	2.65E+2 ±7.03E-1	2.68E+2 ±9.09E+1	2.39E+2 ±6.88E+1
4	3.75E+2 ±2.48E+0	3.63E+2 ±2.58E+0	3.74E+2 ±5.65E+0	3.74E+2 ±4.58E+0	3.81E+2 ±8.91E-1	3.55E+2 ±4.86E+1	3.31E+2 ±4.21E+1
5	6.66E+2 ±3.23E+1	-	7.03E+2 ±2.67E+1	6.79E+2 ±2.47E+1	6.77E+2 ±1.30E+1	5.27E+2 ±1.80E+2	5.24E+2 ±1.72E+2
6	8.29E+2 ±1.66E+2	-	9.58E+2 ±6.17E+1	9.10E+2 ±5.71E+1	1.12E+3 ±5.36E+1	7.90E+2 ±2.80E+2	7.02E+2 ±5.30E+2
	-	-	8.68E+2 ±1.77E+1	8.48E+2 ±1.85E+1	9.77E+2 ±1.77E+1	8.49E+2 ±1.74E+2	7.60E+2 ±1.21E+2
7	-	-	1.62E+3 ±5.27E+1	1.63E+3 ±5.55E+1	2.13E+3 ±1.62E+2	1.35E+3 ±4.10E+2	1.31E+3 ±3.92E+2
	-	-	1.68E+3 ±4.80E+1	1.46E+3 ±4.46E+1	2.22E+3 ±1.98E+2	1.41E+3 ±3.76E+2	1.41E+3 ±2.66E+2
8	-	-	1.81E+3 ±6.60E+1	1.76E+3 ±6.43E+1	2.10E+3 ±1.39E+2	1.55E+3 ±4.27E+2	1.53E+3 ±5.65E+2
	-	-	1.80E+3 ±7.69E+1	2.10E+3 ±1.07E+2	2.43E+3 ±2.74E+2	1.68E+3 ±4.26E+2	1.83E+3 ±4.75E+2
9							

[a] Error estimates are ±1 standard deviation.

[b] Multiple entries are repeat measurements.

Table F.5. Prompt neutron decay constants (sec^{-1}) measured using Li detectors in the pulse mode

Configuration number	G_{22}	G_{33}	$\|G_{12}\|^2$	$\|G_{13}\|^2$	G_{23}	$-\omega \frac{G_{12R}}{G_{12I}}$	$-\omega \frac{G_{13R}}{G_{13I}}$
1							
2	1.92E+2 ±7.33E-1[a]	1.94E+2 ±6.19E-1	1.96E+2 ±7.58E+0	2.02E+2 ±8.46E+0	1.92E+2 ±5.11E-1	1.84E+2 ±7.01E+1	1.58E+2 ±6.10E+1
3							
4	3.79E+2 ±1.58E+0	3.80E+2 ±1.32E+0	3.67E+2 ±6.33E+0	3.56E+2 ±6.37E+0	3.73E+2 ±8.24E-1	3.35E+2 ±4.73E+1	3.45E+2 ±4.17E+1
	3.79E+2[b] ±1.91E+0	3.78E+2[b] ±1.86E+0	3.58E+2[b] ±8.54E+0	3.84E+2[b] ±9.01E+0	3.75E+2[b] ±1.05E+0	3.32E+2[b] ±6.46E+1	3.35E+2[b] ±7.38E+1
5							
6	8.07E+2[b] ±4.44E+1	9.20E+2[b] ±5.41E+1	8.41E+2[b] ±3.93E+1	9.09E+2[b] ±4.62E+1	9.61E+2[b] ±1.83E+1	6.97E+2[b] ±2.68E+2	7.69E+2[b] ±2.46E+2
7	1.07E+3 ±1.53E+2	1.21E+3 ±1.33E+2	1.65E+3 ±3.24E+1	1.54E+3 ±3.30E+1	1.65E+3 ±4.16E+1	1.39E+3 ±1.87E+2	1.47E+3 ±2.68E+2
	1.28E+3[c] ±1.35E+2	1.18E+3 ±1.27E+2	1.62E+3 ±1.99E+1	1.60E+3 ±1.85E+1	1.67E+3 ±1.44E+1	1.40E+3 ±1.26E+2	1.43E+3 ±1.99E+2
	-	-	1.65E+3[b] ±6.30E+1	1.41E+3[b] ±5.63E+1	1.64E+3[b] ±7.15E+1	1.20E+3[b] ±2.79E+2	1.09E+3[b] ±2.42E+2
8	-	-	1.97E+3 ±5.85E+1	1.69E+3 ±3.91E+1	1.86E+3 ±4.25E+1	1.75E+3 ±3.39E+2	1.59E+3 ±1.99E+2
9							

[a] Error estimates are ±1 standard deviation.

[b] ^{252}Cf source located at core location C-6.

[c] Multiple entries are repeat measurements.

Table F.6. Prompt neutron decay constants (sec^{-1}) measured using ^{3}He detectors

Configuration number	G_{22}	G_{33}	$\lvert G_{12}\rvert^2$	$\lvert G_{13}\rvert^2$	G_{23}	$-\omega \frac{G_{12R}}{G_{13I}}$	$-\omega \frac{G_{13R}}{G_{13I}}$
1							
2							
3	3.09E+2 ±1.36E+0[a]	3.12E+2 ±1.27E+0	2.89E+2 ±6.37E+0	2.96E+2 ±6.65E+0	3.06E+2 ±8.90E-1	2.90E+2 ±6.16E+1	2.86E+2 ±6.07E+1
4							
5	6.88E+2 ±2.33E+0	6.96E+2 ±2.16E+0	6.43E+2 ±8.29E+0	6.56E+2 ±7.65E+0	7.15E+2 ±2.17E+0	5.81E+2 ±4.93E+1	5.93E+2 ±6.68E+1
6	1.00E+3 ±7.63E+0	1.01E+3 ±6.46E+0	9.26E+2 ±1.42E+1	9.63E+2 ±1.60E+1	1.06E+3 ±3.99E+0	8.32E+2 ±1.07E+2	8.22E+2 ±1.31E+2
7	1.94E+3 ±1.75E+1	2.07E+3 ±2.42E+1	1.65E+3 ±2.32E+1	1.64E+3 ±2.50E+1	2.11E+3 ±8.65E+0	1.47E+3 ±1.65E+2	1.40E+3 ±2.32E+2
8							
9	2.52E+3 ±1.60E+1	2.78E+3 ±3.29E+1	2.10E+3 ±1.18E+1	2.14E+3 ±1.38E+1	2.67E+3 ±4.58E+0	1.83E+3 ±2.30E+2	1.76E+3 ±1.54E+2

[a]Error estimates are ±1 standard deviation.

Table F.7. Prompt neutron decay constants (sec^{-1}) measured using fission chambers

Configuration number	G_{22}	G_{33}	$\lvert G_{12}\rvert^2$	$\lvert G_{13}\rvert^2$	G_{23}	$-\omega \frac{G_{12R}}{G_{12I}}$	$-\omega \frac{G_{13I}}{G_{13I}}$
1							
2							
3	2.33E+2 ±1.17E+0[a]	2.37E+2 ±9.74E-1	2.20E+2 ±7.28E+0	2.42E+2 ±8.04E+0	2.30E+2 ±6.12E-1	2.42E+2 ±8.19E+1	2.48E+2 ±7.08E+1
4	3.52E+2 ±3.70E+0	3.61E+2 ±2.68E+0	3.32E+2 ±7.89E+0	3.23E+2 ±8.19E+0	3.44E+2 ±1.56E+0	3.32E+2 ±8.67E+1	3.25E+2 ±6.87E+1
5	6.42E+2 ±1.64E+1	6.28E+2 ±1.14E+1	5.61E+2 ±1.52E+1	6.07E+2 ±1.53E+1	5.91E+2 ±7.18E+0	4.52E+2 ±1.17E+2	5.99E+2 ±7.50E+1
6	9.73E+2 ±3.81E+1	9.24E+2 ±3.15E+1	8.58E+2 ±3.12E+1	9.02E+2 ±2.93E+1	8.46E+2 ±1.47E+1	6.07E+2 ±1.04E+2	6.65E+2 ±1.09E+2
7	2.11E+3 ±8.69E+1	1.74E+3 ±4.82E+1	1.45E+3 ±1.79E+1	1.39E+3 ±1.64E+1	1.38E+3 ±1.70E+1	1.24E+3 ±1.27E+2	1.17E+3 ±2.01E+2
8							
9	2.51E+3 ±1.32E+2	1.92E+3 ±6.70E+1	1.84E+3 ±2.61E+1	1.69E+3 ±2.06E+1	1.69E+3 ±3.31E+1	1.40E+3 ±1.72E+2	1.38E+3 ±1.93E+2

[a] Error estimates are ±1 standard deviation.

Table F.8. Reactivities (-$) from α measured using Li detectors in the current mode

Configuration number	G_{22}	G_{33}	$\lvert G_{12}\rvert^2$	$\lvert G_{13}\rvert^2$	G_{23}	$-\omega \frac{G_{12R}}{G_{12I}}$	$-\omega \frac{G_{13I}}{G_{13I}}$
1	1.44E-1 ±3.33E-3[a]	1.50E-1 ±3.31E-3	9.35E-2 ±9.44E-2	1.50E-1 ±8.90E-2	1.44E-1 ±3.36E-3	5.42E-1 ±1.07E+0	3.37E-1 ±7.79E-1
2	-	-	-	-	-	-	-
	4.04E-1[b,c] ±0.00E+0	±4.04E-1[b] ±0.00E+0	4.04E-1[b] ±0.00E+0	4.04E-1[b] ±0.00E+0	4.04E-1[b] ±0.00E+0	4.04E-1[b] ±0.00E+0	4.04E-1[b] ±0.00E+0
3	9.25E-1 ±9.13E-3	9.07E-1 ±1.24E-2	1.12E+0 ±8.12E-2	9.69E-1 ±7.15E-2	9.45E-1 ±6.73E-3	1.02E+0 ±6.85E-1	7.48E-1 ±5.05E-1
4	1.72E+0 ±1.86E-2	1.64E+0 ±1.93E-2	1.79E+0 ±6.48E-2	1.72E+0 ±5.56E-2	1.77E+0 ±8.96E-3	1.65E+0 ±3.66E-1	1.41E+0 ±3.09E-1
5	3.84E+0 ±2.35E-1	-	4.25E+0 ±2.20E-1	3.94E+0 ±1.97E-1	3.93E+0 ±9.55E-2	2.94E+0 ±1.34E+0	2.81E+0 ±1.25E+0
6	5.00E+0 ±1.20E+0	- -	6.13E+0 ±4.76E-1	5.61E+0 ±4.28E-1	7.12E+0 ±3.89E-1	4.82E+0 ±2.09E+0	4.09E+0 ±3.85E+0
	-	-	5.46E+0 ±1.74E-1	5.16E+0 ±1.68E-1	6.09E+0 ±1.30E-1	5.32E+0 ±1.30E+0	4.51E+0 ±8.85E-1
7	-	-	1.03E+1 ±4.17E-1	1.01E+1 ±4.18E-1	1.35E+1 ±1.10E+0	8.42E+0 ±2.86E+0	7.88E+0 ±2.67E+0
	-	-	1.07E+1 ±3.93E-1	8.89E+0 ±3.43E-1	1.41E+1 ±1.34E+0	9.38E+0 ±2.63E+0	8.60E+0 ±1.82E+0
8	-	-	1.16E+1 ±5.11E+1	1.09E+1 ±4.78E-1	1.33E+1 ±9.45E-1	9.83E+0 ±2.98E+0	9.41E+0 ±3.84E+0
	-	-	1.15E+1 ±5.80E-1	1.33E+1 ±7.60E-1	1.55E+1 ±1.86E+0	1.07E+1 ±2.98E+0	1.15E+1 ±3.23E+0
9							

[a] Error estimates are ±1 standard deviation.

[b] Used as calibration measurement. Reactivity obtained from rod calibration.

[c] Multiple entries are repeat measurements.

Table F.9. Reactivities (-$) from α measured using Li detectors in the pulse mode

Configuration number	G_{22}	G_{33}	$\lvert G_{12}\rvert^2$	$\lvert G_{13}\rvert^2$	G_{23}	$-\omega \frac{G_{12R}}{G_{13I}}$	$-\omega \frac{G_{13R}}{G_{13I}}$
1							
2	4.04E-1[a] ±0.00E+0[b]	4.04E-1[a] ±0.00E+0	4.04E-1[a] ±0.00E+0	4.04E-1[a] ±0.00E+0	4.04E-1[a] ±0.00E+0	4.04E-1[a] ±0.00E+0	4.04E-1[a] ±0.00E+0
3							
4	1.76E+0 ±1.24E-1	1.77E+0 ±1.07E-2	1.62E+0 ±1.11E-1	1.47E+0 ±1.13E-1	1.71E+0 ±9.35E-3	1.39E+0 ±3.50E-1	1.39E+0 ±3.06E-1
	1.75E+0[c] ±1.47E-1	±1.76E+0[c] ±1.43E-2	1.56E+0[c] ±1.16E-1	1.66E+0[c] ±1.28E-1	1.72E+0[c] ±1.05E-2	1.37E+0[c] ±4.70E-1	1.32E+0[c] ±5.21E-1
5							
6	4.84E+0[c] ±3.21E-1	5.68E+0[c] ±3.93E-1	4.98E+0[c] ±3.63E-1	5.28E+0[c] ±4.14E-1	5.95E+0[c] ±1.34E-1	3.96E+0[c] ±1.92E+0	4.31E+0[c] ±1.71E+0
7	6.26E+0 ±1.04E+0	7.20E+0 ±9.02E-1	9.99E+0 ±4.77E-1	8.97E+0 ±4.69E-1	1.01E+1 ±2.83E-1	8.24E+0 ±1.29E+0	8.50E+0 ±1.78E+0
	7.69E+0[d] ±9.13E-1	7.04E+0[d] ±8.64E-1	9.78E+0[d] ±4.37E-1	9.32E+0[d] ±4.49E-1	1.03E+1[d] ±1.02E-1	8.27E+0[d] ±9.10E-1	8.27E+0[d] ±1.34E+0
	-	-	9.98E+0[c] ±5.97E-1	8.11E+0[c] ±5.27E-1	1.01E+1[c] ±4.85E-1	6.99E+0[c] ±1.88E+0	6.07E+0[c] ±1.59E+0
8	-	-	1.21E+1 ±6.40E-1	9.90E+0 ±4.95E-1	1.16E+1 ±2.90E-1	1.06E+1 ±2.30E+0	9.30E+0 ±1.36E+0
9							

[a] Used as calibration measurement. Reactivity obtained from rod calibration.

[b] Error estimates are ±1 standard deviation.

[c] ^{252}Cf source located at core location C-6.

[d] Multiple entries are repeat measurements.

Table F.10. Reactivities (-$) from α measured using ^{3}He detectors

Configuration number	G_{22}	G_{33}	$\lvert G_{12}\rvert^2$	$\lvert G_{13}\rvert^2$	G_{23}	$-\omega \frac{G_{12R}}{G_{12I}}$	$-\omega \frac{G_{13R}}{G_{13I}}$
1							
2							
3	1.26E+0 ±1.11E-2[a]	1.28E+0 ±1.06E-2	1.11E+0 ±4.69E-2	1.17E+0 ±4.89E-2	1.24E+0 ±8.21E-3	1.12E+0 ±4.51E-1	1.09E+0 ±4.44E-1
4							
5	4.01E+0 ±2.03E-2	4.07E+0 ±1.94E-2	3.68E+0 ±6.13E-2	3.78E+0 ±5.67E-2	4.21E+0 ±1.96E-2	3.23E+0 ±3.59E-1	3.32E+0 ±4.86E-1
6	6.27E+0 ±5.77E-2	6.34E+0 ±4.96E-2	5.71E+0 ±1.04E-1	5.99E+0 ±1.17E-1	6.66E+0 ±3.36E-2	5.04E+0 ±7.79E-1	4.97E+0 ±9.48E-1
7	1.22E+1 ±1.22E-1	1.31E+1 ±1.67E-1	1.02E+1 ±1.60E-1	1.01E+1 ±1.72E-1	1.33E+1 ±6.68E-2	9.00E+0 ±1.12E+0	8.53E+0 ±1.58E+0
8							
9	1.61E+1 ±1.15E-1	1.79E+1 ±2.27E-1	1.33E+1 ±8.62E-2	1.35E+1 ±9.93E-2	1.71E+1 ±5.10E-2	1.14E+1 ±1.56E+0	1.10E+1 ±1.04E+0

[a] Error estimates are ±1 standard deviation.

Note: The reference measurement used to interpret the CPSD23 results using Li detectors in the current mode was used to interpret these ^{3}He results.

Table F.11. Reactivities (-$) from α measured using fission chambers

Configuration number	G_{22}	G_{33}	$\lvert G_{12}\rvert^2$	$\lvert G_{13}\rvert^2$	G_{23}	$-\omega \frac{G_{12R}}{G_{12I}}$	$-\omega \frac{G_{13R}}{G_{13I}}$
1							
2							
3	7.03E-1 ±9.36E-3[a]	7.34E-1 ±8.11E-3	6.08E-1 ±5.34E-2	7.71E-1 ±5.90E-2	6.84E-1 ±5.85E-3	7.74E-1 ±6.00E-1	8.14E-1 ±5.18E-1
4	1.56E+0 ±2.75E-2	1.63E+0 ±2.04E-2	1.41E+0 ±5.77E-2	1.35E+0 ±5.98E-2	1.51E+0 ±1.27E-2	1.41E+0 ±6.31E-1	1.36E+0 ±5.00E-1
5	3.67E+0 ±1.20E-1	3.57E+0 ±8.34E-2	3.09E+0 ±1.11E-1	3.42E+0 ±1.12E-1	3.30E+2 ±5.32E-2	2.29E+0 ±8.49E-1	3.36E+0 ±5.47E-1
6	6.06E+0 ±2.77E-1	5.70E+0 ±2.29E-1	5.23E+0 ±2.27E-1	5.55E+0 ±2.13E-1	5.14E+0 ±1.07E-1	3.40E+0 ±7.53E-1	3.83E+0 ±7.90E-1
7	1.33E+1 ±5.91E-1	1.08E+1 ±3.28E-1	8.86E+0 ±1.23E-1	8.42E+0 ±1.13E-1	8.37E+0 ±1.17E-1	7.41E+0 ±8.62E-1	6.91E+0 ±1.37E+0
8							
9	1.60E+1 ±8.99E-1	1.20E+1 ±4.56E-1	1.15E+1 ±1.79E-1	1.05E+1 ±1.42E-1	1.04E+1 ±2.26E-1	8.54E+0 ±1.17E+0	8.35E+0 ±1.31E+0

[a]Error estimates are ±1 standard deviation.

Note: The reference measurement used to interpret the CPSD23 results using Li detectors in the current mode was used to interpret these fission chamber results.

Table F.12. Primary fission chamber count rates

Configuration number	Count rates in counts per second for noise measurements using			
	Current mode Li	Pulse mode Li	^{3}He	Fission chambers
1	1.79E+0 ±2.12E-2[a]			
2	-	-		
	7.42E-1[b] ±8.46E-3			
3	2.33E-1 ±7.64E-3		2.05E-1 ±1.01E-3	3.80E-1 ±8.72E-3
4	1.08E-1 ±5.20E-3	1.28E-1 ±8.00E-3		1.47E-1 ±5.43E-3
		6.10E-2[c] ±5.52E-3		
5	5.77E-2 ±4.38E-3		5.35E-2 ±5.17E-3	6.25E-2 ±5.59E-3
6	-	1.68E-2[c] ±2.05E-3	3.35E-2 ±4.09E-3	4.20E-2 ±4.58E-3
	4.07E-2 ±1.71E-3			
7	-	1.69E-2 ±5.81E-4	1.30E-2 ±2.55E-3	1.94E-2 ±6.23E-3
	1.61E-2 ±5.67E-4	1.37E-2 ±1.17E-3		
		1.00E-2[c] ±4.48E-4		
8	-	1.76E-2 ±5.93E-4		
	1.31E-2 ±4.33E-4			
9			1.03E-2 ±4.55E-4	1.18E-2 4.86E-4

[a] Error estimates are ±1 standard deviation.

[b] Multiple entries are repeat measurements.

[c] ^{252}Cf source located at core location C-6.

Table F.13. Auxiliary fission chamber count rates

Configuration number	Count rates in counts per second for noise measurements using			
	Current mode li	Pulse mode Li	^{3}He	Fission chambers
1	-			
2	-	-		
	-			
3	-		8.51E+1 ±2.06E-1[a]	1.35E+2 ±1.64E-1
4	4.17E+1 ±1.02E-1	4.18E+1 ±1.45E-1		6.26E+1 ±1.12E-1
		2.33E+1[b] ±1.08E-1		
5	1.93E+1 ±8.01E-2		2.45E+1 ±1.11E-1	2.75E+1 ±1.17E-1
6	-	5.29E+0[b] ±3.64E-2	1.36E+1 ±8.25E-2	1.49E+1 ±8.62E-2
	1.06E+1[c] ±2.75E-2			
7	-	4.79E+0 ±9.79E-3	6.36E+0 ±5.64E-2	6.67E+0 ±1.16E-2
	4.85E+0 ±9.85E-3	4.88E+0 ±2.21E-2		
		2.78E+0[b] ±7.46E-3		
8	-	3.84E+0 ±8.77E-3		
	3.89E+0 ±7.46E-3			
9			3.78E+0 ±8.70E-3	3.87E+0 ±8.80E-3

[a] Error estimates are ±1 standard deviation.

[b] ^{252}Cf source located at core location C-6.

[c] Multiple entries are repeat measurements.

Table F.14. Reactivities (-$) from primary fission chamber count rates by the source multiplication technique

Configuration number	Current mode Li	Pulse mode Li	^{3}He	Fission chambers
1	1.67E-1 ±2.70E-3[a]			
2	-	-		
	4.04E-1[b,c] ±0.00E+0			
3	1.24E+0 ±4.31E-2		1.41E+0 ±1.81E-2	7.60E-1 ±1.96E-2
4	2.67E+0 ±1.32E-1	2.26E+0 ±1.44E-1		1.96E+0 ±7.60E-2
		-		
5	5.01E+0 ±3.85E-1		5.40E+0 ±5.26E-1	4.62E+0 ±4.17E-1
6	-	-	8.62E+0 ±1.06E+0	6.88E+0 ±7.55E-1
	7.10E+0 ±3.09E-1			
7	-	1.71E+1 ±6.24E-1	2.22E+1 ±4.37E+0	1.49E+1 ±4.79E+0
	1.79E+1 ±6.67E-1	1.65E+1 ±1.82E+0		
		-		
8	-	1.65E+1 ±5.88E-1		
	2.20E+1 ±7.71E-1			
9			2.79E+1 ±1.27E+0	2.45E+1 ±9.95E-1

[a] Error estimates are ±1 standard deviation.

[b] Used as calibration measurement. Reactivity obtained from rod calibration.

[c] Multiple entries are repeat measurements.

Note: Reactivities were not corrected for detection efficiency changes.

Table F.15. Reactivities (-$) from auxiliary chamber count rates by the modified source multiplication technique

Configuration number	Current mode Li	Pulse mode Li	^{3}He	Fission chambers
1	-			
2	-	-		
	-			
3	-		1.24E+0[a] ±0.00E+0[b]	7.82E-1 ±2.12E-3
4	2.61E+0 ±8.71E-3	2.61E+0 ±1.06E-2		1.74E+0 ±5.08E-3
		-		
5	5.67E+0 ±2.64E-2		4.46E+0 ±2.21E-2	3.97E+0 ±1.88E-2
6	-	-	7.80E+0 ±5.06E-2	7.14E+0 ±4.46E-2
	1.00E+1[c] ±3.54E-2			
7	-	2.62E+1 ±6.98E-2	1.97E+1 ±1.52E-1	1.88E+1 ±4.71E-2
	2.59E+1 ±6.88E-2	2.57E+1 ±1.10E-1		
		-		
8	-	2.75E+1[d] ±9.14E-2		
	2.71E+1[d] ±8.37E-2			
9			2.79E+1[d] ±9.32E-2	2.73E+1[d] ±9.06E-2

[a] Used as reference measurement. Reactivity obtained from CPSD23 breakfrequency measurement using Li detectors in the current mode.

[b] Error estimates are ±1 standard deviation.

[c] Multiple entries are repeat measurements.

[d] Reactivities not corrected for detection efficiency changes.

Table F.16. Low frequency coherence (γ^2_{23}) amplitudes

Configuration number	Current mode Li	Pulse mode Li	^{3}He	Fission chambers
1	8.18E-1 ±9.00E-2[a]			
2	6.74E-1 ±1.29E-1	7.24E-1 ±1.05E-1		
	7.73E-1[b] ±5.96E-2			
3	5.25E-1 ±4.43E-2		8.49E-1 ±8.66E-3	3.67E-1 ±1.50E-2
4	1.96E-1 ±2.59E-2	3.88E-1 ±5.64E-2		1.66E-1 ±7.45E-3
		2.29E-1[c] ±8.16E-2		
5	1.70E-2 ±2.97E-3		5.93E-1 ±7.59E-3	3.82E-2 ±3.19E-3
6	2.23E-3 ±9.10E-4	6.00E-3[c] ±1.64E-3	4.34E-1 ±7.76E-3	1.25E-2 ±1.41E-3
	2.57E-3 ±5.81E-4			
7	9.11E-5 ±3.37E-5	9.41E-4 ±1.82E-4	1.87E-1 ±6.40E-3	2.06E-3 ±1.44E-4
	9.21E-5 ±4.76E-5	1.22E-3 ±1.31E-4		
		2.22E-4[c] ±7.77E-5		
8	4.25E-5 ±2.09E-5	5.33E-4 ±1.22E-4		
	4.57E-5 ±2.54E-5			
9			1.27E-1 ±1.12E-3	8.96E-4 ±9.24E-5

[a] Error estimates are ±1 standard deviation.

[b] Multiple entries are repeat measurements.

[c] ^{252}Cf source located at core location C-6.

Note: Only fission chambers were not affected by the background gamma radiation.

Table F.17. Reactivities (-$) from low frequency coherence (γ^2_{23}) amplitudes

Configuration number	Current mode Li	Pulse mode Li	^{3}He	Fission chambers
1	2.31E-1 ±4.06E-1[a]			
2	-	4.04E-1[b] ±0.00E+0		
	4.04E-1[b,c] ±0.00E+0			
3	1.34E+0 ±4.15E-1		1.24E+0[d] ±0.00E+0	6.85E-1[d] ±0.00E+0
4	3.25E+0 ±7.25E-1	1.61E+0 ±6.87E-1		1.53E+0 ±8.14E-2
		-		
5	8.79E+0 ±1.64E+0		3.20E+0 ±1.56E-1	3.25E+0 ±1.56E-1
6	1.60E+1 ±3.28E+0	-	4.53E+0 ±2.03E-1	4.91E+0 ±2.43E-1
	1.54E+1 ±2.80E+0			
7	3.76E+1 ±7.16E+0	1.79E+1 ±4.71E+0	7.80E+0 ±3.30E-1	8.61E+0 ±3.06E-1
	3.75E+1 ±7.95E+0	1.66E+1 ±4.35E+0		
		-		
8	4.58E+1 ±9.47E+0	2.08E+1 ±5.50E+0		
	4.50E+1 ±9.78E+0			
9			9.31E+0 ±3.56E-1	1.09E+1 4.44E-1

[a] Error estimates are ±1 standard deviation.

[b] Used as calibration measurement. Reactivity obtained from rod calibration.

[c] Multiple entries are repeat measurements.

[d] Used as calibration measurement. Reactivity obtained from CPSD23 breakfrequency measurement using Li detectors in the current mode.

Note: Only fission chambers were not affected by the background gamma radiation.

Table F.18. Reactivities (-$) by other methods

Configuration number	IKRD[a]	3-point IKRD[a]	Rod calibration	2-D diffusion calculation[b]
1			1.43E-1	
2			4.04E-1	
3	6.50E-1 ±5.50E-2[c]			6.12E-1
4		1.18E+0 ±8.37E-2		
5	2.66E+0 ±1.90E-1	2.96E+0 ±2.03E-1		2.93E+0
6	4.69E+0 ±3.29E-1	6.10E+0 ±5.87E-1		5.22E+0
7	1.08E+1 ±5.41E-1	1.34E+1 ±7.91E-1		1.17E+1
8				
9				

[a]Rod drop with Li detectors in place. Inverse Kinetics Rod Drop (IKRD) algorithms are described in Appendix G.

[b]Calculations were for the worth of the full length control rods. No corrections were made for the partial insertions in the experiment.

[c]Error estimates are ±1 standard deviation.

APPENDIX G

INVERSE KINETICS ROD DROP ALGORITHMS

Two types of inverse kinetics rod drop algorithms will be reviewed: one for rod drops in a delayed critical reactor and one for rod drops in a steady-state subcritical reactor with an external source. The algorithm for rod drops in a delayed critical reactor is the one being used by Miller[64] for the Nuclear Engineering senior laboratory course at The University of Tennessee (Knoxville). The other algorithm is the three-point method developed by Allen.[65]

A. Rod Drops in a Delayed Critical Reactor

Assuming the point kinetics model (lifetime formulation), the kinetic behavior of a sourceless reactor may be represented by

$$\frac{dN(t)}{dt} = \frac{k(t)[1 - \beta] - 1}{\ell} N(t) + \sum_{i=1}^{6} \lambda_i C_i(t) \quad , \tag{G.1}$$

and

$$\frac{dC_i(t)}{dt} = \frac{\beta_i}{\ell} k(t)N(t) - \lambda_i C_i(t) \quad , \tag{G.2}$$

where

$N(t)$ = neutron population at time t,

$C_i(t)$ = group i delayed neutron precursor population at time t,

λ_i = decay constant of the group i delayed neutron precursors,

β_i = effective group i delayed fraction,

β = effective total delayed fraction = $\sum_{i=1}^{6} \beta_i$,

ℓ = prompt neutron lifetime, and

$k(t)$ = neutron multiplication factor at time t.

Solving for $k(t)$, Eq. (G.1) becomes

$$k(t) = \left(\frac{\ell}{N(t)} \frac{dN(t)}{dt} - \frac{\ell}{N(t)} \sum_{i=1}^{6} \lambda_i C_i(t) + 1 \right) \frac{1}{1 - \beta} \quad , \tag{G.3}$$

or

$$k(t) = \left(\ell \frac{d\ln(N(t))}{dt} - \frac{\ell}{N(t)} \sum_{i=1}^{6} \lambda_i C_i(t) + 1 \right) \frac{1}{1 - \beta} \quad . \tag{G.4}$$

The neutron multiplication as a function of time can be obtained if the derivative term and the values of $C_i(t)$ in Eqs. (G.3) or (G.4) are known. These quantities will be estimated.

Over small time increments after the reactivity of the reactor is changed, the neutron population is assumed to change exponentially, that is

$$N(t + \xi) \approx N(t) e^{\alpha \xi} \quad , \tag{G.5}$$

where α is estimated from two data points by

$$\alpha = \frac{d\ln(N(t))}{dt} \approx \frac{1}{\Delta t} \ln\left(\frac{N(t + \Delta t)}{N(t)} \right) \quad . \tag{G.6}$$

Also, assume that over small time intervals, the first order Taylor expansion of the neutron multiplication is adequate, that is

$$k(t + \xi) \approx k(t) + \frac{dk(t)}{d\xi}\,\xi \quad , \tag{G.7}$$

where the derivative is estimated as

$$\frac{dk(t)}{d\xi} \approx \frac{k(t) - k(t - \Delta t)}{\Delta t} = \frac{\Delta k}{\Delta t} \quad . \tag{G.8}$$

With these assumptions, a recursion relation for $C_i(t)$ can be obtained. Multiplying Eq. (G.2) by the integrating factor $e^{\lambda_i \tau}$ and integrating the resulting equation from $\tau = t$ to $\tau = t + \Delta t$, we get

$$\int_t^{t+\Delta t} \frac{dC_i(\tau)}{d\tau}\, e^{\lambda_i \tau}\, d\tau = \int_t^{t+\Delta t} \frac{\beta_i}{\ell}\, k(\tau) N(\tau) e^{\lambda_i \tau}\, d\tau \quad . \tag{G.9}$$

The left side of Eq. (G.9) becomes, after integration,

$$\int_t^{t+\Delta t} \frac{dC_i(\tau)}{d\tau}\, e^{\lambda_i \tau}\, d\tau = C_i(t + \Delta t) e^{\lambda_i (t+\Delta t)} - C_i(t) e^{\lambda_i t} \quad . \tag{G.10}$$

Using Eq. (G.10), Eq. (G.9), with some rearrangement, becomes

$$C_i(t + \Delta t) = C_i(t) e^{-\lambda_i \Delta t} + \frac{\beta_i}{\ell} \int_t^{t+\Delta t} k(\tau) N(\tau) e^{\lambda_i (\tau - t)}\, d\tau \quad . \tag{G.11}$$

Changing the variable of integration to ξ, where

$$\xi = \tau - t \quad , \tag{G.12}$$

the resulting integral becomes

$$e^{-\lambda_i \Delta t} \frac{\beta_i}{\ell} \int_t^{t+\Delta t} k(\tau)N(\tau)e^{\lambda_i \tau} \, d\tau =$$

$$e^{-\lambda_i \Delta t} \frac{\beta_i}{\ell} \int_0^{\Delta t} k(t + \xi)N(t + \xi)e^{\lambda_i \xi} \, d\xi \quad . \qquad (G.13)$$

Substituting from Eqs. (G.5) and (G.7), we get

$$e^{-\lambda_i \Delta t} \frac{\beta_i}{\ell} \int_t^{t+\Delta t} k(\tau)N(\tau)e^{\lambda_i \tau} \, d\tau =$$

$$e^{-\lambda_i \Delta t} \frac{\beta_i}{\ell} \int_0^{\Delta t} N(t)\left[k(t) + \frac{\Delta k}{\Delta t} \xi\right]e^{(\alpha+\lambda_i)\xi} \, d\xi \quad . \qquad (G.14)$$

Integrate the right side of Eq. (G.14), that is

$$e^{-\lambda_i \Delta t} \frac{\beta_i}{\ell} \int_t^{t+\Delta t} k(\tau)N(\tau)e^{\lambda_i \tau} \, d\tau =$$

$$\frac{\beta_i k(t)N(t)e^{\alpha \Delta t}}{\ell(\alpha + \lambda_i)} \left(1 - e^{-(\alpha+\lambda_i)\Delta t} + \frac{\Delta k}{k(t)\Delta t} \left[\Delta t - \frac{1 - e^{-(\alpha+\lambda_i)\Delta t}}{(\alpha + \lambda_i)}\right]\right). \qquad (G.15)$$

Using the first two terms of the infinite series representation of a^x, which is

$$a^x = 1 + x\ \ln(a) + \frac{(x\ \ln(a))^2}{2!} + \ldots + \frac{(x\ \ln(a))^n}{n!} + \ldots \quad , \tag{G.16}$$

the term $\Delta k/k(t)$ can be approximated by

$$\frac{\Delta k}{k(t)} \approx \ln\left[\frac{k(t)}{k(t - \Delta t)}\right] \quad . \tag{G.17}$$

Substituting Eqs. (G.15) and (G.17) into Eq. (G.15), we get

$$e^{-\lambda_i \Delta t}\ \frac{\beta_i}{\ell} \int_t^{t+\Delta t} k(\tau)N(\tau)e^{\lambda_i \tau}\, d\tau = \left(\frac{\beta_i k(t)N(t + \Delta t)}{\ell(\alpha + \lambda_i)}\right)$$

$$\times \left(1 - e^{-(\alpha+\lambda_i)\Delta t} + \ln\left(\frac{k(t)}{k(t - \Delta t)}\right)\left[1 - \frac{1 - e^{-(\alpha+\lambda_i)\Delta t}}{\Delta t(\alpha + \lambda_i)}\right]\right) . \tag{G.18}$$

The recursion relation for C_i can therefore be expressed as

$$C_i(t + \Delta t) = C_i(t)e^{-\lambda_i \Delta t} + \left(\frac{\beta_i k(t)N(t + \Delta t)}{\ell(\alpha + \lambda_i)}\right)$$

$$\times \left(1 - e^{-(\alpha+\lambda_i)\Delta t} + \ln\left(\frac{k(t)}{k(t - \Delta t)}\right)\left[1 - \frac{1 - e^{-(\alpha+\lambda_i)\Delta t}}{\Delta t(\alpha + \lambda_i)}\right]\right) \quad . \tag{G.19}$$

$C_i(0)$ can be obtained from Eq. (G.2). At steady-state, the time derivative is zero, so

$$C_i(0) = \frac{\beta_i N(0)}{\ell \lambda_i} \quad . \tag{G.20}$$

B. Rod Drops in a Steady-State Subcritical Reactor

Assuming the point kinetics model (generation time formulation), the kinetic behavior of a subcritical reactor with an external source may be represented by

$$\frac{dN(t)}{dt} = \frac{\rho(t) - \beta}{\Lambda} N(t) + \sum_{i=1}^{6} \lambda_i C_i(t) + S \quad , \tag{G.21}$$

$$\frac{dC_i(t)}{dt} = \frac{\beta_i}{\Lambda} N(t) - \lambda_i C_i(t) \quad , \tag{G.22}$$

where

$\rho(t)$ = reactivity in $\Delta k/k$ units at time t,

Λ = prompt neutron generation time, and

S = number of external source neutrons produced per unit time (assumed constant).

Combining Eqs. (G.21) and (G.22), we get

$$\frac{dN(t)}{dt} = \frac{\rho(t)}{\Lambda} N(t) - \sum_{i=1}^{6} \frac{dC_i(t)}{dt} + S \quad . \tag{G.23}$$

Given a detector with detection efficiency W, the detector count rate at time t is

$$CR(t) = \frac{WN(t)}{\Lambda} \quad . \tag{G.24}$$

Combining Eqs. (G.23) and (G.24), we get

$$\Lambda \frac{dCR(t)}{dt} = \rho(t)CR(t) - \sum_{i=1}^{6} \frac{dWC_i(t)}{dt} + WS \quad . \tag{G.25}$$

Divide through by β, that is

$$\frac{\Lambda}{\beta} \frac{dCR(t)}{dt} = \$(t)CR(t) - \sum_{i=1}^{6} \frac{dC_i'(t)}{dt} + S' \quad , \tag{G.26}$$

where

$$\$(t) = \rho(t)/\beta \quad ,$$

$$C_i'(t) = WC_i(t)/\beta \quad , \text{ and}$$

$$S' = WS/\beta \quad .$$

At initial steady-state, the time derivatives in Eq. (G.26) are zero, using discrete time t_j,

$$0 = \$_j CR(t_j) + S' \quad , \tag{G.27}$$

which can be arranged to get

$$\$_j = - \frac{S'}{CR(t_j)} \quad . \tag{G.28}$$

Also, at initial steady-state, the delayed neutron precursor concentration can be obtained from Eq. (G.22) with the time derivative set to zero, that is

$$C_i(t_j) = \frac{\beta_i N(t_j)}{\Lambda\lambda_i} \quad . \tag{G.29}$$

Using Eq. (G.24) and the definition of $C_i'(t)$ in Eq. (G.26), Eq. (G.29) becomes

$$C_i'(t_j) = \frac{\beta_i CR(t_j)}{\beta\lambda_i} \quad . \tag{G.30}$$

Integrating Eq. (G.26) over time intervals $\tau = t_0$ to t_1 and $\tau = t_1$ to t_2, the following equations are obtained:

$$\frac{\Lambda}{\beta}\,[CR(t_1) - CR(t_0)] + \sum_{i=1}^{6} [C_i'(t_1) - C_i'(t_0)] =$$

$$\$_f \int_{t_0}^{t_1} CR(\tau)\, d\tau + S'(t_1 - t_0) \quad , \tag{G.31}$$

and

$$\frac{\Lambda}{\beta}\,[CR(t_2) - CR(t_1)] + \sum_{i=1}^{6} [C_i'(t_2) - C_i'(t_1)] =$$

$$\$_f \int_{t_1}^{t_2} CR(\tau)\, d\tau + S'(t_2 - t_1) \quad , \tag{G.32}$$

where $\$_f$ is the final reactivity if t_0 is chosen after the reactivity change. The integrals in the above equations result in the total number of counts from the detector in the time interval enclosed by the limits. These are known. If a recursion formula could be obtained for C_i', the above equations could be solved for the remaining two unknowns, S' and $\$_f$.

Using Eq. (G.24) and the definition of $C_i'(t)$ in Eq. (G.26), Eq. (G.22) becomes

$$\frac{dC_i'(t)}{dt} = \frac{\beta_i}{\beta} CR(t) - \lambda_i C_i'(t) \quad . \tag{G.33}$$

Using an integrating factor, $e^{\lambda_i \tau}$, and integrating Eq. (G.33) from $\tau = t$ to $\tau = t + \Delta t$, we get

$$C_i'(t + \Delta t) = C_i'(t)e^{-\lambda_i \Delta t} + \frac{\beta_i}{\beta} \int_t^{t+\Delta t} CR(\tau)\, e^{\lambda_i(\tau - t - \Delta t)}\, d\tau \quad . \tag{G.34}$$

Assume that the detector count rate remains constant at $R(t)/\Delta t$ over the time interval Δt, Eq. (G.34) becomes

$$C_i'(t + \Delta t) = C_i'(t)e^{-\lambda_i \Delta t} + \frac{\beta_i}{\beta} \frac{R(t)}{\Delta t} \int_t^{t+\Delta t} e^{\lambda_i(\tau - t - \Delta t)}\, d\tau \quad . \tag{G.35}$$

Changing the variable of integration to ξ, where

$$\xi = \tau - t \quad , \tag{G.36}$$

Equation (G.35) becomes

$$C_i'(t + \Delta t) = C_i'(t)e^{-\lambda_i \Delta t} + \frac{\beta_i}{\beta} \frac{R(t)}{\Delta t} \int_0^{\Delta t} e^{\lambda_i (\xi - \Delta t)} \, d\xi \quad . \qquad (G.37)$$

Integrating Eq. (G.37), the recursion relation for $C_i'(t)$ is obtained, that is

$$C_i'(t + \Delta t) = C_i'(t)e^{-\lambda_i \Delta t} + \frac{\beta_i}{\beta} \frac{R(t)}{\Delta t} \frac{1}{\lambda_i} [1 - e^{-\lambda_i \Delta t}] \quad . \qquad (G.38)$$

The initial reactivity can be obtained from Eq. (G.28) after the calculation of S'.

VITA

Willie Tan King was born in Manila, Philippines, on April 12, 1954. He obtained his primary and secondary education from Xavier School, San Juan, Rizal, Philippines. After graduating from high school in April 1972, he and his immediate family immigrated to Knoxville, Tennessee, the United States of America.

He obtained his Bachelor of Science degree in Nuclear Engineering from The University of Tennessee (Knoxville) in August 1976. He worked on a research assistantship in the Instrumentation and Controls Division of the Oak Ridge National Laboratory and obtained his Master of Science degree in Nuclear Engineering from UT in August 1978. Upon graduation, he started working on his Doctor's degree in Nuclear Engineering at UT again using a research assistantship from the I&C Division of ORNL.

The author is a member of Tau Beta Pi and the American Nuclear Society.

He is, at present, unmarried.